Glacier erosion and response to climate, from Alaska to Patagonia

Michèle N. Koppes

A dissertation
submitted in partial fulfillment of the
requirements for the degree of

Doctor of Philosophy

University of Washington

2007

Program Authorized to Offer Degree:
Department of Earth & Space Sciences

University of Washington
Graduate School

This is to certify that I have examined this copy of a doctoral dissertation by

Michèle N. Koppes

and have found that it is complete and satisfactory in all respects, and that any and all revisions required by the final examining committee have been made.

Chair of the Supervisory Committee:

_____

Bernard Hallet

Reading Committee:

_____

Bernard Hallet

_____

Alan Gillespie

_____

David Montgomery

Date:_____

University of Washington

Abstract

Glacier erosion and response to climate, from Alaska to Patagonia

Michèle N. Koppes

Chair of the Supervisory Committee:
Professor Bernard Hallet
Department of Earth and Space Sciences

Contemporary glacial erosion rates based on sediment yields from tidewater glaciers in coastal Alaska and Patagonia are unsurpassed worldwide, and significantly exceed regional exhumation rates. These erosion rates are exceptionally high because the tidewater glaciers have been anomalously dynamic during a century of rapid retreat. To investigate the influence of climate and retreat on erosion, this dissertation presents seismic data defining the volume of sediments recently produced by one tidewater glacier in southeast Alaska and two glaciers in Chilean Patagonia. These glaciers have all been in steady retreat during the 20th century, and all calve into a fjord, providing an efficient trap for the sediment delivered to the calving front. Using a model of proglacial sedimentation, the annual sediment yield from, and erosion rate of, each glacier are calculated. A strong correlation emerges between glacial retreat and sediment yields, implying that most contemporary sediment yield data from retreating tidewater glaciers may correspond to recent erosion rates that are a factor of 3.5 ± 1.5 higher than over the entire advance-retreat cycle.

To examine the influence of ice dynamics on glacier erosion, the flux of ice into the Patagonian glaciers is compared to the retreat rate and to the sediment flux. Reanalysis climate data, adjusted to local conditions by correlation with weather gauges installed at the glacier termini, and coupled to ablation stakes and a linear model of orographic enhancement of precipitation over the glacier basins, were used to reconstruct the daily ice flux into and out of the glaciers over 50 years. Results indicate that basin-wide erosion rates increase as a function of ice flux through the equilibrium

line. As ice accumulation has decreased, the glaciers have responded by thinning and retreating rapidly, drawing down hundreds of meters of ice and delivering more sediment to the fjords. Interestingly, erosion rates from these glaciers, even after taking into account short-term acceleration during retreat, remain over an order of magnitude higher than long-term exhumation rates derived from detrital apatite thermochronometry in the basins, indicating that current glacier erosion rates far exceed orogenic rates, and reflect short periods of warming climate.

TABLE OF CONTENTS

Page

LIST OF FIGURES

Figure Number

Page

LIST OF TABLES

Table Number Page

ACKNOWLEDGEMENTS

My sincere appreciation goes to the Department of Earth and Space Science for their extensive long-term support, and especially to Professor Bernard Hallet for his vast reserve of knowledge and last minute editing marathons. The work was made possible by the generous support of the National Science Foundation, grants no. EAR-9628675 and OPP-0338371. This dissertation would never have been completed without the encouragement and support of my family and friends over the years.

INTRODUCTION

The importance of glaciers in landscape evolution

Glacial erosion has become a principal issue in contemporary research on the evolution of mountain ranges, as it plays an integral role in the coupling of tectonics and climate through its influence on exhumation and the removal of crustal material from the orogen. The climate-sensitive rate and spatial distribution of erosion can be as important as the tectonic environment in controlling the size, morphology, petrology and structural development of most major mountain ranges (e.g., Molnar and England, 1990; Raymo and Ruddiman, 1992; Brozovic et al., 1997; Beaumont et al., 2001; Montgomery et al., 2001; Koons et al., 2002). Moreover, rapid rock uplift may be localized in regions of rapid erosion due to significant feedbacks between denudation at the surface and the vertical advection of material from depth. Increased advection of material to the surface tends to warm the crust, thereby weakening it, focusing crustal deformation and consequent erosion in these areas (e.g., Zeitler et al., 2001; Finlayson et al., 2002) (Fig. 1).

From a continental-scale topographic analysis of the Andes, Montgomery et al. (2001) demonstrated that hemisphere-scale climatic variations in precipitation control the broad-scale morphology of the range. Zonal atmospheric circulation in the southern hemisphere creates a strong latitudinal precipitation gradient and a correspondingly strong gradient in erosion rate, as well as in the relative importance of fluvial, glacial, and tectonic processes both along and across the Andes. Their large-scale analysis provided insight into how climatic variations correlate with the observed latitudinal variations in width, hypsometry, and maximum elevation of mountain belts. The exhumation pattern determined from thermochronometric (Thomson, 2002) and geobarometric studies (Seifert et al.,, 2004) in the southern Andes, which reveal large differences in bedrock cooling ages across regions of similar topography and relief, also strongly suggest that climatic factors significantly affect exhumation across the Andean Cordillera.

The Montgomery et al. (2001) study also highlighted the close correspondence between mean and total relief and perennial snowline elevation in the southern Andes.

This supports the hypothesis, first presented in the late 19th century, that higher rates of erosion in glacial and periglacial environments effectively limit the elevation of mountain ranges (e.g., Porter, 1981; Brozovic et al., 1997). The idea of the "snow buzzsaw" assumes that glacial processes operating above the equilibrium-line altitude (ELA) place an upper bound on the elevation of topography through which only a small amount of material is allowed to rise, regardless of the rate of rock uplift (see Fig. 2 for an example of the buzzsaw concept in the western Americas). The buzzsaw hypothesis is tantalizing, in particular because it would suggest a lowering of the ELA relative to the peaks would increase the rate of ice flux, and consequently would accelerate erosion, assuming erosion rates scale simply with ice speeds. Thus, to understand the evolution of glaciated mountain ranges, one must understand how the erosion and sediment yields by climate-sensitive glaciers enter into the geodynamic mass balance of active mountain systems.

To improve understanding of how glacial erosion influences orogenic processes and how it may possibly reflect climate variability, the factors controlling glacial erosion rates need to be identified. In more temperate regions where erosion is primarily accomplished by rivers, a substantial set of published investigations provide insights into the factors controlling rates of fluvial erosion and sediment transport (e.g., Hack, 1975; Montgomery and Dietrich, 1992; Schmidt and Montgomery, 1995; Aalto and Dunne, 1998; Whipple and Tucker, 1999). Although the precise physics underlying erosion by water are not completely known, many empirical studies have shown that precipitation rates and basin characteristics such as drainage area and slope exert first-order controls on sediment yields (e.g., Milliman and Syvitski, 1992; Summerfield and Hulton, 1994; Hicks et al., 1996; Milliman, 1997; Hay, 1998; Aalto and Dunne, 2006), and have been supported by the results of hundreds of studies measuring sediment yields from fluvial basins worldwide. Empirical laws for fluvial erosion derived from these studies are robust enough that they have been used extensively in coupled surface-process/geodynamic models to simulate the essential topographic features of mountain ranges with either uniform or spatially varying precipitation (e.g., Tucker and

Slingerland, 1997; Ludwig and Probst, 1998; Whipple and Tucker, 1999; Roe et al., 2006). These models help us understand the key interactions and feedbacks

between surficial and tectonic processes in some of the most dynamic temperate mountain systems in the world.

Similar relationships among basin characteristics, climate and erosion rates have not yet been established for glaciated regions, which has complicated testing of the effects of glacial-interglacial cycles upon the evolution of mountains and relief (e.g., Tomkin and Braun, 2002). Not only are the rates of glacial and periglacial erosion not well known, with only a few dozen glaciated basins studied to date, but their sensitivities to climate changes are poorly understood. For instance, the sediment yields of basins generally increase with increased glacial cover (Harbor and Warburton, 1993), but glacier cover can also prevent other forms of erosion, such as aeolian or periglacial processes, from occurring. Moreover, if glaciers are frozen to their beds they may even effectively protect the land surface from both weathering and erosion (e.g., Drewry, 1986).

Compiling existing data from the limited studies that have empirically determined the rate of basin-wide erosion for a number of glaciers, Hallet et al. (1996) and Gurnell et al. (1996) both demonstrated that sediment yields (as a measure of erosion) from glaciated basins are greater than those from glacier-free basins of comparable size. However, neither compilation addressed what controls these rapid glacial erosion rates, for most of the handful of studies of sediment yields from glaciers were conducted with little attention given to the glaciers themselves, and many of the studies were focused on a small subset of glaciers in Alaska and northern Europe, chosen for ease of access as opposed to specific glacier dynamics. In fact, empirical data quantitatively linking basin-scale glacial erosion rates to pertinent glacier characteristics are scarce, and are confounded with inter-basin differences in bedrock resistance to erosion and with climate.

The paucity of empirical data on basin-scale glacial erosion rates contrasts with the considerable physical insight that has emerged from theoretical studies of the small-scale dynamics of glacial erosion (e.g., Rothlisberger, 1958; Boulton, 1974, 1979; Hallet 1976, 1996; Powell and Alley, 1997; Alley et al., 2000). The key controls on the rates at which individual erosional processes operate are widely recognized as a function of glacier characteristics (such as sliding velocity and variations in ice and water pressure) and bed properties (i.e., roughness, bedrock hardness and fracture toughness). Effectively using this insight into small-scale processes and expanding the scale to

derive basin-scale erosion rates is problematic, however, because we have little information about basal conditions and bed properties, and these are likely to vary significantly with time and space. Progress is being made towards modeling large-scale erosion (Braun et al., 1999; Merrand and Hallet, 2001; MacGregor et al., 2000, 2005; Tomkin and Braun, 2002; Tomkin, 2003) but these models still await validation from field studies.

Understanding the large-scale relationship between climate and glacial erosion is also vital for deciphering climate change from the rich glacial sedimentary record. Molnar and England (1990) first proposed that a transition to a colder climate may be responsible for the apparent increase in the rate of tectonic activity and denudation of valleys during the late Cenozoic, through enhanced glacial erosion. The change to a cooler, more variable climate and the onset of late Cenozoic glaciation coincided with a global increase in sedimentation beginning ~2-4 Ma (Hay et al., 1988; Zhang et al., 2001; Molnar, 2004). The massive late Tertiary and Quaternary glaciomarine sedimentary sequences found on high-latitude continental margins from the Antarctic to the high Arctic (e.g., Vorren et al., 1991; Riis, 1992; Riis and Fjeldskaar, 1992; Lagoe et al., 1993; Bart and Anderson, 1995; Elverhøi et al., 1995; Anderson, 1999) contain a rich history of climate change recorded in both proxy climate data (e.g., ice-rafted debris, fossil foraminifera, oxygen isotopes) and sediment accumulation rates that reflect climate-driven changes in glacial sediment yields from the Quaternary ice sheets. However, the sparse data currently available on both rates of glacial erosion and the spatio-temporal variation in production and transfer rates of sediment from glaciers to the continental shelves currently limit our ability to link these processes to one another.

This study attempts to address explicitly both the sediment yields and the pertinent dynamic characteristics of a number of glaciers in Alaska and Patagonia to determine how glacial erosion on a basin-wide scale and glacier dynamics are related. Constraining this relationship provides a means of quantifying the sensitivity of glacial erosion rate to ice dynamics and, ultimately, to climate, that should help in interpreting variations in sediment delivery to continental shelf margins throughout the Quaternary. The study also provides the first estimates of glacier sediment yields from the southern Andes, a region that contains some of the last significant stores of ice outside the polar ice sheets, and that has been focus of debates over the synchrony of Quaternary climate

change between the northern and southern hemispheres (e.g., Denton et al., 1999; Sugden et al., 2005).

Determining sediment yields from glaciers

The predominant method of determining glacier sediment yield has been to measure sediment collected at the snouts of calving glaciers. Measuring yields from calving glaciers takes advantage of the fact that most of the sediments produced by these glaciers get trapped in proglacial fjord basins, many of which terminate in bedrock sills or other narrow outlets. Unlike the delivery of sediment from land-terminating alpine glaciers, where measuring bedload and suspended load is physically and temporally challenging and much of the sediment may be transported away from the glacial foreland by rivers, the still waters of proglacial lakes and fjords are useful in that they do not differentiate between bedload and suspended load, englacial or glaciofluvial sediments, but tend to collect all the sediment exiting the glacier system in one place. Contemporary sediment accumulation near glacier termini in Alaskan fjords, the high Arctic and the Antarctic have thus been examined using sequential bathymetric maps, seismic reflection surveys, sediment traps and radioisotope analyses (e.g., Molnia, 1979; Carlson et al., 1983; Cowan and Powell, 1990, 1991; Harden, et al., 1992; Hunter et al., 1996; Powell et al., 1996; Powell and Alley, 1997; Elverhøi et al., 1998; Jaeger and Nittrouer, 1999; Koppes and Hallet, 2002, 2006). The basin-averaged erosion rate for a particular glaciated basin is then determined by dividing the volume of sediment delivered to the fjord per unit time by the contributing basin area. Glacial erosion rates can thereby be inferred from sediment yields at the snout of glaciers under the assumption that no significant change has occurred in either the amount of sediment stored under the ice or on hillslopes above the glacier surface. Because the vast majority of glaciers studied in this context have been retreating over the past few decades, the sediment released by them is not likely related to the reworking of proglacial drift. Nor is it likely related to substantial changes in stores of sediment on land, for drainage basins in rugged alpine areas typically have steep hillslopes and little sub- and supra-glacial sediment storage (Hallet et al., 1996). More importantly, given the massive sediment yields documented from these glaciers over periods of decades

and longer, the cumulative contribution of changes in such debris stored at the glacier bed and on the steep hillslopes is likely to be insignificant to the overall yield (Koppes and Hallet, 2002).

Effective glacial erosion rates averaged over entire basins differ considerably from glacier to glacier, and can vary significantly within individual glacier basins. Recently measured rates range from $<10^{-3}$ m/a to $>10^{-2}$ m/a, and can significantly exceed rates from non-glaciated basins of similar size. The highest known contemporary basin-wide erosion rates come from the large temperate tidewater glaciers of coastal Alaska (Hallet et al., 1996) (Fig. 3). These high rates in Alaska are influenced by a number of factors: heavy precipitation from Pacific storms (Wilson and Overland, 1987) that are orographically lifted by the highest coastal mountain range in the world (the Wrangell-St. Elias), glaciers large enough to cover well over half of their basin areas, pervasive fracturing and weakening of the underlying bedrock from extensive shearing along the major strike-slip faults that dissect the region (e.g., Plafker et al.,1994), and the potential input of subaerial, fluvially derived sediments into the fjords from the base-level lowering of tributary streams that were formerly dammed by the glaciers (Meigs et al., 2006).

The glacial erosion rates from Alaska have been regarded as being unusually high because they were measured during a period of rapid terminus retreat, when the glaciers were unusually dynamic and hence erosive (Koppes and Hallet, 2002). Over the past century, ice loss from these glaciers, primarily through calving, must have vastly outpaced the accumulation of ice in the basins in order to account for the regional drawdown of hundreds of meters of ice since the Little Ice Age (Brown et al.,1982). Rapid calving tends to be associated with high ice fluxes and rapid ice motion, as documented at Columbia Glacier in Alaska since the 1980s (Van der Veen, 1996) and more recently in the outlet glaciers of Greenland (Thomas et al., 2004; Howat et al., 2005; Rignot and Kanagatparam, 2006). High ice flux and rapid basal ice motion lead to high sediment flux (Humphrey and Raymond, 1994). Recent sediment yields, therefore, may not be representative of the long-term rates of erosion, but instead reflect a short-term (10-100 year) acceleration in glacier dynamics.

In order to understand how well short-term erosion rates represent the long-term impact of the glacier on the landscape, a simple index of the dynamic state of a glacier

as an indicator of the rate at which it can erode is needed. In this study, I seek a measure of the dynamic response of calving glaciers and their sediment yields to climatic and non-climatic drivers. Relating recent climate change, as well as non-climatic factors such as topography, to glacier dynamics and to short-term erosion rates provides a framework for deciphering the longer-term changes in glacial sediment yields throughout the glacial-interglacial cycles of the late Cenozoic.

Understanding tidewater glacier response to climate

Glacier advance and retreat are often used as indicators of regional climate change, however, this only works if the glaciers are responding to climate on similar time scales. If glaciers can fluctuate independent of climate, then a reliable climate signal cannot be deduced from a simple record of their oscillation history (Warren, 1993). Calving glaciers in particular have a complex relationship with climate change, largely due to their unique sensitivity to a number of non-climatic factors that can also dictate the rate of ice loss at the glacier terminus, including terminus topography, ice-front melt rates, and water depth (Meier and Post, 1987; Powell, 1991, van der Veen, 1996; Warren and Aniya, 1999; Motyka et al., 2003). Responses to climate change may be expressed both in length changes (i.e., change in areal extent) driven by differences in ablation and accumulation rates, and in changes in the calving flux, making calving glaciers more complicated recorders of climate than alpine glaciers.

Resolving the balance between climatic and non-climatic controls on the growth and decay of tidewater glaciers has wide significance because calving glaciers drain many of the remaining temperate icefields on Earth, including those in Alaska and Patagonia, which are a focus of debates concerning the synchrony of climate in the northern and southern hemispheres (e.g.,Steig et al., 1998; Denton et al., 1999; Sudgen et al., 2005). In particular, the overall variations experienced by the Alaskan and Patagonian glaciers and outlet glaciers of the Greenland ice sheet in recent years, and the acceleration of the thinning and recession of these glaciers during the last decade, are inferred to be a direct response to recorded climatic change (Arendt et al., 2004; Rignot et al., 2003; Rignot and Kanagaratnam, 2006). The interannual dynamics of the calving termini of these glaciers, however, and the corresponding sediment yields may

also be controlled by a number of other factors including topographic constraints and water depths (Meier and Post, 1987). Calving dynamics hence can magnify, nullify or reverse the trend that would be expected from climatic change alone (Warren and Aniya, 1999).

According to current models of calving dynamics (Meier and Post, 1987; Van der Veen, 1996), the terminus must be firmly grounded to be stable. Thinning, due to increased ablation or longitudinal stretching, causes the terminus to retreat until the ice thickness is once again enough to be firmly grounded. While the ice front is responding to changes in water depth, backstress from a bedrock high or valley constriction and/or changes in ice-front melt rates, the entire glacier may experience changes in longitudinal stretching, surface slope and/or ice thickness. For example, the start of rapid, long-term terminus retreat at Columbia glacier in Alaska was synchronous with increases in longitudinal stretching rates in the lower 5 km of the glacier (Venteris et al., 1997), which also lowered the surface. Combinations of increased ablation, thinning and fracturing due to longitudinal stretching, along with entry into deeper water by the collapsing terminus were all responsible for inducing rapid retreat at Columbia (Meier and Post, 1987; Venteris et al., 1997; Post, 1997), which continues today.

Understanding the response of calving glaciers and their sediment yields to climate requires not only consideration of changing conditions at the terminus, but the sensitivity of the individual calving glaciers to changing snowline. For example, the question of interactions between climate change and the response of the Patagonian icefields over long time periods has been investigated in a series of numerical modeling studies (Hulton et al., 1994; Hubbard, 1997; Cook et al., 2003), which all highlighted the complexity of the relationship between mass balance and climate in a region where a significant fraction of the icefields drained, via calving, onto the continental shelf. These models also highlighted the sensitivity of the regional ELA to small latitudinal shifts of the atmospheric and ocean fronts that drive changes in precipitation (Kerr and Sugden, 1994). Further modeling, using present-day climate records applied to the glacier surface to simulate mass gain and loss coupled with models of present-day sediment delivery and terminus dynamics, are needed in order to better constrain the response of glacial erosion and the calving glacier system to climate.

Outline of this research

This study compares measurements of sediment accumulation rates, the dynamics of glacier retreat, and modeled ice fluxes from several tidewater glaciers in Alaska and Patagonia during the past century. In comparing these processes, I am testing the hypothesis that glacial erosion rates increase linearly with ice flux through the glacier system, and examining the relationship between ice flux and retreat rate.

Much of our current understanding of the dynamics of tidewater glaciers and the tempo of glacier erosion has been derived from studies in Alaska (e.g., Meier and Post, 1987; Powell, 1991; Humphrey and Raymond, 1994; Van der Veen, 1996; Koppes and Hallet, 2002; Spotila et al. 2004; Gulick et al., 2004), including research at Tyndall Glacier in Icy Bay, which was part of this study (Koppes and Hallet, 2006). The results from studies of glacial erosion rates in the southern Andes, where the topography, glaciers and climate are comparable to those in Alaska, enable us to test whether the empirical relationships developed in the more intensely studied coastal Alaska ranges are widely applicable.

The dissertation is divided into chapters presenting the methods used and the results from each individual glacier studied. Chapter 1 presents the methodology used at each study site to calculate erosion rates. It also describes the use of a mesoscale atmospheric model, applied to a DEM of the glacier surface at two of the glaciers in Patagonia, to model recent ice fluxes through the glaciers. Chapter 2, focusing on Tyndall Glacier in Icy Bay, Alaska, highlights a strong correlation between contemporary erosion rates and retreat rates, and explores the relationship between contemporary glacial erosion rates and long-term rates. It also discusses the effects of glacier retreat on landscape relaxation and the contribution of non-glacially derived sediments to recently vacated fjords, which may inflate calculated erosion rates.

Chapter 3 focuses on Marinelli Glacier in Tierra del Fuego, Chile, providing a comparison between the magnitude and timing of erosion and retreat rates in Icy Bay with a similar system in Patagonia. In this chapter, the simple glacier mass budget model described in Chapter 1 is first applied to the surface of Marinelli glacier to explore possible mass responses of the retreating glacier to local climate change. The dynamics of the retreating glacier are also contrasted with changes in non-climatic controls near the terminus. The comparison in timing between changes in retreat and erosion rates at

Marinelli also provides insight into possible response times of the glacier system to changes occurring at the ice front.

Chapter 4 further elucidates the influence of climate dynamics on terminus retreat. In this chapter, ice fluxes and sediment fluxes from San Rafael Glacier over the past half century are modeled and compared. At San Rafael, the availability of several previously collected datasets of surface velocities and ablation rates have helped to constrain the ice mass budget model, providing additional insight into the response of glacial erosion rates to changes in ice flux.

The centennial history of terminus dynamics and sediment yields from San Rafael Glacier is further developed in Chapter 5, where a comprehensive review of the proglacial lagoon using acoustic reflection profiles illuminates how the glacier terminus responded to its bed as it fluctuated in the lagoon during the late Holocene. In particular, the submerged geomorphology of the lagoon provides constraints on the quantity and spatial distribution of sediments delivered to the moraines, and on the reworking of proglacial sediment during advances.

Chapter 6 looks at estimates of recent sediment yields from another Patagonian glacier, Tyndall Glacier, in the southeastern corner of the South Patagonian Icefield. Ice thicknesses and surface ice motion have recently been measured at Tyndall Glacier, hence ice fluxes could be estimated directly. The recent erosion rate and recent ice flux from Tyndall glacier provides a comparison with the rates and fluxes found at San Rafael.

Finally, Chapter 7 focuses on preliminary thermochronometric data collected in some of the same Patagonian fjords, and compares the contemporary erosion rates measured on times scales of 10^1 to 10^2 years to exhumation ages on scales of 10^5 to 10^6 years. The difference in denudation rates between centennial and orogenic time scale provides further insight into Quaternary erosion rates and their relationship to landscape evolution and the concept of the glacier as buzzsaw.

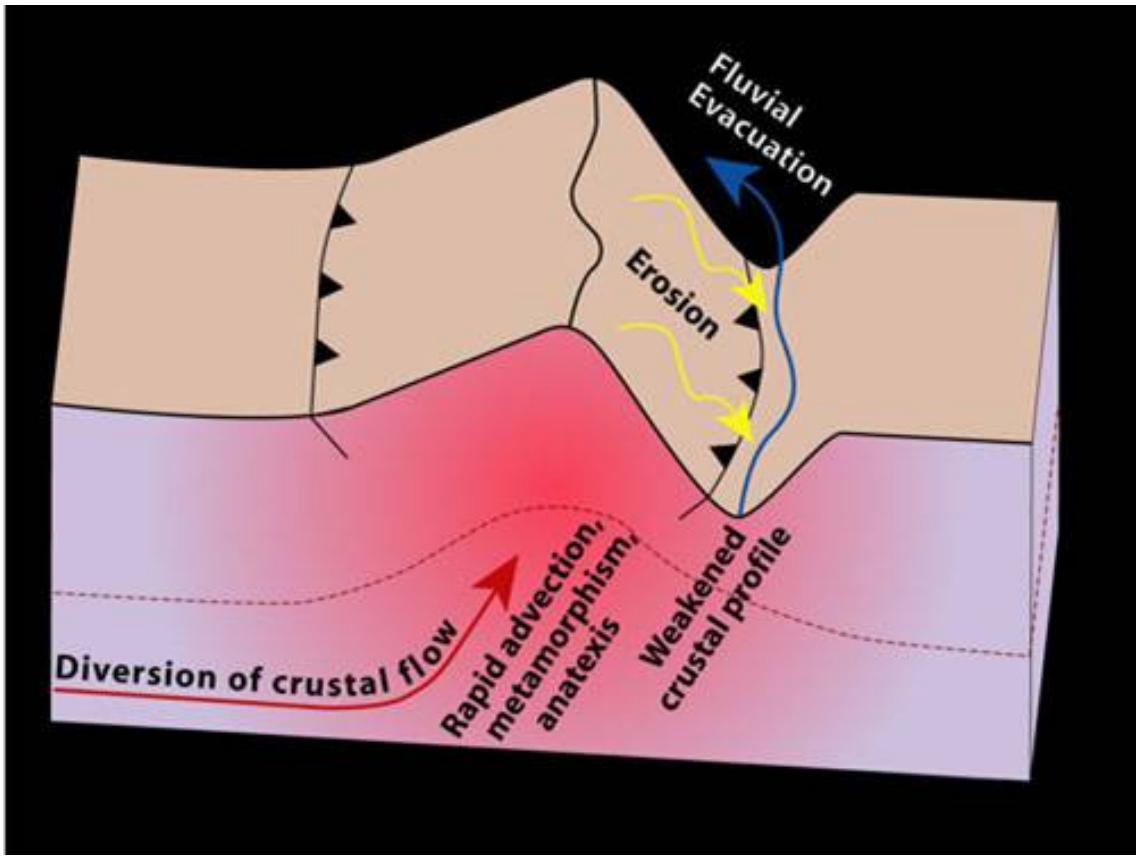

Figure 1. Diagram of the influence of erosion on rock uplift, from Zeitler et al. (2001).

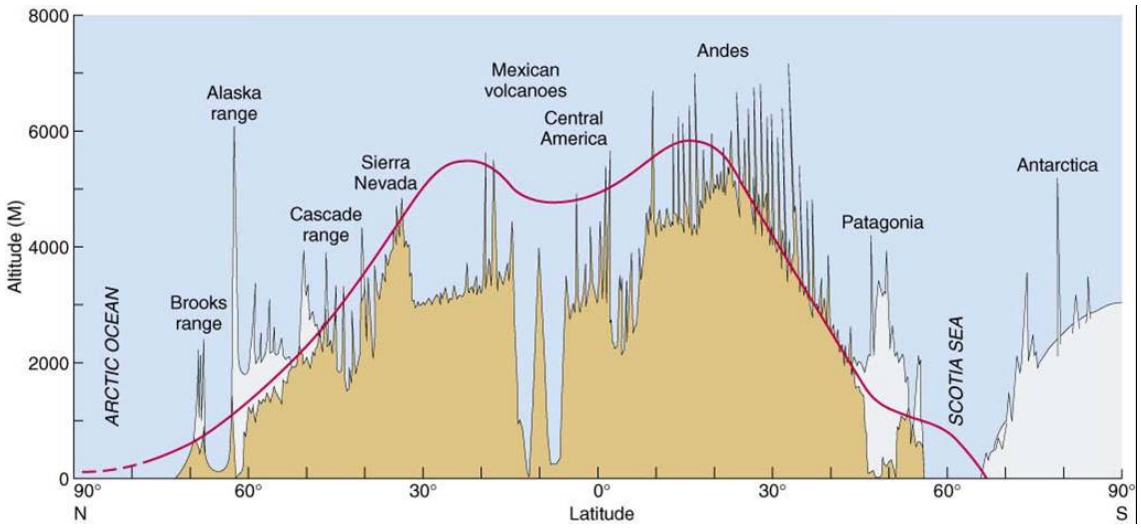

Figure 2. Elevation of the major ranges along the west coast of the Americas and mean snowline, from Skinner and Porter (2000).

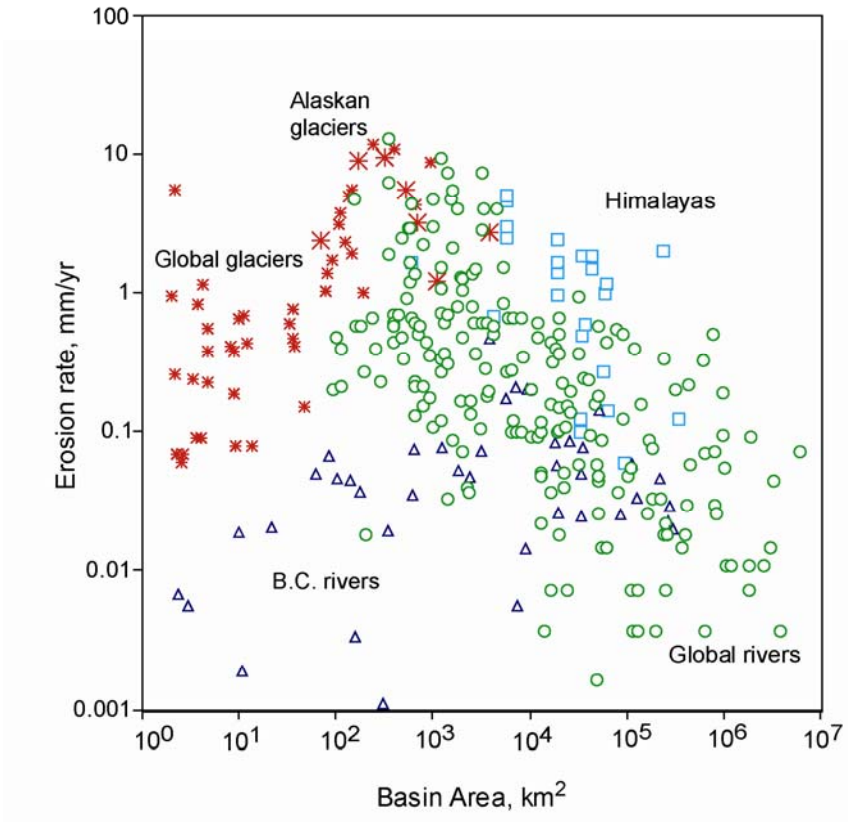

Figure 3. Erosion rates for glaciated and non-glaciated basins, from Hallet et al. (1996).

CHAPTER 1. METHODS

To quantify glacier erosion rates and to understand the relationship between sediment yields and glacier dynamics, several components need to be measured. This study is divided into two major efforts. The first is to quantify the magnitude and timing of sediment yields from several target glaciers in Alaska and Patagonia. The second, focused only on the Patagonian glaciers, is to quantify gains and losses in the volume of ice in these glacier systems, as an index of the basal processes that contribute to erosion. The methods used in each effort are described below.

A. QUANTIFYING SEDIMENT YIELDS

Total sediment accumulation data in each of the fjords was collected using bathymetry, GPS and acoustic reflection profiles (with the exception of Lago Geike, where no acoustic reflection was possible due to the necessity of overland access to the fjord). Bathymetric profiles in the fjords were collected at Laguna San Rafael and Lago Geike using a Lowrance 18-C sonar and GPS in March 2005. The Lowrance system contains a dual 50/200 Hz transducer, with a penetration depth of up to 500 m. The system was extremely portable, able to be deployed from a zodiac and small skiff, and could store up to 200 MB of sonar logs, tracklines and waypoints. It worked without issues in a range of freshwater and saltwater locations, with the exception of locations where the seafloor or lake bottom dropped rapidly, at which point the transducer would lose bottom and we had to stop the traverse and hold position until the system could find bottom again. The one severe limitation of the system was that the sonar logs, which charted latitude, longitude and depth at 20-m or 1-minute intervals, would save and export the coordinate system in Lowrance proprietary coordinates, which required additional software from Lowrance to convert to UTM, for use in further GIS processing.

Seismic interpretation of glacimarine sediments

Acoustic reflection profiles were collected in Icy Bay in July 1999, Laguna San Rafael in June 2005 and April 2006 and in Marinelli fjord in July 2005 using small vessels (the MV Cajun Cruncher in 2005, the MV Petrel IV in 2006) (Fig. 1.1). In 2005, acoustic profiles were acquired using Rice University's 300J, 4000 Hz Boomer and 1000J Sparker transducer with Benthos hydrophone, firing at 0.2-0.5 seconds. In 1999 and 2006, we used Dick Sylwester's Datasonics 750 Hz bubble pulser transducer and Benthos hydrophone, also firing at 0.5 seconds. Both transducer systems were able to penetrate the soft sediment in the fjord bottom and imaged at least one hard reflector at up to 120 m below the sediment surface, with decreasing penetration beneath. Traveling at boat speeds of 3 knots, the 0.5 second acquisition rate produced a record every 2.5 ft along the track.

We also collected CTD (conductivity, temperature, depth) profiles in the Patagonian fjords in June 2005 and April 2006 using a Seacat SBE 19plus to calculate the temperature, salinity and seismic velocity of the brackish water in the fjord, near the ice front and in the center of the fjord (Fig. 1.2). The average seismic velocity of the fjord waters recorded in all the CTD profiles, in both Laguna San Rafael and Marinelli fjord, was 1460 m/s. This velocity was used to convert two-way travel time in the seismic profiles to water depth, and compared to the bathymetry collected with the Lowrance system along the same tracklines to verify the precision of the sonar logs.

The seismic profiles, collected along a dense set of tracklines along and across the fjords and lagoon where ice-free conditions allowed passage, were used to reconstruct the glacimarine sediment thickness and depth to bedrock in the fjord. The seismic profiles were collected in both hard-copy form on an EPC, with a DGPS feed, and as digital files, and imported into the Chesapeake SonarWIZ SBP software program for additional filtering and analysis. A seismic velocity of 1740 m/s for the glacimarine sediments was used to convert two-way travel time to depth, which represents the upper end of measured seismic velocities for glacimarine muds (1640-1740 m/s, Stoker et al., 1997).

In all the fjords profiled, several facies were determined and recorded in the seismic images: 1) a laminated, semi-transparent layer presumed to be predominantly ice-distal glacimarine input with some subaerial fines, 2) a hummocky, chaotic facies

presumed to be ice-proximal, and, and 3) laminated and hummocky facies along the fjord walls associated with landslides and delta-fan complexes prograding into the fjord from tributary streams and fjord walls. These facies are characteristic of Alaskan fjords (e.g., Molnia et al., 1984). They are also evident in the seismic data collected by the USGS using the mini-sparker system on the M/V Growler in lower Taan Fjord in 1981 (A. Post, unpublished data). All three facies were underlain by a strong, often planar reflector interpreted to be the surface compacted by ice overriding during the last glacial advance.

GIS interpretation and error analysis of sediment volumes

From the seismic profiles along the tracklines of the boat, which provide an X,Y,Z database of both water depth and depth to the base of the proglacial sediments, both the bathymetry and the sediment thicknesses in the fjord between tracklines were extrapolated using the triangulated-irregular-network (TIN) function in ArcGIS. All seismic lines, satellite images and bathymetric profiles were projected in to UTM 18N, 18S and 19S coordinates using the NAD 1927 ellipsoid in Alaska, and the South American 1969 ellipsoid in Patagonia. The TIN function creates planar surfaces between three nearest neighbours in x,y,z space. The TIN was masked at the shoreline, derived from a digital elevation model (DEM) where bathymetry and sediment thickness was set to zero (the provenance of the DEM is described later in this chapter). The accuracy of the reconstructed TIN is obviously a function of the proximity of the tracklines to one another and to the shoreline. In order to do further computation on the surfaces, the TINs of bathymetry and subsurface sediment were then rasterized using the GRID function, set to a 60 x 60 m cell size. Once gridded, the difference between the bathymetry and subsurface layers was calculated using the cut-fill function, and the sediment volume determined using the 3D Analyst toolbox.

To determine the magnitude of the error in the sediment thickness measurements, I compared the original spot depths from the seismic profiles to the gridded depths at the same locations, using the leave-one-out cross-validation (LOOCV) method. The LOOCV method relies on removing one or more points or tracklines from the original database, re-running the TIN and GRID functions on the data, and

comparing the depths of the new grid to the depths of the points/tracklines that were removed. The new grid, generated with a subset of the data was then compared to the gridded depths generated when the entire original dataset was included, as a means of quantifying the error for interpolated points between the measured depths. A sample profile generated using the leave-one-out method is plotted in Figure 1.3. I used this method for the seismic records in Laguna San Rafael and Marinelli fjord and for the sequential bathymetric records in Lago Geike, recording the original depths, the gridded depths, and the distance and depths of the three nearest known points to the points that were removed. In the first run, a random assortment of spot depths were removed. In the second run, two E-W transects were removed, one from the outer fjord and one close to the ice front. The third time, two N-S transects were removed. The magnitude and percent difference (error) in the original and gridded depths, as well as the degree of correlation between the error and the distance and variability in the three closest known points, were recorded.

According to the results of the leave-one-out method, the interpolation and gridding of the data from the tracklines introduces on average a 19% error in total sediment thicknesses. The magnitude of the error increases with distance between tracklines and the amount of variability in the depths along the tracks, such that where the tracks are close and the bathymetry and sediment thickness is relatively uniform, the error was less than 10%.

I also estimate that user error in picking depths from the seismic profiles was approximately10μs, corresponding to ±1m (1-2%) error in sediment thickness. Using a seismic velocity in the sediments of 1740 m/s, at the high end of measured velocities for glacimarine muds (Stoker et al., 1997), introduces another up to 5% error in sediment thickness. Total error in the sediment thickness measurements for each fjord therefore approaches 25%.

Calculating erosion rates

To arrive at basin-wide erosion rates, the sediment volumes were binned between known terminus positions over time in the fjord, using the mask feature in ArcGIS. The sediment volume was divided by the time between the two known terminus

positions to obtain the average annual sediment flux into the fjord for that time period. This approach assumes that no deposition of sediment occurs until the ice front retreats past each bin in the fjord, and furthermore that deposition is occurring directly at the ice front and does not extend to bins further donwfjord.

The sediment flux can then by divided by the glacier basin area during that time, measured from DEMs (749 km^2 for San Rafael, 189 km^2 for Marinelli, 154 km^2 for Tyndall (AK), and 408 km^2 for Tyndall (Chile)) to calculate the basin-averaged sediment production rate. To convert this rate to the bedrock erosion rate, the ratio of the estimated density of glacimarine sediments (assumed to be 1.8 g/cm^3, out of a range from 1.7 to 2.0 g/cm^3) and crystalline bedrock (assumed to be 2.5 to 2.7 g/cm^3) was applied to the sediment production rate. Using these estimates for sediment and bedrock densities, neither of which were measured in the field, introduces additional potential error, which approaches 6-12% of the converted erosion rate. Adding this potential error to the error in the sediment thickness estimates described above brings the total error in basin-wide bedrock erosion rates to 30-37%.

The basin-averaged erosion rate at each glacier was then compared to the retreat of the terminus to quantify the effects of glacier retreat on erosion.

Glacimarine sedimentation model

To explore the temporal dimension of sediment production by these glaciers, I developed a simple numerical model of glacimarine sedimentation that enables calculation of the annual sediment output needed to produce the sediment package observed in the proglacial fjord of any retreating tidewater glacier with a known retreat history. The model is described in Koppes (2000) and Koppes and Hallet (2002). The thickness of sediment at any one point in the fjord reflects a combination of two simultaneous processes: the variable rate of sediment delivery to the terminus, and the rate of terminus retreat. Where one of these parameters is known, and the total sediment volume in the fjord is measured, the other parameter can be calculated, given the relationship

$$S = \int_0^t \dot{S}_0 e^{-\dot{R}t / x_*} dt$$

where S is the total sediment thickness, $\acute{S}_0$ is the time-varying sedimentation rate at the ice front, $\acute{R}$ is the time-varying rate of terminus retreat and x_* characterizes the distance away from the calving front over which the proglacial sedimentation rate decreases by 1/e. The model, which reflects prior studies documenting an exponential decrease in sedimentation rates with distance from a tidewater glacier (e.g., Cowan and Powell, 1991), enables one to reconstruct the temporal variability of the sediment flux to the terminus, S_0(t), for glaciers where the annual retreat rate can be interpolated from maps and photos and the total sediment thickness S is known from seismic profiles.

The volume of glacigenic sediment measured in the fjord was parsed into 250-m bins (in the case of Tyndall (AK) and Marinelli) and 100-m bins (for Laguna San Rafael) and input into the model. The annual retreat rate for the ice front was interpolated between years when the terminus position was known from maps, photos and satellite images using a cubic spline function, as available in MATLAB. The terminus position at each year and the distribution of sediment in each bin were then entered into the model. Through an iterative process, I then reconstructed the sediment flux from the glacier at each time step that is required to account for the observed total sediment accumulation at the end of the model run.

Sediment traps

To better understand the decrease in sedimentation rates away from the ice front, a critical parameter for the glacimarine sedimentation model described above, a set of sediment traps was built to be deployed near the glacier termini. Due to logistical constraints and the presence of heavy brash ice in many of the fjords, I was only able to deploy the traps in Marinelli fjord. Due to the limited time available for the field campaign at Marinelli fjord, the traps were collected three days later. The sediment traps were built by Randy Sliester of Raytheon Polar Services based upon a design by Eugene Domack and with some modification of materials for deployment from a small boat into waters covered with significant brash ice. They are cones with an upper diameter of 51 cm and covered with a plastic grid to prevent ice blocks from blocking the opening, and a 500ml polyethylene nalgene bottle to collect sediment screwed into the base (Fig. 1.4). At each deployment station, 331, 478 and 920 m from the ice front, three traps were aligned in a

vertical array, at 5m, 25m and 50m above the seafloor, held together and in a vertical position with nylon line, 200 lbs of bottom weights, two subsurface floats and a surface indicator float. The bottom weights were unfortunately not sufficient to prevent drag on the traps from icebergs and bottom currents, and all three of the trap arrays were dragged up to 400 m away from the ice front during the period of deployment. Because of the probability that dragging of the weights across the bottom stirred up a significant amount of sediment from the sea floor, only the traps 50 m above the seafloor were recovered and the sediment in them collected and measured. I assume that density and salinity gradients of the seawater in the fjord prevented turbidity plumes generated by the dragging of the bottom weights from rising more than 50 m into the water column and infilling the upper traps.

B. QUANTIFYING ICE FLUXES

An important objective of this study is to seek a relationship between an index of glacier dynamics and the sediment yields from each glacier, in order to better understand controls on glacial erosion rates. For steady-state conditions, the volume of a glacier is fixed and the ice motion is such that it conveys sufficient ice into the basin, and it compensates for ice loss below the accumulation area. Under changing climatic conditions, glaciers grow or shrink and the rate of ice motion varies correspondingly. Increases in the ice flux of a glacier generally results in accelerated basal motion – the key variable impacting the rate of erosion. Where direct measurements of ice thickness, ice motion and mass balance on glaciers are available over an extended period, they provide an index of changes in ice speed at the bed of the glacier. In the absence of such direct measurements, (e.g., at Marinelli and San Rafael glaciers), I estimated changes in ice flux at the ELA where erosion is expected to be greatest, by modeling the gain and loss of ice through these glaciers as a function of climatic variables.

Any changes in glacier volume, such as would accompany glacial retreat, would result from a disparity between the rate at which ice is added to, and lost from the glacier:

$$\frac{\partial V}{\partial t} = \frac{\partial Ice_{in}}{\partial t} - \frac{\partial Ice_{out}}{\partial t}$$

The amount of ice added to a glacier per unit time is the sum of snowfall over the glacier surface, and, for a calving glacier, the amount of ice lost is the sum of both ablation from the glacier surface and melting (and calving) from the ice front. Hence, the equation above can be rewritten as:

$$\frac{\partial V}{\partial t} = (P_{snow} * A_{gl}) - (\alpha * A_{gl}) - (C * A_{term})$$

where P_{snow} is the rate of snow addition to the glacier surface (A_{gl}), α is the ablation rate, and C is the rate of ice loss resulting from both iceberg calving and melting across the

terminus area (A_{term}). The snow input and the ablation rate over time are both functions of the local temperature at each elevation (T_{avg}) on the glacier surface, which can be reconstructed from a single point on or near the glacier if the environmental lapse rate (T_{lapse}) is known. The snow input also scales with precipitation (P), which tends to vary orographically (represented by a spatially varying factor k)

$$P_{snow} = f(k, P, T_{avg}, T_{lapse})$$
$$\alpha = f(T_{avg}, T_{lapse})$$

For a stable glacier where $\partial V / \partial t = 0$, snow input ($P_{snow}*A_{gl}$) integrated over time should balance the ice loss due to both ablation ($\alpha *A_{gl}$) and calving ($C*A_{term}$). P_{snow} and α should also be equal at the ELA.

The glacier responds to any changes in ice budget in one of two ways: thinning (thickening) of the glacier and loss (gain) of ice at the terminus, expressed, respectively as changes in glacier surface elevation, z, and glacier length, x, as follows:

$$A_{gl}\frac{\partial z}{\partial t} + A_{term}\frac{\partial x}{\partial t} = (P_{snow} * A_{gl}) - (\alpha * A_{gl}) - (C * A_{term})$$

The first term represents thinning of the glacier surface over time, while the second represents the volume of ice lost from the terminus over time.

To explore the impact of climate forcing on these glaciers and the rate at which they erode over time, I compare changes in glacier volume (left side of equation), which can be measured from the topography and a recorded history of retreat, to the ice added and lost from the glaciers (right side of equation), which can be modeled using estimates of local climate variables. The biggest unknown in these systems is the last term of the equation, the calving flux, which is a function of both melt and calving rates along the terminus ice face. This calving flux provides a index of the ice flux at the ELA, the variable we are seeking. By adding measured and modeled volumes of ice into the

balance equation, where known, the flux of ice through the glacier can thereby be estimated over time.

The ice mass budget model accounts for estimated snow input and ablation (right side of equation), and it incorporates glacier geometry (A_{gl}), reconstructed climate data over the period that sediment accumulation has been measured (P_{snow}, T_{avg}, T_{lapse}), ablation rates (α), and orographic influences to reconstruct ice transfer rates through the glacier system (see Fig. 1.5 and described below).

Glacier geometry from DEM

To calculate the fluxes of ice into and out of a glacier where direct measurements of glacier dynamics do not exist, a quantitative measure of the surface area and elevation of the glacier is needed, as well as any changes to these parameters over time. These parameters were obtained from an SRTM 30-m digital elevation model (DEM), generated from NASA's Shuttle Radar Topography Mission in 2000. The DEM has a horizontal resolution of ~50 m. The SRTM mission spanned the globe from 60ºN to 60ºS. For field areas close to 60º, the shuttle imagery unfortunately contains many holes, due to the angle of the shuttle to the ground surface and the effects of topographic shielding from the steep relief in these glaciated landscapes. These holes in the DEM, most prevalent in Alaska and Tierra del Fuego, were filled with vertical information from the U.S. Geological Survey global 1km DEM datatset, with help from Harvey Greenberg.

The gridded cell location, cell count, basin area, surface area, and elevations were exported from ArcGIS into Matlab to constrain the glacier geometry in the ice flux model (A_{gl}) and the bathymetry at the ice front (A_{term}). The cell sizes of the grid differed dependent upon the size of the glacier and the size of the submarine basin, to more efficiently run the model: at Marinelli, the glacier surface was parsed into a cell size of 66 x 66 m^2 and the bathymetry into 60 x 60 m^2; at San Rafael, a cell size of 96 x 96 m^2 for the glacier surface and 60 x 60 m^2 for the bathymetric surface was used. From the combined SRTM DEM of the ice surface above sea level and the gridded bathymetric data from the seismic profiles, the volume of ice lost from the terminus over time, and an estimate of the thinning rate upstream of the terminus, could be calculated as well.

Local climate data collection

To assess local climate at the glaciers and be able to estimate the flux of ice in and out of the glacier system, I installed three automated weather stations near the glacier termini in Patagonia during the 2005-2006 field seasons. Each station was comprised of two ONSET R2M 0.2mm tipping bucket rain gauges to measure precipitation (water only, not snow), and one 2-channel internal-external ONSET HOBO temperature gauge, measuring ambient air temperature (internal) and soil temperature (through an external probe). The soil temperature was measured at 2 cm below the surface as an indicator of snow cover, and hence recorded periods when the rain gauge measurements should be used with caution. When snow was present, the external probe recorded uniform temperatures over the diurnal cycle, and the rain gauge data was excluded from the precipitation totals.

The gauges were deployed approximately 5-40 m above sea level, at the entrance to the fjords. At Laguna San Rafael, the gauges were set up in a clearing next to the park headquarters, approximately 8 km from the ice front, so that they could be monitored by the park rangers who live there year-round. Another station was deployed on a nunatak on the Little Ice Age moraine at the entrance to Marinelli fjord. At both sites, two rain gauges were deployed to check for consistency, and one temperature gauge was installed at ~1 m above the ground surface (above the potential snow surface and out of the way of rodents). A third station was installed ~8 km from Lago Geike and the terminus of Tyndall glacier, but was unable to be recovered.

The gauges collected temperature data at 15-minute intervals from March 2005-June 2005 and at 1-hour intervals from June 2005 onwards; precipitation data were collected with a time and date stamp for each 0.2mm tip. A machined cone was added to one of the two tipping buckets at each site to decrease its surface area by 40% and hence increase the volume of rainfall necessary to generate a tip from 0.2 to 0.5 mm, so that the memory card would not fill up and overwrite data before the end of the period of deployment (Onset only installed memory to measure 8000 tips, or 1.6 m of rainfall, before shutting off). The rain gauges were deployed in open clearings at ground level, leveled and secured to an aluminum platform with carriage bolts. The platform, which

extends 3’ in a cross configuration and was buried with large cobbles, helped to secure the gauges on the ground.

Gauges at the San Rafael site were installed and deployed on March 29, 2005. The gauges were first revisited and downloaded on June 30, 2005 during the NBP 05-05 cruise. A data shuttle and instructions were left with the park rangers, who downloaded the gauges on November 1, 2005 (one of the tipping bucket gauges was not functioning after this deployment). The gauges were revisited, downloaded, checked and new batteries added on April 18, 2006, during the following field season and bubble pulser work with the M/V Petrel IV.

Gauges were installed and deployed at Marinelli fjord during NBP05-05 cruise on July 11, 2005. One rain gauge was installed on the low moraine behind a large erratic, approximately 6 m above sea level. The other rain gauge and temperature probe were installed on a bedrock bench on the nunatak, 27 m above sea level (Fig. 1.6). They were checked and downloaded 3 days later. Gauges were revisited and downloaded by Charlie Porter and Brenda Hall on April 16, 2006. The soil temperature probe had evidently been chewed by animals, and no data were collected on soil temperatures. The records from the tipping buckets were slightly offset – perhaps due to one of the cones detaching from the bucket, but no information was provided about the state of the gauges during data retrieval.

All in all, 12 months of rain and temperature data were collected at San Rafael, and 9 months at Marinelli. Annual rainfall at San Rafael for the period March 2005-March 2006, at sea level, was 3.2m. Annual rainfall at Marinelli was much lower: 811 mm in 278 days (midwinter to mid-autumn), which, if assumed to be representative for the whole year, would be 1.07 m annually. High precipitation occurs throughout the year, but maximum precipitation falls during the austral summer and early autumn.

Average annual temperatures for 2005-2006 were 8.6º C at San Rafael, 6.3º C at Marinelli. Daily and seasonal temperature variability is quite limited due to the vicinity and moderating influence of the Pacific Ocean. The maximum difference in monthly temperature between the warmest and coldest months was only 27º C at San Rafael, and only 15º C at Marinelli.

NCEP-NCAR reanalysis data

The gauge records were then compared to daily temperature, precipitation and wind speeds calculated from the Reanalysis Climate dataset generated by NCEP-NCAR (see Kalnay et al., 1996). The NCEP-NCAR Reanalysis dataset is a web-accessed, daily updated backcast global climate data collection. Based on global radiosonde and sea level pressure measurements first collected in 1948, the NCEP-NCAR model reconstructs multiple climate parameters at geopotential heights throughout the troposphere on a 2.5º by 2.5º grid (approximately 1.875º longitude by 1.9º latitude on a Gaussian grid). The NCEP-NCAR dataset provides, among many parameters, 6-hourly near-surface minimum and maximum temperature, daily zonal and meridonal wind speeds, snowfall and precipitation rates, from the present back through January 1, 1948. The benefit of this dataset is a comprehensive history of temperature and precipitation at gridpoints closer to the glaciers in question, and at higher temporal resolution, than existing climate records for the region. The only climate records in existence in Chilean Patagonia through the last century were limited to 12 Chilean Navy lighthouses on the coast, and the towns of Puerto Montt (43ºS) and Punta Arenas (53ºS). Given the high variability of climate and the sparse weather stations along this long latitudinal transect, the NCEP dataset helps to fill in variability in the climate record, and helps determine a more realistic record of the climate over San Rafael and Marinelli glaciers.

To estimate average temperature and accumulation rates on the glaciers since 1950, the closest NCEP gridpoint to the terminus of each glacier, and to the gauges installed, was chosen. For San Rafael, the nearest gridpoint is 46.6ºS, 73.125ºW, referred to as MSV (Monte San Valentin); at Marinelli, the nearest reference gridpoint is 54.285ºS, 69.375ºW. Parameters collected from the NCEP-NCAR daily dataset at these gridpoints include: the daily maximum and minimum temperatures at 2 m above ground (T_{max}, T_{min}, output in Kelvin), the precipitation rate at the surface (prate, output in $kgms^{-1}$), the zonal and meridonal wind speeds at 10 m above ground (u,v, output in ms^{-1}; westerly is positive for zonal speeds, northerly is positive for meridonal speeds), and the temperature at various geopotential heights (1000, 925, 850, 700, 600, and 500 mb).

The measurements of precipitation and temperature at the glacier termini were compared to the NCEP-NCAR reconstructed minimum and maximum above ground temperatures and precipitation rates at the nearest gridpoint for the time period of gauge deployment (March 2005 to April 2006 at San Rafael, July 2005 to April 2006 at

Marinelli). Daily precipitation rates were also compared to the zonal and meridonal winds to illuminate any relationships between storm strength and local precipitation. A least-squares fit regression was done to compare each parameter. The regression was then applied to daily NCEP-NCAR results for the timeframe 1950-2004 to estimate precipitation and temperature at the glacier terminus prior to our instrumental records. The best-fit regressions used at San Rafael were:

$T_{maxSR} = 0.8945(T_{maxNCEP}) + 6.625$ (R^2=0.719; n=398, P<0.0001)
$T_{minSR} = 0.6115(T_{minNCEP}) + 3.33$ (R^2=0.614; n=398, P<0.0001)
$P_{SR} = 0.7797(P_{NCEP}) + 0.913(U_{NCEP}) + 0.8217$ (R^2=0.495; n=396, P<0.0001)

Where $T_{maxSR,}$ T_{minSR} and P_{SR} are the daily maximum and minimum 2m air temperature and daily precipitation rate from the gauges at the CONAF guard station, and $T_{maxNCEP}$, $T_{minNCEP}$, P_{NCEP} and U_{NCEP} are the maximum and minimum 2m air temperature, daily precipitation rate and zonal wind speed (m/s) from the NCEP-NCAR reanalysis dataset at the gridpoint MSV. The regression captures the timing of rain events quite well, but tends to underestimate the magnitude of rainfall in the larger storms (Fig. 1.7). It also captures the tendency of the NCEP data to underestimate both minimum and maximum daily temperatures (Fig. 1.8). Using the NCEP 10 m. above ground wind data improved the fit of the precipitation regression (the R^2 increased from 0.38 to 0.495), however, the NCEP data may overestimate the importance of surface wind speeds in the calculations of precipitation: the one record of wind speeds measured over the terminus of San Rafael in 1983 were on the order of 4-5 m/s (Kobayashi and Saito, 1985), while wind speeds in the NCEP model are typically 10-15 m/s.

The best fit regression equations for the gauges at Marinelli Glacier were:

$T_{maxMAR} = 0.647 (T_{maxNCEP}) + 3.43$ (R^2=0.627; n=279, P<0.0001)
$T_{minMAR} = 0.578 (T_{minNCEP}) + 1.00$ (R^2=0.615; n=279, P<0.0001)
$P_{SR} = -0.284(P_{NCEP}) + 1.006(V_{NCEP}) + 1.187$ (R^2=0.275; n=279, P=0.0002)

As a north-facing glacier in an east-west trending mountain range, with higher variability in the dominant westerly flow of wind and moisture wrapping around Cape Horn and arriving at Marnelli from the southwest to northwest, precipitation rates at Marinelli

appear to be more influenced by the magnitude of meridonal winds (N-S) than zonal winds (E-W) (Fig. 1.9). Hence, a multiple least-squares fit using meridonal wind strength (V_{NCEP}) and not U_{NCEP} , as in the equations used for San Rafael, was chosen for estimating local precipitation rates at this location (Fig. 1.10), however the correlation with the NCEP data still only accounted for less than 30% of the variability.

The NCEP-NCAR reanalysis data were also used to calculate the daily snowline altitude on the glaciers. The daily atmospheric temperatures at 1000 mb, 925 mb, 850 mb, 700 mb and 600 mb (corresponding to elevations of approximately 0, 750, 1500, 3100 and 5500 m.a.s.l.) at the nearest gridpoint were used to reconstruct the daily environmental lapse rate from 1950-2005, which averaged 5.44ºC/km for San Rafael, and 6.01ºC/km at Marinelli. This lapse rate (T_{lapse}) was then applied to the daily reconstructed average temperature at the glacier terminus (i.e., the gauge location) to locate the elevation of the 2ºC degree isotherm. All daily precipitation above this elevation on the glacier surface was then assumed to fall as snow, and was used to compute the daily snow flux into the glacier system. The daily snow flux (P_{snow}) is calculated as the modeled precipitation at sea level in water equivalents, multiplied by the surface area of the glacier at each elevation band above the 2ºC isotherm. The 2ºC isotherm was used, assuming that snowflakes generated at the freezing point fall from higher in the air column, and their rate of descent far exceeds the melt rate (Roe, 2005). This daily snowfall was then added up to compute the snow/ice input to the glacier. The flux of precipitation that fell as rain at altitudes lower than the 2ºC isotherm was computed but not included in the annual ice flux calculation. I assume that the input of rain did not affect the rate of ablation. I also did not include any percolation and refreezing of meltwater at depth, so the all the ice ablated was presumed to be lost from the system. As a first-order measurement, I assume uniform precipitation over the glacier surface, which is false (Carrasco, 2002), however, this provides a minimum estimate of the flux of ice into the glacier during the 1950-2005 timeframe.

Ablation model

The snow flux into the glaciers is then compared to the rate of ablation loss from the glacier and the loss of ice at the terminus to compute the yearly balance of ice for the

study glaciers. At San Rafael glacier, we were fortunate to be able to use an existing, short-term dataset on ablation rates collected by a Japanese expedition in the summer of 1983. The team set up a linear transect of 17 ablation stakes from the glacier terminus to just below the ELA, at 1050 m.a.s.l., for the month of December 1983 (Ohata et al., 1985). They also collaborated with the Chilean Air Force to set up a meteorological station, measuring daily temperature, precipitation and radiation, on the shores of Laguna San Rafael for the same time period (Enomoto and Nakajima, 1985). Using the cumulative results from the ablation stakes at the range of elevations, I was able to reconstruct the average rate of ablation as a function of the local air temperature and elevation. The local air temperature for each stake was calculated by 1) comparing the daily temperature registered at the meteorological station to the calculating the daily environmental lapse rates in temperature from the NCEP dataset, using the same method as described above, and then applying the lapse rate to the regressed NCEP ground temperature to estimate the air temperature at the elevation of each stake.

The Japanese study showed that the average rate of ablation decreases by 0.56 cm/day for every 100 m rise of elevation (Fig. 1.11). By recalculating the local air temperature, and summing the ablation from all the stakes, the results can be represented by a simple equation relating the rate of ablation to the local temperature:

$\alpha = 0.6645 * T_{avg}$ (R^2=0.20, n=49, P<0.0001)

where α is the ablation rate in mm/day, and T_{avg} the average daily local air temperature. For stake C2 (418 m.a.s.l.), which represented the longest record in the study (and highest cumulative ablation), yielded the following relation:

$\alpha = 0.803 * T_{avg} - 1.0899$ (R^2=0.98, n=8, P=0.0007)

Using the data from all the stakes provided a much poorer correlation with T_{avg}, therefore this latter equation was used in the ice flux model to calculate the daily ablation from San Rafael glacier. Since the ablation rate represents early summer melt rates only, and were predominantly measured on bare ice surfaces which are known to melt faster than snow, the ablation flux is assumed to be the maximum possible ablation from the system. In a second iteration of the model, I set the model to track whether precipitation

fell as snow or rain at the previous time step for each elevation. The ablation rate was then lowered by a ratio of 3/8 (the difference in positive degree day melt between snow and ice (Braithwaite and Oleson, 1989)) where fresh snow was present at each elevation above the 0ºC isotherm.

No direct information on mass balance exists at Marinelli Glacier, or anywhere in the Cordillera Darwin. To estimate ablation rates on Marinelli glacier, I turned to the nearest record of ablation and associated climate, at Glacier Lengua in the Gran Campo Nevado. (C. Schneider et al., pers. comm.). The Gran Campo Nevado is located approximately 285 km to the northwest of the Cordillera Darwin, at the western entrance of the Strait of Magellan. Though distant, the Gran Campo receives moisture from the same westerly and southwesterly storms that impinge on the Cordillera Darwin, and air temperatures are also heavily influenced by the cold Humboldt current running up the western shelf of Patagonia. Ablation stakes were set out in the lower reaches of Glaciar Lengua during the summer of 1999-2000 and measured daily by a German research team. Daily minimum and maximum temperatures were also collected at a nearby refuge, of similar elevation, during this period. The raw data was kindly provided by Christoph Schneider, from which I was able to compare the daily ablation rate to the mean daily air temperature at the refuge, to calculate a regional ablation rate in mm/day as a function of temperature (Fig. 1.12):

$\alpha = 7.416 * T_{avg} - 23.96$ ($R^2=0.987$, n=183, P<0.0001)

This was then applied to the surface of Marinelli Glacier in the ice budget model.

Orographic enhancement of precipitation

Assuming uniform precipitation rates over the glacier surface that equal those at the sea level rain gauges results in yearly ablation rates that far exceed accumulation, which is inconsistent with the presence of a glacier. Due to the size of the gridpoint spacing, the NCEP-NCAR model is unable to resolve topographic influences on the atmospheric dynamics from the presence of the Andes, which is only 40-60 km wide at the latitude of San Rafael and even less at Tyndall and Marinelli. A more realistic

representation of the precipitation into the glacier system would include some form of orographic enhancement, as the moisture laden weather systems from the Pacific are forced over the topographic barrier of the Andes. Anecdotal evidence indicates that precipitation rates on the plateau of the Northern Patagonian Icefield are up to 3 times the rates on the Taitao Peninsula to the west (Carrasco, 2002). To estimate the orographic enhancement factor at San Rafael glacier, I implemented Ron Smith's linear numeric orographic precipitation model over the centerline topographic profile of the glacier surface (with a lot of help from Gerard Roe). The model, described in Smith and Barstad (2004) and Roe (2005), incorporates a linear atmospheric response over complex terrain. Cloud microphysics in the model are represented by characteristic time delays for hydrometeor growth and fallout. The large-scale atmospheric flow is computed as a function of wind and temperature, and the amplitude and pattern of precipitation are then calculated as a function of that flow. Tunable parameters include the horizontal wind speed (u), meteoric fallout (tau_f), conversion time (tau_c), moisture scale height (H_m), moist static stability (N_m) and wave number (m,k). The most realistic response, which produced a peak enhancement factor of 2.5x that best fit observations of precipitation rates at coastal station and on the plateau of the HPN (Cararasco, 2002), was obtained with the following input parameters:

$u = 15$ m/s

$tau_f = tau_c = 1000$ s

$H_m = 3000$ m

$N_m = 0.005\ s^{-1}$

(see Fig. 1.13). The orographic model results in a precipitation distribution with enhancement up to 30 km west of the crest of the Andes, with the maximum enhancement ~17 km east of the rangefront, at ~1000-1200 m.a.s.l. on the glacier surface (Fig. 1.14). Interestingly, this peak coincides with the ELA; hence, the orographic model may amplify any impact of precipitation on changing ice fluxes in this target region of the glacier.

Unfortunately, the complexity of the terrain and the significant variability of wind directions at Marinelli glacier made the inclusion of a linear orographic model at this location unfeasible. A simple uniform enhancement factor of 3 due to orography, guided by observations of precipitation rates at coastal stations and on the Patagonian icefield

plateaus (Carrasco, 2002), was therefore used in lieu of the Smith and Barstad model for estimating precipitation onto Marinelli glacier.

Calving flux

Responses to climate change may be expressed not only in length changes but through changes in the calving fluxes (the ice flux at the terminus) of the glacier. In this model, the annual calving flux out of each glacier can be calculated by taking the difference between the snow flux in (with orographic enhancement) and ablation flux out, assuming steady-state conditions. Of course, these glaciers are not in steady state; for the purposes of calculating recent erosion rates, we are targeting systems that by necessity have been in steady retreat for the past few decades, opening up fjords for imaging. The calving flux (the last term of the equation) therefore represents the difference between accumulation and ablation, minus the other terms (the thinning of the ice surface and the ice lost from the terminus). The volume of ice loss at the terminus can be computed from the bathymetry and ice cliff height. The amount of thinning has been measured at San Rafael and Tyndall (Chile) glaciers only and is known for one period only, from 1979 to 2001, as measured from sequential Landsat images by Rivera et al. (2005). The overall thinning rate at the terminus of these glaciers can be estimated, however, from the difference between prominent trimlines on the valley walls and the ice cliff height, if the age of abandonment of the trimline is known.

At San Rafael glacier, the calving flux calculated in the ice flux model can be compared to surface velocities near the terminus of San Rafael measured during four time periods: through field observations in 1983 (Onata et al., 1985) and 1992 (Warren et al., 1994), and calculated from SAR interferometry during 1994 and 2001 (Rignot et al. (1996) and E. Rignot (pers. comm., 2006)). The annual surface velocities are multiplied by the terminus cross-section at that time, measured from the bathymetry of the ice front position on those dates and assuming an average ice cliff height above water of 40 m, to estimate the flux of ice through the calving front. The difference between the two calving fluxes – one the difference between the modeled snow flux in and ablation flux out and accounting for any changes in glacier size, the other based on ice velocity measurements near the terminus -- represents the annual variability in the

amount of thinning not accounted for and/or the level of error in the ice mass budget model.

Numeric model of glacier mass transfer

The glacier geometry, NCEP reconstructed climate data, orographic model and ablation-temperature model were used to reconstruct the volume transfer of ice through the glacier system. The model calculates the rate of ice accumulation from snowfall, and the ice loss from ablation. The difference represents, at a minimum, the annual calving flux through the ice front. Assuming mass conservation, the model also estimates the flux of ice through the ELA. For a flow chart of all inputs and components of the model, see Fig. 1.15.

Figure 1.1. Photograph of acoustic reflection profiler, deployed from the MV Cajun cruncher, outside Marinelli fjord.

Figure 1.2. Photograph of CTD deployment, Laguna San Rafael.

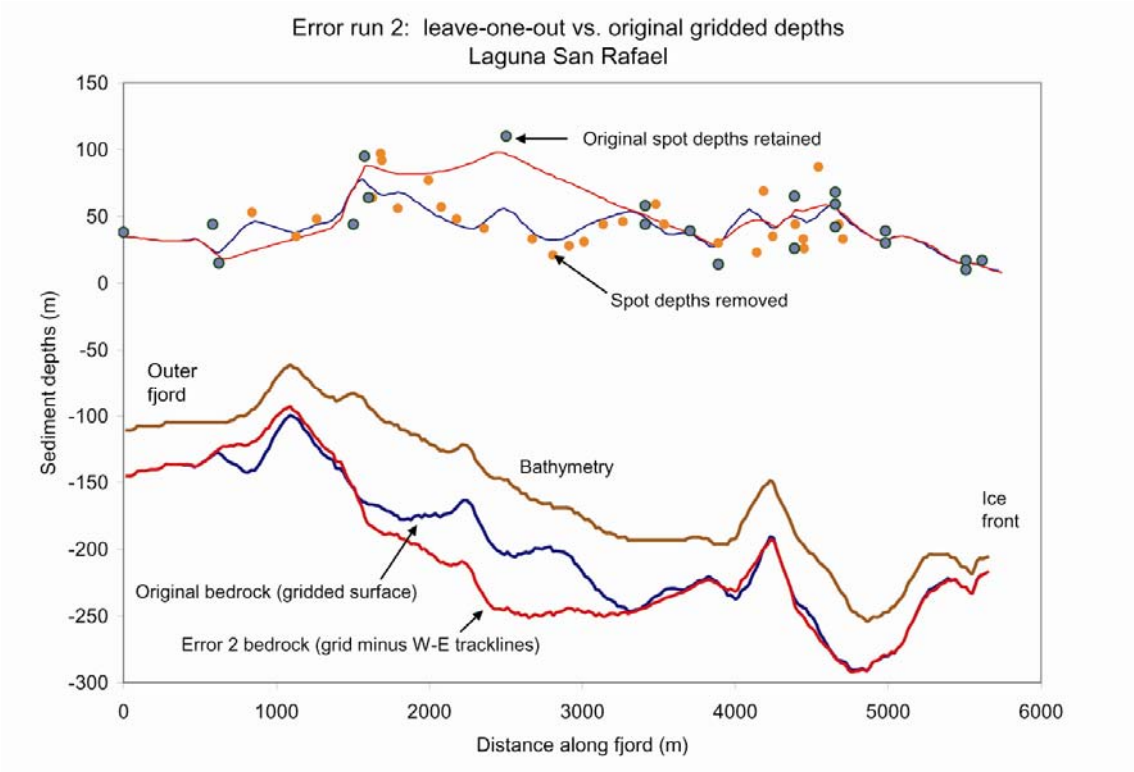

Figure 1.3. Example of the difference between original gridded bathymetric and sediment thickness surfaces and remeasured surfaces using the leave-one-out cross-validation method for error analysis. The error in triangulating surfaces from point depths was calculated by removing several sets of tracklines from the original dataset and then re-TINing and gridding the data to generate a new surface. The new surface is then compared to the original surface and to original spot depths to calculate the amount of offset in between known and unknown depths, and estimate the overall error in estimating sediment volume in the fjords.

Figure 1.4. Photograph of sediment traps used to measure sediment accumulation with distance from the glacier terminus, Marinelli fjord.

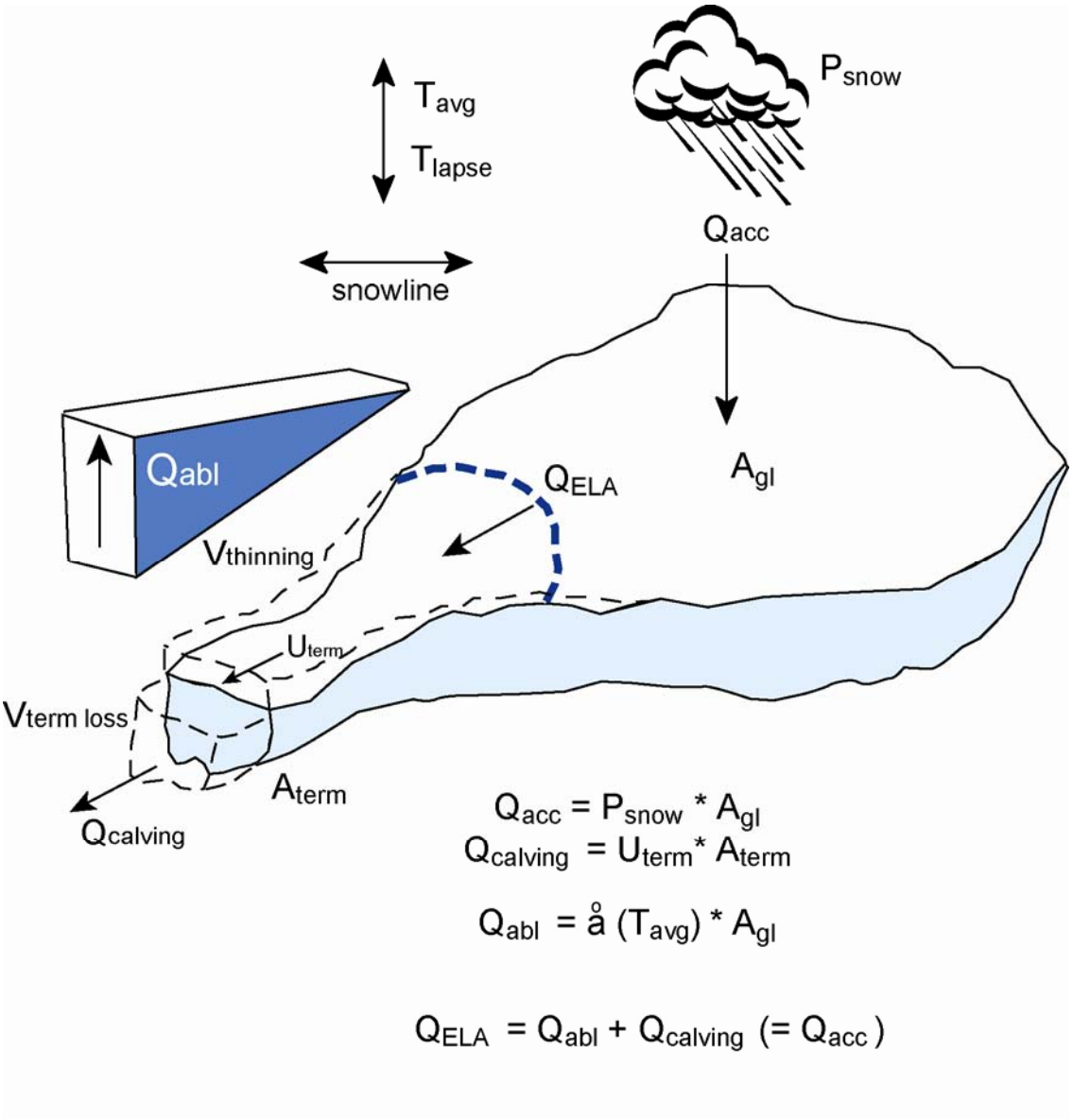

Figure 1.5. Cartoon of ice mass budget model.

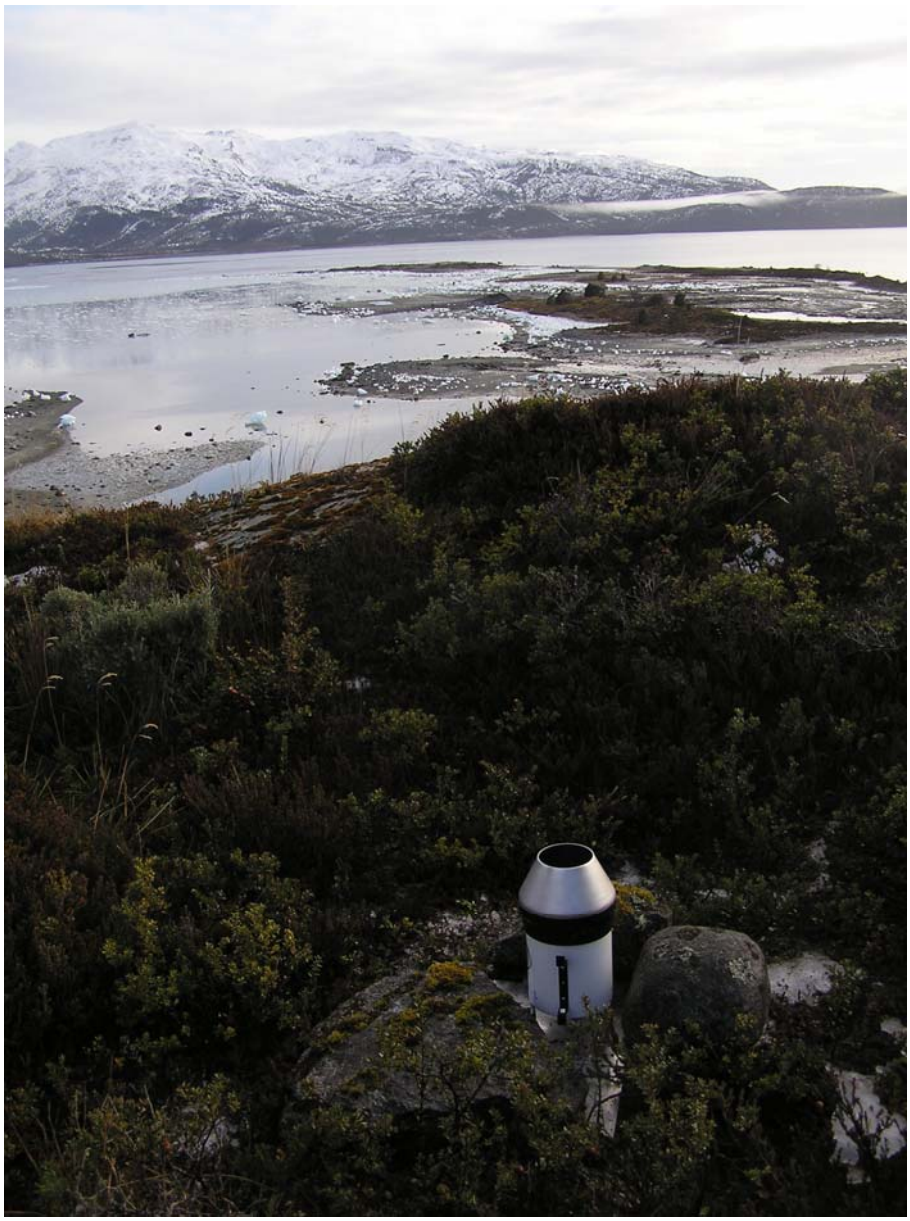

Figure 1.6. Photograph of an automated meteorological station, Marinelli fjord.

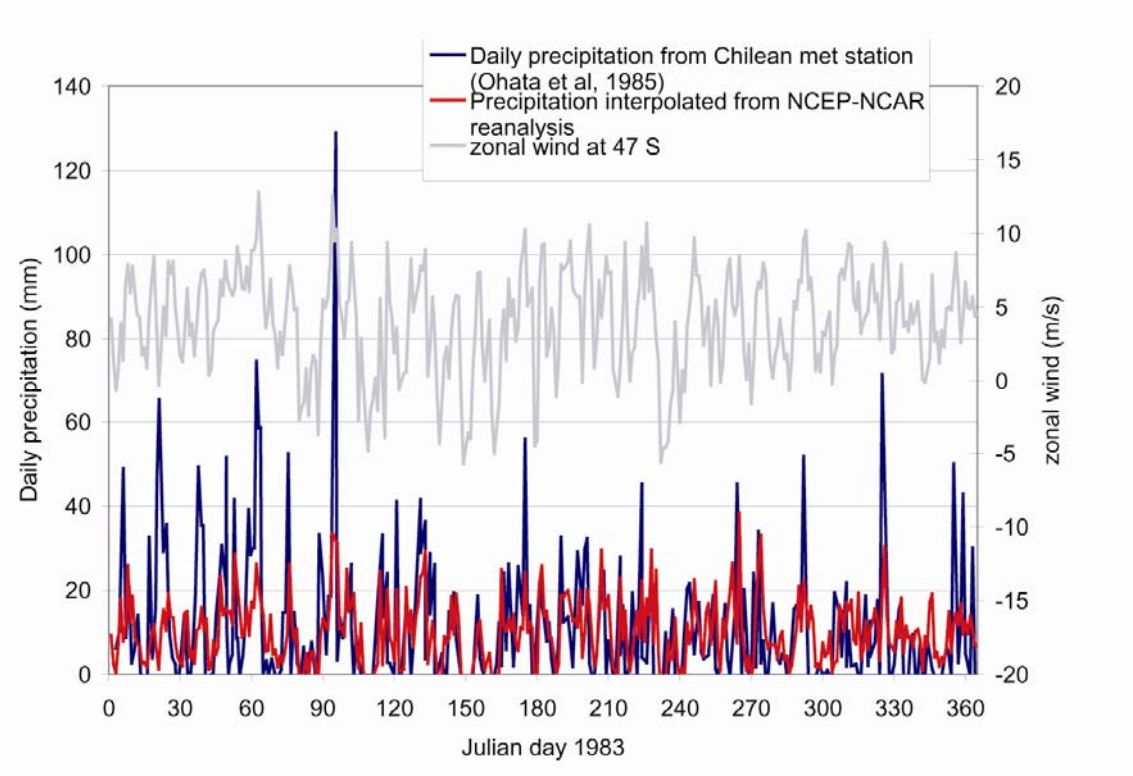

Figure 1.7. Comparison of gauge and NCEP precipitation rates in 1983, Laguna San Rafael.

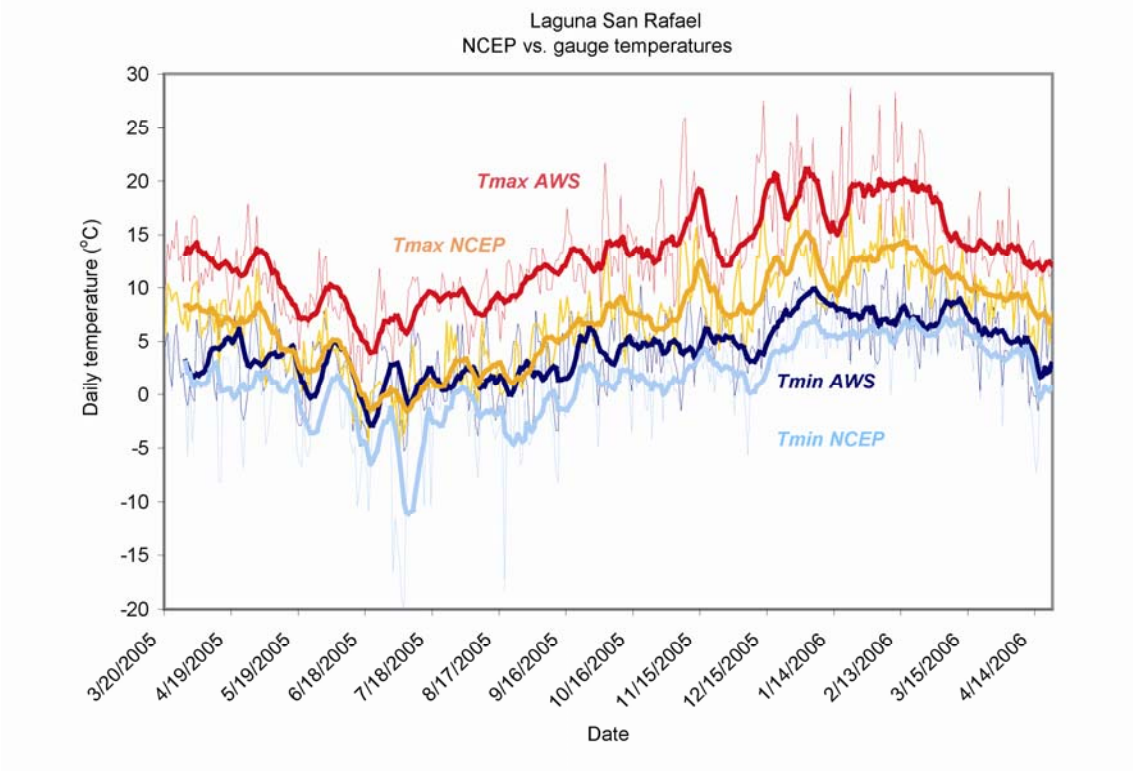

Figure 1.8. Comparison of gauge and NCEP temperature, March 2005 to April 2006, Laguna San Rafael.

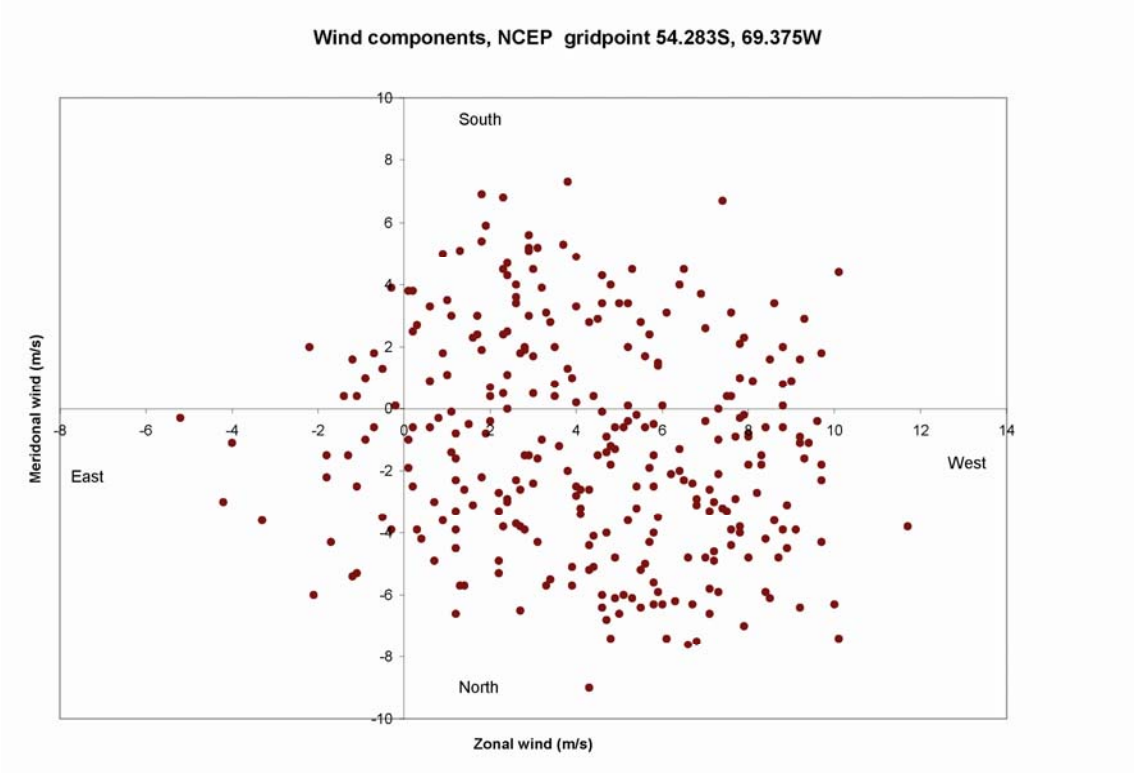

Figure 1.9. Daily wind direction and wind strength for 2005, Marinelli fjord.

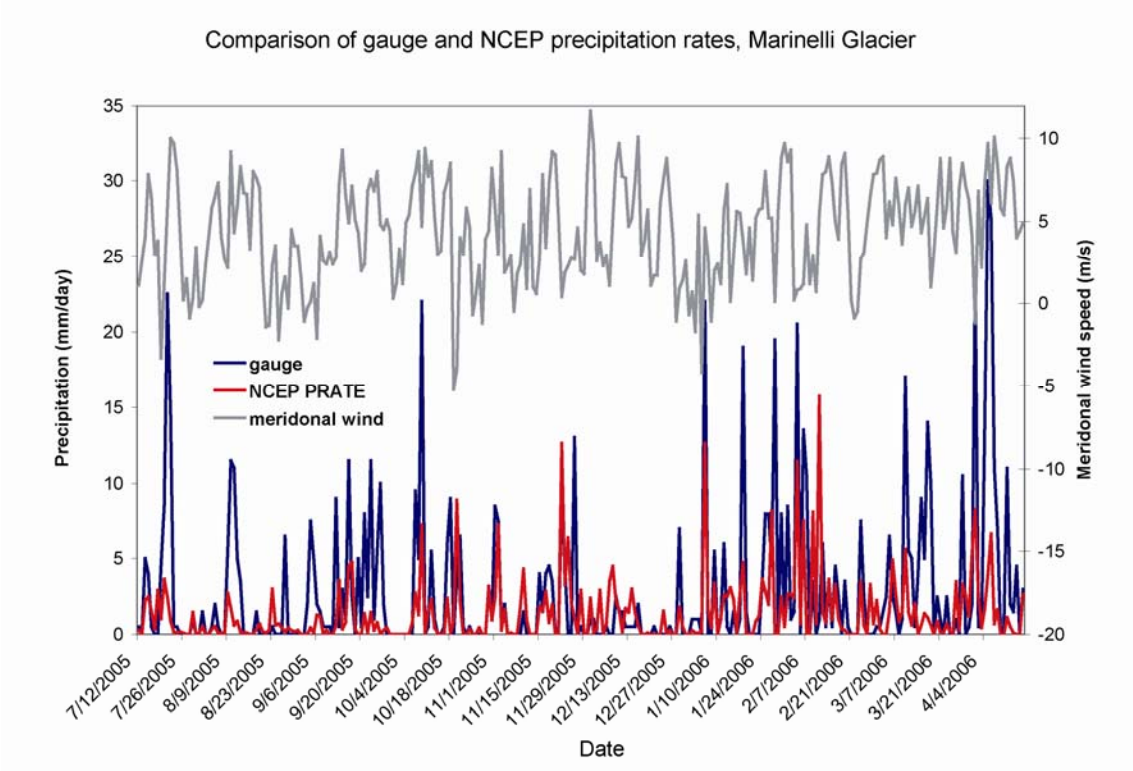

Figure 1.10. Comparison of gauge and NCEP precipitation rates, Marinelli fjord.

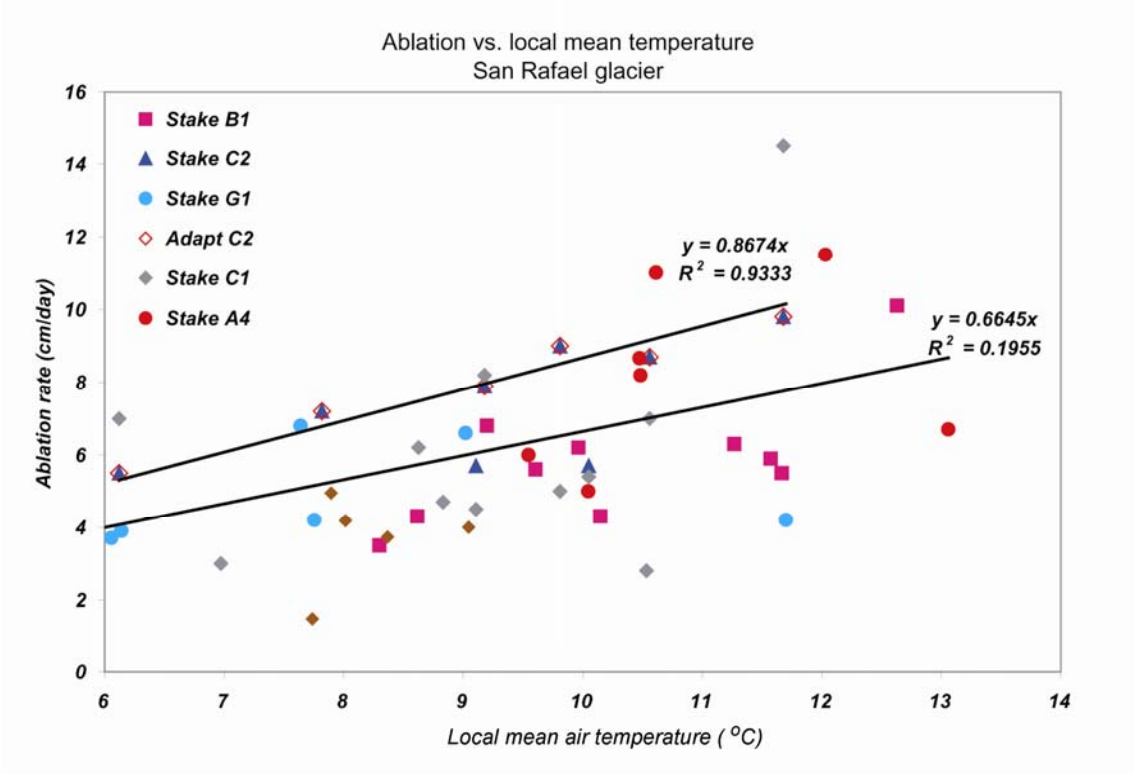

Figure 1.11. Ablation rate in cm/day vs. local mean daily temperature, San Rafael.

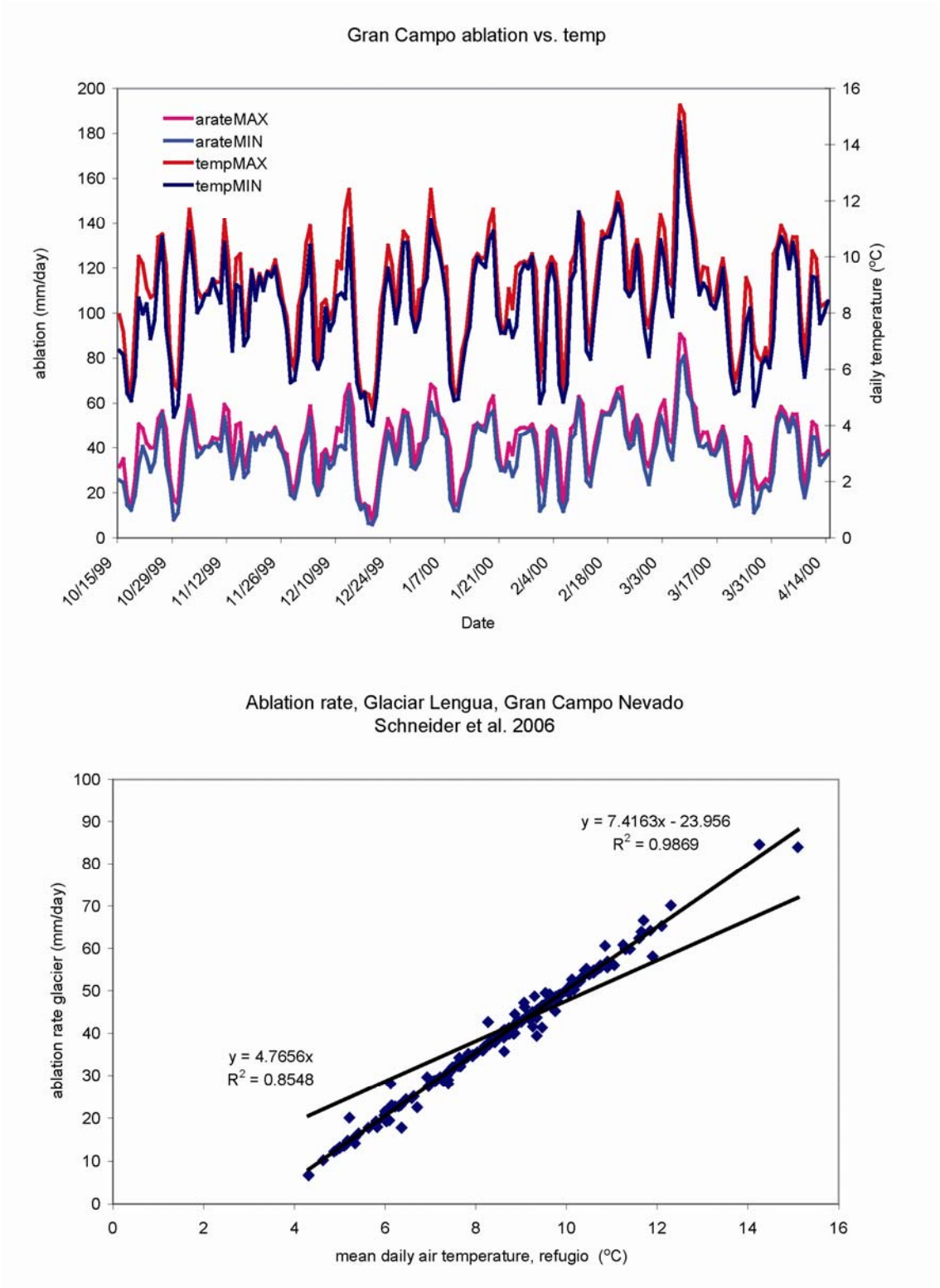

Figure 1.12. Ablation rate in mm/day vs. local mean daily temperature, Glaciar Lengua.

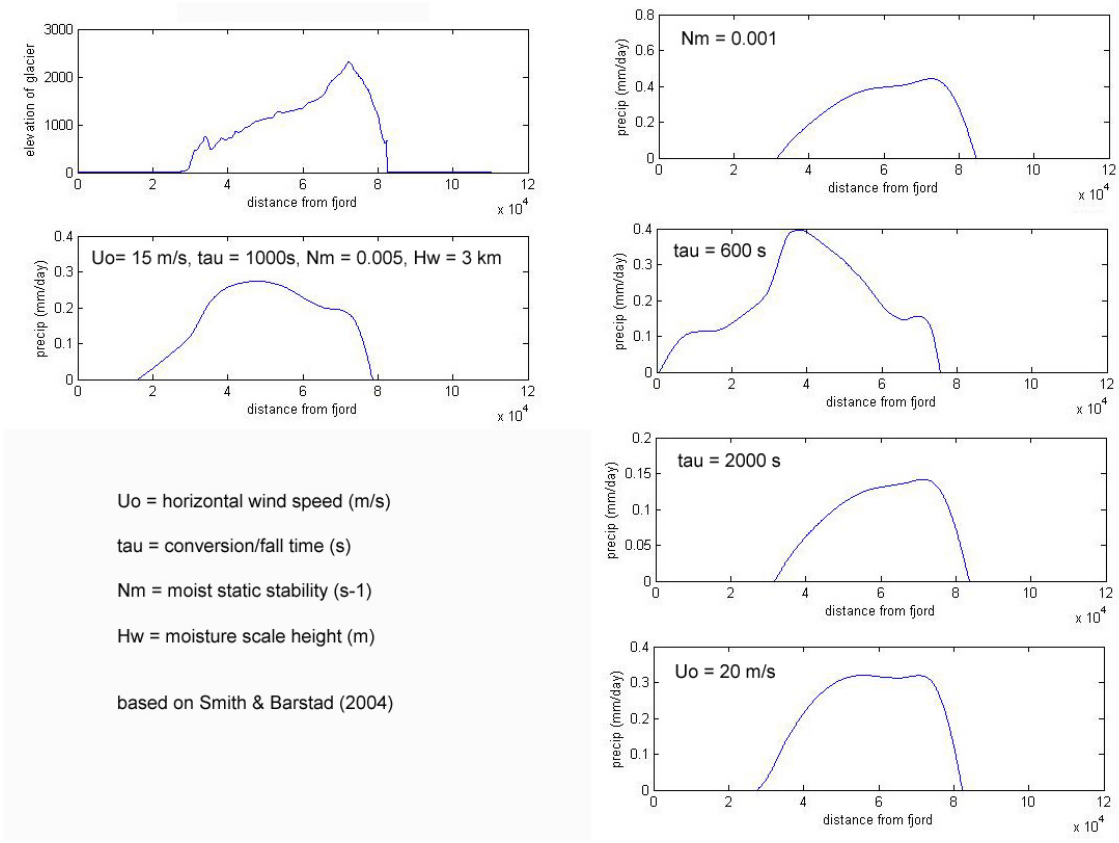

Figure 1.13 Parameters used in the 1D model of orographic precipitation, and the range of orographic enhancement curves possible by varying each parameter.

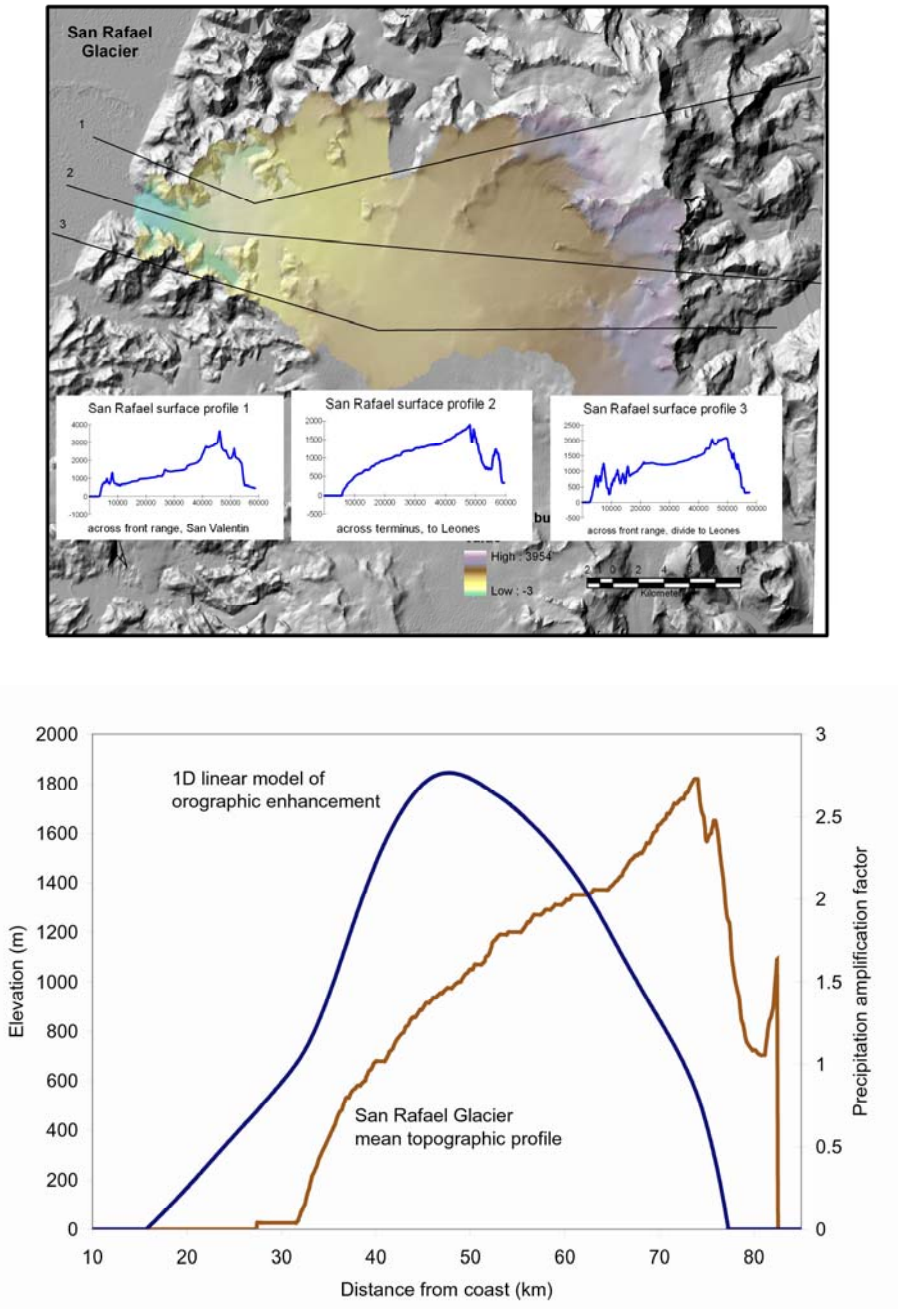

Figure 1.14 Orographic enhancement curve used to simulate precipitation on the surface of San Rafael Glacier (blue), and a representative longitudinal elevation profile of the glacier (brown).

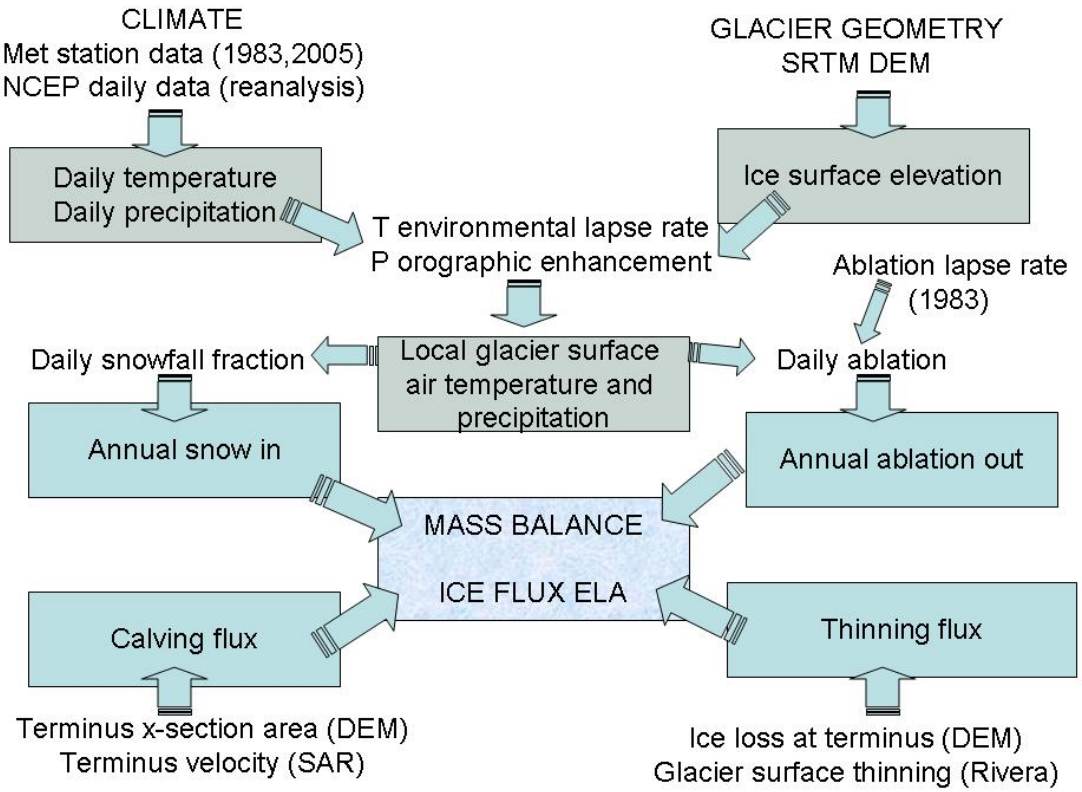

Figure 1.15 Flow chart of variables input into the ice mass budget model for San Rafael glacier.

CHAPTER 2.

Erosion rates during rapid deglaciation in Icy Bay, Alaska

Introduction

The highest known erosion rates in the world have been measured from the large Alaskan coastal glaciers (Hallet et al., 1996; Gurnell et al., 1996). These rapid erosion rates, up to as high as 100 mm/a, presumably arise from a number of factors: the tidewater glaciers of Alaska are among the largest and fastest glaciers worldwide, they drain the highest coastal mountain range in the world (the Wrangell - St. Elias), they cover well over half of their basin areas, they drain an area that experiences heavy precipitation from North Pacific storms (2-3 m/a according to Wilson and Overland, (1987)), and they overly bedrock that is pervasively fractured due to extensive shearing along the major strike-slip faults that dissect the area (Plafker et al., 1994; Bruhn et al., 2004; Spotila et al., 2004). Moreover, these high rates may actually be underestimated because significant volumes of sediment bypass the fjords and are deposited on the continental shelf (Molnia, 1979; Jaeger and Nittrouer, 1999).

The estimates of contemporary rates of glacial erosion in coastal Alaska are intriguing in that they are considerably higher than regional exhumation rates interpreted from both low temperature thermochronometry and modeling, which range from 1-3 mm/a (Spotila et al., 2004) to ~7 mm/a (Bird, 1996). Although thermochronometric interpretation is inherently difficult and non-unique, the difference between regional erosion and exhumation rates suggests that contemporary erosion rates are not sustainable in the long term (i.e., on the time scale of millennia). If contemporary erosion rates were representative of long-term rates, erosion would quickly outpace uplift and rapidly eliminate the exceptionally high ranges and relief that characterize the area. This cannot be the case because a major range, sufficiently high to sustain large tidewater glaciers, has persisted in the region for the past 5.5 million years (Lagoe et al., 1993).

Reported contemporary glacial erosion rates are currently receiving heightened scrutiny as a result of two recent findings. First, sediment yields from tidewater glaciers may have been substantially overestimated because they are based on measured volumes of sediments in fjords that may include considerable material derived not from the glaciers themselves but from the adjacent glacier-free landscape. In recently

deglaciated landscapes, rates of erosion of loose sediments in ice-marginal deposits can be exceptionally high because fjord walls are oversteepened and because base levels of tributary streams that were formerly dammed by the glacier have suddenly dropped (Meigs et al., 2002) due to the removal of the ice dam and, to a lesser degree, to isostatic rebound. Second, in a previous study of Muir Glacier in Glacier Bay, Alaska (Koppes and Hallet, 2002), we found that contemporary sediment yields from tidewater glaciers in southeast Alaska are likely to be far greater than long-term yields because these glaciers have been anomalously dynamic and, by inference, erosive as they retreated rapidly throughout the last century.

This study parallels Koppes and Hallet (2002), and presents new data documenting the volume of post-glacial sediment in a fjord recently exposed by the retreat of Tyndall Glacier. I refine the means of determining long-term glacial erosion rates by explicitly accounting for both the contribution of sediment to the fjord from non-glacial sources and the effect of rapid glacial retreat on sediment yield. I determine the fraction of sediment produced by Tyndall Glacier by subtracting from the total volume in the fjord the volume of sediment derived from two predominant subaerial sources, a pair of now-perched sediment-filled basins that formerly graded to the glacier surface. I also examine the effect of terminus retreat on sediment yield to arrive at an estimate of glacial erosion rates on time scales much longer than the 40 years of retreat covered in this study, and to offer insight into controls on glacial erosion rates.

Taan Fjord

Tyndall Glacier, in Wrangell-St.Elias National Park, south-central Alaska, descends steeply from the southwest flank of Mount St. Elias to sea level in Icy Bay, a dramatic drop of over 5400 m in under 18 km. Taan Fjord was most recently deglaciated starting in 1961 when Tyndall glacier separated and retreated from the main trunk of Guyot Glacier in Icy Bay (see Fig. 2.1). The glacier has since retreated 17.25 km in 30 years from its mouth in Icy Bay. In 1991, the terminus stabilized at a shallow bedrock constriction (Hoof Hill) at the head of the fjord, where it is still located (Fig. 2.2).

Continuous sedimentation from the glacier and from tributary valleys has accompanied retreat, filling the fjord bottom with as much as 90m of sediment locally, and producing some of the highest short-term sedimentation rates ever reported (Porter, 1989). The fjord bottom sediments were imaged using acoustic radio echo-sounding from a 750Hz bubble pulser in the summer of 1999 (see Figure 2.2 for tracklines). The profiling revealed three dominant facies in the fjord, all underlain by a strong, acoustically impenetrable reflector: 1) a laminated, semi-transparent layer presumed to be predominantly ice-distal glacimarine input with some subaerial fines, 2) a hummocky, chaotic facies presumed to be ice-proximal, and 3) laminated and hummocky facies along the fjord walls associated with landslides and delta-fan complexes prograding into the fjord from tributary streams (Fig. 2.3). The reflector underlying all three facies is interpreted to be the surface of the substrate that was compacted by glacial overriding during the Little Ice Age advance that started around 1400 A.D. (Porter, 1989). These facies are characteristic of other Alaskan fjords (e.g., Molnia et al., 1984). They are also evident in the seismic data collected by the USGS using a mini-sparker system on the M/V Growler in lower Taan Fjord in 1981 (Post, 1983), which we used to verify the accuracy of our identification and digitization of recently added sediment to the fjord.

The majority of the recently deglaciated fjord south of the current terminus has been cut into the Yakataga Formation, a tectonically uplifted, massive glacimarine sedimentary sequence dating as far back as 5.5 Ma (Lagoe et al., 1993). The sediment currently being deposited in the fjord is therefore similar in texture and composition to the underlying ‘bedrock’. The recent sediment deposited since retreat, however, can be distinguished seismically as transparent facies above a clear reflector. This reflector is interpreted to be the upper surface of either denser Yakataga bedrock or more recent glacimarine sediment that was consolidated by overriding ice and/or overlying sediment evacuated by the glacier during the last advance. The bedrock constriction at the current terminus of Tyndall Glacier marks the east-west trending contact between the Yakataga Formation to the south, and the Poul Creek and Kultieth Formations to the north, meta-sedimentary crystalline lithologies that underlie the entire current glacier basin and form the Mount St. Elias massif. Hence, the sediment yields we report in this study from Tyndall glacier over the last half-century are high despite the relatively resistant bedrock lithologies underlying most of the glacier.

Sediment influx into Taan Fjord

To determine the total volume of sediment deposited in Taan Fjord over the past 40 years, the difference between the 1999 sediment surface and the strong underlying reflector was calculated. Much like previous workers (e.g., Molnia, 1979; Molnia et al., 1984; Powell, 1991; Hunter et al., 1996), I assumed that no part of the transparent and chaotic seismic facies represent glacigenic sediments overridden by the glacier as it advanced to its Little Ice Age maximum position or retreated back to the mouth of Taan Fjord. Sediment thickness was determined from time-delays recorded in seismic profiles using seismic velocities of 1460 ms^{-1} for seawater and 1680 ms^{-1} for poorly consolidated glacimarine muds. The latter seismic velocity is known to within 3%, as measured seismic velocities for glacimarine tills and muds range from 1640 ms^{-1} to 1740 ms^{-1} s (Stoker et al., 1997; Hunter and Pullan, 1990); hence I estimate uncertainties in sediment thickness to be of the same order of ~3%. Key horizons were digitized in the seismic profiles and interpolated to map the upper and lower surfaces bounding the unconsolidated sediments to the fjord edges between the dense tracklines of our acoustic profiling survey, using a triangular irregular network (TIN) in ArcINFO. The maximum distance between tracklines was approximately 500 m. Assuming that sediment reworking through turbidity flows and slumping is efficient at smoothing the sediment surface, as noted by Jaeger and Nittrouer (1999), the piece-wise planar surface of the reconstructed bed using the TIN method appears to adequately represent the sediment surface between tracklines, and represents the bedrock surface with 15% uncertainty (comparison of our TIN grid with seismic profiles revealed a root-mean-square difference of approximately 10 m; due to the general concavity of the bedrock subsurface in the fjord and low relief of the upper sediment surface, the TIN method tends to underestimate the sediment thickness). All obvious delta-fan complexes and fjord wall slumps were identified by their seismic facies and excluded from the sediment thickness measurements.

The sediment thicknesses reconstructed using the TIN method were contoured and the resulting map is shown in Figure 2.4. Uncertainties arise from our estimates of the seismic velocity of the glacimarine sediments, as mentioned previously, as well as from interpolation of the sediment and bedrock surfaces. All uncertainties, including

minor errors in digitizing, as well as the potential for some submarine fan facies to be interfingered with distal glacimarine sediments along the fan edge and thus erroneously included in the volume computation, collectively result in an estimated 20% uncertainty in glacimarine sediment thickness in the fjord.

The total post-glacial sediment volume in Taan Fjord as of 1999 was 5.6×10^8 m^3. Assuming the entire sediment package was deposited between 1962 and 1999, the annual flux of sediment into Taan Fjord over the 37-year period has averaged 1.5×10^7 m^3/a.

Subaerial sediment contribution:

The delta-fan complexes imaged in the seismic profiles reflect point sources of subaerial sediments derived not from Tyndall Glacier but from tributary streams first highlighted by Meigs (1998; 2002). Several actively prograding deltas were identified in our seismic survey and can be seen contributing significant sediment to the fjord in turbid plumes visible in aerial photos and in a 1996 Landsat 7 image, which begs the questions of what proportions of the delta-fan complexes were imaged and excluded from our measurements in the seismic surveys, and how much of the fine sediments from these streams was deposited distally in the fjord and would appear indistinguishable from the distal glacimarine facies. Based on their large, recently excavated valleys, as well as their large sediment plumes in the Landsat image, two major streams stand out as obvious contributors to the sediment accumulation in the fjord: the Hoof Hill stream and the 1974 Moraine stream (Fig. 2.5). The lower reaches of both valleys were blocked by Tyndall Glacier throughout much of the past century, as recorded in aerial photos of the glacier system since 1938 (see Fig. 2.1). Aerial photos from 1958 (lower fjord) and 1986 (upper fjord) show sediment backfilling the valleys nearly to the glacier surface, approximately 350 m.a.s.l. in the upper fjord and 270 m.a.s.l. in the lower fjord (elevations were obtained from SRTM DEM data, and accuracy is approximately 50 m). The sediment in these valleys is glaciofluvial in origin, presumed to be deposited both laterally from the main trunk of Tyndall glacier, as well as from streams eroding the ice-free valleys in the Chaix Hills to the east of the fjord. Although there are several other tributary valleys contributing delta-fan complexes to Taan fjord, especially on the west side of the fjord, these valleys were filled by tributary glaciers that merged with Tyndall Glacier as recently as 1986. Hence, they are counted as part of the

glacial contribution to the fjord sediments rather than non-glacial, fluvial sources, although their potential importance in the transfer of a significant pulse of sediment to the fjord as both tributary and trunk glaciers retreated is noted.

To determine the volume of fluvial sediment that was rapidly transferred from both major tributary valleys to the fjord since the glacier retreated I compared the original sediment surfaces in the valleys to the incised valley surface as of February 2000, using a 15m digital elevation model (DEM) generated from SRTM data. The original surface was identified in aerial photos, and was assumed to extend to the edge of the fjord, which I believe may overestimate the volume of sediment evacuated from the valley by 20% or more. This sediment surface cannot be identified clearly in the photos because it extended partially under and around tongues of ice that intruded laterally from Tyndall glacier. The surface probably did not extend all the way to the fjord edge, but rather sloped steeply towards the fjord. Using the ArcGIS package, the difference between the original and the 2000 surface was calculated and compared to the sediment volume in the associated alluvial fan complex prograding into the modern fjord. The sediment volume in the fans was calculated using the SRTM DEM data for the portion of the fans that have prograded into the fjord above sea level, and the seismic profiles for the submarine portion. The volume of sediment removed from the valleys exceeded the volume in the fans substantially, indicating that a significant fraction of the sediment may have been transported past the fans to the center of the fjord, presumably through remobilization by sediment gravity flows and shallow turbidity plumes (Jaeger and Nittrouer, 1998; Syvitski, 1989).

In total, I estimate that at most 15.6×10^7 m^3 of sediment was removed from Hoof Hill valley since 1989, of which 4.1×10^7 m^3 and 4.5×10^7 m^3 are now in the delta and submarine fan, respectively. The remaining 7.0×10^7 m^3 was deposited more distally in the fjord bottom, and is indistinguishable from the distal glacimarine facies. This distal subaerial sediment contribution is significant, accounting for 12% of the total post-glacial sediment volume in the fjord. Locally it is even more dominant. If we assume that the finer sediment from Hoof Hill valley did not start accumulating in the fjord bottom until the glacier had retreated past the valley in 1988-1989, and that both this subaerial sediment and the sediment delivered by Tyndall glacier since 1990 have been largely confined to the upper 5 km of the fjord (in part due to a strong gyre at the head of the fjord observed in the field and in Landsat imagery), it accounts for up to 80% of the infilling in the

uppermost basin of the fjord. The large input of fine sediment from Hoof Hill valley is perhaps in part due to the valley being the surface expression of an active strike-slip fault between the Coal Creek and Kultieth Formations (Plafker et al., 1994). This highly fractured bedrock and significant fault gouge would be readily eroded and transported by the tributary stream.

A similar calculation for the 1974 Moraine stream suggests that it has contributed 1.71×10^7 m^3 of finer sediment to the fjord beyond the delta, or 3% of the total volume of fjord sediment. Thus, these two streams, which were observed to be the two most significant generators of non-glacial fine sediment to the fjord system during the past few decades, account for ~15% of the postglacial sediment in the fjord. This value may slightly underestimate the subaerial contribution, however, as we have not accounted for the potential contribution of other sources of fine sediment such as gullying of the fjord walls. Although we have no quantitative data on this more distributed sediment source, the relative size and number of gullies suggest that their collective contribution is minor. More precise definition of the longer-term relaxation of the post-glacial landscape will require direct measurement of this 'distributed' subaerial sediment input.

40-year average sediment flux and glacial erosion rate

After accounting for the subaerial sediment input into the fjord since retreat, our seismic data show that Tyndall Glacier has produced, on average, 1.3×10^7 m^3 of sediment annually.

To arrive at basin-averaged glacial erosion rates, I divide the sediment flux by the contributing basin area, and take into account the difference in density between the eroded bedrock and the sediment in the fjord. We assume an average bedrock density, ρ_{rock}, of 2700 kg m^{-3}, which is appropriate for the crystalline bedrock underlying Tyndall Glacier. Prior to 1991, the glacier was also overriding the less dense Yakataga glacimarine sediments that underlie the lower basin; hence, if parts of the Yakataga Formation were eroded to contribute to the sediment flux, our use of the average bedrock density underestimates the rate of bedrock erosion in that part of the basin. To assure that these calculations do not overestimate bedrock erosion rates, I use the lower

end of known glacimarine sediment densities, ρ_{sed}, which range from 1700 kg m^{-3} to 2000 kg m^{-3}. For the calculated average sediment flux of Q_{sed} = 1.3 x 10^7 m^3/a, the average flux of eroded bedrock from Tyndall Glacier ($Q_{rock} = \rho_{sed} Q_{sed} / \rho_{rock}$) divided by the contributing basin area (256 km^2 for the watershed in 1959, decreasing in a step-wise fashion to 154 km^2 by 1991, as measured from SRTM DEM data imported into ArcGIS), yields a basin-averaged erosion rate of 28 ± 5 mm/a for the past 40 years.

Temporal variation in sediment flux from Tyndall Glacier

To explore the temporal dimension of sediment production by Tyndall Glacier, we can use a simple numerical model of glacimarine sedimentation that enables us to calculate the annual sediment output needed to produce the sediment package observed in the proglacial fjord of any retreating tidewater glacier with a known retreat history (described in Koppes and Hallet, 2002). The thickness of sediment at any one point in the fjord reflects a combination of two distinct rates: the variable rate of sediment delivery to the terminus, and the rate of terminus retreat. Where one of these parameters is known, and the total sediment volume in the fjord is measured, the other parameter can be calculated, given the relationship

$$S = \int_0^t \dot{S}(x,t)dt = \int_0^t \dot{S}_0 e^{-\dot{R}t / x_*} dt$$

where S is the total sediment thickness, $\dot{S}$ and $\dot{S}_0$ are the time-varying sedimentation rates at a distance x in front of the ice and at the ice front, respectively, $\dot{R}$ is the time-varying rate of terminus retreat and x_* characterizes the distance from the terminus over which the sedimentation rate decreases by 1/e. Our model, which assumes an exponential decrease in sedimentation rate with distance from a tidewater glacier as reported in previous studies (e.g., Cowan and Powell, 1991), enables us to reconstruct the temporal variability of the sediment flux as a function of the sedimentation rate at the terminus, S_0(t), for glaciers where the annual retreat rate can be reconstructed from maps and photos, and the total sediment thickness S is known from seismic profiles.

A smoothly varying annual retreat rate of the terminus of Tyndall glacier since 1962 was calculated using a piece-wise spline function (Rasmussen, 1995) to interpolate between 17 known terminus locations over time. Terminus positions since 1962 were acquired from maps (Roche, 1996; Porter, 1989), USGS aerial photos and Landsat images. The volume of glacigenic sediment measured in the fjord was parsed into 250 m bins and used as input to the model. By entering the annual retreat rate and the distribution of sediment thickness into the model, I reconstructed the variable annual sediment flux, and hence the erosion rate, from the glacier that is required to account for the observed sediment accumulation (Fig. 2.6). The annual sediment flux necessary to produce the sediment thickness at any point in the fjord is also tempered by the remobilization of sediments in the fjord bottom through sediment gravity flows and turbidity plumes. To model this, at each time step sediment was redistributed between adjacent bins until a critical, effective "angle of repose" was reached (Jaeger and Nittrouer, 1999). We varied this angle of repose for soft sediment under water between 1º to 8º, according to observed submarine slopes in Taan Fjord and similar submarine environments, to calculate the envelope of annual sediment flux, and hence erosion, required from the glacier to produce the fjord sediment package. Decreasing the angle of repose effectively reduced the annual erosion rate required to fill the bins, as the sediment was more evenly distributed in the fjord. The envelope of erosion rates is outlined in grey in Figure 2.6.

For Tyndall Glacier, the model indicates that the sediment flux, and by inference the erosion rate, generally parallel the retreat rate (Fig. 2.6). During years when the terminus was retreating most rapidly, exceeding 1500 m/a, basin-wide erosion rates exceeded 90 mm/a. During years when the ice margin remained stable, such as from 1991-1999, the rate of erosion dropped to 7-9 mm/a. Most notably, the erosion rate and retreat rate are strongly correlated ($R^2 = 0.79$) (Fig. 2.7).

Implications for long-term erosion by Alaskan glaciers

Most tidewater glaciers spend significantly longer periods of their cycle in an advance phase or quasi-stable mode, and tend to retreat quite quickly at the end of the cycle (Meier and Post, 1987). Tyndall Glacier is a perfect example: it first started to advance out of Taan Fjord around 1400 A.D., reached its Little Ice age maximum at the mouth of Icy Bay sometime before 1794 A.D. (when Captain Vancouver first sailed by and mapped the ice extending out of the bay), and began to retreat quite rapidly in 1905, reaching the mouth of Taan fjord in 1961 (Porter, 1989). The rate of advance through lower Icy Bay averaged 60 m/a, lasting almost 400 years, while the rate of retreat for the period until 1961 averaged 450 m/a, lasting only 60 years, with over 100 years of standstill in between.

In order to interpret the 'long-term' erosion rate for Tyndall Glacier on millenial time scales (i.e., over one or several glacial advance-retreat cycles), I assume the correlation between erosion rate and retreat rate can be extrapolated to periods of no retreat, represented by the intercept of a linear best-fit relationship of the data. The extrapolated erosion rate is the best estimate we have of the rate of erosion during periods of standstills, such as at the peak of the Little Ice Age. During the protracted advance phase the rate of bedrock erosion may tend to be less than during standstills because, at least in the lower reaches of the glacier, considerable proglacial sediment has to be evacuated before the glacier can erode the bed. Accordingly, since a substantial portion of a normal tidewater glacier cycle is spent in a quasi-stable phase, and the relatively short period of rapid erosion during the retreat phase tends to be offset by the slower bedrock erosion during the longer advance phase, we can assume that the extrapolated erosion rate for periods of standstill, represented by the y-intercept in Figure 2.7, is most representative of the 'long-term' erosion rate for Tyndall Glacier. This long-term erosion rate is 9 ± 2 mm/a. It is 3.5 ± 1.5 times lower than the recent 40-year average rate, and an order of magnitude lower than the peak erosion rate circa 1985, when Tyndall was retreating most rapidly.

These results showing that sediment yields are high when Tyndall Glacier retreats rapidly, together with similar results for Muir Glacier (Koppes and Hallet, 2002), suggest that most of the sediment yield data from tidewater glaciers in Alaska collected to date correspond to contemporary erosion rates that are significantly higher than those in the long-term. I have confidence that this bias towards unusually high sediment yields in the short-term is applicable to other published rates of erosion for Alaskan tidewater

glaciers, since all the other studies (e.g., Molnia et al., 1984; Powell, 1991; Cowan and Powell, 1991; Hunter et al., 1996; Jaeger and Nittrouer, 1999) were measured using similar methods from calving glaciers that have also been in steady retreat since the end of the Little Ice Age (with the exception of Taku Glacier (Motyka et al., 2005)). At Muir Glacier, we found that contemporary rates of erosion were a factor of five higher than the long term rate. Accordingly, we present a revision of the compilation of glacial erosion rates originally published by Hallet et al. (1996) in which contemporary rates for all Alaskan basins drained by tidewater glaciers are reduced by a factor of four to conservatively approach their 'long-term' rates, such as those derived for both Tyndall Glacier and Muir Glacier (Fig. 2.8).

Implications for controls on glacier erosion

The strong correlation we find between erosion rate and retreat rate for Tyndall Glacier (and for Muir Glacier) is not surprising if one presumes both that ice velocity is proportional to retreat rate, as was observed for another tidewater glacier in the region, Columbia Glacier (Van der Veen, 1996), and that sediment delivery to the terminus increases with glacial sliding speed, as was documented for Variegated Glacier (Humphrey and Raymond, 1984) and Bench Glacier (Riihimaki et al., 2005).

In the case of Columbia Glacier, the inception of terminus retreat in 1982 was accompanied by a concomitant increase in glacier surface speed, which was associated with thinning near the terminus and assumed to be due to an increase in surface slope and along-flow stretching as ice was drawn down through the glacier system (Van der Veen, 2002; Brown et al., 1982). Unfortunately, we do not have any measurements of glacier speed for Tyndall Glacier throughout our study period to make a similar comparison. Two observations, however, support the suggestion that during this period of retreat the speed of Tyndall glacier was higher than average. First, the surface slope increased along the length of the glacier from 3.9º in 1961 to 6.5º in 1999, as the total glacier length decreased by half. Second, the ice flux into Taan fjord necessary to reduce the glacier volume and draw down its surface must have exceeded the balance flux considerably, since most of the ice in these tidewater glacier systems is lost by calving. In just 40 years of retreat, approximately half of the total volume of the glacier in 1961 has been lost (~3.19 x 10^{10} m^3), and the glacier thickness has decreased over

~300 m at the present glacier terminus and in decreasing amounts towards the drainage divide. These decreases in ice thickness along the glacier are of the same magnitude as the accumulation of ice expected over the glacier over the 40-year period, using a plausible accumulation rate of 2-3 m/a (Wilson and Overland, 1987). This suggests that ice fluxes, and by inference basal velocities, may have been roughly twice their long-term (i.e., balance) values during this time.

Increases in ice velocity can increase glaciofluvial sediment flux to the terminus either through accelerated erosion of bedrock, or through enhanced evacuation of sediments stored under the glacier. Englacial and supraglacial sediment flux will also increase with increasing ice flux to the terminus, but these sources of sediment are of an order of magnitude smaller than the glaciofluvial sediment flux (e.g., Hunter et al., 1996), and hence would not significantly affect the overall sediment output of the glacier. Decreases in subglacial sediment storage may be significant in the short-term such as during a surge, periods of local ice acceleration and subglacial cavity expansion (e.g., Anderson et al., 2004), or at the start of the melt season when efficient subglacial water conduits start to form. At Variegated Glacier, both the sediment yield at its outlet streams and sliding speed increased by two orders of magnitude during a surge in 1981-1982 (Humphrey and Raymond, 1984). At Bench Glacier, periods of enhanced sliding at the start of the melt season during three consecutive years were accompanied by increases in both sediment and water discharge (Riihimaki et al., 2005). In both of these examples, the pulse of sediment discharge could be related not only to increased glacier sliding but also to short-term changes in efficiency of the subglacial hydrologic system. A sudden increase in the water discharge would evacuate sediments more readily and enhance the correlation between glacier sliding and sediment flux for short periods.

Such increases in water discharge, however, could not be sustained over decades to account for the massive sediment flux from Tyndall Glacier. Likely volumes of sediment stored beneath Tyndall Glacier are but a small fraction of the sediment delivered to Taan Fjord during the 40-year period examined in this study. To attribute this increase in sediment flux solely to enhanced evacuation of stored sediments under Tyndall Glacier would require the removal of a ~20m-thick layer of basal sediment stored under the entire ablation area of the glacier (~25 km^2), where such debris is most likely to accumulate. Such a requisite thickness of mobile basal debris is excessive compared to the characteristic thickness of only a few decimeters that has been documented in the

few boreholes that have penetrated to the base of coastal Alaskan glaciers, such as Columbia Glacier (Humphrey et al., 1993) and Variegated Glacier (Kamb et al., 1985). Only in one instance has up to 7 m of mobile debris been cored and instrumented, under Black Rapids Glacier (Truffer et al., 1999); in this case, evacuation of basal debris could cause periodic increases in sediment flux. Such rapid debris evacuation could only be sustained, however, if it was offset by rapid erosion. Moreover, a thick blanket of basal debris would preclude bedrock erosion as it would tend to prevent sliding ice from having direct access to the underlying bedrock.

Recent studies of the evacuation of proglacial and subglacial debris by Taku Glacier during its current advance document the evacuation of approximately 1.9 m/a of soft sediment during the 20th century, flushed from beneath the advancing snout (Motyka et al., 2005). Such rapid evacuation of unconsolidated sediment, approaching 200 m per century, provides confidence in our assumption that all the sediment stored subglacially, as well as in the fjord, prior to the last advance of Tyndall Glacier had been effectively removed and transferred to the Gulf of Alaska long before the retreat of the ice from Taan Fjord nearly five centuries later. Hence, the large sediment flux documented at Tyndall Glacier most probably reflects enhanced bedrock erosion due to accelerated basal ice motion associated with rapid retreat, with only a minor contribution derived from the relatively small volume of sediment likely to be stored subglacially.

The long-term erosion rate of 9 ± 2 mm/a derived for Tyndall glacier approaches the maximum expected tectonic uplift rates (e.g., Bird, 1996) in the region. The proposed extrapolation of contemporary sediment yields to obtain long-term erosion rates therefore helps resolve the apparent conundrum of contemporary erosion rates exceeding tectonic uplift rates significantly -- in the long-term, the two must balance each other to maintain the relief that is known to have existed in the region over millions of years. It remains of interest, however, that these derived long-term erosion rates are still significantly higher than those inferred from the simplest possible interpretations of the thermochronology of the region (Spotila et al., 2004). I suggest two possible reasons for this discrepancy. One is that the erosion rates inferred from thermochronology, which represent temporal averages over periods of order 10^6 years, are actually lower than those for shorter periods of order 10^3 years with which we are concerned. Alternatively, some of the poorly constrained assumptions required for the interpretations of the thermochronology may lead to unreliable estimates of exhumation rates. Notably, the

simple, common assumption that packets of crustal material follow vertical trajectories to the surface, whereas ascent along paths that are in general gently inclined is more likely in this tectonic setting, would tend to underestimate cooling rates and, hence, exhumation rates substantially.

Conclusions

The model of proglacial sedimentation reveals a clear correlation between glacial retreat rates and glacial sediment yields from Tyndall glacier, which I believe reflects the tendency for ice velocities to increase with retreat rates and for glacial erosion rates to scale with ice velocity. Taking into account the correlation between sediment flux and retreat rate, and the remobilization of subaerial sediments formerly ponded by ice, the long-term erosion rate for Tyndall Glacier is 9 ± 2 mm/a. The significant contribution of subaerial sediments to the fjord system, which comprised ~15% of the total volume of postglacial sediments in Taan Fjord, is a product of the immediate response of the landscape to changing base levels following glacial retreat.

These results showing that sediment yields are high when Tyndall glacier retreats rapidly, together with similar results for Muir Glacier (Koppes and Hallet, 2002), imply that most sediment yield data from tidewater glaciers in Alaska over the last century correspond to contemporary erosion rates that are a factor of 3.5 ± 1.5 higher than in the long term. Contemporary glacier erosion rates in Alaska and elsewhere are high because rapid retreat has been characteristic of the entire period of study, extending back to the end of Little Ice Age. For many of these heavily glaciated basins, even the improved estimates of long-term erosion rates in southern coastal Alaska remain among the highest known rates worldwide, and exceed million year time-scale exhumation rates derived from low-temperature thermochronometry in the region.

Figure 2.1. Tyndall Glacier and Mount St. Elias (5489 m.a.s.l.), with Icy Bay in the foreground, looking to the northeast, 1938. Tyndall Glacier is joined with Guyot Glacier in the lower left of the photograph. Between 1938 and 1961 the terminus retreated approximately 3 km until it separated from Guyot Glacier at the mouth of Taan Fjord. Since 1961, it has retreated a further 17.25 km upfjord to its current terminus position at Hoof Hill (dashed line) (Photo kindly provided by B. Washburn).

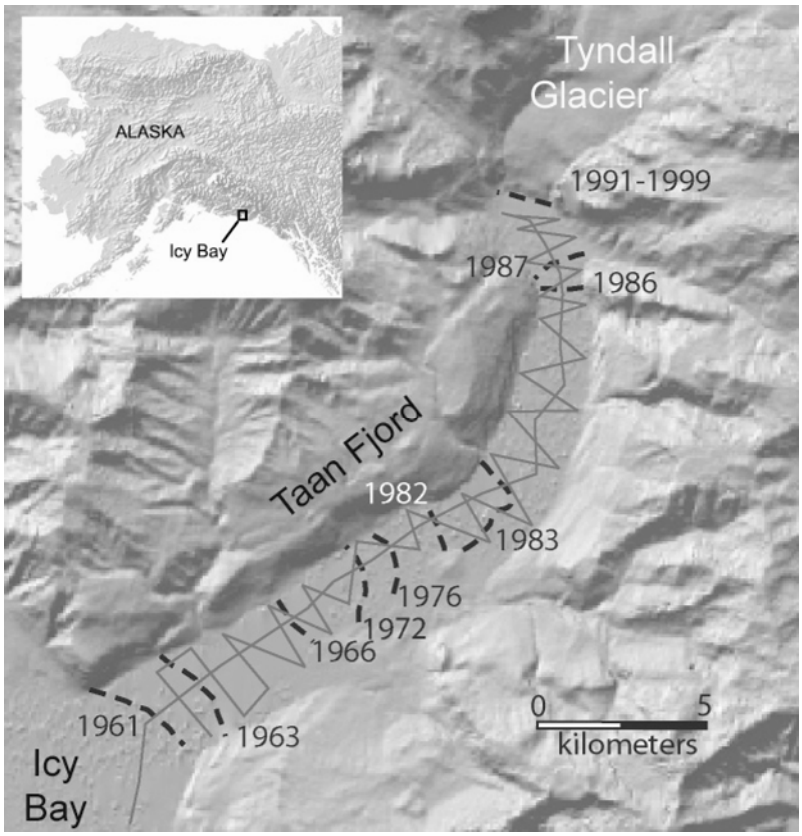

Figure 2.2. DEM of Taan Fjord showing ice retreat history and tracklines from 1999 seismic survey. Tracklines are marked by grey lines; ice margin positions were derived from USGS aerial photos and Porter (1989). Inset shows location of Icy Bay and Taan Fjord within Alaska.

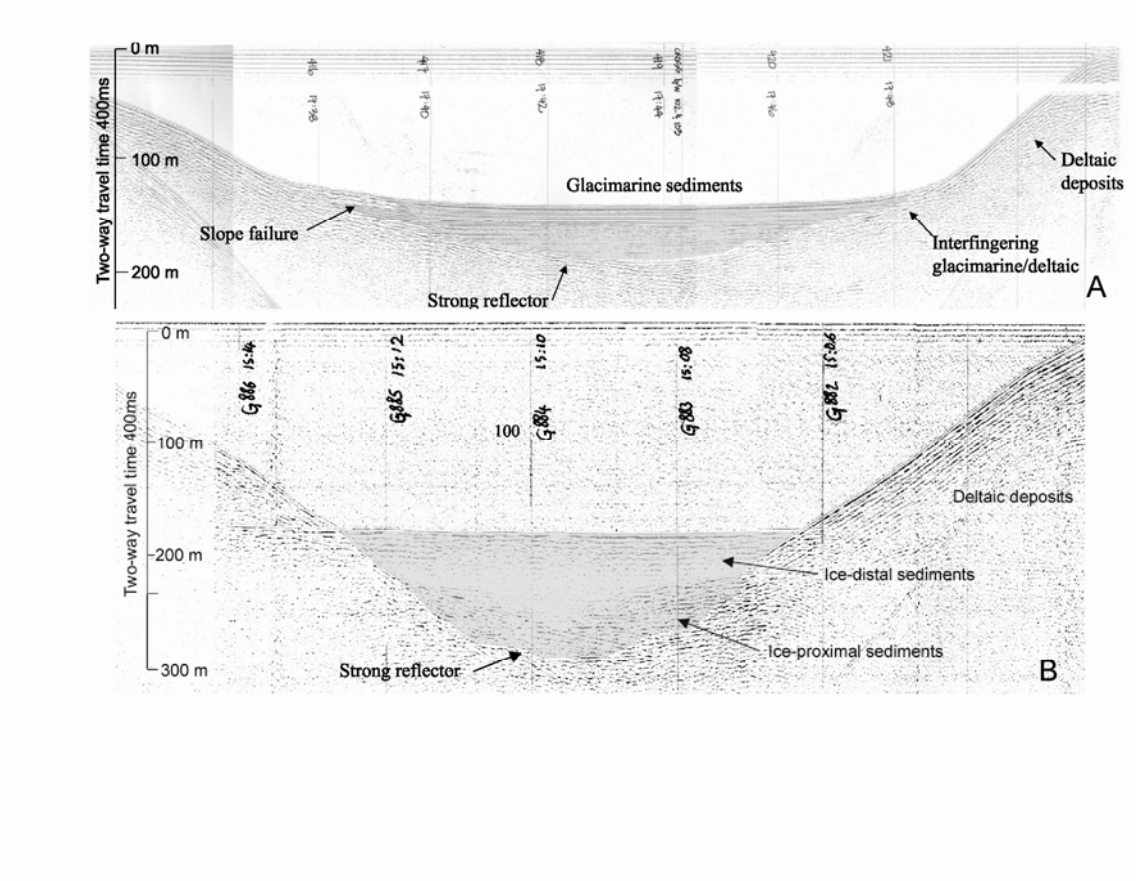

Figure 2.3. Sample acoustic profiles from which sediment thicknesses were measured: a) from lower Taan Fjord (in vicinity of 1966 terminus position), b) from upper Taan Fjord (in vicinity of 1989 terminus position). Laminated, semi-transparent facies are interpreted as distal glacimarine deposits, while chaotic, hummocky facies represent ice-proximal deposits and laminated, hummocky facies represent fan delta complexes. The strong reflector underlying all three facies is assumed to be indicative of compression and dewatering of the underlying sediments, or Yakataga glacimarine 'bedrock', by overriding ice and/or sediment.

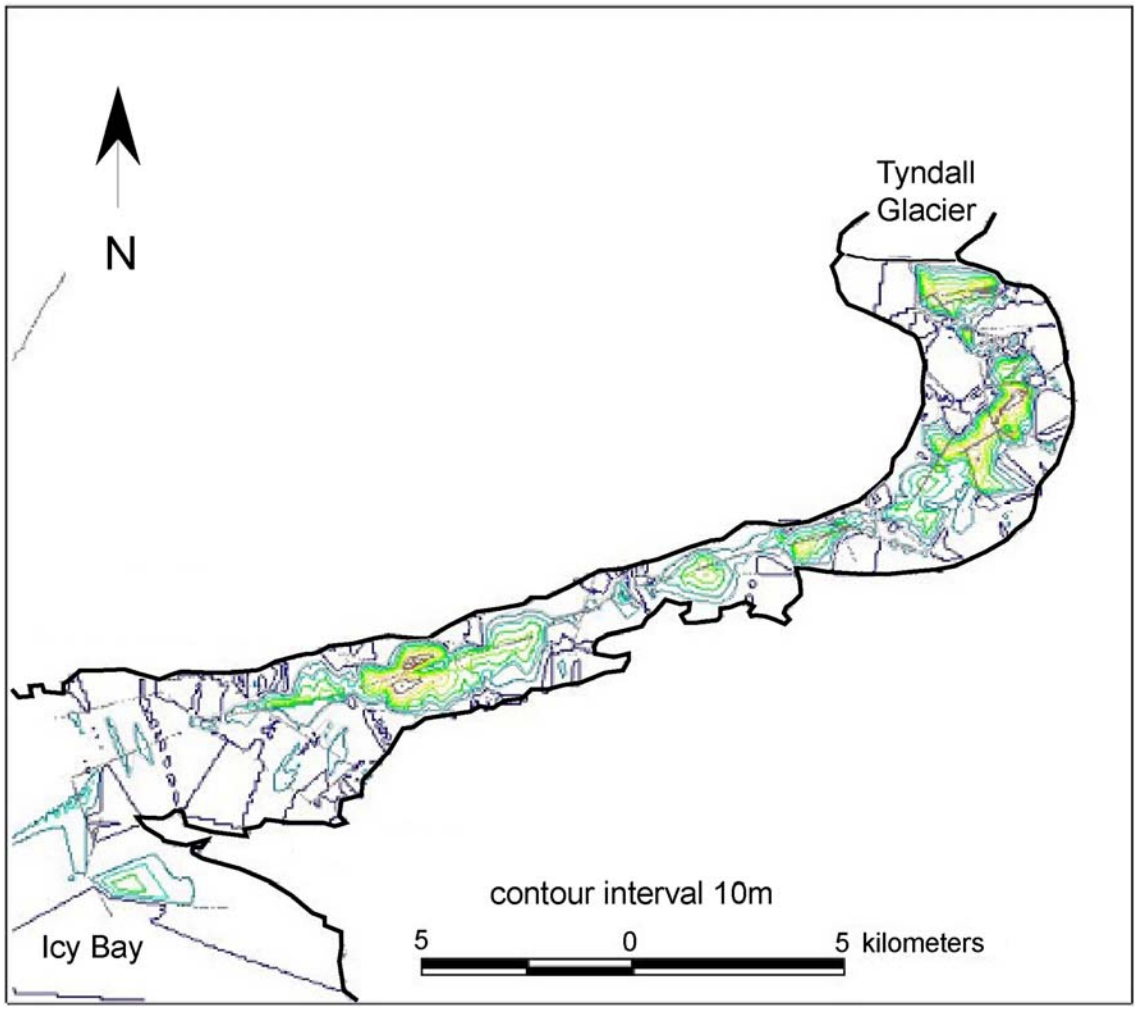

Figure 2.4. Contours of sediment thickness in Taan Fjord, from 1999 seismic survey of fjord sediments, derived from surface and subsurface reflectors. The lightest contour is 10 m, with a subsequent contour interval of 20 m. The maximum sediment thickness is 90 m. Projection is in Lambert conical.

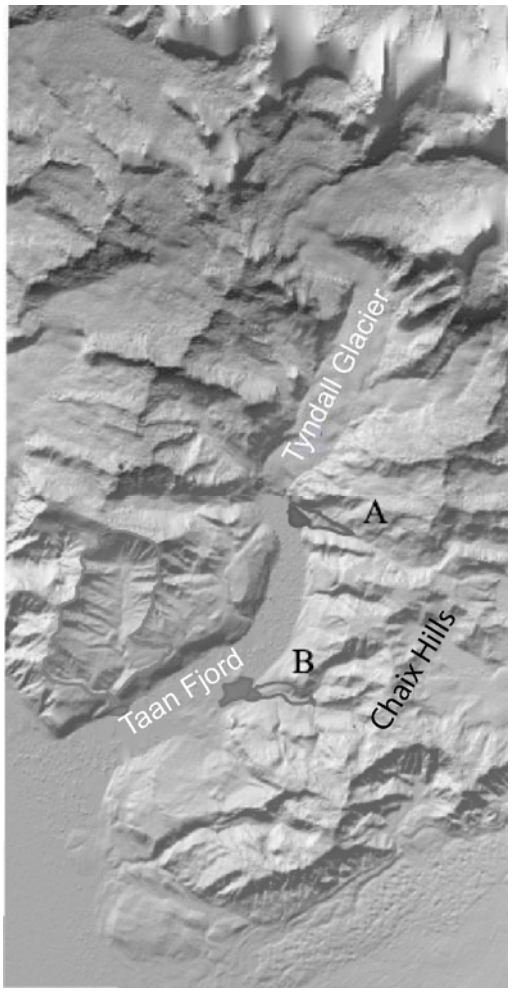

Figure 2.5. DEM of Taan Fjord and Tyndall Glacier, derived from Feburary 2000 SRTM data. The prograding deltas and back-filled basins of the two predominant non-glacial streams contributing sediment to the fjord are outlined (basin) and filled (delta): A= Hoof hill, B = 1974 Moraine.

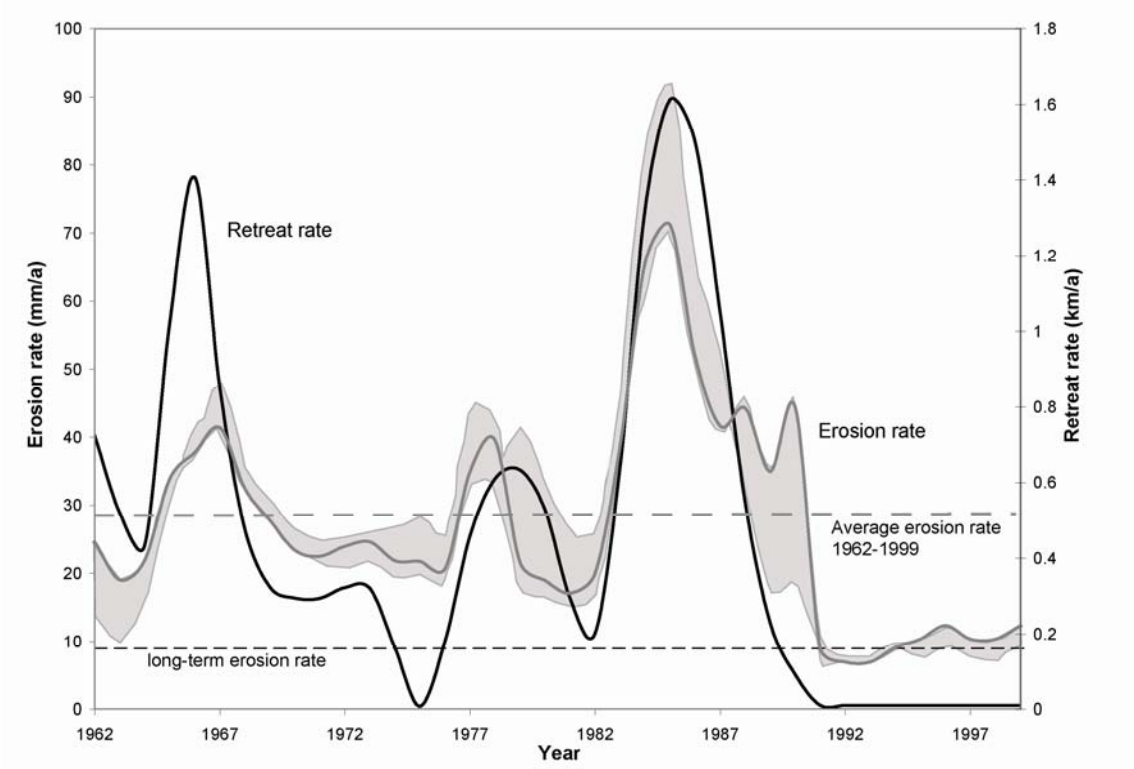

Figure 2.6. Comparison of erosion rate and retreat rate for Tyndall Glacier since 1962. Average contemporary erosion rate for 1962-1999 is 28 ± 5 mm/a. Grey shading indicates the range of erosion rates produced using a range of critical slope angles for sediment reworking in the fjord.

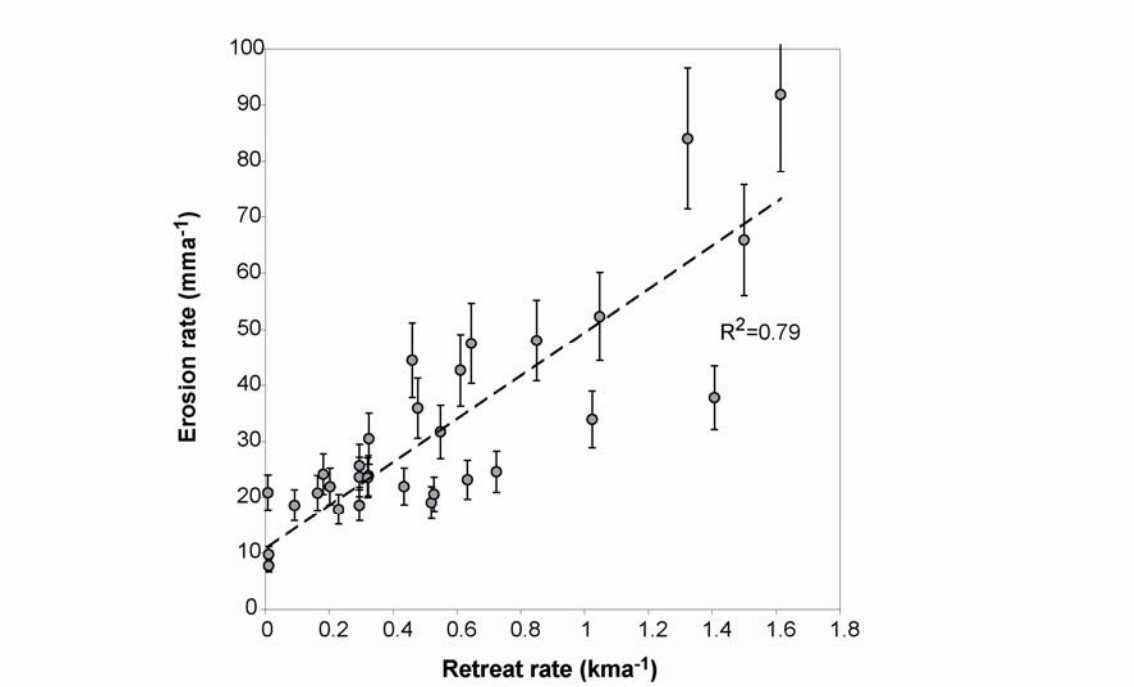

Figure 2.7. Correlation of erosion rate and retreat rate for Tyndall Glacier since 1962. Error bars indicate a 20% uncertainty in calculating erosion rates. Extrapolating the erosion rate to times when the glacier is effectively stable, the long-term erosion rate is 9 ± 2 mm/a.

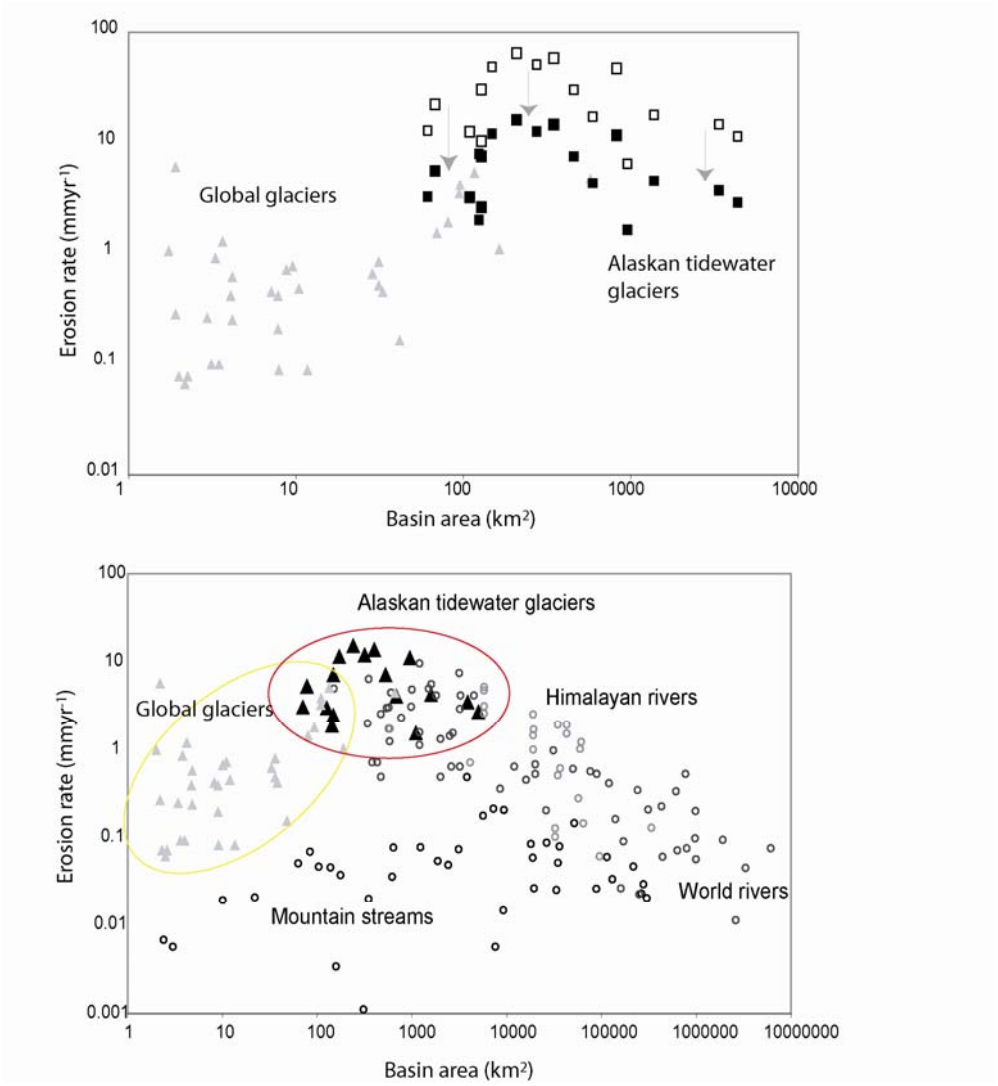

Figure 2.8. Erosion rates for glacial and non-glacial basins, revised from data originally compiled by Hallet et al. (1996) by reducing contemporary rates derived from retreating tidewater glaciers in SE Alaska (black squares) by a factor of 4 to estimate long-term erosion rates (filled squares). This reduction is based on our estimate that tidewater glaciers undergoing rapid retreat produce sediment ~4 times faster than in the long-term (see text). A) Erosion rates for glacial basins, including tidewater glaciers in SE Alaska (black squares) and glacial erosion rates (grey triangles) elsewhere in the world. B) Comparison of glacial erosion rates (triangles) and fluvial erosion rates (circles) from global rivers (Milliman and Syvitski, 1992), mountain basins in British Columbia (Church and Slaymaker, 1989) and mountain basins in the high Himalaya.

CHAPTER 3.

Late 20th century retreat and erosion from Marinelli Glacier, Tierra del Fuego

The physiography and climate of the southern Andes is comparable to those in coastal Alaska mountains, where much of our current understanding of the dynamics and erosion of tidewater glaciers originates (e.g., Meier and Post, 1987; Powell, 1991; van der Veen, 1996; Koppes and Hallet, 2002; Sheaf et al., 2003) and where the relationship between glacier erosion and tectonics is starting to be explored (e.g., Spotila et al., 2004; Gulick et al., 2004). Comparing findings of glacial erosion rates and the response of tidewater glaciers to climate in the southern Andes permits us to assess empirical relationships between glacier dynamics and erosion developed in Alaska, and to explore whether these relationships are universal.

In this chapter, I present measurements of the sediment accumulated in Marinelli fjord, in the southernmost Andes, since the start of its recent rapid retreat, and infer the basin-averaged bedrock erosion rates from the glacier during the latter half of the 20th century. I then use data from reanalysis climate models and maps and images documenting the changes in the area of Marinelli glacier to explore the controls on glacier retreat and its impact on erosion rates over the past 50 years.

Field area

The Cordillera Darwin Icefield is in the mountainous southwestern region of Tierra del Fuego. The mountains of the cordillera exceed 2000 m in elevation and trend northwest to southeast for approximately 120 km, with a summit at Monte Shipton (2469 m.a.s.l., also known as Monte Darwin). The range is approximately 50% ice-covered. Although the 2300 km^2 of the icefield is mostly contiguous, steep topography and structural constraints define most of the ice masses within individual catchments. Meteorological gradients across the range are steep, with heavy precipitation and solid cloud cover being typical over the southern and western fjords and drier conditions to the north and east (Holmlund and Fuenzalida, 1995; Porter and Santana, 2003). Automated

weather stations deployed by the University of Magallanes show annual precipitation averages of 1600mm at Bahia Pia, in the southern part of the range, dropping to 800 mm at Seno Almirantazgo, just north of Marinelli Fjord (A. Santana, pers. comm., 2005). Precipitation, mostly in the form of snowfall, is mainly associated with westerly and southwesterly winds that pick up moisture from the cool Humboldt current offshore, although the coldest air masses arrive from the south (NCEP-NCAR dataset, Kalnay et al., 1996).

The Marinelli glacier, the largest glacier in the Cordillera Darwin, drains the northern flanks of Monte Shipton and calves into Bahia Ainsworth, an arm of Seno Almirantazgo, to the northeast of the range (Fig. 3.1). Located at 54°32'S, 69°35'W, the glacier is approximately 21 km long, with a basin area in 2005 of 154 km^2. Until the mid-20th century, the glacier was stable, calving directly into Bahia Ainsworth. Retreat accelerated in the early 1960s. The western half of the terminus receded onto bedrock above sea level in the late 1990s, and the remaining tidewater terminus has pulled back another 3.5 km in the eastern half of the fjord. The terminus in 2005 was 1.8 km wide, with an average ice cliff height of 45 m. Trimlines that can be traced from the moraine at the fjord mouth to the 2005 terminus are around 250 m.a.s.l. at the glacier front (Fig. 3.2).

Marinelli fjord is 13 km long and narrows upfjord from approximately 4 km at its opening into Bahia Ainsworth, to 2 km near the ice front, with an average width of 2.4 km. It is bounded at its northern end by an emerged arcuate terminal moraine that marks the Little Ice Age advance of the glacier (Porter and Santana, 2003). The terminal moraine ranges from 90 m above sea level to 5 m below mean low water. It acts as an efficient trap to capture most of the sediments and icebergs calving from the glacier, creating a backlog of brackish ice in the fjord that can extend up to the ice front in winter.

Marinelli glacier was first visited during a 1913 expedition and documented in a map by de Gasperi and photographs by Alberto d'Agostini. They observed the glacier filling the fjord and abutting the arcuate terminal moraine, with a steep surface profile near the ice front descending sharply from ~140 m.a.s.l. (Porter and Santana, 2003). The basin area during that time exceeded 252 km^2. Since 1945, the glacier front has receded from the moraine and into steadily deepening water (over 210 m below sea level in the center of the fjord). A series of seven aerial photographs and satellite images document the retreat of the ice front. At first retreat was gradual, but accelerated after

1980. In the last three decades, the terminus has retreated several hundred meters per year. The dramatic recession of Marinelli is in stark contrast to the general pattern of standstill or minor recession of calving and non-calving glaciers around the Cordillera Darwin, in particular to the slow advance of the south-facing glaciers of Bahia Pia, which drain the other side of Monte Shipton (C. Porter, pers. comm., 2006).

The bedrock of the region is comprised of metasediments and metavolcanics, intruded by small batholiths (Dalziel and Cortes, 1972). Soil cover is sparse, and often limited to the moraines. The vegetation is dominated by young forest of southern beech (*Nothofagus betuloides* and *Nothofagus Antarcticus*) and canelo (*Drymis winterii*). The mouth of the Bahia Ainsworth opens into ESE trending Seno Almirantazgo (Fig. 3.1), one of the deepest basins along a chain of en echelon depressions along the Magallanes-Fagnano Transform system (MFT). The Tierra del Fuego region is bounded by several prominent west-east trending, left-lateral strike-slip faults, which experienced significant motion in the mid- to late-Holocene (Rabassa et al., 2002). More recently, the 1949 Punta Arenas earthquake (magnitude 7.8) (Bentley and McCulloch, 2005) may also have been associated with subsidence and/or glacier retreat.

Regional climate

Climate stations in Tierra del Fuego are scant and discontinuous, limited to Chilean Navy lighthouses on the west coast and entrance to Magellan Strait, and the few towns in the region (Puerto Williams, Punta Arenas, Ushuaia) that have been inhabited for more than a century. The few climate stations that have operated for more than a decade show large variability over short distances, as weather masses are forced over the narrow spine of the southern Andes and over the icefields (e.g., Rosenbluth et al., 1995). The range of variability indicates that records from nearby stations may poorly represent local conditions on the glaciers, particularly as all the stations are located at sea level, and those located in the towns were by necessity placed in the lee of the major mountain ranges, where they would be sheltered from the renowned Patagonian winds.

To understand variability in local climate around the Magellan Strait, Schenider et al. (2004) compared sea level pressure, wind speed and precipitation rates from 1970-2001 at four NCEP gridpoints and two long term weather stations in the region: Faro

Evangelista (at the western entrance to the Strait) and Punta Arenas. They found that the precipitation rates from the NCEP reanalysis model correlated well with regional wind speeds at Faro Evangelista.

Climate records at Bahia Felix and Punta Arenas to the west and north, respectively, show a slight downward trend in annual precipitation after 1920 (Holmlund and Fuenzalida, 1995). Precipitation in the region falls mainly in the spring and summer, with no significant change in seasonal trend over the past century. Records from Punta Arenas and Puerto Williams also indicate a sustained regional warming since 1915 and a drier period around Tierra del Fuego in the mid-1960s (Porter and Santana, 2003).

Retreat of Marinelli

Holmlund and Fuenzalida (1995) first documented the unique dynamics of Marinelli Glacier, noting that a relatively warm 20th century may have caused significant thinning of the glacier tongue through ablation, while the glacier continued to be grounded on the terminal moraine. When the glacier front thinned sufficiently in the latter half of the century the ice broke up quickly and the front retreated extremely rapidly. Porter and Santana (2003) also documented the retreat of Marinelli in the latter half of the 20th century from aerial photographs and satellite images. They compared the timing of retreat to the climate record at Punta Arenas, and surmised that decades of negative mass balance in the first half of the 20th century led to significant surface thinning that eventually initiated the rapid terminus retreat after the mid-1960s.

Both studies suggest that dramatic recession after 1967 was induced by the local topography, as the glacier pulled back from its Little Ice Age (LIA) moraine (Holmlund and Fuenzalida, 1995) and into deep water. The trimline along the eastern margin of the fjord shows a significant slope from approx. 60 m.a.s.l. close to the LIA moraine to ~250 m.a.s.l. at the current glacier terminus (Fig. 3.2), which suggests that the entire glacier tongue was grounded during its maximum (i.e., if the tongue was floating, trimlines would be nearly level). When the glacier thinned sufficiently in the mid-20th century, bringing the terminus closer to flotation, it pulled back from the moraine and broke up quite quickly, rapidly receding into the deeper water of the inner fjord. It has continued to retreat rapidly since, pulling back over 13 km in under 40 years.

Field methods

In this study, I examine how sediment yield and glacier retreat progressed in response to climate and topographic changes in the latter half of the 20th century. To calculate the sediment delivery to the glacier front, our research team collected acoustic reflection profiles in Marinelli fjord in July 2005. These data were acquired using 300J Boomer and 1000J Sparker transducers with a Benthos hydrophone, firing at 0.2-0.5 seconds. Both transducers penetrated the soft sediment in the fjord bottom and imaged a distinct reflector at up to 100 m below the sediment surface, which was interpreted as bedrock. To convert two-way travel time in the water to depth, an average seismic velocity of 1460 ± 6 m/s in the fjord waters was used, which was measured using a Seacat SBE 19plus CTD near the ice front and in the center of the fjord. The glacimarine sediment thickness and depth to bedrock in the fjord were reconstructed along a dense set of seismic profiles along and across the fjord, using a seismic velocity of 1680 m/s for glacimarine sediments. This velocity is the median of measured seismic velocities for glacimarine muds (1640-1740 m/s, Stoker et al., 1997). Two distinct facies above the strong reflector were recognized in the seismic images: a laminated, semi-transparent layer interpreted to be predominantly ice-distal glacimarine input with some subaerial fines, and a hummocky, chaotic facies presumed to be ice-proximal sediments and/or submarine slumps. Both facies have been described as typical of deposits in temperate, tidewater fjords (e.g., Molnia et al., 1984; Anderson, 1999).

From the seismic profiles, both the bathymetry and the subsurface bedrock elevations between the tracklines in the fjord were interpolated using the triangulated-irregular-network (TIN) function in ArcGIS. The TIN function creates planar surfaces between three nearest neighbors in x,y,z space. The TINs of the prominent subsurface reflector and the surface of the sediment were then rasterized into 60 x 60 m grids, and the sediment volume was calculated as the difference between the fjord bottom and prominent reflector.

To determine the uncertainty in the sediment thickness measurements, I compared the original spot depths from the seismic profiles to the gridded depths at the same locations, using the leave-one-out cross-validation method. The interpolation and gridding introduces at least an 18% uncertainty in total sediment thicknesses. The magnitude of the error increases with the distance between tracklines and the actual

variability in the depths and sediment thickness. Adding in a user error of approximately10μs, or 1-2%, in picking sediment depths from the seismic profiles, and another <5% error in using the seismic velocities for glacimarine muds, the total error in the determination of sediment thickness is estimated to be 25%.

The total sediment volume in the fjord can be divided by the time since the glacier occupied the fjord to calculate the average sediment flux into the fjord over the period since retreat. The sediment flux, and by inference, the erosion rate, from Marinelli Glacier might well have varied during over the past 45 years of retreat, a period when the ice flux may have varied substantially due to rapidly changing geometry and climate. To examine this temporal variation, I used a numerical model of proglacial sedimentation (described in Koppes and Hallet, 2002) to calculate the debris flux as a function of time. The model calculates the annual sediment flux necessary to produce the observed volume of sediment in the fjord, given independent data documenting the rate of terminus retreat, and interpolating the rate of retreat between known terminus positions over time. The annual sediment flux is converted to a basin-wide erosion rate by dividing by the glacier basin area during that period, measured from SRTM DEMs (with a 50-m horizontal resolution), assuming that changes in subglacial and englacial storage of the sediment are not significantly modulating the sediment output (this assumption is discussed below and in Chapter 4). To convert this sediment production rate to the bedrock erosion rate, it was divided by the ratio between the density of glacimarine sediment (1.8 g/cm^3, out of a range of 1.7-2.0 g/cm^3) and crystalline bedrock (assumed to be around 2.7 g/cm^3) – these estimates introduce another error in the bedrock erosion rate of up to 12%, so that the total error in the calculation of basin-wide erosion rates approaches 38%.

The proglacial sedimentation model represents the transport and deposition of glacially-derived sediment as a function of distance from the ice front, as debris rains out of both the calving front and the turbid plumes that rise buoyantly at the ice front and flow away from the terminus near the surface of the fjord (Syvitski, 1989). Some basic knowledge of the variation in the rate of sedimentation as a function of distance from the terminus is therefore needed to reconstruct the temporal variation in sediment flux emanating from the glacier. To date, only a few empirical studies of the variation in proglacial sedimentation rates have been measured at temperate tidewater glaciers (e.g., Cowan and Powell, 1991, Syvitski, 1989). Little is known about whether the

exponential decay in sedimentation measured at these glaciers is universal. Hence, sedimentation rates were measured by installing sediment traps in an array away from the terminus of Marinelli. The traps were deployed and collected over one week in July 2005, when the fjord was filled with brackish ice. The sedimentation rates measured are therefore only representative of mid-winter rates (Fig. 3.3), a time when subglacial meltwater plumes are expected to be least active. While the volume of sediment may vary seasonally and hence the short-lived sediment traps may not represent the annual yield, the observed reduction in sedimentation rates with distance from the ice front, however, is not likely to change with the seasons. The linear decay in sedimentation rate away from the ice front measured from the sediment traps in mid-winter was used in the model of the temporal variation in proglacial sediment yield with annual resolution (see Koppes and Hallet, 2002).

Erosion rates for Marinelli Glacier

The acoustic reflection survey of Marinelli fjord indicates that over 3.9 x 10^8 m^3 of sediment have been deposited in the fjord since the glacier retreated from its Little Ice Age moraine, in a string of interconnected basins along the thalweg of the fjord. The basins are in general separated by transverse bedrock ribs; little sediment has accumulated on the crest of the ribs (Fig. 3.4). There is also little indication subaerially or in the submarine record of sediment slumping from the valley walls and contributing to the sediment accumulating in the fjord, with the exception of deltaic deposits from a small tributary valley at the western midpoint of the fjord. Aerial photos of the tributary valleys along the west side of the fjord show perched ponds in the valleys, with thin fluvial deposits draping over roche moutonnées, and negligible downcutting of the fluvial sediments. Trimlines of the last glacial advance are high and distinct with few signs of rilling, which would suggest substantial subaerial erosion and redeposition of glacial or non-glacial sediments into the fjord subsequent to retreat. Unlike in Icy Bay (Chapter 2), the three small tributary streams entering the western edge of the fjord show no evidence of significant sediment delivery to the fjord; there are no subaerial deltas forming at waterline in the fjord, and only one of the three streams appeared from the seismic record to have formed a small submarine delta, which was defined and excluded

from the measurement of glacimarine sediment volume. In the upper third of the fjord (south of the year 2000 terminus position) up to 20 m of remnant ice lines the edges of the fjord at the waterline, acting as a buffer and preventing any sediments that are being eroded from and transported down the valley walls from entering the fjord. I hence regard the non-glacial, subaerial sources of sediment as being negligible volumetrically, as they account for no more than a few percent of the post-glacial sediment volume in the fjord.

The post-glacial sediment package is well defined in the acoustic record as a semi-transparent, laminated layer. It overlies a distinct reflector containing many parabolic point reflections, which rises along the sides of the fjord and emerges as bedrock above the waterline (Fig. 3.5). The hummocky, chaotic facies found in several Alaskan fjords (Molnia et al., 1984; Stravers et al., 1994; Koppes and Hallet, 2002, 2006) and interpreted as ice-proximal deposits, are limited to the base of the steep fjord walls and the edges of bedrock highs in the outer portion of the fjord. It appears that most of the sediment in the fjord consists of fines that rained out from the water column, or were mobilized and reworked by strong bottom currents to produce the well-laminated, near horizontal layers.

The glacier front completely pulled back from the LIA moraine some time between 1945 and 1967 (see Fig. 3.6). Since the year when the glacier completely pulled away from the moraine is unknown within this timeframe, I assume that the glacier retreated the ~2 km at a constant rate between 1945 and 1967, and pulled away from the foot of the moraine around 1960. Hence, all the laminated, transparent sediments imaged in the fjord bottom are assumed to have been deposited since that time. Dividing the total sediment volume in the fjord, 3.9×10^8 m^3, by the length of time since retreat from the foot of the moraine (Fig. 3.6), the sediment flux into the fjord over the 1960-2005 period averaged $1.1 \pm 0.4 \times 10^7$ m^3/a.

For any year, the sediment flux can be divided by the drainage area of the glaciated basin, which decreased by over 40% during the 1960-2005 period, to estimate the annual basin-wide erosion rate. Taking into account differences in density between the glacimarine sediment collecting in the fjord and the bedrock that produced this sediment (described in Chapter 1), the estimated basin-wide bedrock erosion rate from Marinelli glacier during the latter half of the 20^{th} century averages 39 ± 12 mm/a. This basin-wide rate of erosion includes subglacial erosion and any sediment delivered to the

glacier surface by periglacial processes or stored beneath the glacier and subsequently entrained by the glacier and transported to the fjord. Given that much of the basin is covered by ice (>65%) and the portion of the basin above the glacier surface is steep and covered with a perennial mantle of snow, most of the sediment must be produced and stored subglacially. The conversion of sediment flux to basin-wide erosion assumes that there has been no significant change in subglacial sediment storage in the basin during this period, an assumption that appears robust given the massive amount of sediment deposited recently in front of the glacier, as discussed further below.

Annual variability in erosion

.

The annual erosion rate changes considerably through time along with the interpolated rate of retreat from 1962 to 2005 (Fig. 3.7). The annual erosion necessary to produce the volume of sediment in the fjord varies greatly; for the first 20 years it averaged 9 mm/a, and steadily increased, starting in 1982, up to a peak of almost 130 mm/a in 2000, subsequently decreasing to 65 mm/a in 2005. Similarly, the retreat rate increases from 100 m/a in the 1960s and 1970s to over 1000 m/a in 1996, then slowly decreased back to 300 m/a in 2005. Intriguingly, the peak in retreat rate appears to lead the peak in erosion rate by ~3 years, suggesting a lag between the processes that are controlling retreat of the ice front, and those that are promoting an increase in the rate of erosion.

The correlation between retreat rate and erosion at Marinelli glacier is similar to our findings at Icy Bay. This is not surprising given recent observations from outlet glaciers in Greenland and Alaska that ice velocities scale with retreat rates (Van der Veen, 1996; Thomas et al., 2004; Howat et al., 2005), and that sediment yields increase with sliding speeds, as was documented at Variegated and Bench glaciers in Alaska (Humphrey and Raymond, 1994; Riihimaki et al., 2005). It suggests that unusually high ice fluxes associated with the rapid retreat of Marinelli over the past 40 years has induced unusually rapid erosion of the basin. To explore this relationship further, I examine potential variations in ice flux during the period for which erosion rates were measured.

Estimating the flux of ice through Marinelli glacier over the past 50 years

To date, there have been no measurements of ice thickness or ice velocity at Marinelli glacier, from which one could calculate the ice flux through the system, let alone any changes in this ice flux over time associated with the retreat. To examine the flux of ice through Marinelli glacier over the past 50 years, in a region with sparse climate records, I reconstructed the budget of ice in the glacier using a simple model based on local environmental conditions, together with the NCEP-NCAR reanalysis dataset to reconstruct local precipitation and temperature conditions at the glacier since 1950. The ice budget model is described in Chapter 1. The NCEP-NCAR Reanalysis data (see Kalnay et al., 1996) is a web-accessed, daily updated backcast climate dataset based on global radiosonde measurements and measured sea level pressures. The NCEP-NCAR model uses atmospheric physics to reconstruct multiple climate parameters at geopotential heights throughout the troposphere on a 2.5º by 2.5º grid (approximately 1.875º longitude by 1.9º latitude on a Gaussian grid) providing, amongst other parameters, daily near-surface minimum and maximum temperature, zonal and meridonal wind speeds, snowfall and precipitation rates at each gridpoint. The nearest gridpoint to Marinelli Glacier in the NCEP model is at 54.285ºS, 69.375ºW. From these measurements, the daily and yearly accumulation and ablation of ice over the surface of the glacier can be reconstructed, and the annual budget of ice through the glacier modeled, as described in Chapter 1.

Due to its low spatial resolution, the NCEP-NCAR model is unable to resolve topographic influences of the Andean Cordillera and Cordillera Darwin, which are less than 40 km wide at this latitude, on the atmospheric dynamics of the region. In order to best adapt the regional NCEP record to local conditions at Marinelli, I thereforeused local data measured with two rain gauges and one temperature gauge installed on the terminal moraine at the mouth of the fjord in July 2005. The gauges were revisited and downloaded in April 2006. The daily results from the temperature and precipitation gauges were then compared to the minimum and maximum above ground temperatures and precipitation rates, as well as to zonal and meridonal winds reconstructed from the NCEP-NCAR model for the period of gauge deployment, to calibrate the NCEP data to local conditions (Fig. 3.8). Least-squares regressions were used to relate measured and NCEP-modeled data, and each regression was then applied to the daily NCEP record at

the nearest gridpoint for the period 1950-2004 to estimate precipitation and temperature at the glacier terminus during the 50+ years preceeding our measurement period. The following regressions were obtained between measured values and NCEP-NCAR model values:

$T_{maxMAR} = 0.647\ (T_{maxNCEP}) + 3.43$ $(R^2=0.627;\ n=279,\ P<0.0001)$

$T_{minMAR} = 0.578\ (T_{minNCEP}) + 1.00$ $(R^2=0.615;\ n=279,\ P<0.0001\ )$

$P_{SR} = -0.284(P_{NCEP}) + 1.006(V_{NCEP}) + 1.187$ $(R^2=0.275,\ n=279,\ P=0.0002)$

where T_{maxMAR}, T_{minMAR}, $T_{maxNCEP}$, and $T_{minNCEP}$ are the maximum and minimum measured and NCEP daily temperatures, respectively, P_{MAR} and P_{NCEP} are the measured and NCEP daily precipitation rates, and V_{NCEP} is the mean daily meridonal wind speed from the NCEP dataset. As a north-facing glacier in an east-west trending mountain range, with higher variability in the dominant westerly flow of wind and moisture wrapping around Cape Horn and arriving at Marinelli from the southwest to northwest, precipitation rates at Marinelli appear to be more influenced by the magnitude of meridonal winds (N-S) than zonal winds (E-W). Hence, meridonal wind strength (V_{NCEP}) was included in the regression above, and used to infer past local precipitation rates at the glacier. While the reanalysis data captured the timing of larger rainfall events accurately, the NCEP precipitation rates appeared to systematically underestimate the magnitude of the larger storm events by up to 4-fold (see Fig. 3.8), and hence their correlation with locally measured precipitation values is relatively poor ($r^2 = 0.275$). Caution should therefore be used in interpreting the accumulation component in the ice budget model.

The NCEP-NCAR reanalysis temperature data at geopotential heights of 1000 mb, 925 mb, 850mb, 700mb and 600 mb were used to calculate the daily mean environmental lapse rate, from which the daily snowline altitude on the glacier could be determined. The average lapse rate for Marinelli, around 6.01 ºC/km, was then applied to the reconstructed daily average temperature at the terminal moraine (sea level) to locate the elevation of the 2ºC degree isotherm. All daily precipitation above this elevation on the glacier surface, inferred from the regression analyses, was then assumed to fall as snow, and was used to compute the daily, and annual ice flux (in snow water equivalent) into the glacier system (P_{snow}). The glacier surface (A_{gl}) was obtained from an SRTM 30-m digital elevation model (DEM), generated from NASA's

Shuttle Radar Topography Mission in 2000, and parsed into a grid with cell size of 66 x 66 m. The surface area of Marinelli glacier in 2005, derived from the DEM, is189 km^2. A three-fold orographic enhancement factor *k*, based on observations of the difference in accumulation between coastal stations and on the Patagonian icefields to the north (e.g., Escobar et al., 1992; Carrasco, 2002), was applied to the precipitation rates at sea level to estimate, to first order, the influence of the orographic enhancement of accumulation rates on the glacier. The sensitivity of the ice budget to this enhancement factor will be discussed below.

The snow input onto the drainage basin can then be combined with the ablation loss from the glacier surface ($\alpha * A_{gl}$), the loss of ice at the terminus ($A_{term} * dx/dt$) and the thinning of the glacier surface ($A_{gl} * dz/dt$) to compute the yearly budget of ice through the glacier system. To estimate ablation rates on Marinelli glacier, I used the nearest record of ablation and associated climate, at Glacier Lengua in the Gran Campo Nevado. (C. Schneider et al., pers comm., 2006), 285 km to the northwest. Gran Campo receives moisture from the same westerly and southwesterly storms that impinges on the Cordillera Darwin, and air temperatures are also heavily influenced by the cold Humboldt current running up the western shelf of Patagonia. Ablation stakes were set out in the lower reaches of Glacier Lengua during the summer of 1999-2000 and measured daily. Daily minimum and maximum temperatures were also collected at a nearby refuge of similar elevation during this period (C. Schneider, pers. comm.). From these data, the daily ablation rate could be compared to the mean daily air temperature at the refuge, to calculate a regional ablation rate in mm/day as a simple function of temperature:

$$\alpha = 7.416 * T_{avg} - 23.956 \quad (R^2 = 0.987)$$

This correlation was then applied to calculate the daily ablation rate over the surface of Marinelli Glacier as a function of the locally-calibrated NCEP temperature, and compute the annual ice volume lost through ablation. This ablation flux can be subtracted from the accumulation flux, to calculate the flux of ice that calved from the terminus, assuming a glacier in balance. Any additional ice removed from the system would result in retreat and/or thinning of the ice surface.

Contribution of climate to retreat

According to the locally-calibrated NCEP-NCAR climate model results, annual precipitation totals at Marinelli glacier decreased, with considerable variability, from the 1950s until the present (Fig. 3.9a). In the 21st century, the mean annual precipitation has remained at almost half the annual precipitation in 1960. Similarly, annual temperatures in the local area have been steadily rising since the 1950s, with mean annual temperatures since 1997 remaining over 1ºC warmer than during the 1960s (Fig 3.9b). Both trends have contributed to an increasingly negative mass balance over the past 50 years, with steadily decreasing inputs of snow onto the glacier, and increasing loss of ice due to ablation (Fig. 3.10).

If we assume that Marinelli glacier was relatively stable (i.e., volume essentially constant) during the 1950s, before significant retreat commenced, the flux of ice reaching the terminus and calving (i.e., the calving flux) from Marinelli glacier during this period can be estimated from the inferred balance between ice gains and losses in the ice budget model. The model suggests that the 'balance' calving flux during this period approached 2-3 x 10^8 m^3/a, ~2x the ablation flux, assuming a 3-fold enhancement of snowfall due to orographic influence in this region. Given that the ice was grounded in shallow water (<60 m. below sea level) on the up-glacier ramp of the terminal moraine, with an ice cliff averaging 40 m and a terminus ~4 km wide, this balance flux suggests that calving speeds approached 500-700 m/a during this period. Observations of the linear relationship between calving speed and water depth from a number of glaciers in Alaska, Greenland and Svalbard indicate that for a calving margin grounded in 60 m of water, calving speeds should average between 550 m/a (Pelto and Warren, 1991) and 1.6 km/a (Brown et al., 1982). That our estimate of the 'balance' calving flux in the ice budget model is within the range of empirical observations of tidewater calving rates suggest that, although significant uncertainties in snow input parameters exist, a function of the choice of orographic enhancement factor and poor correlation between the local climate and the NCEP results, the model nonetheless provides useful estimates of snow input and output over a long period when local environmental measurements are lacking.

The 13 km of retreat since 1960 and the presence of high trimlines clearly indicate, however, that Marinelli glacier has not been in balance but has been losing

volume at a rate that far exceeds the loss simply to ablation. Hence, the flux of ice out of the system must have increased over this time, and contributed to the overall loss of glacier volume. These additional volumes of ice loss can be quantified and added to the 'balance' calving flux to estimate the total flux of ice through the glacier over time.

From the subsurface bathymetry and the retreat rate, the volume of ice lost per year from the terminus since it began to retreat can be estimated and included in the ice budget model as a part of the calving flux. This ice was presumably lost via calving, and hence can be added to the difference between snow accumulation and ablation (the balance flux to the terminus) to estimate the total calving flux (Figure 3.11a). The volume of ice lost below sea level is 3.3×10^9 m^3. If we assume an above board ice surface of 40 m.a.s.l., averaged across the ice front, Marinelli glacier lost a total of 4.4×10^9 m^3 (4.4 km^3) of ice from the glacier snout between 1960 and 2005, with an average 'additional' ice flux delivered to and lost from the terminus of 1×10^8 m^3/a. This 'additional' ice flux is in excess of the ice loss due to surface ablation.

The volume of ice lost from the glacier terminus associated with the retreat appears to have responded slowly at first to the warmer and drier conditions. Once retreat was underway, however, the pace of ice loss at the terminus accelerated markedly, in particular in the mid-1990s following a year when ablation exceeded accumulation considerably, suggesting that the glacier was rapidly losing mass through both excess melting and excess calving. As the terminus retreated into deeper water, subject to increased submarine melting and more rapid calving, calving rates increased, contributing additional ice flux to the terminus and more rapid ice front retreat. Interestingly, although the trend of strongly negative mass balance continued to 2005, retreat rates, and hence calving fluxes, decreased after 1997, probably due in part to the emergence of almost half of the terminus, which reduced the surface area of the ice front subjected to submarine melting and thereby reduced the calving rate that drives retreat (Motyka et al., 2003).

The presence of high, fresh trimlines indicates that Marinelli glacier has not only been retreating but also drastically thinning for the past 50 years due to unusually rapid ablation, and/or longitudinal extension of the glacier as calving rates increased. The average rate of glacier thinning can be assessed from the trimline above the current glacier terminus, which represents the glacier surface in 1945 according to a Chilean Navy oblique aerial photo taken at that time. Given a trimline elevation of 250 m.a.s.l.

and a current surface elevation of approximately 45 m.a.s.l., the glacier surface at the current terminus has descended 3.5 m/a on average over the past 60 years. As the lowering rates tend to be greatest near the terminus of retreating glaciers due to their convex profiles, thinning over the entire ablation area (~60 km^2) at this rate would correspond to a maximum volume loss of 2 x 10^8 m^3/a from the glacier since 1945, equivalent to the average annual ablation flux during this period, and twice the average annual volume of ice lost from the terminus. Assuming that this thinning was caused by extension and increased calving, the corresponding ice volume loss should also be added to the estimate of annual calving flux in the model. As shown in Fig. 3.11b, the calving flux increased dramatically during the period of most rapid retreat. The reduction in the calving flux at the terminus after 1997, when retreat also slowed, in turn may have contributed to a reduction in the rate of erosion of the basin in the 21st century, by reducing the rate of basal ice motion.

The loss of ice from the glacier front as it retreated and the glacier surface as it thinned together have reduced the volume of Marinelli glacier by an average of 3 x 10^8 m^3/a over the latter half of the 20th century. By comparison, on average only 2.1 x 10^8 m^3/a was lost to ablation during the past 50 years. Together, these volumetric losses from the glacier have vastly outpaced the snow input since the initiation of retreat in the early 1970s, which steadily decreased to average only 2.9 x 10^8 m^3/a in the past decade (see Fig. 3.11). This suggests that the strong negative balance of Marinelli glacier caused the drawdown of the glacier surface and initiated rapid calving into deep water, which together have contributed to both increased ice fluxes to the terminus and a period of unusually rapid retreat.

Implications

The close correlation between the sediment flux from the glacier and the retreat of the ice front suggests several possible mechanisms at work. First, the volume of ice lost from the terminus due to retreat, coupled with any increase in the ice flux to the terminus during this time, would automatically increase the volume of englacial sediment delivered to the fjord. Second, the retreat of the ice front could be associated with a

change in conditions at the bed, prompting accelerated erosion and/or increasing sub-glacial fluvial evacuation of stored sediment beneath the ice.

In the first scenario, the volume of sediment arriving at the fjord scales with the englacial debris concentration and the ice flux at the terminus. As both the ice flux and the volume of ice lost from the terminus increased during retreat, this ice-entrained debris contribution must have increased proportionally. The dearth of debris visible at the terminus ice cliff, on the surface of Marinelli glacier, and in the multitude of icebergs that clog the fjord, however, suggests that the englacial debris concentration is far too low to produce the large volumes of sediment delivered to the fjord. Indeed, a study by Hunter et al. (1996) at three massive tidewater glaciers in Alaska concluded that the supraglacial and englacial debris concentration in active tidewater systems does not exceed 1% per unit ice volume, and account for at most 5-10% of the total sediment delivered to the fjord. Assuming a similar, upper limit of 1% debris concentration for the Marinelli glacier, and the estimate of the flux of ice to the terminus over time from the ice budget model, this englacial debris flux can be estimated to first order. The resulting englacial debris flux is less than 20% of the average sediment flux during this time (Fig. 3.12). Any changes in the englacial flux during retreat hence cannot be the main driver of the large fluctuations in sediment flux we are observing over this period.

Instead, the correlation of erosion rate and retreat rate at Marinelli glacier more likely reflects changing conditions at the glacier bed, as the glacier thinned, shortened, steepened and sped up in response to retreat. First order estimates in the change in calving flux, from the ice budget model, suggest that ice speeds at the terminus increased from around 1 km/a to over 2 km/a during the period of maximum retreat. The dominant controls on the speed of ice at the glacier bed are the basal shear stress and effective pressure, both of which are a function of the ice thickness. Given that the mean ice thickness at the terminus today is 145 m, with a maximum ice thickness of 193 m, the infinite slope approximation of the basal shear stress at the terminus today averages ~91 kPa. The ice thickness at the 2005 terminus position was over 220 m greater in 1945 (measured from the trimline). As the ice thinned and the glacier lost volume during the past 60 years, the drawdown of hundreds of meters of ice necessitated a large increase in ice flux to the terminus, and correspondingly, accelerated sliding and erosion at the bed.

The marked acceleration in both the rate of retreat and the ice flux to the terminus of Marinelli glacier in the mid-1990s appears to be caused by unfavorable climate change in the past few decades, and not simply by changing topography at the ice front. While the area of the ice front subject to calving and submarine melt slowly increased from 2 to 4 $x10^5$ m^2 from 1967 to 1989, it decreased again starting in 1989, reaching 2.3 x 10^5 m^2 in 2005, while both retreat and calving fluxes were accelerating. Water depth at the ice front and glacier width did not change appreciably during this period, with the exception of a narrow bedrock knob that the terminus passed over quite rapidly in 1997. Hence, calving and submarine melt conditions at the glacier terminus were not changing appreciably. Instead, the rate of retreat peaked shortly after a year of largely negative mass balance, when the ice input to the glacier was more than balanced by ablation, and hence all calving resulted in net ice loss from the terminus. It is worthy of note that unfavorable climate in the past few decades appears to have induced dramatic retreat in this one glacier system, while neighbouring glaciers in the same icefield appear to be stable or slowly advancing during the same period (Holmlund and Fuenzalida, 1995; C. Porter, pers. comm., 2006). This difference in response to the same climatic forcing suggests that absence of calving at neighbouring glaciers and/or differences in calving rates and valley morphology may be the primary controls on retreat. Without a calving margin and a deep fjord in which to calve, the ice budget model results for Marinelli glacier suggest that, until the mid-1990s, the snow input exceeded the loss to ablation, and the glacier could have remained stable or even advanced, as seen in nearby glaciers.

The sustained, mean erosion rate of 39 ± 12 mm/a over the past 50 years is extremely high, particularly given the size and relief of the Marinelli basin. In the absence of significant tectonic or isostatic uplift, for example, such an erosion rate applied to Mt. Shipton, at 2469 m.a.s.l., would remove it in only 63 ka. This rapid erosion therefore cannot be sustainable in the long term, otherwise the Cordillera Darwin massif would easily have been flattened within one glacial cycle. Maximum estimated tectonic uplift rates in the region do not exceed 1 mm/a in the past few million years (e.g., Diriason et al., 1997). These rapid rates must therefore be indicative of a short-lived transient period of rapid transfer of glacial ice from highlands to the ocean and, correspondingly, rapid erosion. Similarly, the glacier thinning and recession observed at Marinelli must also be

highly unusual, for at recent rates of retreat (over 13 km in 50 years) and thinning (over 200 m in 50 years) there would be no ice remaining in the basin within a century.

Since much of a normal tidewater glacier cycle is spent in a quasi-stable mode (Meier and Post, 1987), the period of rapid retreat, rapid ice motion and associated rapid erosion, such as we are currently measuring at Marinelli and the other glaciers in this study, tends to be relatively short. During the much longer advance phase, the glacier first must evacuate a significant amount of proglacial sediment before it could start eroding the bed. Although total sediment yields would be high during such an advance, actual bedrock erosion and production of relief would be a small component of the overall yield. Only once the proglacial sediment, including the sediment reworked and redeposited by the advancing glacier, is evacuated from the glacier basin could significant bedrock erosion begin anew. The erosion rate during the quasi-stable phase, when the glacier was at a standstill, would therefore be more representative of the long-term rate (i.e., the rate for the entire advance-retreat cycle). We therefore take the extrapolated erosion rate for periods of standstill, represented by the y-intercept (zero retreat rate) in Figure 3.7b, to yield the best available estimate of the long-term erosion rate: for Marinelli Glacier, it is ~10± 3 mm/a.

The recent and long-term sediment yields and erosion rates at Marinelli glacier are amongst the highest reported rates worldwide, on par with recent specific sediment yields measured from the largest Alaskan tidewater glaciers, in a considerably more active tectonic setting. The similarity in the correlation between rapid erosion and retreat of tidewater glaciers in both hemispheres suggests that this relationship is widespread.

Conclusions

Marinelli glacier has retreated almost 13 km since 1960, a period of gradually warming temperatures and decreasing precipitation. Annual retreat rates have varied from 100 m/a in 1960 to a peak exceeding 1 km/a in the mid-1990s, and have since decreased. Erosion rates have varied similarly from 9 mm/a to almost 130 mm/a, averaging 39 mm/a over the last 45 years, an almost 4-fold increase over estimates of the long-term erosion when the glacier is neither retreating or advancing. These results, showing both contemporary erosion rates exceeding 10 mm/a and sediment yields

increasing as Marinelli glacier retreated rapidly in the latter half of the 20th century, are similar to results from two tidewater glaciers in Alaska, Muir Glacier (Koppes and Hallet, 2002) and Tyndall Glacier (Koppes and Hallet, 2006, Chapter 2). The similarities in sediment yield data from a number of glaciers in two different hemispheres suggest that, in general, contemporary basin-wide erosion rates for fast-moving tidewater temperate glaciers are very high, far exceeding tectonic uplift rates. They also suggest that erosion rates over the last few decades greatly exceed erosion rates over the entire glacier advance-retreat cycle primarily because this period has been characterized by exceptionally rapid ice motion.

The marked retreat and thinning of Marinelli glacier in the past 50 years indicates that much more ice is being conveyed through the glacier to the fjord than can be sustained by the input of snow. For Marinelli glacier, and many of these heavily glaciated basins, the recent period of warming and rapid retreat coincides with a significant increase in the flux of ice to the terminus, and associated acceleration of sliding at the bed. The recent erosion rates measured from these glaciers during retreat, as well as estimates of long-term erosion rates which take into account a significant decrease in erosion rates during glacier standstills and advances, remain among the highest known basin-wide erosion rates worldwide. Moreover, this rapid glacial erosion is not due to the substrates being unusually erodible because of inherently weak lithologies, or fracturing along fault zones, since the erosion rates measured represent a range of geologic and tectonic settings.

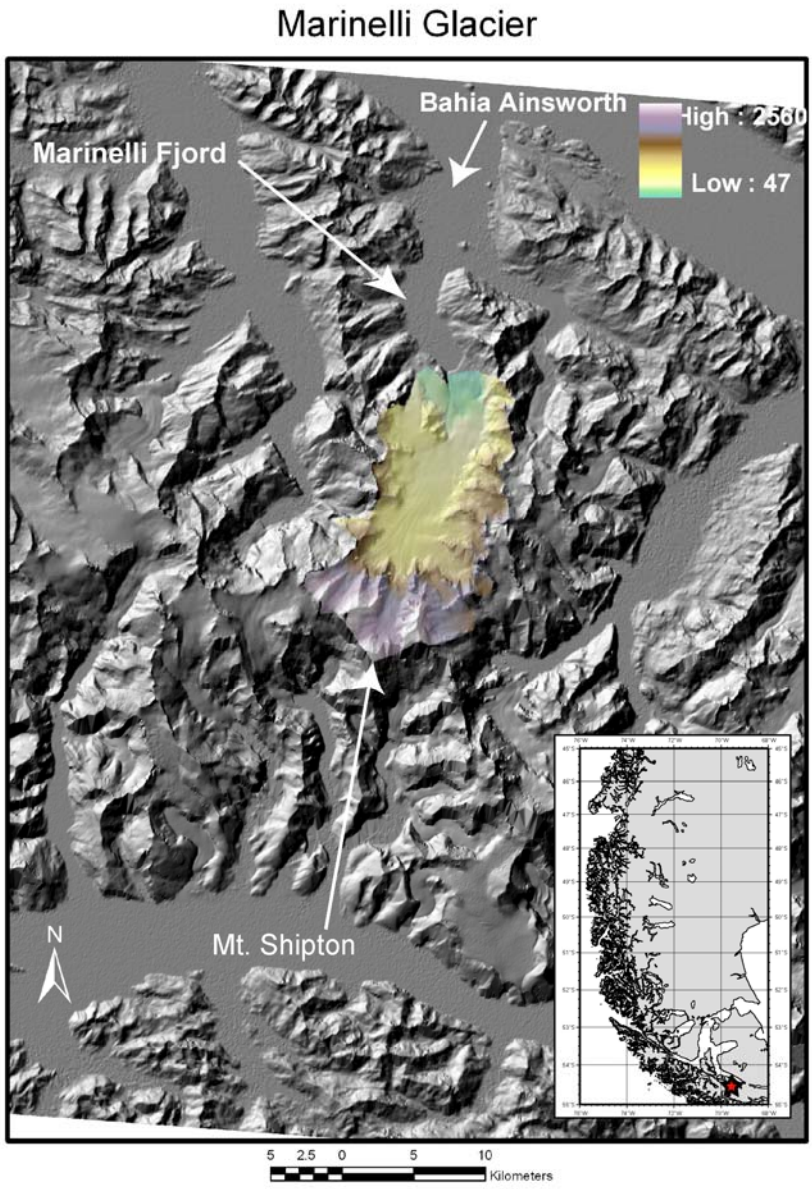

Figure 3.1 Location map of Marinelli Glacier in Chilean Tierra del Fuego, South America, with shaded-relief representation of a digital elevation model of Marinelli Glacier and Marinelli fjord, derived from February 2001 SRTM data. Elevations are in meters.

Figure 3.2 Photograph of the head of Marinelli Fjord taken 2 km from the terminus of Marinelli glacier in March 2005, looking east. A prominent trimline at ~250 m.a.s.l. is evident on the eastern wall of the fjord.

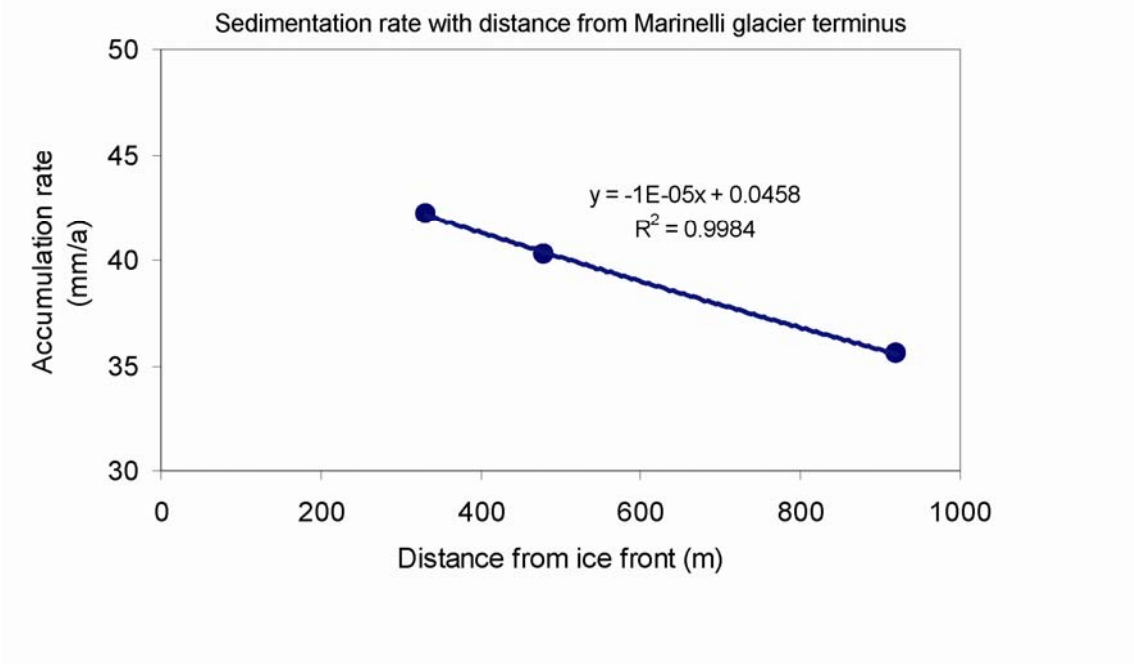

Figure 3.3 Sedimentation rate as a function of distance from the calving terminus, collected in sediment traps set 50 m above the sea bed. The sediment accumulated in the trap represents debris raining out from the water column above the trap. It does not include any sedimentation from dense, turbid plumes and mass movements that may occur at the sea bed. The average sediment accumulation rate within 1 km of the ice front for the period 2000-2005, including the contribution of these dense plumes, is approximately 2.4 m/a. Winter accumulation in the traps averaged only 40 mm/a, or approximately 2% of the total average annual sedimentation.

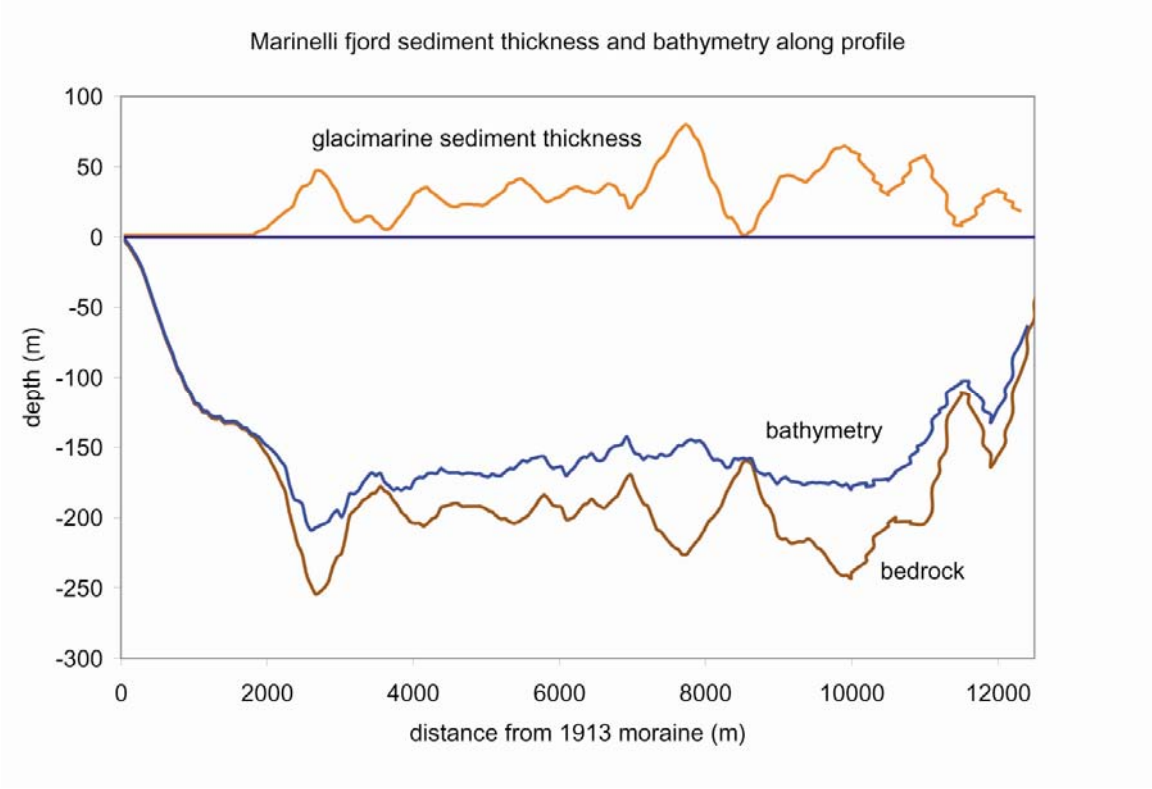

Figure 3.4 Profile of bathymetry and glacimarine sediment thickness along the thalweg of Marinelli fjord. The sediment is ponded in a series of small basins along the length of the fjord.

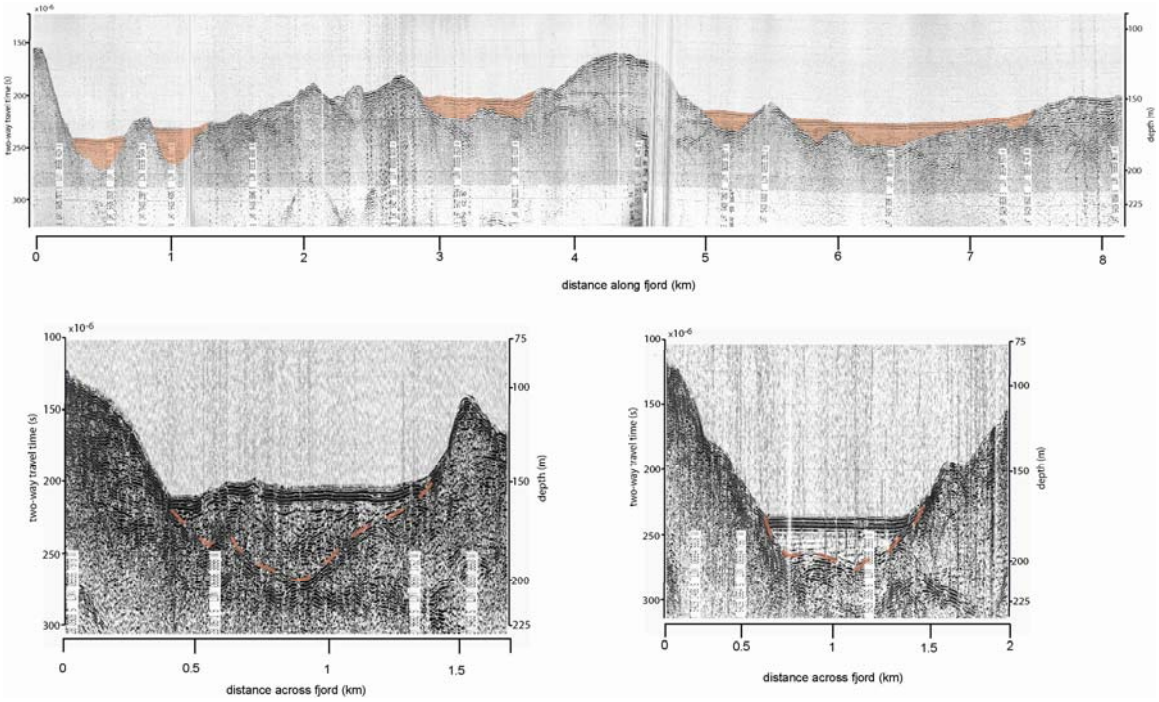

Figure 3.5 Examples of acoustic reflection profiles from which the sediment thickness in Marinelli fjord was measured. a) longitudinal profile along the thalweg from the foot of the terminal moraine (left) to approximately 2 km from the ice front (right). b) seismic profiles across the fjord, 1.1 km from the ice front, and c) close to the 1992 terminus position. Semi-transparent, laminated seismic facies, filling in the deeper basins are interpreted as ice-distal glacimarine sediments. The hummocky, chaotic seismic facies found near bedrock highs are interpreted as ice-proximal deposits and submarine slumps. The top of the underlying crystalline bedrock appears as the dominant reflective layer beneath the other two facies.

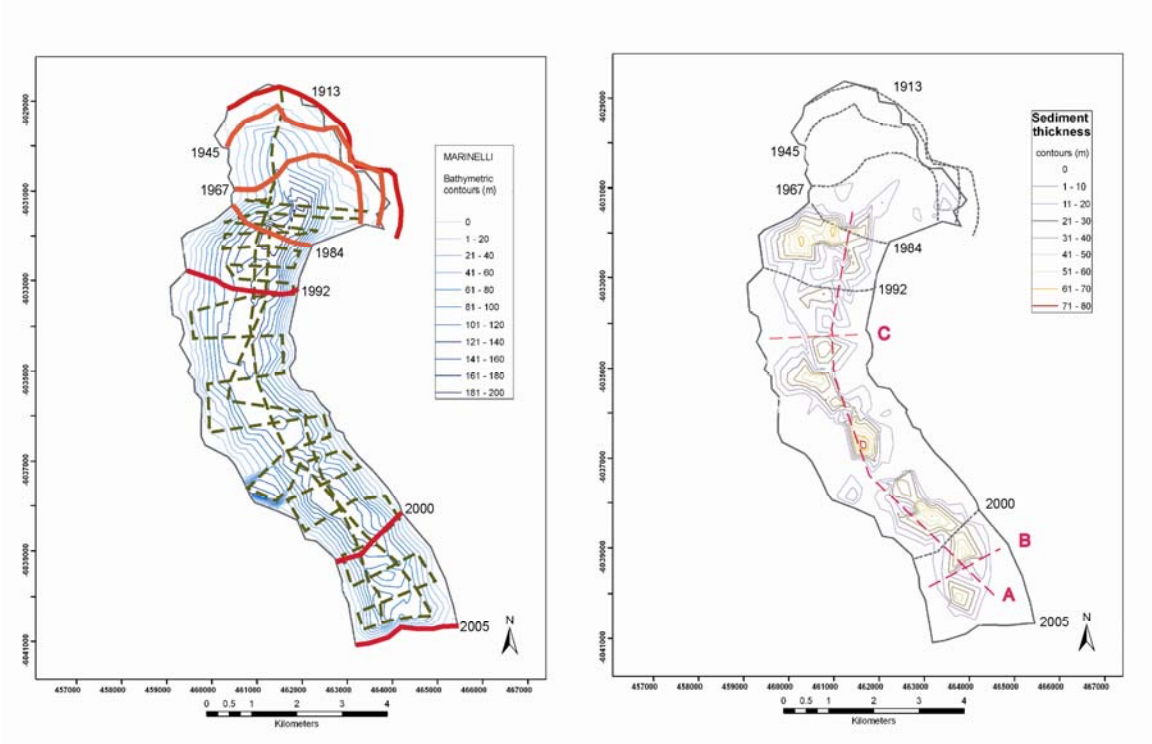

Figure 3.6 a) Contour map of 2005 bathymetry in Marinelli fjord (20-m interval), tracklines of the acoustic reflection survey (olive dashed lines), known terminus positions since 1913 (red lines), and locations of seismic profiles (A-C) in Fig 3.5. b) Contours of sediment thickness in Marinelli fjord, derived from the acoustic reflection profiles. Contour interval is 10 m. Known terminus positions are labeled.

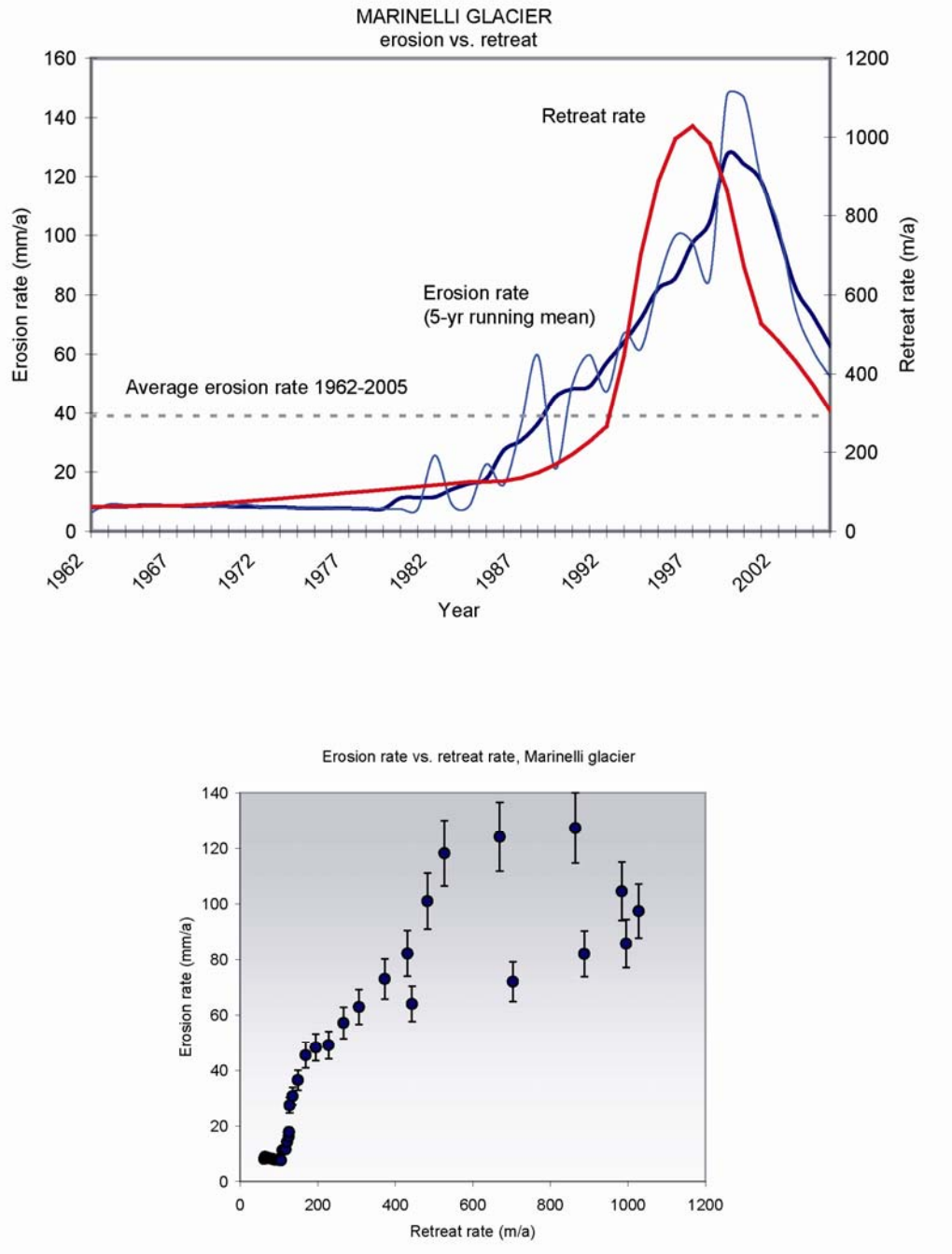

Figure 3.7 a) Time series comparison of erosion rate and retreat rate for Marinelli Glacier since 1962. The contemporary erosion rate averages 39 ± 12 mm/a. b) Comparison of erosion and retreat rates since 1962. Error bars represent a 30% uncertainty for calculated erosion rates. A hysteresis loop emerges, a function of the time lag between the peak in retreat rate and the peak in erosion rate. Extrapolating the erosion rate to times when the glacier is effectively stable, on average neither advancing nor retreating, the long-term erosion rate is 10 ± 3 mm/a.

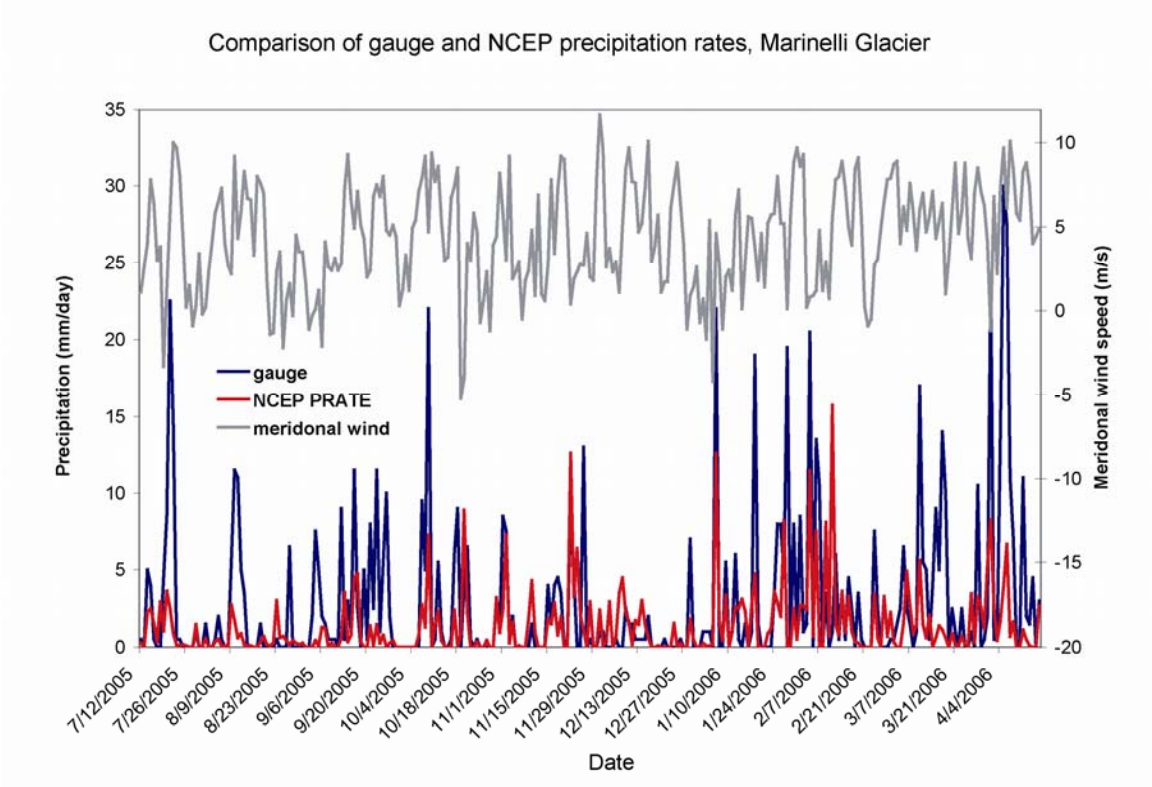

Figure 3.8 Comparison of surface precipitation rates from the NCEP reanalysis dataset for gridpoint 54.675ºS, 69.375ºW, and rainfall from gauges installed at the mouth of Marinelli fjord, July 2005 – April 2006. Surface wind speeds from the NCEP dataset are also plotted.

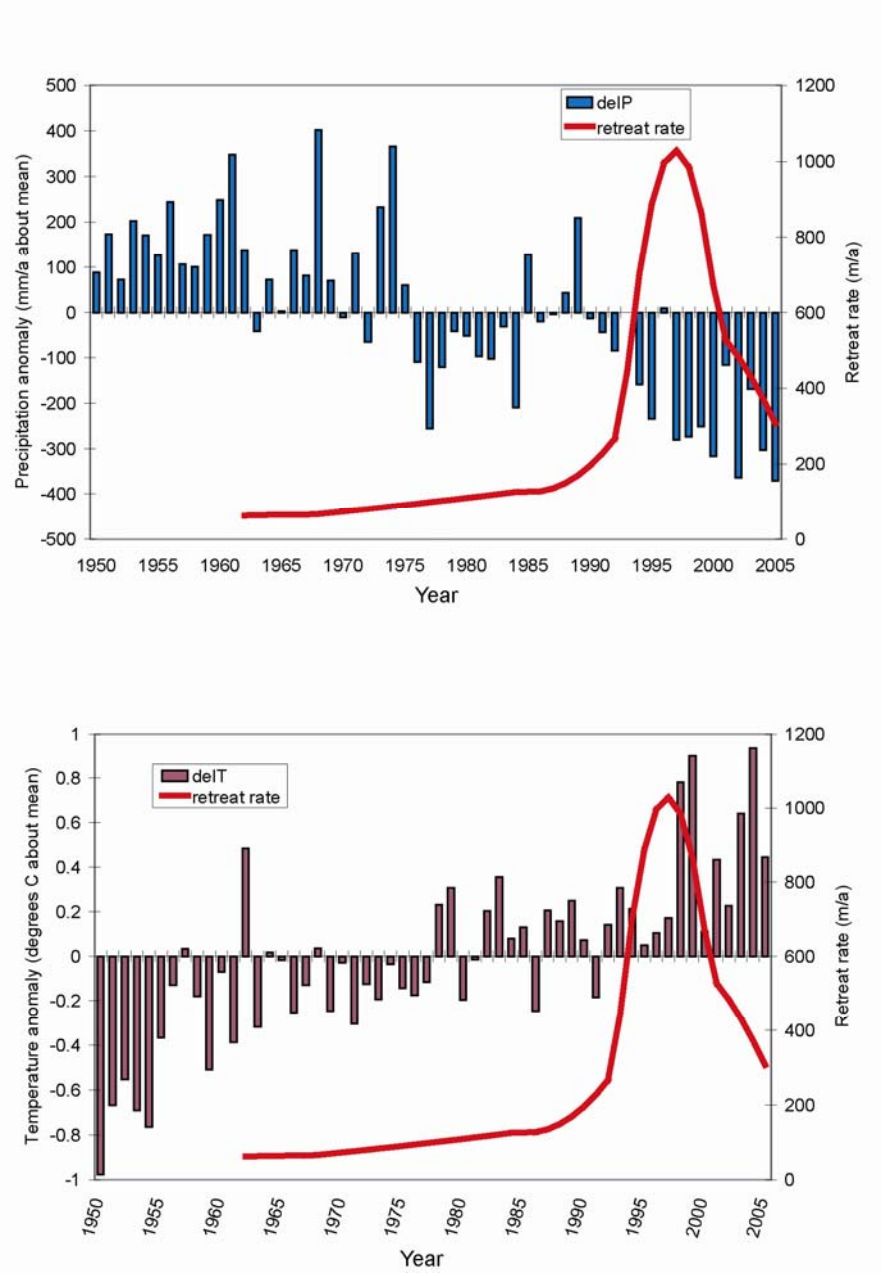

Figure 3.9 Time-series comparison of temperature and precipitation from 1950-2006, and retreat rate of Marinelli glacier. Climate parameters were derived from the NCEP dataset, adapted to local conditions by a least-squares fit with the gauge data from July 2005 to April 2006. a) Precipitation anomaly, in mm/a about a mean annual precipitation of 1272 mm, and terminus retreat rate. b) Temperature anomaly, in ºC about a mean annual temperature of 5.2ºC, compared to retreat rate.

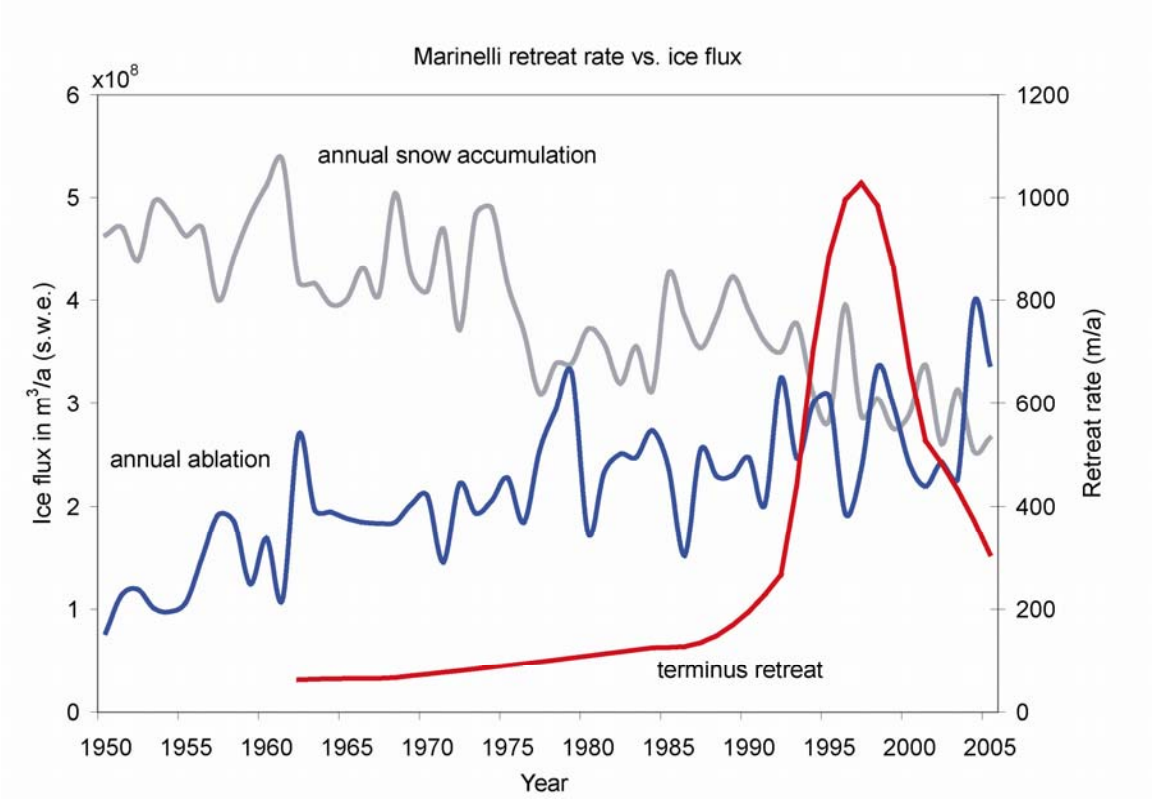

Figure 3.10 Ice addition to and ablation loss from Marinelli glacier, expressed as ice fluxes and compared to retreat rate from 1950 to 2006. Ice fluxes are in annual m^3 water equivalent.

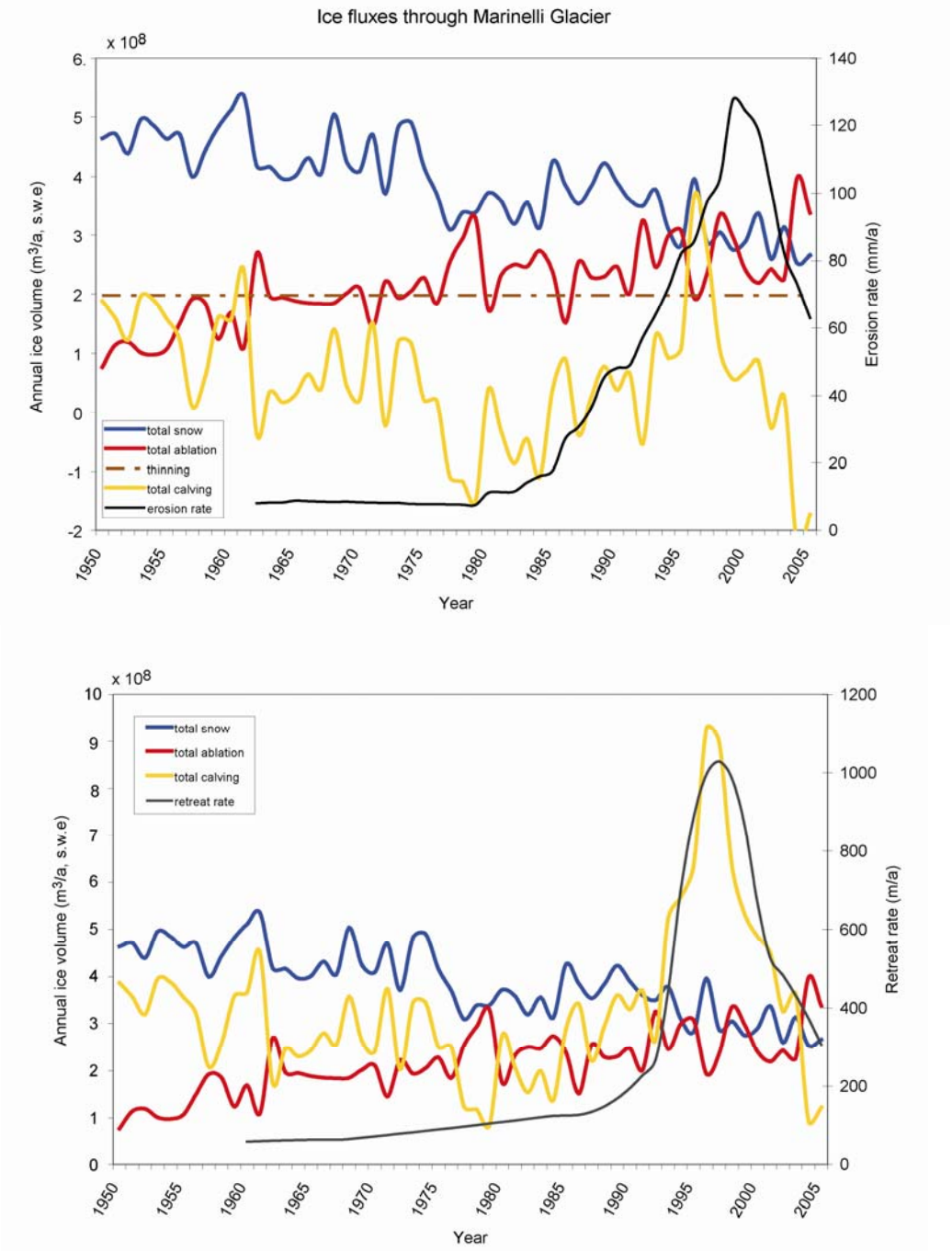

Figure 3.11 Ice addition to and loss from Marinelli glacier from 1950 to 2006, expressed as ice volumes in annual m^3 water equivalent. a) The annual snow input (blue), annual ablation loss (red), average annual volume of ice lost to thinning (dashed brown), and resulting calving flux (the sum of the difference between snow input, ablation and volume of ice lost from the terminus due to retreat (yellow)), compared to erosion rate (black) from 1960 to 2006. b) The annual snow input (blue), annual ablation loss (red), and resulting calving flux (the difference between snow input and all losses, including ablation, thinning and ice front retreat)(yellow), compared to retreat rate (dark grey), 1950-2006.

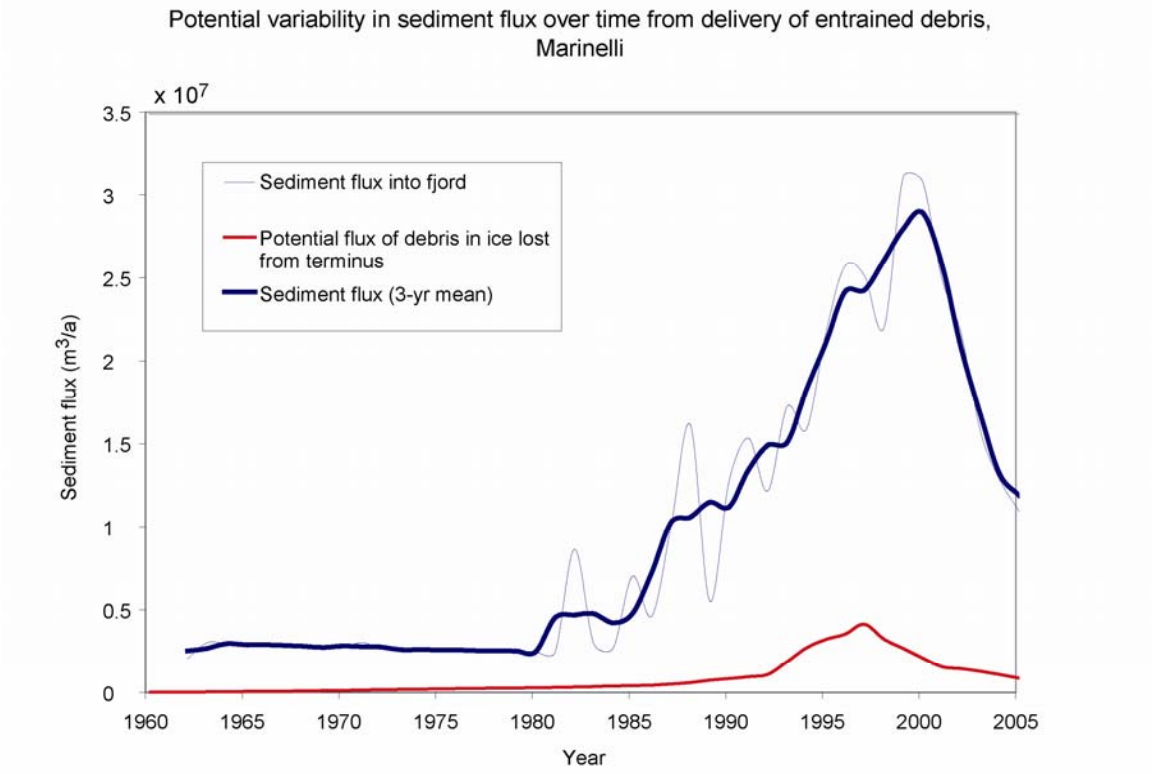

Figure 3.12 Potential variability in the annual sediment flux to Marinelli fjord over time and the delivery of entrained debris due to ice lost from the terminus of Marinelli glacier, assuming an upper limit in debris concentration of 1% per unit volume of ice.

CHAPTER 4.

Relating glacier erosion to ice dynamics, San Rafael Glacier

INTRODUCTION

The Patagonian Icefields of the southern Andes provide an outstanding opportunity to shed light on the controls on glacial erosion rates. In particular, the calving glaciers that drain the icefields are responding to both climate and non-climatic controls, and are delivering vast volumes of sediment to the fjords that border the range, where the sediment becomes trapped and can be measured. Elucidating these controls has wider significance because calving glaciers drain many of the remaining temperate icefields, including those in Alaska and Patagonia that contain the largest stores of ice outside of the polar ice sheets. The recent acceleration in thinning and recession of the outlet glaciers of the Patagonian icefields and the Greenland ice sheet are inferred to be a direct response to recent climatic change (e.g., Rignot et al., 2003; Rignot and Kanaparatnam, 2006). This glacier response, particularly the ice acceleration that has been documented as these glaciers start to retreat, can be compared to changes in sediment yields to shed light on the connections between climate and glacial erosion rates. These connections are of considerable interest as they are fundamental to studies of landscape evolution in many convergent orogens and the interpretation of glaciogenic sedimentary records.

Montgomery et al. (2001) found a close correspondence between total relief and perennial snowline elevation in the southern Andes, supporting the concept of the glacial buzzsaw in this region. No quantitative measures of glacier sediment yield or erosion rates, however, have yet been made in the area, but relatively high sediment yields and rapid erosion are expected in view of the dynamic nature of the glaciers of this temperate maritime region. Thomson (2002) found exhumation rates ranging from 0.4 to 1.3 mm/a since the Miocene, close to the North Patagonian Icefield. The relative uniformity of the surface topography and relief in this region, coupled with highly varying cooling and emplacement ages in the southern Andes, implies regional rates of

erosion sufficient to keep pace with variable uplift rates that range of up to 1.3 mm/a over the past few million years.

Most empirical studies of glacial erosion rates have relied upon measuring total sediment yield in a fjord and averaging the yield over the entire period of retreat and the entire basin, or comparing yields to the percent of glacial coverage in a single basin (e.g. Harbor and Warburton,1993) Herein, I present one of the first studies of basin-wide rates of contemporary glacial erosion in the Southern Andes, and develop an empirical relationship between sediment yields over time and the dynamic state of the San Rafael glacier. The importance of the rate of ice motion was first demonstrated by Humphrey and Raymond's (1994) study of Variegated Glacier, Alaska, where a two-order of magnitude variation in sediment yield accompanied a similar variation in ice velocity over a surge cycle. For Variegated Glacier, sliding speed was an excellent indicator of sediment yield, which is entirely in accord with theoretical models in which both abrasion and quarrying rates increase with sliding speed (Hallet, 1979; 1996). One can therefore reasonably expect that basin-wide erosion rates scale with basal ice motion. A convenient index to represent both the rate of basal sliding and the glacier size (cross-sectional area) is the flux of ice at the equilibrium line (ELA). The advantage of using ice flux in considerations of erosion is that this flux can be related to net accumulation and ablation on the glacier, and hence to climate through precipitation rates and temperature. This permits exploration of how erosion rates might vary within a glaciated basin due to variations in accumulation and ablation rates over time and space.

To determine the erosion rate of a fast-moving glacier in Patagonia, and to examine the relationship between erosion rate and ice flux, I measured the volume of sediment from San Rafael glacier, collected in a pro-glacial lagoon during the 1959-2006 period. From the measured sediment distribution and historical records of retreat of the glacier terminus, I model the annual sediment flux produced by the glacier. I then compare this annual sediment yield, converted to a basin-averaged erosion rate, to the ice flux. This annual flux of ice through the glacier is both measured (during periods when ice motion records were available) and obtained from a model of the annual budget of ice into and out of the glacier using daily values of key climate variables from the National Centers for Environmental Prediction- National Center for Atmospheric

Research (NCEP-NCAR) global reanalysis climate data set. Using a DEM of the glacier surface, and this reanalysis dataset, I calculate accumulation and ablation rates as a function of altitude to reconstruct the changing flux of ice at the terminus and at the ELA over the past ~50 years (see diagram in Chapter 1 for discussion and diagram of the ice mass budget model). This simple reconstruction of the time-varying budget of ice through San Rafael glacier provides clues into the relative importance of climatic and non-climatic controls on terminus retreat and erosion during the past half century.

Location

The Northern Patagonian Icefield, or Hielo Patagonico Norte (HPN), is ~120 km long and 40-60 km wide and caps the spine of the Andean Cordillera from around 46º30'S to 47º30'S (Fig. 4.1). It is among the largest temperate ice masses on Earth, covering an area of ca. 4200 km^2. Ice cover is sustained by heavy precipitation reaching 3.5-6.7 m/a on the western edge of the icefield as the Southern Westerlies are forced over the Andes (Escobar et al., 1992), and decreasing sharply to the east. Of the outlet glaciers draining the HPN, San Rafael glacier is the only glacier that calves into seawater. It is the most equatorial tidewater glacier in the world at 46º40'S, with surface speeds known to exceed 8 km/a at its terminus (Kondo and Yamada, 1988; Warren et al. 1995; Rignot et al., 1996), making San Rafael one of the fastest-moving glaciers worldwide, alongside the much larger Jakobshaven Isbrae in West Greenland (Thomas et al., 2004). It is also the second-largest outlet glacier of the HPN behind its neighbor to the south, San Quintin Glacier. With a glacier surface area of 747 km^2, San Rafael drains approximately 19% of the HPN, an area ranging from sea level up to a peak of 3910 m at Monte San Valentin, the highest point in the HPN. The glacier displays characteristics typical of temperate tidewater systems, with an accumulation area ratio of 0.78 (Aniya, 1988), and a substantial fraction of its annual ice volume lost via calving (Rignot et al., 1996).

San Rafael glacier descends steeply from the icefield through several icefalls, and calves into a brackish lagoon (salinity of 14.5 ‰), Laguna San Rafael. The lagoon is bounded by a prominent arcuate moraine. The Liquine-Ofqui mega fault, a major left-lateral strike-slip system defining the western edge of the Northern Patagonian

Batholith, forms an abrupt rangefront escarpment that defines the eastern edge of the Laguna San Rafael, creating its distinctive semi-circular shape. Since around 1978, the terminus of San Rafael glacier has retreated into and been topographically constrained by a steadily narrowing valley outlet that crosses the fault zone from the broad plateau of the icefield to the lagoon. During this retreat, the terminus shifted from an extensive, arcuate surface fronting a piedmont lobe to a narrow calving front. At the fault scarp, the inner valley is at its widest, 2.7 km across, whereas the valley width at the current ice front is 2.2 km. The outer lagoon west of the fault scarp is located in the Longitudinal Valley, a deep trench separating the Andean rangefront from the Coastal Cordillera, and filled with 1500-2000 m of Tertiary to Quaternary age soft sediments (Bangs and Cande, 1997).

The terminus of San Rafael glacier has been in stop-start retreat since at least 1871, the date of the first maps of the Laguna San Rafael (Casassa and Maringunic, 1987). Terminus positions in the lagoon over the last century were gleaned from historical maps in 1897 and 1905 (Glasser et al., 2006), aerial photos taken by the Chilean and US air force in 1945 and 1959, satellite images since 1979 and field observations, including a series of paint marks on the northern fjord wall that marked the yearly position of the northern edge of the calving cliff, originally marked in 1983 by a Japanese scientific expedition and continued to 2002 by a Chilean tourism company. The 20^{th} century change in position of the terminus was first summarized by Warren (1993). We have additional, more current information about terminus positions from Landsat and ASTER images in 1986, 2001, 2002, and field measurements using marine radar in 2005 and 2006.

The glacier currently terminates in a 2-km-long calving cliff in the inner fjord. The top of the ice cliff ranges from 30-70 m above water level and the glacier stands in water up to 280 m deep. Calving events from both above and below the waterline occur every few minutes. Warren et al. (1995) measured a summer mean daily calving flux exceeding 2×10^6 m^3. Our observations of calving events in the winter of 2005 suggest they are as frequent in mid-winter as in summer (Warren, 1993).

Climate

San Rafael glacier lies in the midst of the 'roaring Forties', an area characterized by a cool, wet climate throughout the year, with frequent rain-bearing storms. It is a zone of strong westerly winds and lush temperate rainforest that descends to sea level. Seasonal variations in precipitation and temperature are small, summers are wet and windy (Fujiyoshi et al., 1987), and snow can fall year round (Kondo and Yamada, 1988). Ablation rates in the terminus region remain large throughout the year. Relatively mild winters suggest year-round production of meltwater, which would facilitate basal sliding of the glacier throughout the year (Warren et al., 1995).

Although seasonal variations are small, interannual variation in temperature and precipitation can be large (Enomoto and Nakajima, 1985). Consequently, accumulation and ablation can vary greatly from year to year. Warren and Sugden (1993) suggested that interannual variability in precipitation is more important in driving glacier dynamics in Patagonia than in other temperate, maritime ranges such as Alaska. Decadal means in regional winter precipitation totals, the key season that affects glacier mass balance, show distinct variability, with the mean in the 1980s 2.5 times greater than the mean for the 1960s (Warren, 1993). Temperature and precipitation also appear to covary, so that when the climate is wetter, it is also warmer.

Glacier dynamics

San Rafael Glacier is one of few tidewater glaciers in the Southern Hemisphere that has been periodically, if sparsely, monitored over the past few decades. These observations provide us with a sparse history of glacier dynamics from which we can constrain an ice mass budget model and compare recent sediment yields to ice fluxes. Several scientific expeditions have focused on the glacier terminus and ablation region, including a study quantifying meteorological impacts on ablation and velocities near the terminus in the summer of 1983 (Ohata et al., 1985; Enomoto and Nakajima, 1985), and one documenting calving dynamics in 1991 and 1993 (Warren, 1993; Warren et

al., 1995). The HPN, and San Rafael in particular, have also been the focus of periodic photogrammetric and satellite surveys since the mid-1980s, which tracked terminus extent, thinning rates and surface velocities.

Aniya (1988) and Warren (1993) first documented the retreat of the ice front of San Rafael glacier in the 20th century. They noted considerable thinning of the HPN and the emergence of substantial vegetation trimlines in the last few decades of the 20th century. While the termini of most of the western outlet glaciers of the HPN remain near their Little Ice Age maxima, San Rafael glacier retreated over 8 km, reducing the width of its calving front from almost 18 km to a little over 2 km. Based on coarse comparison of changes in retreat rates between 12 known positions and climate records from over 150 km to the north and northwest of the glacier, Warren (1993) concluded that San Rafael retreated primarily due to decreases in winter precipitation, and showed little sensitivity to changes in mean annual temperature.

The Japanese expedition in 1983 installed a linear transect of 17 ablation stakes from the glacier terminus to just below the ELA, at 1050 m.a.s.l., for the month of December (Ohata et al., 1985). They also collaborated with the Chilean Air Force to establish a meteorological station, measuring daily temperature, precipitation and radiation, on the shore of Laguna San Rafael for the same time period (Enomoto and Nakajima, 1985). The cumulative results from the ablation stakes indicated that the average rate of ablation was 9.3 mm/ºC near the terminus and decreased by 5.6 mm/day for every 100 m rise of elevation (Ohata et al., 1985).

The Japanese study also recorded ice velocities of 17-22 m/day (8 km/a) near the terminus in the summer of 1983 (Naruse, 1985; Kondo and Yamada 1988). This rapid ice motion is most likely sustained by high precipitation rates, with estimated net annual accumulation rates on the glacier ranging from 3.5 m/a (Yamada, 1987) to 4.9 m/a (Matsuoka and Naruse, 1999). Rapid ablation, which can deliver significant meltwater to the bed and help lubricate the base, as well as a steep surface gradient of 4.8º near the terminus, also contribute to the fast ice motion in the terminal zone.

The first comprehensive surface gradient and velocity maps for San Rafael were developed by Rignot et al. (1996), who used synthetic aperture radar interferometry (InSAR) to provide the first quantitative information about surface speeds along the longitudinal profile and in the accumulation area. The InSAR map

indicated that average speed near the terminus in 1994 was 6200 m/a, decreasing to 1300 m/a at 6 km upglacier, to 1130 m/a at the ELA (1200 m.a.s.l., approximately 17 km upglacier from the terminus). Rignot et al. (1996) used Glen's flow law and Weertman's sliding rule to estimate the ice thickness at the ELA from these surface speeds. They estimated an ice thickness at the ELA of between 175 m, if all motion is accomplished by sliding, and 475 m, if accomplished by pure deformation.

Rignot et al. (1996) compared the rapid flow acceleration and consequent high rates of longitudinal strain in the lower 6 km of the glacier in 1994 with similar strain rates at Columbia Glacier, Alaska (Venteris et al., 1987). They suggested that pronounced longitudinal stretching of glacier ice in the terminal zone may be a fundamental feature of rapidly calving tidewater glaciers, promoting calving rates in excess of the balance flux of the glacier and resulting in retreat. During a two year period in the early 1990s, however, the terminus of San Rafael maintained a quasi-stable position despite continuing rapid calving rates of over 5000 m/a (Warren et al., 1995). That rapid terminus retreat ceased while stretching rates were maintained indicates that large stretching rates alone are not necessarily associated with terminus retreat, yet rapid calving occurs in both cases (Venteris, 1999).

COMPUTING EROSION RATES

To calculate erosion rates for San Rafael glacier, total sediment accumulation in the Laguna San Rafael was collected using bathymetry, GPS and acoustic reflection profiling. Acoustic reflection profiles were collected in June 2005 and April 2006. Profiles were acquired using a 300J Boomer and a 750Hz Datasonics bubble pulser transducer and Benthos hydrophone. Both transducer systems penetrated the soft sediment in the fjord bottom and imaged several strong reflectors at up to 120 m below the sediment surface, with diminishing penetration beneath. Traveling at speeds of 5.5 km/hr with a 0.5 second acquisition rate produced a record every 0.76 m along the track.

The seismic profiles, collected along a dense set of tracklines along and across the lagoon, were used to reconstruct the glacimarine sediment thickness and depth to

bedrock. A seismic velocity of 1740 m/s for the glacimarine sediments was used to convert two-way travel time to thickness, which represents the upper end of measured seismic velocities for glacimarine muds (Stoker et al., 1997) and therefore the minimum probable sediment thickness. Imaging of the sediment in the inner fjord, to the east of the Liquine-Ofqui fault, showed sediment collecting in deep pockets of uneven bedrock (Fig. 4.2). West of the fault, in the outer part of the lagoon, the sediment forms a thicker, more uniform cover over a strong reflector (or set of 2-3 stacked reflectors), with the thickest sediment accumulating in a wide (>2 km) channel in the center of the lagoon (see Chapter 5 for more detail on the sediment distribution and morphology in the outer lagoon).

From the measured sediments under the tracklines, the surface and subsurface bathymetry and hence sediment thicknesses between our tracks in the fjord were interpolated using the triangulated irregular network (TIN) function in ArcGIS, then rasterized into 60 x 60 m cells for further analysis and comparison (Figs. 4.3 and 4.4). Total error in our sediment thickness measurements is estimated to be 25% (see Chapter 1 for error analysis).

To arrive at basin-wide erosion rates, the sediment volumes in each submarine basin were binned and divided by the time between known terminus positions to obtain the average annual sediment flux into the fjord on decadal time scales. The sediment flux was next divided by the glacier basin area during the same time period (Fig. 4.5) to calculate the basin-averaged sediment production rate. To convert this to the bedrock erosion rate, the bedrock production rate was multiplied by the ratio of the densities of glacimarine sediments (1.8 g/cm^3) and crystalline bedrock (2.7 g/cm^3). These density estimates introduced another ≤12% error in the final estimate of bedrock erosion rate, so that the total error in calculated basin-wide bedrock erosion rates approaches ~37%. (Table 1).

As a final step, the basin-averaged bedrock erosion rate and rate of retreat of the terminus were parsed into annual values to examine the potential effects of glacier retreat on erosion. The annual rate of retreat of the ice front can be interpolated between years when the terminus position was known from maps, photos and satellite images, using a cubic spline function. An annual erosion rate was calculated by reconstructing the annual sediment flux required to account for the total sediment

accumulation observed in the fjord, given the retreat rate and assuming an exponential decay in sedimentation away from the retreating ice front (for a detailed description, see Koppes and Hallet, 2002). In this model, sediment is redistributed in the fjord when a critical slope angle is reached, which can affect the magnitude of the sediment flux calculated at each time step. The annual and mean erosion rate derived from the time-varying proglacial sedimentation model can hence differ slightly from the decadal erosion rates derived from the binned approach described above (and listed in Table 1).

RESULTS

Sediment in the inner part of the fjord appears ponded in deep, narrow channels between bedrock highs (Fig. 4.2). The bedrock highs have steep sides and little to no sediment drape, and the channels and basins between become more isolated from one another as one travels upfjord towards the ice front, with little opportunity for any significant sediment transfer between the channels and ponds since deposition. It appears from the seismic images that most of the proglacial sediment was delivered to the ice front via the glaciofluvial system, which presumably followed (and was most probably once eroded by) the deep channels. Any sediment delivered outside of the channels and "rained" over the steep slopes of the bedrock ridges was quickly transferred to the deep channels via mass movements and turbidity flows. As the sediment is distributed in numerous small, deep pockets, separated by bedrock highs, we can be confident that the binned approach to measuring sediment fluxes between known terminus positions, listed in Table 1, is a good representation of the sediment delivery on decadal time scales, as there has been negligible redistribution of sediment post-deposition that would influence the sediment flux estimates.

Around 1979, the terminus retreated past the range front delineated by the dramatic Liquine-Ofqui fault. The substrate along this range front changes from a thick, laminated sediment basin to a hard, knobby granitic bed. The proglacial sediment drape beyond the inner fjord (i.e., pre-1979) is in the form of flat basin fill in a broad channel sloping gently upfjord at around 200 m water depth. Within the inner fjord, the substrate is dominated by the narrow, anastamosing channels.

The sediment flux from San Rafael glacier was surprisingly low, in comparison to the average sediment fluxes measured from the other glaciers in this study. Average annual sediment yield from San Rafael glacier since 1959 was $1.7 \pm 0.4 \times 10^7$ m^3, corresponding to a mean annual erosion rate of 16 ± 5 mm/a for the time period 1959-2005. For such a large, dynamic tidewater system, this lower mean erosion rate is indicative of the resistant underlying granitic lithology of the North Patagonian batholith.

Basin-wide erosion rates, as measured from the sediment yields, varied significantly over this period, appearing to scale loosely with the rate of retreat (Fig. 4.6). Erosion rates rose to a peak of 40 ± 14 mm/a in 1979, dropped to around 17 ± 6 mm/a in 1985, rose to 25 ± 9 mm/a around 1988, and then slowly decreased to only 9 ± 3 mm/a in 2005. Similarly, the glacier front retreated increasingly rapidly until 1982, experienced a short standstill in 1986-1987, started to retreat again with a peak in the early 1990s, and has been slowing down in the past decade. It is noteworthy that although San Rafael glacier retreated over 4 km since 1959, losing 273 km^3 of ice from the terminus and reducing the width of the calving front from over 7 km in 1959 to a little over 2 km in 2005, retreat has been slow in comparison to other temperate tidewater glaciers, with a maximum rate of terminus retreat of less than 240 m/a. The standstill in 1986 corresponds with the retreat of the ice front from the open piedmont of the outer fjord to the narrowest constriction of the inner fjord.

By fitting a trendline to the erosion rates as a function of retreat, the long-term (glacier cycle) rate of erosion can be estimated from the y-intercept, i.e., where retreat = 0 (see Fig. 4.6b). Using this approach, more fully described with respect to Tyndall glacier in Chapter 2, the long term erosion rate for San Rafael glacier approaches 9 ± 3 mm/a.

Differentiating debris entrainment vs. basin erosion during retreat

The close correlation between the sediment flux from the glacier and the retreat of the ice front at all three glaciers in this study suggests the influence of several possible mechanisms. First, the variability we are seeing in the sediment flux could be modulated by the rate by which sediment is being delivered to the terminus through

englacial entrainment and calved straight into the fjord. This delivery rate is the product of the ice lost from the terminus and the concentration of debris in the ice. Any changes in the rate of ice lost during retreat, and/or in the flux of ice to the terminus, could result in a change in the rate ice-entrained debris delivered to the terminus that could co-vary with the rate of retreat. Alternately, changes in the climatic and non-climatic controls that are triggering the retreat of the ice front are also impacting conditions at the bed, prompting accelerated erosion and subglacial fluvial evacuation of sediment during periods of rapid retreat. Below, I address each of these mechanisms, and their potential contributions to the variability and magnitude of the sediment fluxes (and by inference erosion rates) measured from these glaciers.

Englacial entrainment

With regard to the entrainment mechanism, the glacier acts as a conveyor belt and the volume of sediment delivered to the fjord per unit time reflects the concentration of debris entrained in and on top of the ice (the englacial (and supraglacial) sediment flux) and the speed of the conveyor belt. In a steady-state (i.e., non-retreating) glacier, this englacial sediment flux is ice flux to the terminus (the product of the cross-sectionally averaged ice velocity at the terminus and the cross-sectional area of the ice front), multiplied by the debris concentration. Changes in ice velocity will change the rate by which sediment ‘in the pipeline’ will arrive in the fjord. Any variations in debris concentration along the glacier would also result in a change in sediment delivery over time, without any change in the ice flux. For a glacier in retreat, the rate of englacial sediment delivery to the fjord is augmented by the rate of ice loss corresponding to the retreat at the terminus. A period of rapid retreat would tend to produce a pulse of ice-rafted debris to the fjord, contributing to the observed co-variation of sediment flux and retreat rate. The issue addressed here is the extent to which these changes are likely to be significant enough to explain the correlation we are seeing between sediment flux and retreat, and by inference the extent to which the sediment flux at the terminus is truly a reflection of erosion or simply a change in delivery of sediment already ‘in the pipeline’.

In 2005 and 2006, very little supraglacial and englacial debris was evident in the ablation zone and in icebergs from San Rafael glacier. From historical photographs, this appears to have been the case throughout much the 20th century. The dearth of debris visible at the terminus ice cliffs, on the surface of these glaciers, and in the multitude of icebergs that clog the fjords, suggests that englacial debris concentrations in these glaciers, and particularly at San Rafael are far too low to produce the large volumes of sediment imaged in these fjords. Indeed, one of the few studies of the distribution of sediment in temperate tidewater glaciers concluded that, at three massive tidewater glaciers in Alaska, supraglacial and englacial debris amount to at most 1% per unit volume of ice calving from the terminus. This study, and others, also suggest that this englacial flux contributes at most 5-10% of the total sediment flux delivered to the fjord (Hooke et al., 1985; Hunter et al., 1996), with the vast majority (>90%) of the sediment being delivered by the subglacial hydrologic network. Changes in the englacial flux therefore should not significantly affect the overall sediment output of the glacier.

Assuming that the debris concentration in the Patagonian glaciers in this study is similar to that for the Alaskan tidewater glaciers in the Hunter et al. (1996) study, the potential contribution of the entrained (englacial) sediment flux during rapid retreat can be estimated from the annual volume of ice lost from the terminus due to retreat. If we assume that the ice flux to the terminus remained constant over time, any changes in englacial sediment flux will result from 'excess' ice lost from the glacier per unit time, which can be measured from the fjord bathymetry, the ice cliff height and the rate of retreat. Figures 3.12 and 4.7 compare the total annual sediment flux from Marinelli glacier and San Rafael glacier, respectively, with the volume of entrained debris that would have melted out from the volume of ice lost due to retreat, assuming a debris concentration of 1% per unit ice volume. For Marinelli glacier, the potential contribution from the meltout of englacial debris that was contained in the ice lost from the terminus, per unit time, averages less that 10% of the total annual sediment flux during the study period. For San Rafael glacier, the potential contribution of entrained debris from ice loss is much less, averaging ~4% of the total annual sediment flux. Entrained debris rainout as these glaciers lose ice during rapid retreat hence is such a small

portion of the total sediment flux that it cannot be the dominant mechanism that explains the large changes in sediment flux over the past half-century.

Changes in the flux of ice to the terminus over time may also be contributing to variations in the total sediment flux by varying the rate of englacial and supraglacial sediment delivery to the ice front. The englacial flux from San Rafael and Marinelli glaciers can be approximated, assuming a debris concentration of 1% per unit ice volume, to correspond to a layer of debris between 1 and 3 m thick across the width of the glacier. Taking into account the cross-sectional area of the glacier terminus over time (measured from the bathymetry and a mean ice cliff height of 40 m.a.s.l.), one can estimate the ice speed required to reproduce the annual ice flux, and entrained debris flux, that would produce the annual sediment flux observed. Variations in the rate of entrained debris delivered to the ice front (i.e., the ice speed) at San Rafael glacier and Marinelli glacier, after accounting for the contribution of debris in the ice lost due to retreat, are shown in Figures 4.8 and 4.9, respectively. The figures show the annual ice speeds required to produce the annual sediment flux via entrainment only, using a range of thicknesses from a likely debris concentration equivalent to a layer 1 m thick to an overestimate of 5 m (double the maximum debris concentration observed in the Alaskan glaciers in the Hunter et al. (1996) study), and assuming that this debris concentration is held constant through time. If we assume that an englacial debris concentration equal to a layer 5 m thick exists throughout San Rafael glacier, short term variations in ice speed between 1 km/a and 3 km/a, within the range of ice speeds measured through SAR interferometry of the glacier by Rignot et al. (1996) and Rignot (2001), could play an important role in producing the observed variability in sediment flux to the terminus. Entrainment of such a high concentration of debris in the ice that would produce these sediment fluxes over decades could only be sustained, however, if the debris was replenished by rapid erosion up-glacier. For instance, at average ice speeds of 2 km/a, it would take only ~20 years for the ice at the headwall of San Rafael glacier to reach the terminus and move all entrained debris from the accumulation area to the ice front, after which new debris would have to be generated and incorporated into the ice to account for the sustained high sediment flux throughout the 20th century. Assuming a more realistic debris concentration in these glaciers corresponding to a layer of debris 1 m thick, the ice speeds required to produce the annual sediment

fluxes measured from these glaciers by only delivering sediment already ‘in the pipeline’ approach 10-20 km/a and more over periods of decades, and are clearly unrealistic given the observed surface velocities at San Rafael (described below), and estimated average ice velocities of 400 m/a at Marinelli, calculated from the calving flux in the ice budget model. The amount of debris entrained in the ice, even given rapid changes in the ice flux, hence cannot fully account for the large observed sediment fluxes, and cannot be sustained without concomitant bedrock erosion and/or a change in storage of subglacial sediments at the bed.

Changes in storage vs. enhanced basin erosion

The correlation of sediment flux from and retreat rate of these glaciers more likely results from the acceleration of glacier sliding, which has been documented to accompany the retreat of a number of calving glaciers (e.g., Van der Veen, 1996; Thomas et al., 2004; Howat et al., 2005). Increases in glacier sliding would tend to increase the glaciofluvial sediment flux, which generally accounts for more than 90% of the total flux, either through accelerated erosion of bedrock or enhanced evacuation of sediments stored under the glacier. Decreases in subglacial sediment storage may be significant in the short-term such as during a surge, periods of local ice acceleration and subglacial cavity expansion (e.g., Anderson et al., 2004), or at the start of the annual melt season when efficient subglacial water conduits start to form. At Variegated Glacier, both the sediment yield at its outlet streams and sliding speed increased by two orders of magnitude during a surge in 1981-1982 (Humphrey and Raymond, 1984). At Bench Glacier, periods of enhanced sliding at the start of the melt season during three consecutive years were accompanied by increases in both sediment and water discharge (Riihimaki et al., 2005). In both of these examples, the pulse of sediment discharge was inferred to be related not only to increased glacier sliding but also to short-term changes in efficiency of the subglacial hydrologic system. A sudden increase in the water discharge would evacuate sediments more readily and contribute to the correlation between glacier sliding and sediment flux for short periods.

Such decreases in subglacial sediment storage by water discharge, however, could not be sustained over the decades required to account for the massive sediment flux we are seeing from these glaciers. Likely volumes of sediment stored beneath the glaciers that could be remobilized are but a small fraction of the volume of sediment delivered to these fjords during the decadal to centennial periods examined in this study. Typical thicknesses of mobile basal debris that have been documented in the few boreholes that have penetrated to the base of coastal tidewater glaciers, such as Columbia Glacier (Humphrey et al., 1993) and Variegated Glacier (Kamb et al., 1985), do not exceed a few decimeters. The total volume of sediment delivered to the Laguna San Rafael over the past century is 3.5×10^9 m^3; at Marinelli fjord, 3.5×10^8 m^3 was delivered over the past 45 years. To attribute these sediment volumes solely to the enhanced evacuation of subglacial sediment stores under these glaciers over these periods of study would require the removal of layer of basal sediment >40 m thick at San Rafael and >20 m thick at Marinelli under the entire ablation area of each glacier, where such debris is most likely to accumulate. In both cases, such a requisite thickness of entrainable basal debris far exceeds the characteristic thickness of under 0.5 m. Only in one instance has up to 7 m of mobile debris been cored and instrumented, under Black Rapids Glacier (Truffer et al., 1999); it should be noted that this glacier straddles the Denali fault, and that significant fault gouge would be expected to contribute to an easily erodable and mobile substrate (and may be very difficult to differentiate from debris entrained subglacially) . If such a thick layer of mobile basal debris were available under the Patagonian glaciers, the periodic evacuation of several meters of stored basal debris could potentially cause periodic increases in sediment flux. Evacuation of such a thick packet of basal debris, however, could also only be sustained over the multi-decadal period of these studies if it were replenished by rapid erosion. Moreover, it should be noted that a blanket of basal debris of a few decimeters could not be sustained over the long term as it would prevent sliding ice from having direct access to the underlying bedrock, precluding bedrock erosion, which clearly is not the case given the capability of these glaciers to erode the deep fjords in which they reside.

Recent studies of the evacuation of proglacial and subglacial debris by Taku Glacier during its current advance document the evacuation of approximately 190 m of

soft sediment during the 20th century, flushed from beneath the advancing snout (Motyka et al., 2005). Such rapid evacuation of unconsolidated sediment provides confidence in the assumption that all the sediment stored subglacially, as well as in the fjord, prior to and during the last advance of these glaciers, which lasted at least a few hundred years, had been effectively removed and transferred to the outer basins (or continental shelf) long before the current retreat of the ice started. Hence, the large sediment flux I have documented at these glaciers over the past half century most probably reflects enhanced bedrock erosion due to accelerated basal ice motion associated with rapid retreat, with only a minor contribution derived from changes in the relatively small volume of sediment likely to be stored subglacially and entrained in the ice.

A possible increase in the calving flux through San Rafael glacier may also be contributing to increased fracturing and longitudinal stretching near the terminus, as well as increased sediment delivery to the terminus and increased basal ice motion, as has been observed at Columbia Glacier (Venteris et al., 1997). The fracturing of the ice as it cascades from the icefield plateau to the terminus tends to accelerate calving, which accelerates ice motion and increases both the efficiency by which the glacier erodes its bed and the rate at which sediment is delivered to the terminus. A steadily decreasing flux of ice through the terminus over the past half century, in part through topographic controls as the width of the terminus decreased, may instead be controlling both ice loss at the terminus and erosion rates since 1959. To resolve this relationship, an estimate of changes in ice flux and calving flux over this period is needed.

ICE DYNAMICS OF SAN RAFAEL GLACIER

To understand how climate may have influenced the retreat of the terminus during the past half century, and to reconstruct the ice flux through the glacier that may underlie recent variations in sediment delivery to the fjord, I built a simple model of ice budget to constrain the rate of ice added to and lost from San Rafael glacier over the past 50 years. The model is described in Chapter 1. To calculate the budget of ice in

the glacier over time, I looked to the NCEP-NCAR Reanalysis dataset to reconstruct the climate at Laguna San Rafael over the past 50 years, and applied a number of daily climate parameters to the glacier surface determined from NASA's 30-m SRTM global DEM dataset to estimate snow accumulation and ablation on San Rafael glacier. The NCEP-NCAR Reanalysis dataset is a web-accessed, backcast atmospheric model based on global radiosonde measurements and global measured sea level pressures (Kalnay et al., 1996). The NCEP-NCAR model reconstructs multiple climate parameters at geopotential heights throughout the troposphere on a 2.5º by 2.5º grid and provides, among many parameters, 6-hourly near-surface minimum and maximum temperature, daily zonal and meridonal wind speeds, snowfall and precipitation rates at each gridpoint, back through Jan. 1, 1948. The benefit of this dataset is a comprehensive history of temperature and precipitation at gridpoints closer to San Rafael glacier, and at higher temporal resolution, than existing climate records for the region. The only climate records in existence in Chilean Patagonia through the last century are limited to 12 Chilean Navy lighthouses on the coast, and the towns of Puerto Montt (43ºS) and Punta Arenas (53ºS). Given the high variability of climate along this long latitudinal transect, the NCEP dataset provides a useful index of climate close to San Rafael glacier.

To best understand how the climate reconstructed from the nearest NCEP gridpoint (46.67ºS, 73.125ºW, henceforth referred to as MSV, or Monte San Valentin) reflects local climate over the glacier, two 0.2 mm tipping bucket rain gauges and one 2-channel temperature gauge were deployed from March 2005 to April 2006 at the Chilean Forest Service (CONAF) guard station, situated approximately 7 km from the glacier front on the shores of Laguna San Rafael (46.66ºS, 73.86ºW). The temperature gauge measured air and soil temperature at 1-hour intervals. The soil temperature at 2 cm below ground surface was recorded to indicate snow cover, and was used to indicate periods when rain gauge measurements should be used with caution.

Results from the rain and temperature gauges at the CONAF guard station were compared to the daily maximum and minimum above ground temperature, precipitation and wind speeds calculated from the NCEP-NCAR dataset at MSV, for the same period, and the following least-squares linear regressions were derived:

$T_{maxSR} = 0.8945(T_{maxNCEP}) + 6.625$ $(R^2=0.719)$

$T_{minSR} = 0.6115(T_{minNCEP}) + 3.33$ $(R^2=0.614)$

$P_{SR} = 0.7797(P_{NCEP}) + 0.913(U_{NCEP}) + 0.8217$ $(R^2=0.495)$

where $T_{maxSR,}$ T_{minSR} and P_{SR} are the daily maximum and minimum 2 m air temperature and daily precipitation rate from the gauges at the CONAF guard station, and $T_{maxNCEP}$, $T_{minNCEP}$, P_{NCEP} and U_{NCEP} are the maximum and minimum 2 m air temperature, daily precipitation rate and zonal wind speed (m/s) from the NCEP-NCAR reanalysis dataset at the gridpoint MSV. These regressions were then applied to the NCEP-NCAR results for the timeframe 1950-2004 to estimate precipitation and temperature at San Rafael during the time no weather records were available.

The NCEP-NCAR dataset was also used to calculate the daily snowline altitude on San Rafael Glacier. The published daily atmospheric temperatures at 1000 mb, 925 mb, 850 mb, 700 mb and 600 mb at gridpoint MSV were used to reconstruct the daily environmental lapse rate, which averaged 5.54 ± 0.9ºC/km. This lapse rate was then applied to the daily reconstructed average temperature at the guard station to locate all parts of the glacier surface above the 2ºC isotherm. All daily precipitation falling above this elevation on the glacier surface was assumed to fall as snow (P_{snow}), and was used to compute the daily snow input into the glacier system ($Q_{acc} = P_{snow} * A_{gl}$). The daily snow input is the product of the regression applied to the NCEP precipitation rate at sea level in water equivalent, multiplied by the surface area of the glacier at each elevation increment above the 2ºC isotherm. The daily flux for each increment was then added up to compute the annual snow input to San Rafael.

To represent the upward forcing of the Andean front and the icefield on moisture-bearing storms, the daily flux computation included a 1D linear orographic enhancement of precipitation, based upon the model of Smith and Barstad (2004). The orographic model tracks the motion of moist parcels of air over the topography. Tunable parameters include the fall time (tau_f) and conversion time (tau_c) of hydrometeors, the moisture scale height (H_w), the moist static stability for upward advection (N_m) and horizontal wind speed (u). The parameters of the orographic model were tuned so that the precipitation rate at sea level is amplified by approximately 2.5 times at its peak (Fig. 4.10), to best approximate annual accumulation rates rising from

around 4 m/a at Laguna San Rafael to over 8-10 m/a on the broad plateau of the icefield (Escobar et al., 1992; Fujiyoshi et al., 1987). The peak in precipitation, at around 1100 m.a.s.l., happens to coincide with the ELA. The form of the orographic enhancement curve was then applied, as a constant *K,* to the precipitation rates at sea level inferred from the gauges and NCEP measurements to model the distribution of precipitation along elevation bands on the glacier surface ($K*P_{snow}$).

Using the 1983 measurements of ablation stakes and temperature (Enomoto and Nakajima, 1985), I reconstructed the average rate of ablation as a function of local air temperature and elevation at each stake, using the same least-squares fit between the NCEP model temperatures and lapse rates. By recalculating the local air temperature at each stake, and summing the results of ablation rates from the stakes, a simple equation relating the rate of ablation to the local air temperature at each elevation on the glacier surface was derived:

$$\alpha = 0.6645*T_{avg} \quad (R^2=0.20, n=49, P<0.0001)$$

where α is the ablation rate in cm/day, and T_{avg} the average daily local air temperature. This equation was used in the ice mass budget model to calculate the daily total ablation over the surface of San Rafael glacier (Q_{abl}). Since the ablation rates were measured by Ohata et al. (1985) in early summer, predominantly on bare ice surfaces which are known to melt faster than snow, the ablation rates probably approached maximum values for the San Rafael Glacier. .

The input of snow to the glacier could then be compared to the annual volume of ice ablated from the surface of the glacier, as well as to the annual loss of ice from surface thinning and from the terminus, to derive the yearly flux of ice through the glacier system necessary to account for the observed change in glacier volume.

RESULTS

The correlation between precipitation rates generated at the MSV gridpoint by the NCEP model and the gauge precipitation is weak, accounting for less than half the

variance, and although NCEP values capture the timing of storm events, they tend to underestimate the magnitude of the larger storms. The NCEP minimum and maximum daily surface temperatures also underestimate the local temperature. The regression for the gauge and NCEP-generated precipitation is better if the zonal (W-E) surface wind component is included in the regression (R^2=0.495).

As was reported from climate stations nearer to the coasts (e.g., Warren and Sugden, 1993), mean annual temperatures at the glacier front varied only 1.3ºC about a mean of 8.9ºC (Fig. 4.11a), demonstrating a strong maritime influence buffering annual temperatures. Annual precipitation varied more significantly, by ± 600 mm about a mean of 3600 mm/a (Fig. 4.11b). Precipitation was relatively high during the period 1950-1975, and has since dropped by over 25% from 1975 to 2005.

In comparing the locally-calibrated NCEP climate records and the retreat history of San Rafael since 1950, retreat rates appear to be more sensitive to precipitation than to temperature in this warm, temperate region, supporting prior observations from distant climate stations (Warren 1993; Warren and Sugden, 1993) as well as results from ice sheet models of the Patagonian Icefields (Hulton et al., 1994; Cook et al., 2003). The glacier started to retreat rapidly after 1975, the start of a decade of lower than average precipitation, with maximum retreat rates occurring following 2-3 years of anomalously low annual precipitation. Not withstanding the short terminus standstill in 1986-1987, which corresponds closely to a topographic constriction at the terminus, retreat rates continued at above 50 m/a, with the highest rates following years of anomalously low precipitation. Retreat also coincided with a period of slow warming from 1950 to 1980, however, temperatures remain quite stable between 1982 and 1995, while retreat rates fluctuated considerably and remained high. The subordinate or weak influence of temperature is most evident during an anomalously cold period, 1998-2003, when retreat accelerated.

The relationship between climate controls and terminus retreat, and by extension erosion rates, can be examined more precisely by comparing the rate of retreat of the terminus to the modeled rates of ice input and output through the glacier. Calving is clearly a major component of the ice budget, accounting for the difference between the modeled input by accumulation and output by ablation, which is more than twice the ablation flux during periods of slow retreat (Fig 4.12, 4.13). Retreat

accelerates as the accumulation flux decreases and the ablation flux increases, reaching a maximum when these two fluxes approach each other and the remaining calving flux results in ice loss from the system. The ice budget model suggests that accumulation fluxes decreased from 8 km^3/a to 5 km^3/a from 1950 to ~1980, a period of rapid retreat, as temperatures increased and precipitation rates decreased. Ablation fluxes also increased from 3 to 5 km^3/a between 1950-1980, following the gradual warming trend. The peak in ablation flux and nadir in accumulation correspond to the peak in retreat over this period (Fig. 4.12). The mass budget model then indicates a slow increase in accumulation from 1980 to 2003, averaging 6.5 km^3/a in the most recent years, that correlates with a steady decrease in retreat. Ablation rates also slowly decreased from 1980 to 1997, and dropped precipituously during the relatively cold period from 1998-2003.

An important, non-climatic control on the retreat rate is the area of the ice front in contact with fjord water and subject to submarine melt, as documented at Le Conte Glacier (Motyka et al., 2003). Any decrease in the cross-sectional area of the ice front should diminish the volume of ice subject to melting and calving and decrease terminus retreat, assuming the flux of ice to the terminus does not vary significantly. Figure 4.14 compares the retreat rate to the progressive decrease in ice front surface area as the glacier retreated into the steadily narrowing but slightly deepening outlet across the Liquine-Ofqui fault zone. The expected correlation between a decrease in retreat rate and a decrease in ice-front area is evident in 1982-1987 and 1993-1998. The lack of correlation at other times, however, suggests that other mechanisms, most likely the flux of ice to the terminus, often dominate in controlling the ice front position.

San Rafael glacier has also experienced substantial lowering of the glacier surface in the recent past, as evident from the prominent trimlines along the valley walls. Rivera et al. (2005), comparing Landsat MSS and ETM+ images taken 1979 and 2001, estimated an average of 1.8 ± 1.0 m of thinning per year around the edges of the North Patagonian Icefield. Aniya (1999) estimated similar thinning rates of 1-2 m/a over the ablation area of San Rafael. Recent trimlines along the inner fjord are also emerging, and can be traced back using aerial photos. The most prominent trimline above the current glacier terminus was estimated in the field in 2005, using a laser rangefinder, at ~120 m above the current glacier surface. A Chilean Air Force photo

taken in 1959 shows the glacier surface parallel to this trimline. From this trimline, we estimate that the glacier has thinned 2.6 m/a on average in the terminal zone over the past 46 years, within the range of thinning rates measured previously.

If we assume the range of thinning rates, from 1 - 2.6 m/a, occurred over at least the entire ablation area of 175 km^2, the average annual volume of ice lost via thinning at the glacier surface is at a minimum 1.8 - 4.6 x 10^8 m^3/a, somewhere between 7 and 17% of the average annual flux of ice that arrives the terminus (i.e., the calving flux, the difference between the annual snow input and the annual ablation loss). Much of this thinning is most probably due to accelerated calving and ice motion in the ablation zone drawing down the glacier surface, but may also result from accelerated surface loss due to high ablation rates. Given the potential influence of calving and retreat of the terminus on longitudinal extension in the terminal zone, the rate of thinning in the terminal zone probably varied significantly during this period, but by how much is unknown, for only two direct measurements of the elevation of the ice surface exist. The volume of ice lost from the glacier snout due to retreat during this period and its variability over time, on the other hand, can be calculated from the subsurface fjord bathymetry and the retreat rate, assuming an average ice cliff height of 40 m above a constant lake level over the past 50 years. The volume of ice lost from the terminus averaged 5.9 x 10^7 m^3/a, with a maximum loss of up to 1.7 x 10^8 m^3/a during a phase of rapid retreat in the early 1980s. In comparing the two types of volume loss, San Rafael glacier appears to be losing volume through surface lowering at 3-7 times, on average, the rate it is losing volume from retreat of the calving front. In other words, the glacier appears to be responding to the warmer and drier climate of the past 50 years by thinning much more strongly than by ice front retreat.

Assuming mass conservation of the glacier, the ice budget model can be used to simulate the flux of ice delivered to the terminus over time, and compare this flux to the erosion rate over the same period. For a calving glacier in steady-state, the difference between annual accumulation (Q_{acc})and ablation (Q_{abl}) must be lost through the glacier snout via calving ($Q_{calving}$). As the volume of San Rafael has decreased through both shortening (retreat) and surface lowering (thinning) during the past 50 years, estimating the calving flux must also take into account these ice volume losses, so that the calving flux becomes the difference between the ice input and the sum of

surface ablation, thinning, and excess ice lost at the terminus. Expressing all components as fluxes, this difference takes the following form with dz/dt and dx/dt being the rates at which the glacier thickens and advances, respectively, and A_{gl} *and* A_{term} are the surface area of the entire glacier and the cross-sectional area of the terminus, both of which have varied over time:

$$Q_{calving} = Q_{acc} - (Q_{abl} + A_{gl}*dz/dt + A_{term}*dx/dt)$$

Estimating the calving flux in this fashion, I am assuming that, to first order, the lowering of the glacier surface is accomplished by longitudinal stretching and increased ice drawdown, and not by surface melting, and that this drawdown has been uniform since 1959 (i.e., thinning rates have not varied significantly during this time).

As shown in Figure 4.13, according to the mass budget model, the ice flux to the terminus ($Q_{calving}$) has varied significantly during the past half century. The calving flux out of the terminus averaged 4 x 10^9 m^3/a during the period 1950-1975, dropping to a low of less than 1 x 10^9 m^3/a around 1980 and again in 1988, years when the model suggests almost all accumulation was lost through ablation and all calving resulted in volume loss from the glacier. The calving flux slowly increased in the 1990s to almost 5 x 10^9 m^3/a, and dropped again in the past few years. The mean calving flux since 1950 has been 3 x 10^9 m^3/a.

If retreat and erosion are driven by changes in ice flux through the glacier, as was observed at other calving glaciers in the last decade, erosion rates and retreat rates should vary in concert with changes in this ice flux, best approximated by the calving flux. Our model results suggest the contrary, however. That both retreat rates and erosion rates do not appear to co-vary with the calving flux in this model, and in fact appear predominantly out of phase with the modeled calving flux, suggests that several of our inputs and assumptions need revisiting. In particular, caution is needed with regard to the accuracy of the flux of snow into the glacier given the poor correlation between local measurements and the NCEP precipitation rates used to constrain this flux, as well as with regard to our assumptions of both uniform thinning rates, and of surface lowering exclusively due to ice drawdown (and not excess melt). It is worth noting that the erosion rate, in particular, appears to co-vary with the ablation

flux, suggesting that excess meltwater to the bed during years of increased ablation could be promoting both basal sliding and accelerated erosion as well as more efficient fluvial evacuation of subglacial sediment.

Ice flux and erosion

Given these uncertainties in the ice budget model, a more direct approach to estimating the ice flux through San Rafael glacier is needed. The potential relationship between basin-wide erosion rates and ice flux can be examined more precisely during four periods over the past 25 years when the surface ice speed near the terminus of San Rafael was measured, using velocity stakes (Kondo et al., 1985), photographic observations (Warren et al., 1994) and InSAR (Rignot et al., 1996; Rignot, 2006, pers. comm.); the measured speeds and fluxes are listed in Table 2. Although these surface speeds were all measured over a period of one month or less, the lack of seasonal variability in precipitation and temperature has led prior researchers to assume that ice speeds do not vary significantly over the year, and hence monthly measurements can be extrapolated to estimate annual speeds at San Rafael. We can thus compute the ice flux at the terminus (i.e., the calving flux, $Q_{calving}$) by multiplying the near-terminus surface speeds (U_{term}) with the terminus cross-sectional area (A_{term}) during the years 1983, 1992, 1994, and 2001. In so doing, we are assuming that the sliding velocity greatly exceeds the component of ice velocity at the surface that is due to internal deformation, so that measured velocities averaged across the glacier surface closely approximate the sliding velocity.

Using these calving fluxes measured at the terminus, we can then roughly estimate the flux of ice through the ELA during each of the four years, by summing the flux of ice lost through ablation (Q_{abl} from the ice budget model), the average volume of ice lost to surface lowering ($A_{gl}*dz/dt$), and the calving flux ($Q_{calving}$) (see Table 2). This estimate assumes that all ablation and thinning occurred at or below the ELA, providing an upper limit for the ice flux through the ELA (Q_{ELA}). The sediment flux for each year, expressed as the basin-wide erosion rate, is then compared to the ice flux through the ELA, shown in Figure 4.15. As the ice flux at the ELA decreased from 7.1 km^3/a to 5.1

km^3/a from 1983 to 2001, the erosion rate decreased from 18 ± 6 mm/a to 8 ± 3 mm/a. A rough linear relationship between the erosion rate, $\dot{e}$ (in mm/a), and ELA flux (in km^3/a) emerges:

$$\dot{e} = 2^* Q_{ELA} \quad (R^2 = 0.67)$$

Although the constant in this equation should be regarded with caution and may vary considerably from glacier to glacier, the pace of basin-wide erosion clearly increases with ice flux, consistent with the findings of Humphrey and Raymond (1994) and theoretical studies of glacier erosion (e.g., Hallet, 1996).

The measured calving fluxes can also be used to quantify some of the uncertainties in the ice budget model. The annual input of snow (Q_{acc}) into the glacier in the ice budget model was less than the reconstructed flux of ice at the ELA (Q_{ELA}) extrapolated from the calving and ablation flux in 1983; in contrast, the modeled accumulation was greater than the ELA flux in 1992, 1994 and 2001. The accumulation fluxes, in particular, in these model results should therefore be interpreted with caution. The concentration of orographic enhancement in snowfall at the ELA could potentially be a major driver in the model, unrealistically tipping the balance towards net accumulation or ablation across the broad plateau of the icefield.

In the absence of precise measurements of ice thickness with which to constrain the flux of ice at the ELA in our model, however, the current thickness of ice at the ELA can be estimated from the surface slope, assuming a uniform basal shear stress for this temperate tidewater system. Given a median terminus ice depth (measured from the bathymetry) of 240 m in 2005, and a current surface slope near the terminus of 2.8º, the infinite slope approximation of the basal shear stress near the terminus is essentially 1 bar (104 kPa). Assuming the basal shear stress is also close to 1 bar at the ELA, where the surface slope is approximately 1.6º, then the average ice thickness there is around 403 m, close to the upper limit of ice thicknesses estimated by Rignot et al. (1996). With an ice thickness of 400 m and average surface velocity of 1 km/a (Rignot, 2001), the flux of ice at the ELA today is therefore only about 3×10^9 m^3/a, a little over half the ELA flux derived from the model. As direct measurements of ice thickness at the ELA from airborne radar become available, we

will be able to compare measured ice fluxes through the ELA (coupling ice thickness measurements with ice velocity measurements) to our modeled fluxes, in order to better constrain the ice budget model.

IMPLICATIONS

From direct measurements of erosion and ice motion at San Rafael glacier, the erosion rate scales roughly with the ice flux through the ELA. This relationship supports our inference that the correlation between erosion and retreat observed at San Rafael and at the other glaciers in this study is the result of increases in ice flux driving the drawdown of the glacier surface during retreat. The relationship also concurs with two prior observations from other calving glaciers, which together suggested that erosion rates should be high during retreat: 1) that increasing rates of retreat were accompanied by ice speed up as seen at Columbia Glacier, Helheim Glacier and Jakobshaven Isbrae, and 2) that sediment flux was proportional to ice velocity at Variegated Glacier. At San Rafael glacier, retreat rates over the last two decades have decreased, as have calving fluxes, with a concomitant decrease in erosion rates.

The geometry of San Rafael glacier, with a broad, relatively flat accumulation area funneled into a narrow constriction across the hanging wall of the Liquine-Ofqui fault and into Laguna San Rafael, renders the glacier capable of withstanding a substantially warmer and drier climate without necessarily causing much retreat of the glacier snout. Although the terminus has not retreated substantially during this period, the entire glacier has thinned significantly. This thinning is coupled with a steady decrease in ice flux to the terminus in the past two decades. The recent reduction in erosion rates at San Rafael may therefore be causally related to the rapid thinning of the glacier surface as the climate got warmer and drier, and not merely to the rate of retreat, which is a function of competing influences between both climate and terminus geometry. As an example, in 1986, when the terminus retreated into a narrow valley constriction and retreat temporarily slowed, calving speeds most probably did not, and hence erosion rates did not decrease dramatically during this time.

. Contrary to what has been observed at other glaciers, such as at Marinelli glacier, the surface thinning at San Rafael glacier over the past few decades has not yet resulted in substantial increases in the rate of retreat. If the ice thickness at the ELA is estimated to be only ~400 m, however, continuous thinning rates of 2 m/a over the broad plateau of the icefield, where the ELA is located, would remove the glacier in less than 200 years. Such substantial changes in ice thickness will also affect buoyancy at the glacier terminus, and given continued speed up near the ice front, is likely to destabilize the terminus and result in drastic retreat in the not too distant future.

CONCLUSIONS

The average basin wide erosion rate for the latter half of the 20th century from San Rafael glacier is 16 ± 5 mm/a, within the range of the highest known rates for tidewater glaciers in Alaska (Koppes and Hallet, 2006) and Patagonia (this study). Erosion rates have been relatively low over the most recent decade, however, as have retreat rates, even though San Rafael is one of the fastest-flowing tidewater glaciers in the world. The decrease in net accumulation over the last few decades, as the climate warmed and dried, has primarily resulted in a pervasive thinning of the glacier, as well as retreat. Our measurements of sediment yield and calving fluxes at San Rafael over the last few decades indicate that, as observed at Icy Bay, Alaska and at Marinelli glacier, the basin-wide erosion rate tends to scale with the ice flux.

Table 1: Sediment volume in the Laguna San Rafael, binned between known positions of the terminus 1959-2002, and associated sediment and bedrock erosion rates.

Years	Retreat (m)	Volume x 10^7 (m^3)	Sed flux x 10^7 (m^3/a)	E_{sed}[1] (mm/a)	E_{bed}[2] (mm/a)
1959-1974	810	13	0.8	11.7	7.8
1974-1979	747	7.5	1.5	20.8	13.8
1979-1986	773	9.1	1.3	17.9	11.9
1986-1992	964	8.3	1.4	19.2	12.8
1992-2002	678	0.1	0.01	0.15	0.1
Total:	**3972**	**3.8×10^8**	**5.0×10^7**	**12.4**	**8.3**

1. E_{sed} is the sediment production rate, per unit basin area
2. E_{bed} is the basin-averaged bedrock erosion rate.

Table 2. Direct measurements of terminus ice speeds and terminus retreat, modeled ice fluxes and associated glacier dynamics for San Rafael glacier.

Year	Retreat rate	Mean T	Ablation flux[1]	Terminus Ice speed	Terminus area	Calving flux[2]	ELA flux[3]	Erosion rate	Source of calving speed
	ma^{-1}	°C	m^3a^{-1}	ma^{-1}	m^2	m^3a^{-1}	m^3a^{-1}	mma^{-1}	
1983	96	9.36	4.7×10^9	5110	4.1×10^5	2.1×10^9	7.1×10^9	17.6	Kondo et al., 1985
1992	133	8.94	4.2×10^9	4500	4.0×10^5	1.8×10^9	6.3×10^9	13.1	Warren et al., 1995
1994	69	9.19	4.4×10^9	4015	4.0×10^5	1.6×10^9	6.3×10^9	16.3	Rignot et al., 1996
2001	80	8.41	3.4×10^9	3085	4.3×10^5	1.3×10^9	5.1×10^9	8.7	E. Rignot, pers.comm., 2006

1. Annual ablation is calculated from the ice mass transfer model using local climate and measured ablation rates as a function of temperature
2. Annual calving flux is the product of ice speed at the terminus and the terminus cross-sectional area
3. The flux of ice at the ELA is estimated as the sum of the calving flux, ablation flux and average ice loss to thinning below the ELA (3.5×10^8 m^3/a)

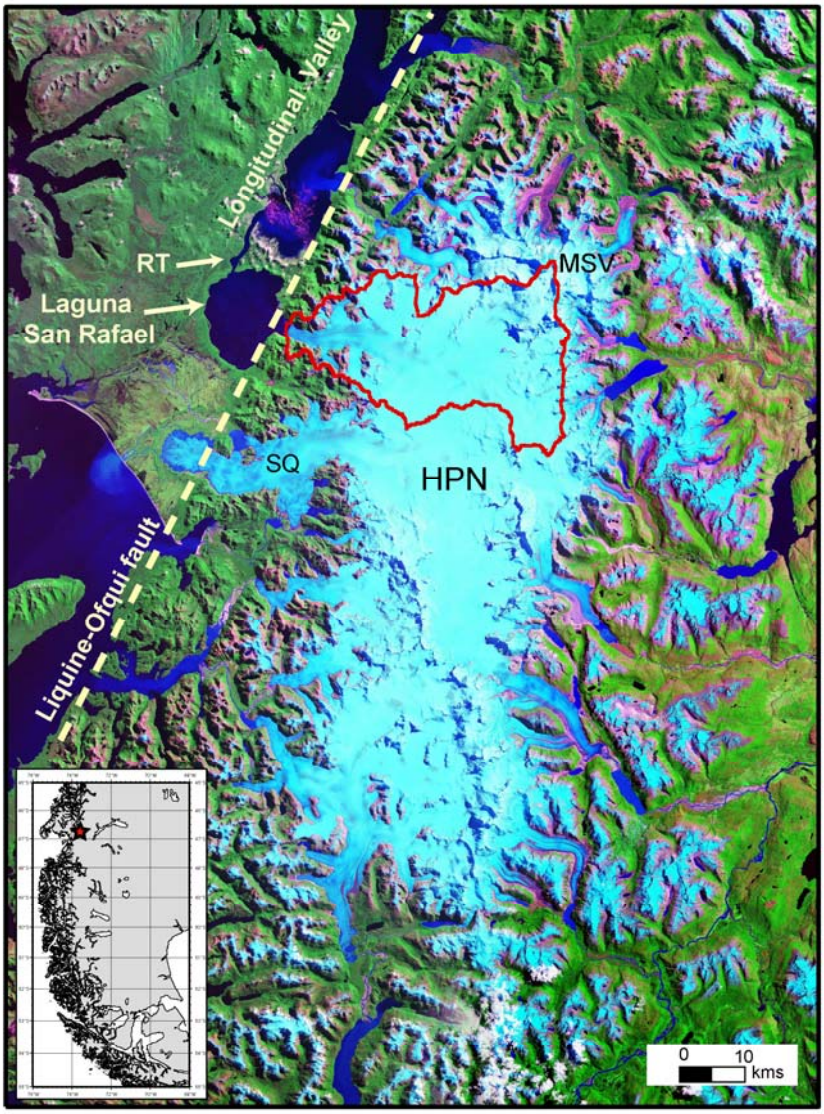

Figure 4.1 Location of San Rafael Glacier in the Campo de Hielo Patagonico Norte (North Patagonian Icefield (HPN)), Chile, outlined in red. San Rafael Glacier (SR) calves into the Laguna San Rafael, a brackish lagoon linked to the sea by a narrow channel, the Rio Tempanos (RT). The Liquine-Ofqui mega fault (yellow dashed line) scarp forms an abrupt rangefront that bounds the eastern side of the lagoon and constrains the glacier terminus in a narrow outlet that crosses the fault zone into the Longitudinal Valley (LV).

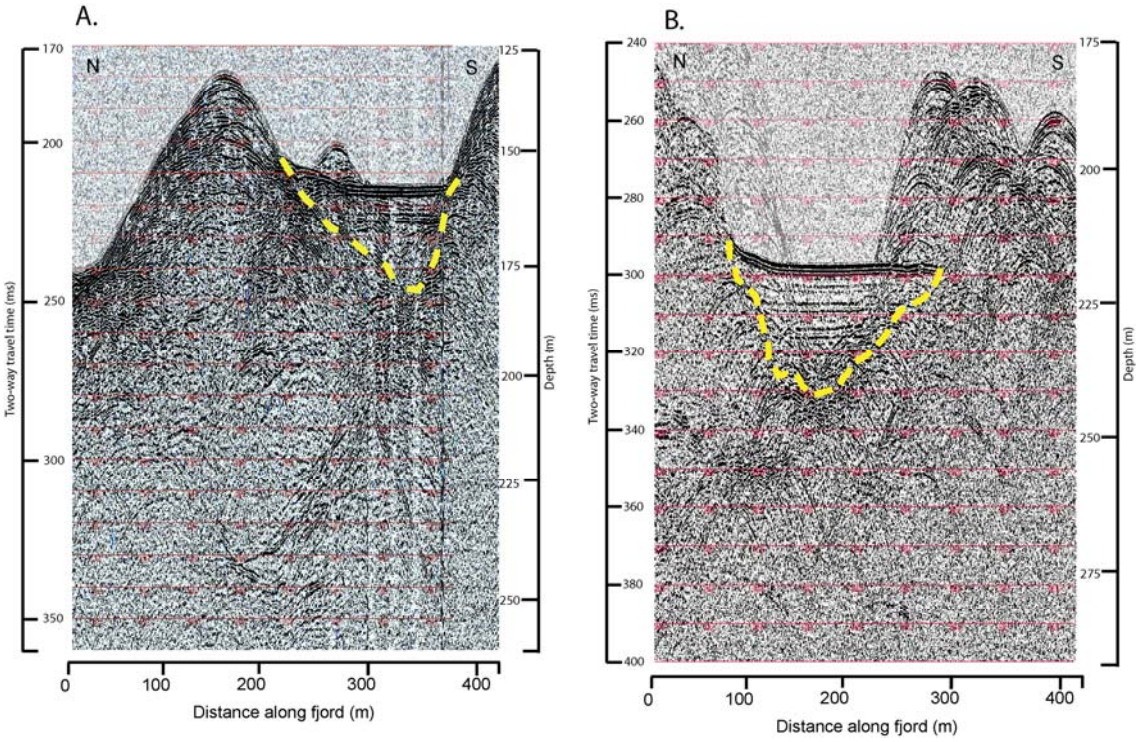

Figure 4.2 Samples acoustic reflection profiles from which the sediment thickness in Laguna San Rafael was measured. Locations are shown in Figure 3. a) seismic profile across a perched bench along the northern edge of the fjord, close to 1990 position of the terminus, b) seismic profile across a channel in the center of the fjord, at the 1986 terminus position. The semi-transparent, laminated seismic facies, filling in the deep channels indicates glacimarine sediment. The underlying crystalline bedrock is imaged as a series of parabola, indicative of a hard, uneven surface, with little sediment drape. Submarine slumps can also be seen in the chaotic hummocky facies lining the edges of the deeper channels.

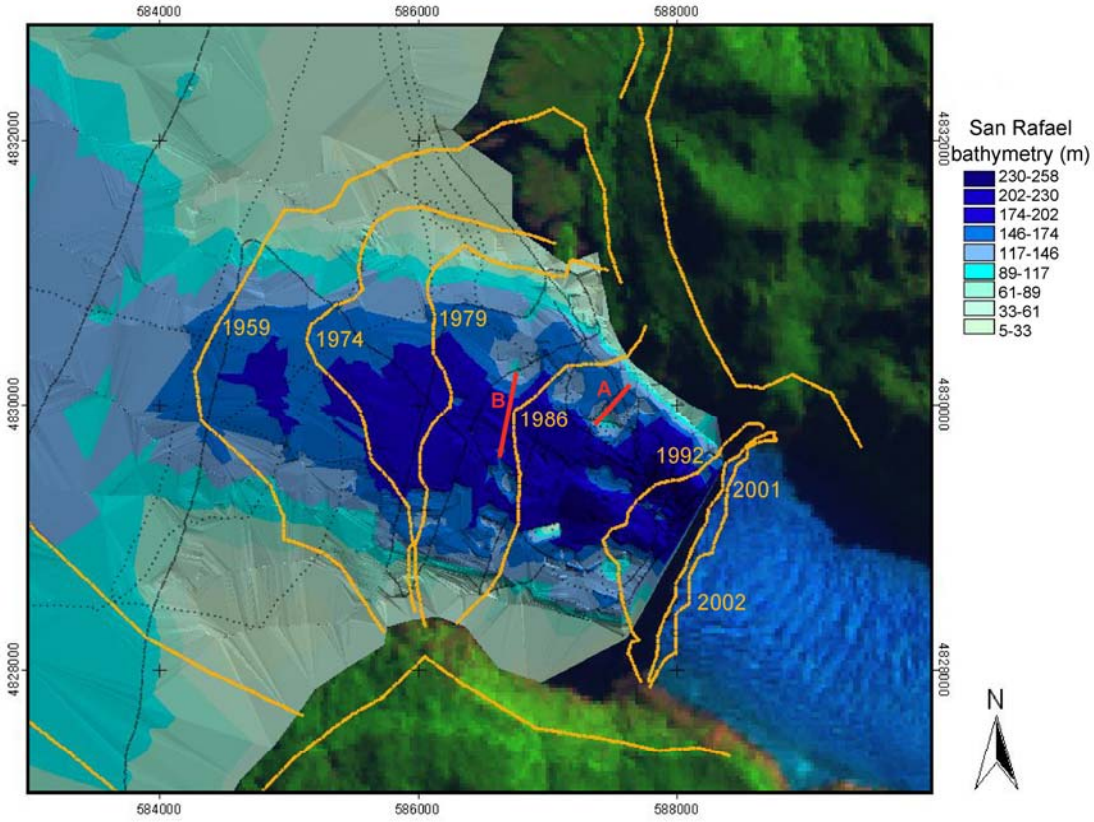

Figure 4.3 Map of bathymetry in the inner portion of Laguna San Rafael, 2005, superimposed on a 2001 Landsat ETM+ image of the terminus of San Rafael Glacier. Measurements of surface and subsurface bathymetry from the acoustic reflection survey are indicated with black dots; known terminus positions since 1959 are indicated with dashed lines. The locations of the seismic examples in Figures 2a and b are indicated with red bars.

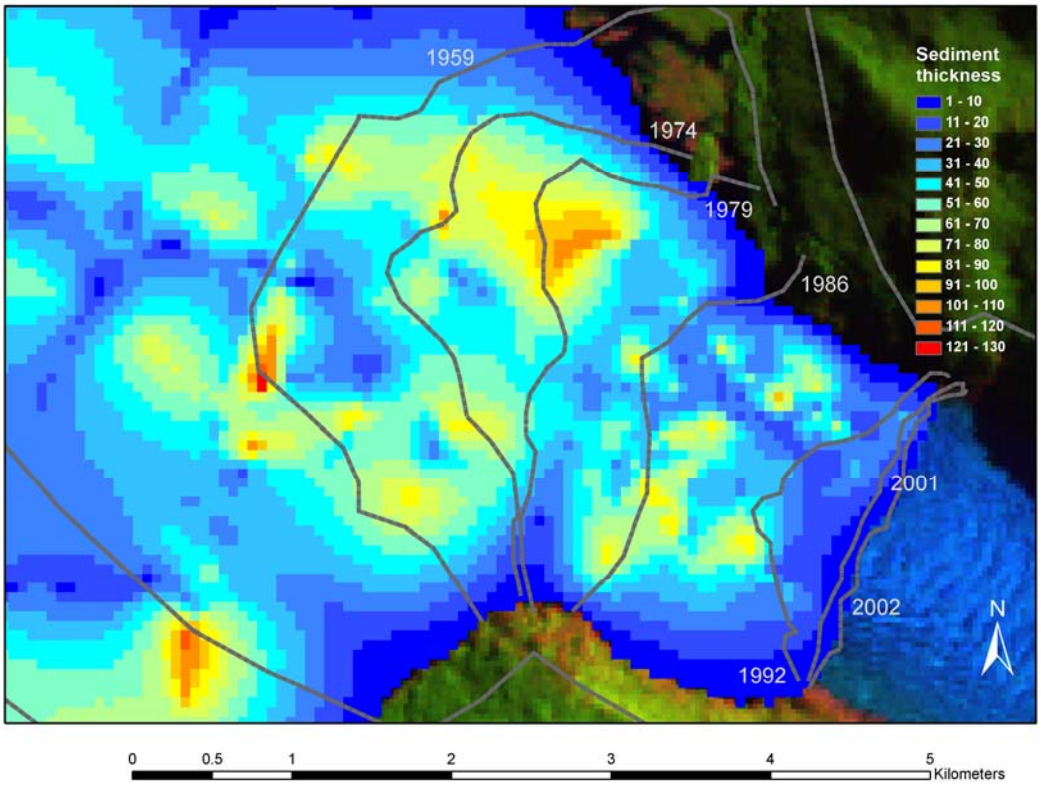

Figure 4.4 Map of pro-glacial sediment accumulation in the inner portion of Laguna San Rafael, 2005, interpolated and gridded from the acoustic reflection profiles. Known terminus positions since 1959 are indicated with dashed lines. Scale and location are the same as for Fig.3.

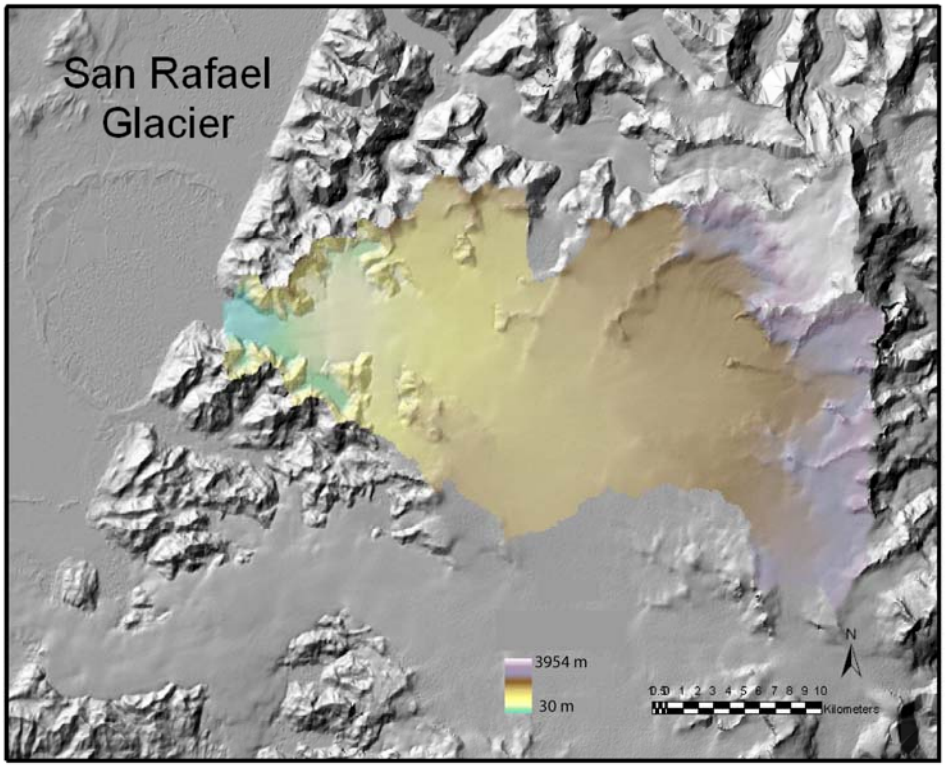

Figure 4.5 Digital elevation model (DEM) of San Rafael glacier, derived from the SRTM 30 m. DEM global dataset, shown with sun in upper left. The DEM was regridded into 96 x 96 m cells, and snowline, snow accumulation rates and ablation rates were applied to the glacier surface to model the mass flux through the glacier.

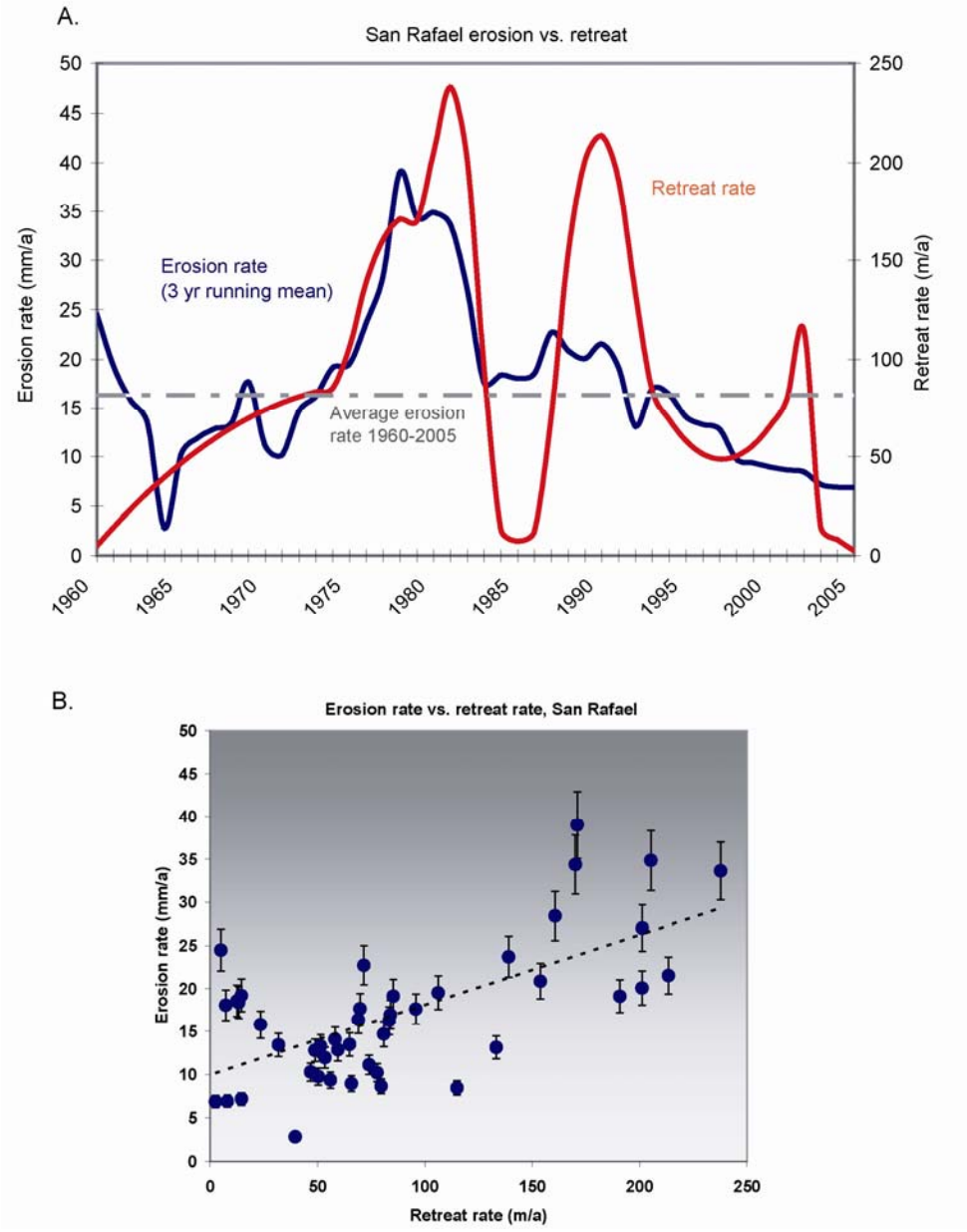

Figure 4.6 a) Comparison of bedrock erosion rate and retreat rate for San Rafael Glacier, 1960-2005. Average contemporary erosion rate for this period is 16 ± 5 mm/a. b) Correlation of erosion rate and retreat rate for San Rafael Glacier, 1960-2005. Error bars indicate a 30% uncertainty in calculating erosion rates. Extrapolating the erosion rate to times when the glacier is effectively stable, on average neither advancing nor retreating (i.e., dx/dt = 0), the long-term erosion rate is 9 ± 3 mm/a.

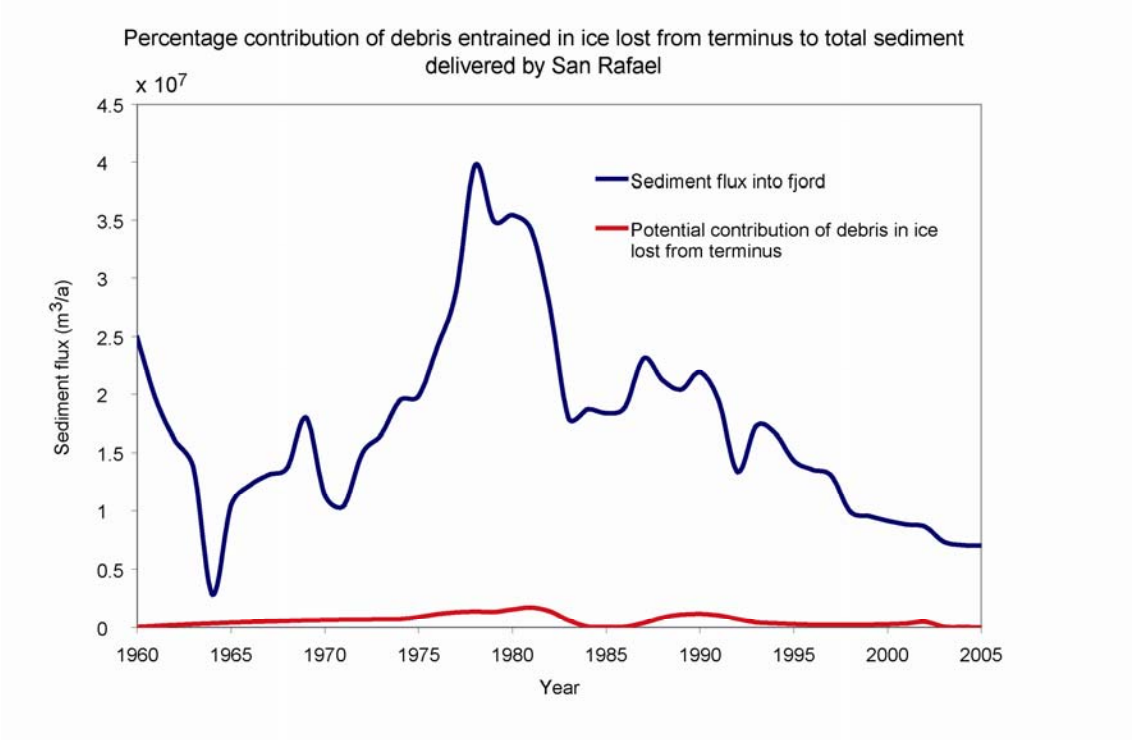

Figure 4.7 Potential variability in the contribution of debris entrained in the ice lost from the terminus to the total sediment flux delivered by San Rafael glacier, 1960-2005, assuming an upper limit in debris concentration of 1% per unit volume of ice.

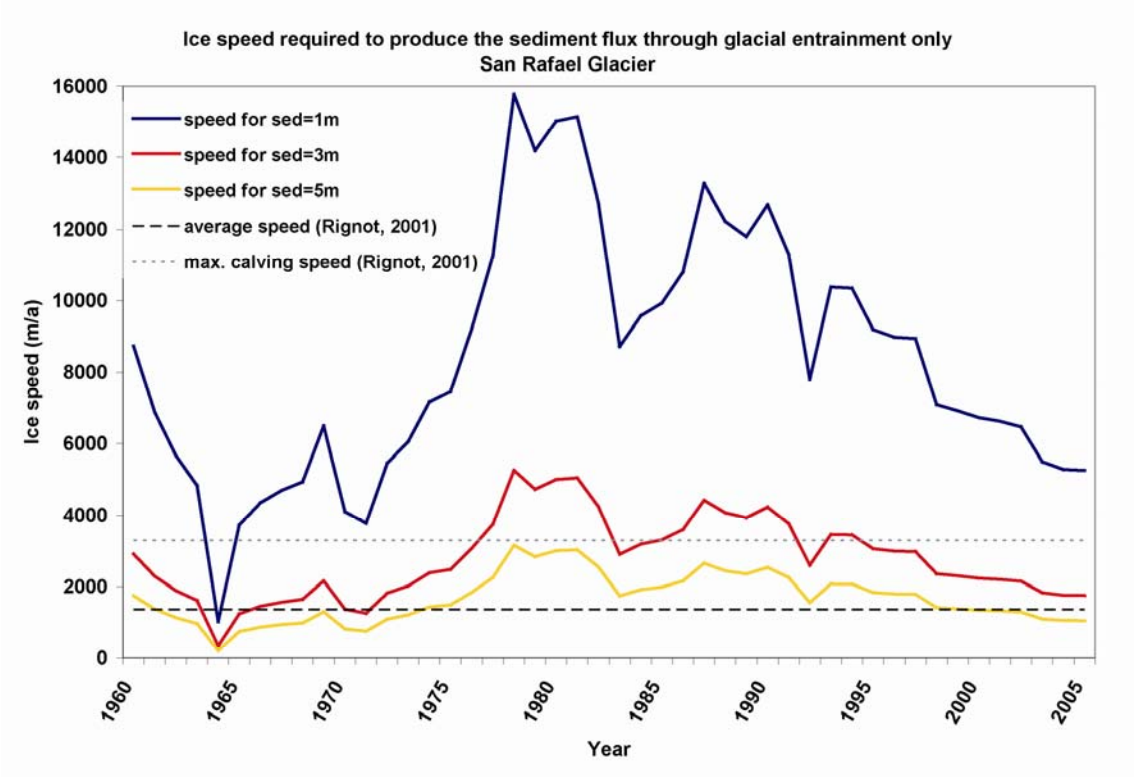

Figure 4.8 Calving speeds required to produce the observed sediment flux from San Rafael glacier, assuming the sediment is delivered exclusively through englacial entrainment.

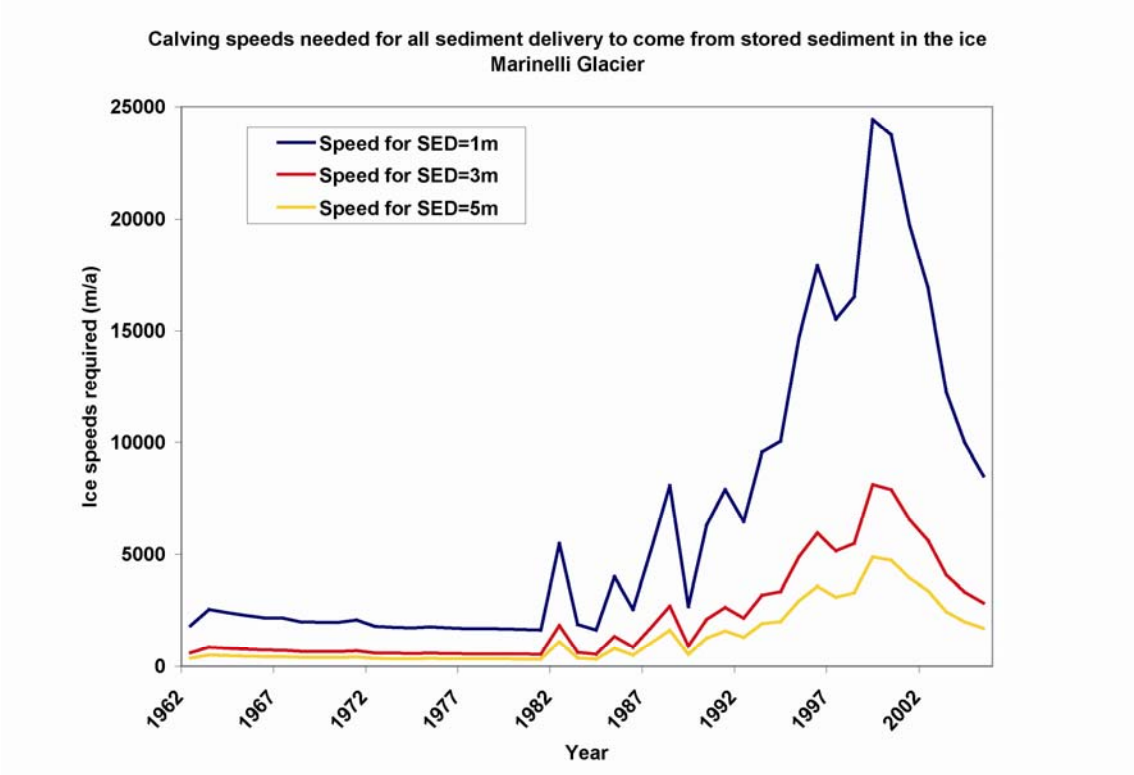

Figure 4.9 Calving speeds required to produce the observed sediment flux from Marinelli glacier, assuming the sediment is delivered exclusively through englacial entrainment.

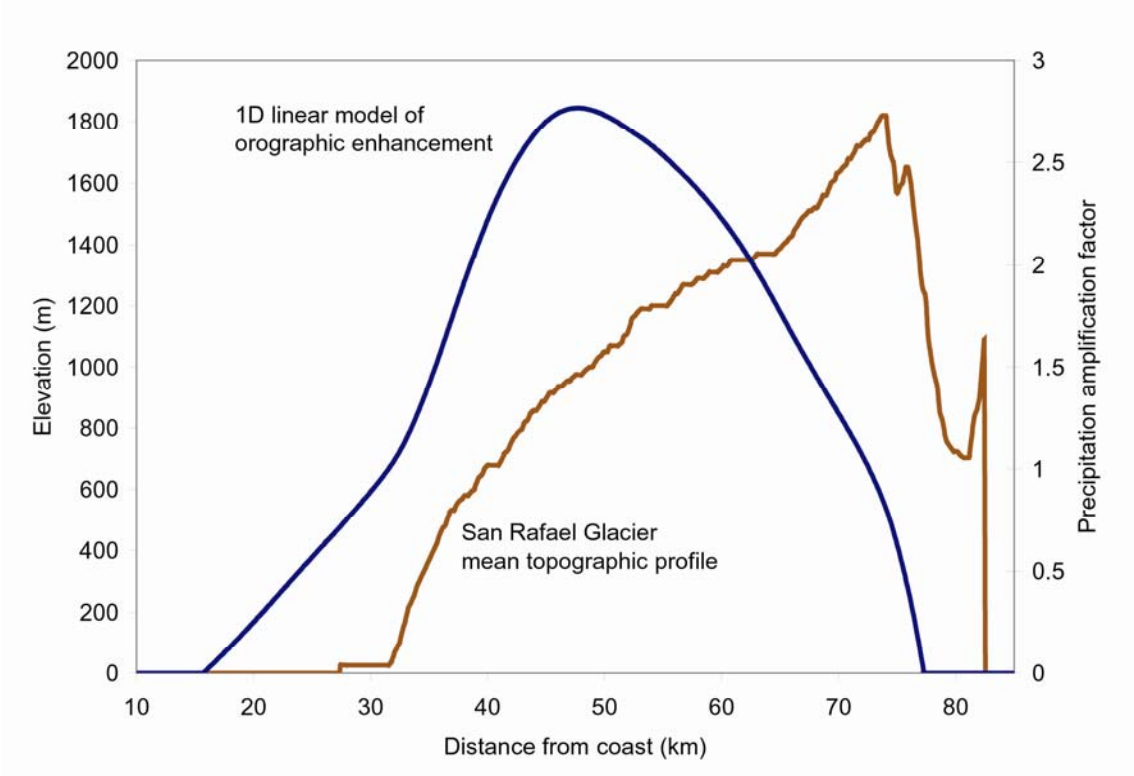

Figure 4.10 Calculated orographic enhancement of precipitation over San Rafael Glacier shown in blue (see text). The mean longitudinal profile of San Rafael glacier is in brown. The model was used to calculate the precipitation (snowfall) over the glacier.

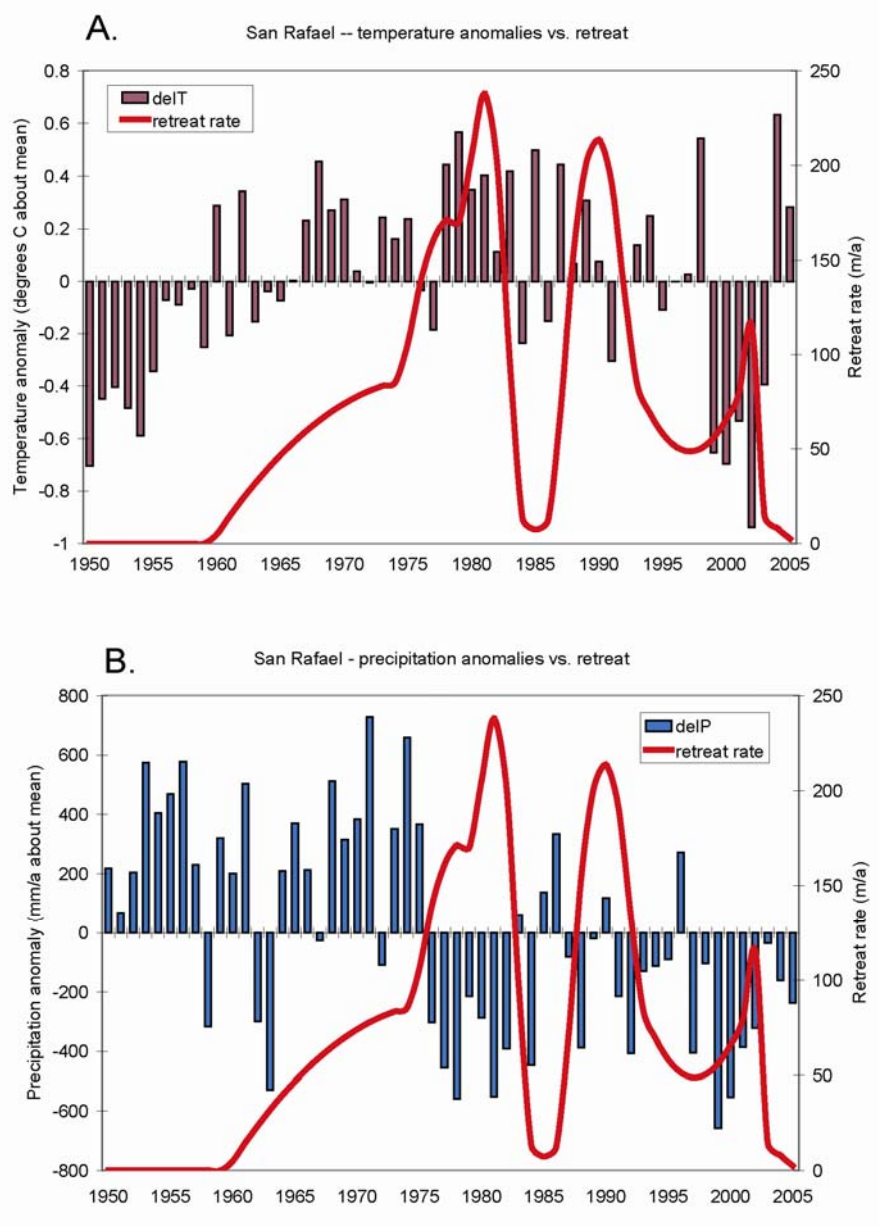

Figure 4.11 Comparison of temperature and precipitation variability at Laguna San Rafael from 1950-2006 with retreat rate. The climate parameters were derived from the NCEP dataset, adapted to local conditions by a least-squares fit with the gauge data from March 2005 to April 2006. a) Temperature anomalies, in ºC about a mean annual temperature of 8.9ºC for the period 1950-2006, compared with retreat rate. b) Precipitation anomalies, in mm/a about a mean annual precipitation of 3600 mm from the period 1950-2006, and terminus retreat rate.

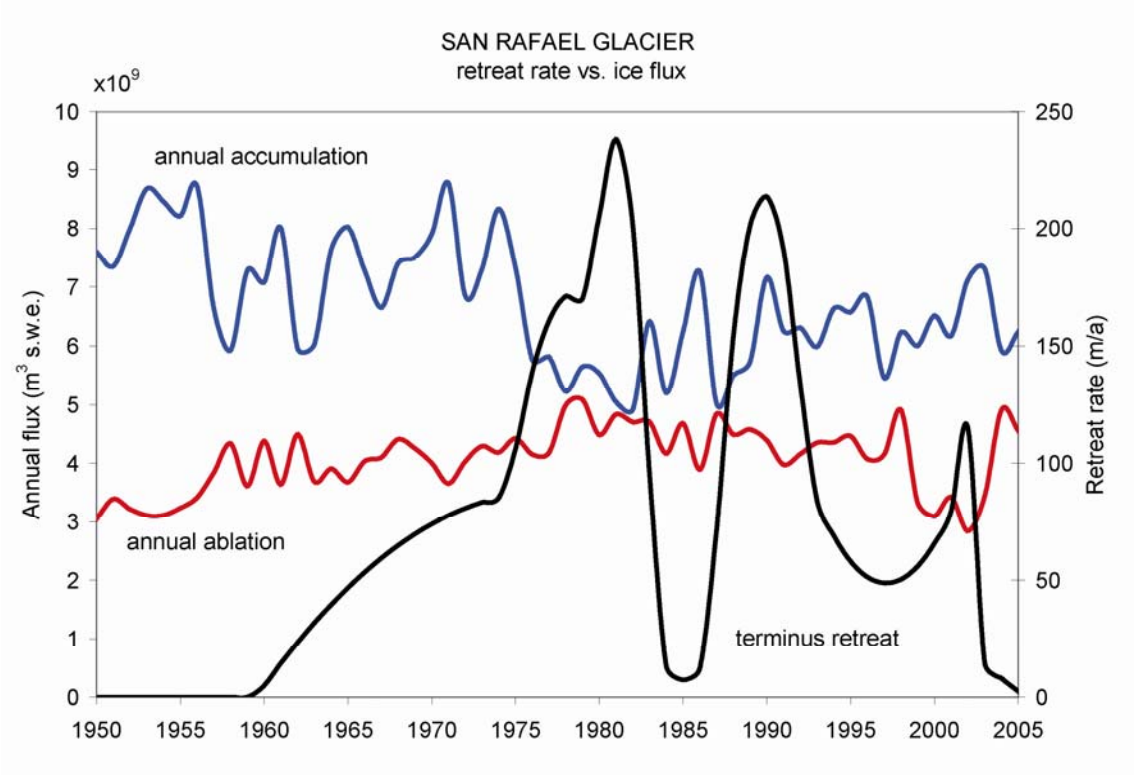

Figure 4.12 Annual accumulation of ice, in cubic meters of snow water equivalent, onto the glacier surface and annual ablation flux out of the glacier surface, 1950-2006, compared to the rate of terminus retreat, in meters per year.

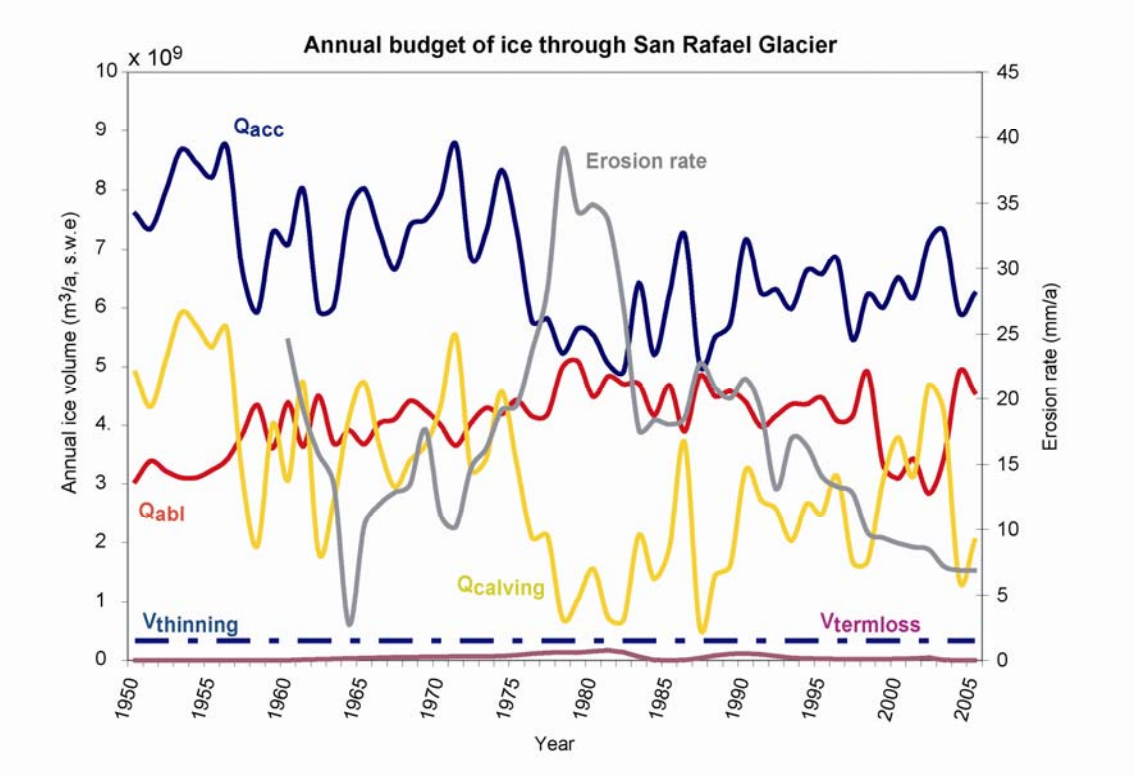

Figure 4.13 Comparison of basin-wide erosion rate and modeled ice fluxes through San Rafael glacier, 1950-2006, including the annual snow input (Q_{acc}), annual ablation (Q_{abl}), annual loss of ice at the terminus due to retreat ($V_{termloss}$), annual loss of ice due to thinning ($V_{thinning}$), and resulting calving flux (Q_{acc}), in cubic meters of snow water equivalent. The calving flux is calculated as (Q_{acc} - (Q_{abl} + $V_{termloss}$ + $V_{thinning}$)), assuming a constant thinning rate of 3.5 x 10^8 m^3/a.

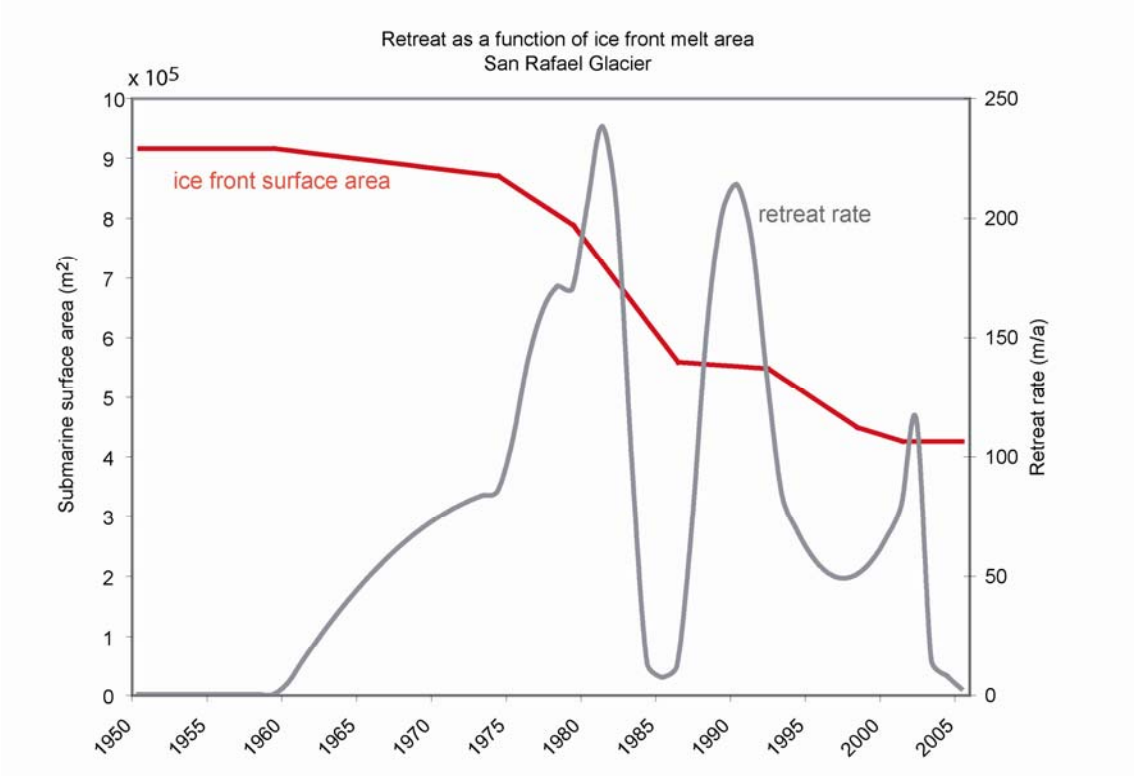

Figure 4.14 Comparison of the annual rate of terminus retreat and the surface area of the ice front subject to melt, from 1950-2006.

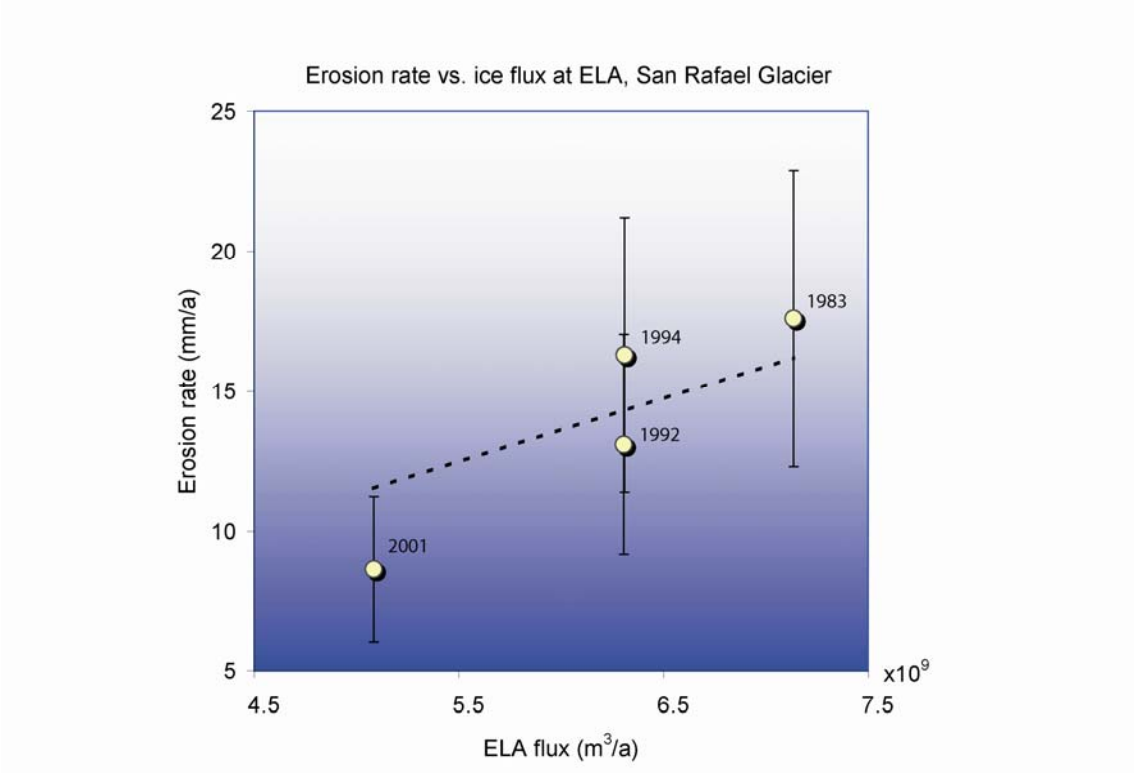

Figure 4.15 Comparison of basin-wide erosion rate and flux of ice at the ELA, for four years in which surface velocities at the glacier terminus are known. The flux of ice through the ELA was calculated as equal to the sum of the calving flux (measured), the average ice loss to thinning in the ablation zone (estimated) and the ablation flux (modeled) for each year.

CHAPTER 5.

Centennial sediment yields and submarine landforms during retreat of a tidewater glacier, Laguna San Rafael, Chilean Patagonia

San Rafael glacier is of special interest because it is one of the fastest flowing glaciers worldwide (Rignot et al., 2003), and drains almost 20% of the North Patagonia Icefield (HPN). Understanding how fast outlet glaciers such as San Rafael drain the icefields and contribute to their rapid shrinkage is of considerable importance for understanding the glacier contribution to sea level rise. Located at 46º40 S, 73º49 W, San Rafael glacier is in a strategic location to receive ample moisture from the mid-latitude Southern Westerlies, a dominant feature of global atmospheric circulation. It is therefore quite sensitive to global changes in temperature and atmospheric circulation. Significant fluctuations of the terminus, and perhaps in erosion and sediment delivery to the glacier front have occurred over recent geologic time. The sediments deposited and sculpted by the glacier leave a rich record of the interaction of the glacier and its bed near the ice front, as well as a history of the delivery of sediments generated from the entire glacier basin. This record may help us understand the glacier response to both conditions at the terminus, and to climate, prior to the advent of historical records in the region, as well as how the sediment yield from a glacier varies throughout a ~200 year period of retreat.

Observing the sedimentation processes and patterns of sediment accumulation near the ice front of a calving glacier is challenging due to the inherently dangerous conditions at the calving margin. A few studies have succeeded in using ice-penetrating radar near the calving front to image the evolving subglacial surface and bedforms and to relate them to dynamics near the terminus (e.g., Truffer et al., 2005; Smith et al., 2007); most radar studies, however, suffer from heavy crevassing and significant englacial water common to the terminal zone of glaciers, which disrupts and attenuates radar signals from the bed. Geomorphologists are often left to decipher subglacial and near-glacial conditions from the landforms that survive the retreat of the ice. However, the morphology of these landforms often reflects only the final phase of the advance/retreat cycle, the last chapter in ice-bed interactions as the ice front pulls

away. To better understand the history of the sediment accumulation and the timing of its deposition in relation to the terminus, imaging what is below the sediment surface is invaluable.

This chapter describes the submarine morphology, structural forms and sediment accumulation in Laguna San Rafael since the last substantial advance of the glacier, using sub-bottom acoustic profiles of the sediments in the lagoon. The submarine landforms that have survived are used *to interpret the dynamics at the terminus of San Rafael glacier that created them, and to estimate sediment yields from the glacier since the Little Ice Age.* The landforms provide a rich descriptive history of the recent dynamics at the glacier terminus which, when combined with new radiocarbon dates from the surrounding moraines that will become available in the next year (N. Glasser, pers.comm., 2005), will provide a comprehensive story of the Neoglacial oscillations of San Rafael glacier.

Laguna San Rafael and glacier fluctuation history

San Rafael Glacier terminates in a brackish lagoon, the Laguna San Rafael, that is encircled by the Tempanos moraine, a massive terminal moraine arcing for 35 km and 15-30 m.a.s.l. that contains the lagoon (Fig. 5.1). The moraine, a complex multi-crested ridge, was formed during one or more advances of the glacier out of the range front during the Holocene (Glasser et al., 2006). It is breached to the northwest by the Rio Tempano (Iceberg River), a shallow river that connects the lagoon to Gualas Fjord and the ocean, and allows seawater to enter the lagoon. In the past, the lagoon may have been connected to the ocean by a shallow river draining to the south, but it has since been blocked by an advance of neighbouring San Quentin glacier, and has subsequently silted in. The east edge of the lagoon is bounded by the front range of the Andes at the Liquine-Ofqui mega fault. The lagoon therefore acts as a very efficient trap for sediment delivered by the glacier, and the relatively still waters of the lagoon and narrow ‘release valve’ of the Rio Tempano have acted to preserve submarine structure in the lagoon quite effectively.

San Rafael glacier has the longest documented fluctuation history of any glacier in southern South America. Early historical records indicate that in 1675 the glacier was less extensive than today, and started to advance into Laguna San Rafael between 1742 (when it was first described by John Byron) and 1766, when the ice front advanced into water deep enough to initiate calving (Casassa and Maragunic, 1987). The glacier reached its Little Ice Age maximum sometime around the middle of the 19th century (Lawrence and Lawrence, 1959); prior studies speculated that the glacier did not cross the lagoon completely during this advance, but was restricted to a piedmont lobe protruding into the center of the lagoon due to rapid calving into deep water along a broad terminus (Warren, 1993; Glasser et al., 2005). The first precise description of the piedmont-type ice front was recorded by Comandante Enrique Simpson in 1871, who was surveying Laguna San Rafael for a potential inland waterway through the Patagonian fjords. Simpson described the terminus as extending approximately 9 km out from the Andean front, ending approximately 3 km from the arcuate moraine that bounded the lagoon (Simpson, 1875; Cassasa and Maragunic, 1987). The ice front was in the same approximate location when Dr. Hans Steffen visited Laguna San Rafael in December 1898 (Steffen, 1910). The start of the latest retreat phase of the glacier from its Little Ice Age maximum began sometime around Dr. Steffen's visit, dated from vegetation at the prominent trimline along the rangefront (Lawrence and Lawrence, 1959). Retreat then progressed slowly, but erratically, reaching the vicinity of the now-destroyed hotel/park headquarters in 1900 (see Fig. 5.2), and forming a recessional moraine next to the airstrip in 1910 (Glasser et al., 2005). Over 4 km of retreat occurred between 1905 and 1935 (Lliboutry, 1956), followed by a standstill until around 1959. Retreat of the ice front has since continued from the early 1960s onwards to its position 3 km east of the range front today (described in Chapter 4), a retreat attributed to glacier downwasting driven by a significant decrease in winter precipitation since the 1920's (Harrison and Winchester, 1998).

The Tempano moraine was deposited on a pre-existing outwash plain vacated since the last major glacial advance, dubbed the Llanquihue event, which occurred 14-34 ka (Mercer, 1976). During that advance, glaciers occupied almost the entire continental margin out to the shelf break south of 40ºS (Hulton et al., 1994). Around 11 kyr ago, the icefield shrank back approximately to its present extent, and San Rafael

glacier has fluctuated within the area of the lagoon since (Winchester and Harrison, 1996). The age of the Tempano moraine is debated, with ^{14}C ages from the moraine ranging from 6850 ± 200 ^{14}C yr B.P. (Heusser, 1960) to 3600 ^{14}C yr B.P. (Muller, 1960). Dating has been problematic because of the complex sedimentology, the result of the terminus occupying the same position more than once during the Holocene, and of the glacier possibly reworking older sediments and redepositing them in the terminal moraine during each readvance (Glasser et al., 2005, 2006). Given the high probability that such reworking occurred, it is possible that the Tempano moraine is actually much younger than the apparent ^{14}C ages would suggest, and may date to early in the Little Ice Age (1200-1900 A.D.). The non-consolidated sediments currently imaged in the lagoon are therefore the result of sediment delivery by the glacier since this last advance, sometime within the past millennium, possibly within the last 100-300 years.

Approach

In April 2006, we collected acoustic reflection profiles in the Laguna San Rafael over the period of one week using a Datasonics Bubble Pulser and aboard the MV Petrel IV, the national park boat owned and operated by the Corporacion National Forestal de Chile. Penetration depth exceeded 200 m in the soft lacustrine sediments, and several stacked reflectors and facies were imaged. The acoustic signals were digitally imported into the SonarWiz-SBP software suite for post-processing and analysis. An average seismic velocity of the brackish water in the lagoon was calculated to be 1460 m/s from a series of six CTD profiles measured near the ice front, in the center of the lagoon, and near the outlet of the Rio Tempano. The thickness of sedimentary facies were estimated using a seismic velocity of 1740 m/s. The post-glacial sediment in the lagoon was measured from the deepest, most prominent reflector imaged in the profiles, which was interpreted to reflect bedrock and/or deformable lacustrine sediment compacted by glacier overriding during the prior advance. The tracklines and sediment thicknesses were imported in ArcGIS and gridded to estimate sediment volumes, using the methods described in Chapters 1 and 4. Bathymetry was also determined using a Lowrance 18-C depth profiler with GPS.

Submarine landforms in Laguna San Rafael

The bathymetry of Laguna San Rafael (Fig. 5.2) roughly correlates with maps of the lagoon published by the Chilean Navy in 1992 (Warren, 1993; Vieira, 2006), however, the sparse coverage that was used to generate the prior maps missed some significant bathymetric highs and deep basins that were revealed by our denser coverage of the lagoon. The bathymetric maps illuminate several distinct features, notably two prominent, discontinuous submarine moraines. The larger of the two forms an almost continuous arc, of the same form as the Tempano moraine, approximately 3 km from the edge of the lagoon. This moraine corresponds well to descriptions of the ice front position in 1871 (Simpson, 1875) and 1898 (Steffen, 1910), and is henceforth dubbed the Little Ice Age (LIA) moraine. It is breached to the northwest, in a channel that aligns with the outlet of the Rio Tempano, suggesting that the glacier and lagoon drained out from the Rio Tempano during the last advance.

A second obvious, discontinuous moraine was deposited around the mouth of the narrow outlet valley that crosses the rangefront. It forms two slightly arcuate spurs that extend westward from the rangefront along the valley sides, and is breached in the center by a deep, broad basin that slopes toward the inner fjord and current ice front. Its location corresponds to the location of the terminus standstill from around 1935 to 1959.

Between these two moraines is a broad basin of ~180-200 m depth, with two small, arcuate forms within 2 km of the LIA moraine, presumably formed by deposition during the period of retreat between 1900 and 1935.

The two prominent moraines each can be traced onto land in the northern portion of the fjord. The LIA moraine emerges from the lagoon, and corresponds to a doublet moraine dated to 1910 (Winchester and Harrison, 1996). The 1959 moraine aligns with low amplitude ridges along a beach close to the park headquarters (see Fig. 5.2).

Provided that calving rate is related to water depth (Meier and Post, 1987; Van der Veen, 1996), the shallower northern end of the lagoon helps explain prior

observations that the terminus pulled back from the south post-LIA while remaining pinned at its northern end for several decades.

Sediment structures

Five distinct seismic facies were imaged. They are interpreted as:

a) morainal deposits: moraines in the lagoon were primarily determined by morphology (see Fig. 5.5). Crests ranged from narrow (<200 m) and high (>40 m) (J in Fig. 5.5), to broad (>600 m) and double-crested (C in Fig. 5.5). The facies within the moraines is chaotic, with parabolic reflectors near the surface and a strong double reflector at the surface, suggestive of a hard or compacted layer. A shallow, wavy and hummocky layer was imaged on the surface of some of the moraines (A,D in Fig. 5.5), indicative of slumping off the moraine crest. Deeper in the moraines, light lamination can be found (best seen in A). The moraines overlay one or more deep, low angle reflectors, indicative of an unconformable bottom (described below).
b) ice proximal deposits: a facies comprised of hummocky, wavy seismic units with many discontinuous, layered reflectors (Fig. 5.8), also seen in the upper portion of the moraines
c) ice distal deposits: a semi-transparent, sub-horizontal to horizontal, strongly layered facies (Fig. 5.6) that infills and drapes over angled reflectors (e.g., B) and chaotic facies (K).
d) unconformities/compacted surfaces: a low-angle, prominent, single or multiple reflector (Figs. 5.5-5.8), 30-150 ms below the sediment surface is mostly continuous across the lagoon west of the range front. In the inner fjord to the east (Fig. 5.10, G), the unconformable surface has considerable relief and the contact is defined by distinct parabolic reflectors, suggestive of hard bed. The semi-transparent, layered ice distal deposits end abruptly at the contact with this surface in profiles where the contact is at an angle to the surface (see B in Fig. 5.6).

e) deltaic deposits: an opaque, distinctly layered facies, often laps onto the moraines or other rising landforms at the edges of the lagoon (e.g., I in Fig. 5.9, west end of C in Fig. 5.5). The layers are sometimes overlain with a shallow chaotic facies (i.e., slump deposits, as seen in I).

We interpret all the sediments above the continuous compacted surface (the flat reflector) to be postglacial, with the exception of deltaic deposits near the edges of the fjord that were interpreted to be non-glacial in origin. This package includes the LIA and 1959 moraine deposits that also overlie a flat, prominent reflector. The distribution of postglacial sediments is mapped in Figures 5.3 and 5.4; a diagram of the major submerged landforms can be found in Figure 5.11.

Moraine morphology

The structure and size of the LIA moraine correlate well with those of the Tempano moraine complex (Winchester and Harrison, 1996; Glasser et al., 2006). As exemplified in seismic image C (Fig. 5.5), the moraine exhibits a doublet crest in many places, with slump deposits upglacier of the inner crest, and the outer crest prograding onto distal deltaic deposits. Both features have been related to plowing of soft sediment by the glacier front (e.g., Powell, 1991). The structure of the LIA moraine, with its sharp crest (J in Fig. 5.5) overlapping and onlapping thick distal, layered deposits (A in Fig. 5.5), supports prior speculation that the glacier did not advance past its1871 position during the last, Little Ice Age advance. Any advance prior to this time must have occurred before the deposition of the thick (70-80 m) moraine and associated distal layered deposits, which necessitated up to one hundred years to accumulate (as discussed below).

Within 1-2 km east of the LIA moraine, two small arcuate, hummocky deposits of sediment on top of a laminated facies (M, N in Fig. 5.8) are presumed to be recessional moraines, 15-20 m in amplitude, formed sometime around 1905. Their presence suggests that the terminus was grounded and paused temporarily as it pulled back from the LIA moraine.

There are also hummocky, ice proximal deposits ~ 20 m thick, overlying >100 m of sub-horizontal layered sediments at the location of the 1935-1959 standstill (H in

Fig. 5.8). Unlike the LIA moraine, which appears to be constructed on top of an earlier flat sediment surface (Fig. 5.5), the 1959 ‘moraine’ appears to have been cut into a pre-existing layered deposit over 100 m thick (H in Fig. 5.8). These layers are truncated along the breach between the two spurs of the moraine. It appears that San Rafael glacier flowed out from the valley that crossed the fault scarp eroding and overdeepening the center of the basin while leaving in place the deposits that filled the lagoon to the north and south of the central basin. The significant relief (~120 m) between the ice-proximal deposits that crown the spurs of the moraine and the broad, deep basin of the valley outlet suggests that the glacier evacuated over 100 m of soft sediment from the center of the channel during the prior advance (or advances), a phenomenon resembling that seen at Taku Glacier during its current advance phase (Motyka et al., 2005).

Basin infill

Ice-distal sediments fill the ‘moat’, or depression, between the LIA moraine and the Tempano moraine that bounds the lagoon (B in Fig. 5.6). That these distal fines and onlap the LIA moraine (e.g., right side of J in Fig. 5.5) suggests that deposition was co-eval. The thick laminated sediment package in the ‘moat’ also suggests that the ice front did not reach the shores of the lagoon during the LIA advance; more likely the terminus remained at the the LIA moraine for a significant period during which these thick deposits accumulated. Once the ice retreated from its LIA maximum positions, the fines delivered to the glacier front appear to have been trapped eastward of the LIA moraine, filling the central basin (e.g., M).

Eruptive gas features (morphologically similar to liquefaction features (D. Sylwester, pers. comm., 2006)) are common in the top few meters of sediment in the distal deposits at the north end of the lagoon where water depth is less than 10 m. These features may reflect anaerobic decomposition of vegetation trapped in the sediment. If this vegetation is a drowned forest or other vegetated terrain, it suggests that the lagoon has subsided >10 m , and a large pulse of sediment from the glacier since the LIA overwhelmed a formerly subaerial, forested outwash plain similar to the ones currently bordering the lagoon.

Pro-glacial evacuation during advances

Several prominent, sub-parallel reflectors within the sediment package were imaged between the LIA moraine and the 1959 moraine (M and N in Fig. 5.8). The distinct, continuous trace of the reflectors suggest compaction of distal fines during the last advance and retreat of the glacier front. The known piedmont configuration of the San Rafael terminus during its LIA advance, including evidence of a low surface gradient near the LIA terminus from dated trimlines along the Andean front (Winchester and Harrison, 1996), also suggest flow across a soft substrate. The presence of such horizontal reflectors is consistent with erosion and plowing of the substrate (deposited during retreat phases) during subsequent glacier re-advances.

Subaerial contributions:

The thick (>40 m) sequence of distinct, laminated deltaic deposits at the southeastern end of the lagoon between the LIA and 1959 moraines (I in Fig. 5.9) suggests significant mass wasting or erosion of sediment from the range front. Indeed, subaerial sediments may contribute significantly to the overall sediment budget in the lagoon. The range front slopes are densely vegetated, making it hard to decipher whether the fines accumulating in the lagoon derive from glacigenic material plastered to the mountain front during the maximum advance (and hence should be considered as sediment eroded and delivered from the glacier in glacial erosion estimates), or from non-glacial fault-weakened material slumping into the lagoon. As these inclined, laminated deposits appear to lap onto the 1959 moraine (Fig. 5.9), they may represent one or more deep-seated landslides following the 1960 Valdivia earthquake (magnitude 9.0), an event that produced large ground accelerations in the region, and 1-2 m of subsidence at Laguna San Rafael (Glasser et al., 2006).

Bergy bits

Notably, there was no evidence of iceberg furrowing in the acoustic profiles, even in shallow areas along moraine crests and flanks where such furrows might be expected. This absence most likely indicates that the vast majority of the icebergs calving into the lagoon are small and do not extend into deep water, and therefore

rarely come in contact with the bed, until they drift into the shallows at the outskirts of the lagoon (many of the icebergs in the lagoon in 2005 and 2006 were observed drifting towards the outer shores, becoming trapped at water depths of less than 60 m). The icebergs may be small because the glacier descends through a series of steep icefalls as it cascades rapidly from the icefield plateau to the terminus. The ice, hence, is heavily fractured as it reaches the glacier and tends to calve off in small pieces. This pervasive fracturing also contributes to the rapid calving rates observed at the terminus (e.g., Warren et al., 1995).

Sediment volumes

The total volume of post-advance sediment in lagoon, including all recent moraines, ice-proximal deposits, and ice-distal laminated sediments since San Rafael glacier last advanced across the lagoon, approaches 6 x 10^9 m^3. The volume in the LIA moraine is 1.5 x 10^9 m^3, 25% of the total volume of post-glacial sediment in the lagoon, suggesting that, in this case, much of the sediment accumulated close to the terminus, instead of being evacuated by water. The volume of sediment in the 1935-1959 moraine is 1.9 x 10^8 m^3, ~3% of the total.

Using the 1871, 1905,1935 and 1959 terminus positions in existing maps (Warren (1993) and Glasser et al. (2006), we can estimate the sediment yield from San Rafael glacier sequentially through the early part of the 20th century, at the start of the current phase of retreat. The average sediment yield is measured by dividing the sediment volume between these dated terminus positions by the corresponding time interval. 1.3 x 10^9 $m^3$of sediment accumulated between 1871 and 1905, a period when the glacier started to recede into deeper water (and may have experienced a short standstill that deposited a recessional moraine in the center of the fjord); this volume excludes the LIA moraine itself, much of which most likely pre-dated 1871. The average sediment flux during this period was 3.9 x 10^7 m^3/a, which corresponds to an average basin-wide bedrock erosion rate of 34 ± 12 mm/a (estimated error was propagated as described in Chapter 1). 1.6 x 10^9 m^3 of sediment accumulated between 1905 and 1959 (including a standstill from 1935-1959), including 2.6 x 10^8 m^3 of deltaic deposits near the range front in the southeastern portion of the lagoon. Excluding the

deltaic deposits, as they may originate subaerially, the mean basin-wide glacial erosion rate during this period is 23 ± 9 mm/a. These rates are up to twice as high the mean erosion rate estimated for San Rafael glacier since 1959 (16 ± 5 mm/a (Chapter 4)), suggesting that basin-wide erosion processes have generally been steadily decreasing throughout the retreat cycle (Fig. 5.12).

The thick deposits in the LIA moraine and fines that fill the distal moat beyond it together account for 2.4×10^9 m^3, implying that significant erosion of the basin also occurred during the Little Ice Age advance and standstill. Assuming the glacier entrained all material that it had produced earlier and redeposited this material near the ice margin as it advanced out from the rangefront, generating the moraine and the push structures imaged in the seismic profiles, then the total volume of sediment collected at the LIA position and beyond necessitates that over 2 m of bedrock was eroded basin-wide over the period of the prior retreat, readvance and standstill. If we assume that, at a minimum, the advance and standstill occurred over the same length of time as the later retreat phase, ~100 yrs, then the average bedrock erosion rate during advance was at most ~20 mm/a, similar to the erosion rate averaged over the past century of retreat. If the advance of the glacier snout took two to four times as long as the retreat, as is more commonly seen over tidewater advance-retreat cycles, then the average erosion rate would be lower by a half to a fourth.

The presence of several angled, compacted layers and the deep channel eroded into the layered sediments in the center of the lagoon imply that there has also been significant entrainment of pre-existing debris, particularly fines deposited since the prior retreat, as the glacier readvanced across the lagoon. These sediments would have been remobilized and redeposited at the maximum extent of the advance and would therefore make up a substantial portion of the total volume in the LIA moraine, further lowering any estimate of bedrock erosion during the Little Ice Age advance and standstill.

The substantial volumes of sediment accumulated over the past century at Laguna San Rafael give me confidence in the assumption that the sediment yields we are measuring since the start of retreat primarily reflect bedrock erosion, as opposed to the emptying of subglacial stores of sediments. The total volume of sediment delivered to the fjord since deposition of the LIA moraine in 1871 and 2005 is 3.5×10^9 m^3.

Likely volumes of sediment stored under San Rafael glacier that could be remobilized are but a small fraction of the sediment delivered to the lagoon during this time. To attribute this sediment flux solely to enhanced evacuation of subglacial sediment stores would require the removal of layer of basal sediment >20 m thick under the entire ablation area of the glacier (~175 km^2), where such debris is most likely to accumulate; if sediment was preferentially remobilized from under the fast moving ice tongue that cascades down from the icefield plateau, as is more likely, the thickness of subglacial sediment necessary to produce the sediment in the fjord is closer to 140 m. Given that the characteristic thickness of mobile basal debris, measured from boreholes that have penetrated coastal tidewater glaciers, is only a few decimeters (Humphrey et al., 1993; Kamb et al., 1985), the sediment storage required is excessive, and would preclude bedrock erosion by preventing sliding ice from having direct contact with the underlying bed.

Implications

The morphology of the Little Ice Age moraine and the prominent compacted layers that underly it suggest that the piedmont lobe of San Rafael glacier was grounded throughout its advance. The distal deposits that onlap the moraine and fill the moat between the moraine and the shores of the lagoon support previous speculation (e.g., Glasser et al., 2006) that the glacier did not advance all the way across the lagoon for a significant period of time prior to this Little Ice Age advance, allowing for significant deposition of fines in the outer 3 km of the lagoon. The ice-proximal deposits 1-2 km east of the LIA moraine suggest that the glacier was also grounded across its centerline as it started to retreat from its LIA position. The lack of proximal deposits in the deeper center of the basin upfjord of the recessional moraines suggest that the center of the piedmont lobe may have floated for short periods during retreat (such as around 1905 and after the terminus pulled back from the 1959 moraine), and a floating tongue may have buried a small recessional moraine in the southern part of the fjord with distal fines, while the northern edge of the piedmont remained grounded. (Alternately, the buried moraine in the south end of the fjord northeast of the LIA moraine may have been deposited during a prior advance, and its survival indicates

that the glacier did not erode and rework enough sediment during the LIA advance to remove all the sediment from the prior retreat.) There is little evidence, however, of widespread separation of the glacier from its bed that would indicate flotation driving collapse and rapid retreat.

The thick sequence of layered deposits near the range front indicates significant unraveling of the fault scarp once the glacier pulled back from the steep walls of the range. The >80m-thick slump deposits at the eastern edge of the lagoon along the scarp of the Liquine-Ofqui fault, which have accumulated since 1935, is similar to the massive landsliding observed near the terminus of Tyndall Glacier (along the Hoof Hill fault) in Icy Bay, Alaska (Chapter 2, Meigs et al., 2006). The contribution of sediment from changes in base level and the removal of a backstop as the glacier terminus retreats can be substantial -- approaching 15% of the total volume of sediment in the fjord from this single glacial valley -- particularly in tectonically active orogens where active faults can contribute to mass movements and localized crustal weakening.

The thick sediment deposits in the Laguna San Rafael highlight the importance in understanding the timing of sediment transfer from the orogen to the continental shelf. The substantial deposition of glacially-derived sediments that are trapped in lagoons and fjords imply that much of the sediment produced during the periods between major glacial advances collects right at the range front, in proximal basins, very close to the higher source areas. The sediment is not evacuated until the next major advance out to the continental shelf. The accumulation of vast volumes of sediment in close proximity to the glaciers and icefields that produce them can dampen the isostatic response that might be expected from the loss of ice following retreat. The significant delays between producing and mobilizing sediment from glaciated basins and depositing them in basins off the continental shelves needs to be incorporated into landscape evolution models, as well as in attempts to interpret sediment archives of climate-dependent exhumation and sediment production.

Conclusion

Detailed investigation of the bottom surface and subsurface of Laguna San Rafael reveals an extensive sequence of glacio-lacustrine deposits created during the last advance and subsequent recession of San Rafael glacier into the lagoon. The precise timing of this advance, which formed a large submarine moraine in the outer portion of the lagoon, remains undated, but most likely occurred during the Little Ice Age. The end of the LIA, sometime around 1871, is used to bracket the centennial sediment yield out of the glacier. The basin-wide erosion rates of San Rafael glacier have averaged 19 ± 7 mm/a since the Little Ice Age; rates must have been much lower during the Little Ice Age advance and standstill. The rates were higher during the first half of the 20th century, averaging 34 ± 12 mm/a between 1871 and 1905, and 23 ± 9 mm/a between 1905 and 1959, than have been measured since 1959 (Chapter 4). This work highlights the value of collecting sub-bottom information, that enables us to calculate sediment volumes and document sequences of erosional and depositional events. The sub-bottom images also help in the interpretation of plowing and reworking of sediments in the fjords, which need to be taken into account when estimating sediment yields from glaciers over the long term.

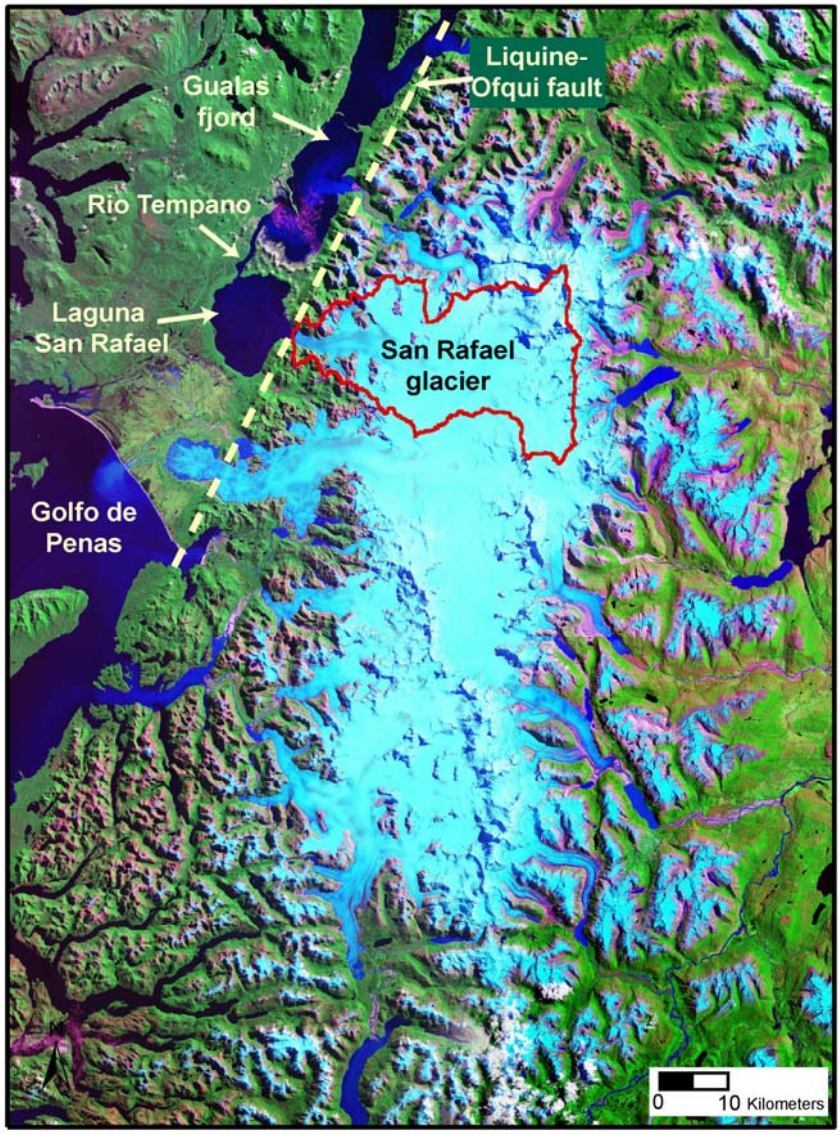

Figure 5.1 Location map of Laguna San Rafael, including the major geographic feaures of the area. The lagoon is bounded by the arcuate Tempano moraine and the Andean rangefront to the east.

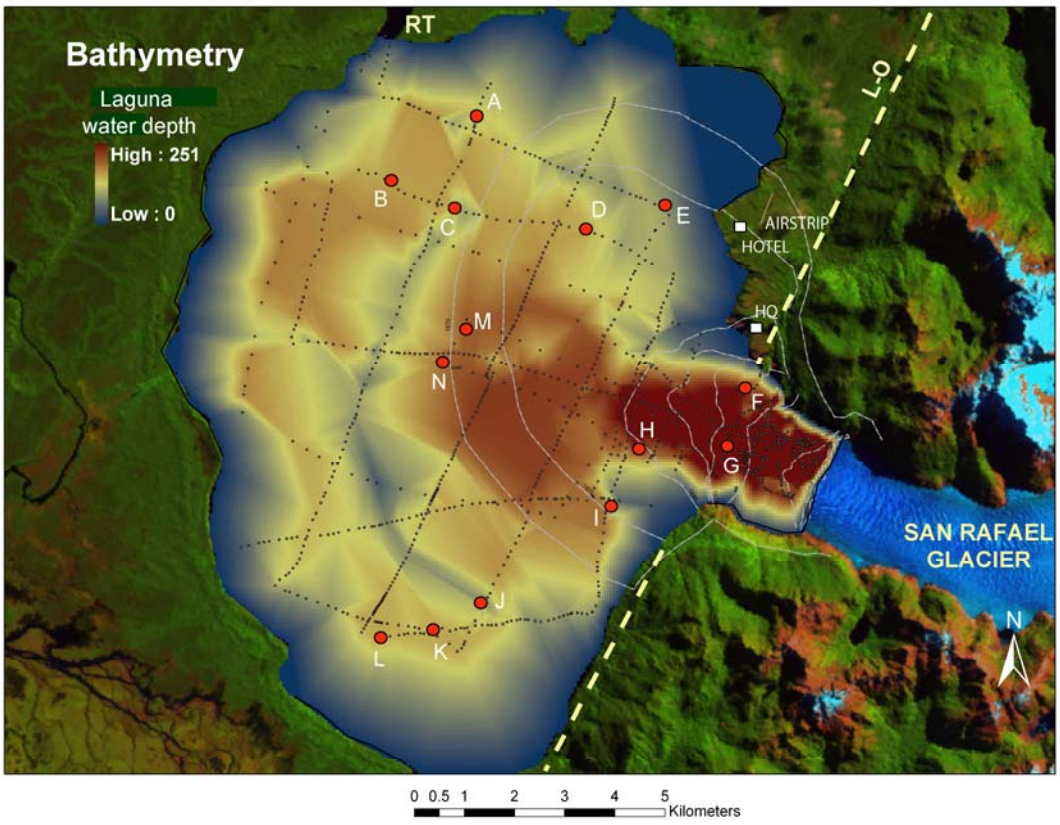

Figure 5.2 Bathymetry of Laguna San Rafael, including tracklines from the acoustic profiles, and the location of seismic images A-N in Figures 5-10.

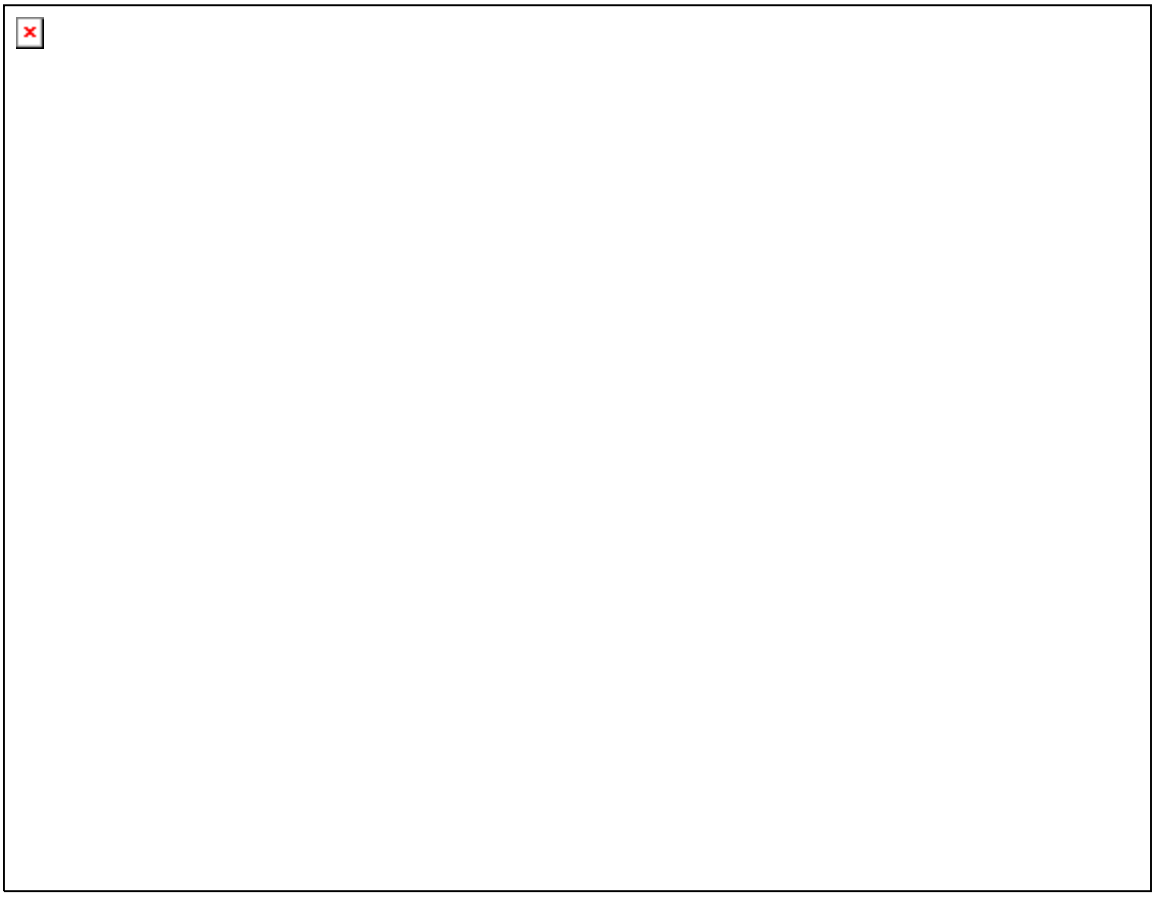

Figure 5.3 Total sediment accumulation in Laguna San Rafael from the most recent advance and retreat, including spot depth measurements along tracklines

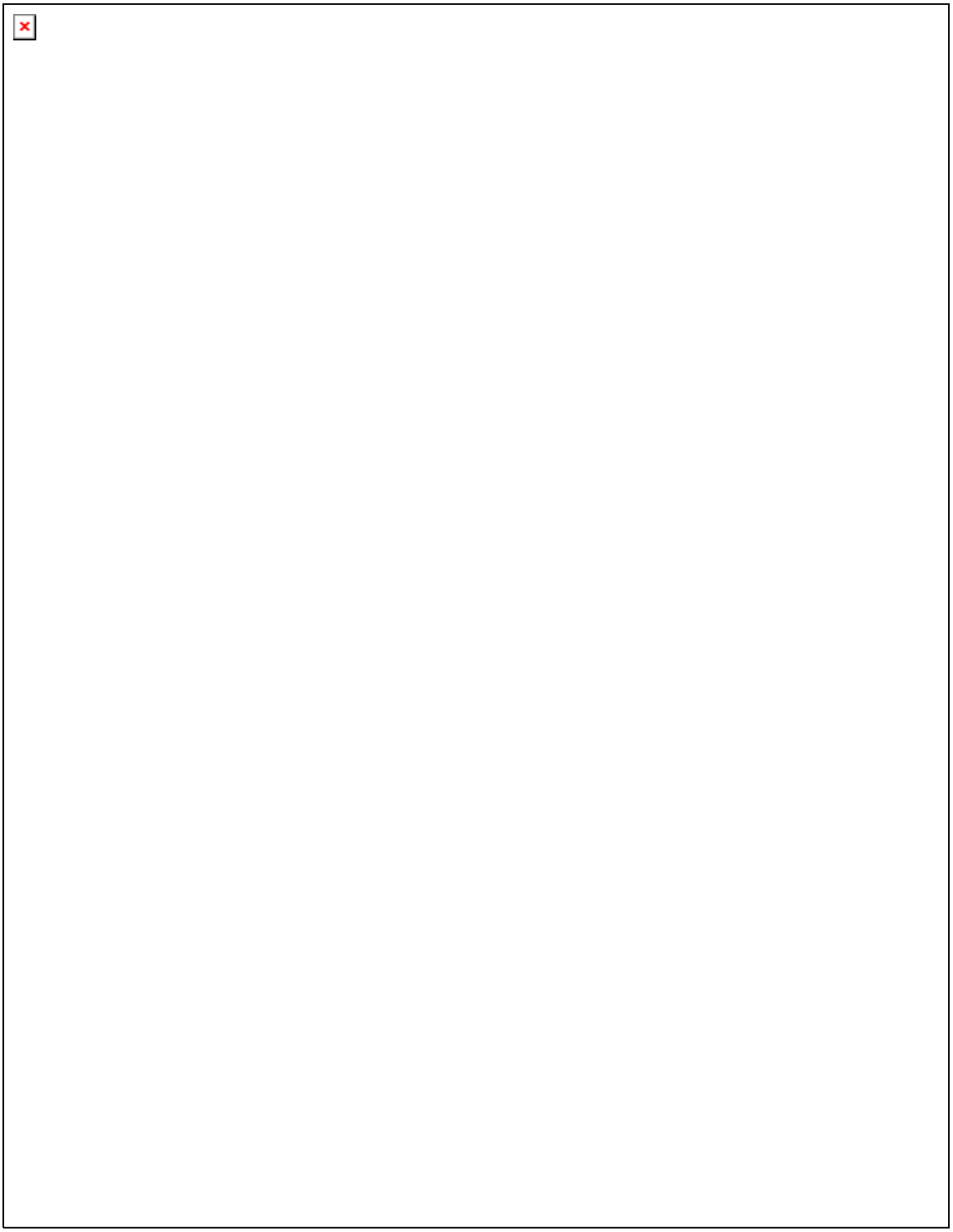

Figure 5.4 Post-glacial sediment accumulation, superimposed with bathymetric contours

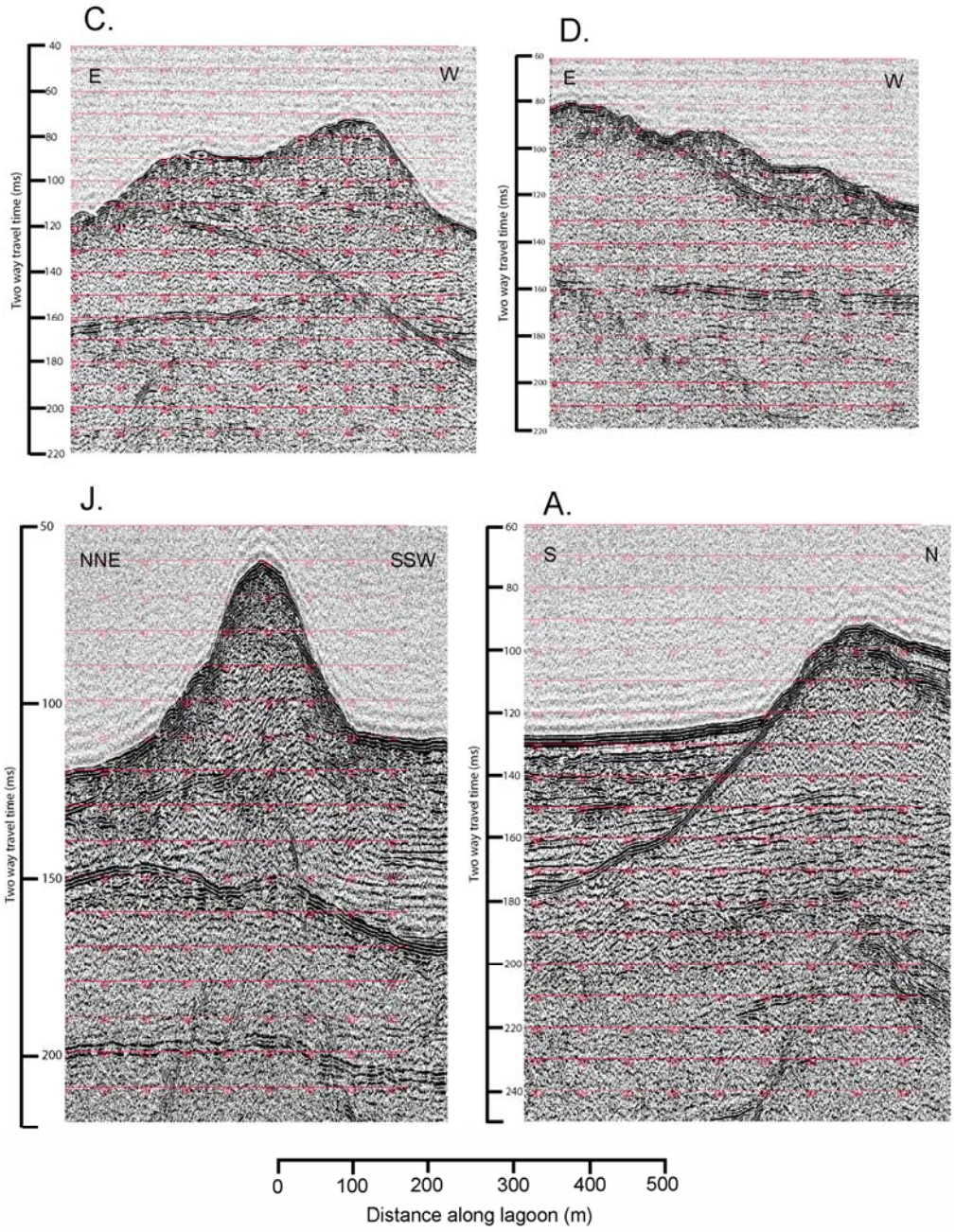

Figure 5.5 Representative seismic profiles of moraines in Laguna San Rafael. See Figure 5.2 for the location of the profiles. The two-way travel time was converted to sediment depth assuming a seismic velocity in glacimarine sediments of 1680-1740 m/s, so that 100 ms is equal to 84-87 m of sediment. Many of the moraines overly a strong, planar reflector, interpreted as the surface compacted by the previous glacier advance. A laminated facies

onlaps the distal face of the moraines, suggesting rain out of distal fines as the glacier front pulled away from the moraine.

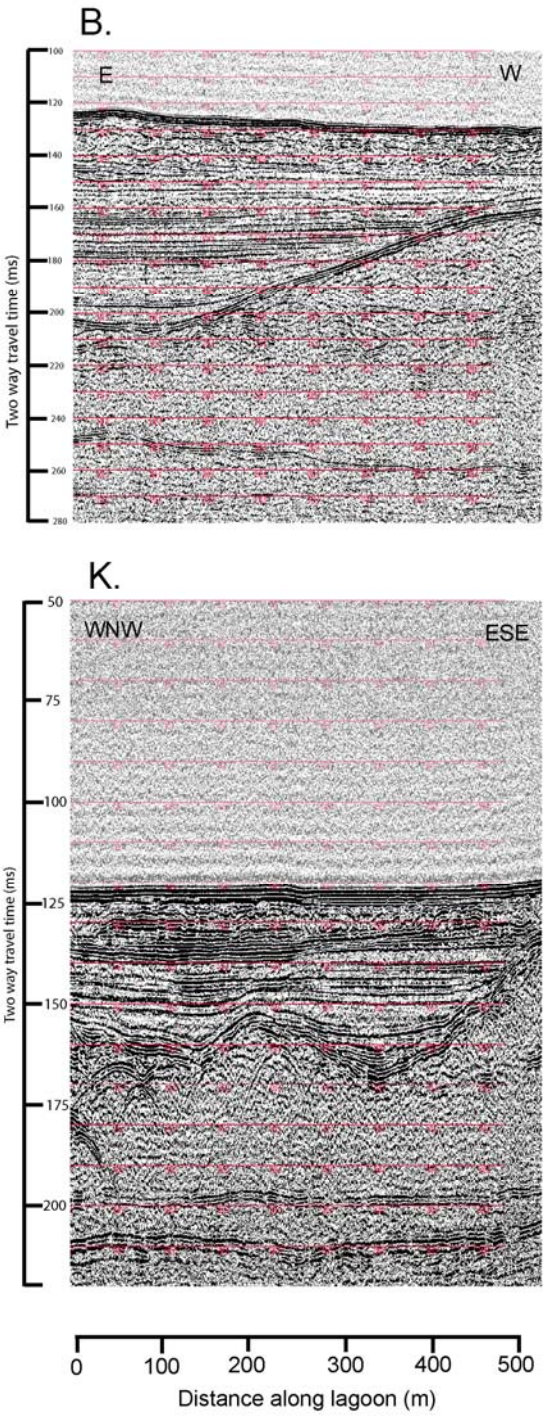

Figure 5.6 Seismic profiles of laminated sediments in Laguna San Rafael, interpreted as ice-distal deposits. The subhorizontal laminated sediments overlap either a hummocky facies (K) interpreted as ice-proximal deposits, of a distinct planar reflector, interpreted as the ice surface compacted by the prior advance.

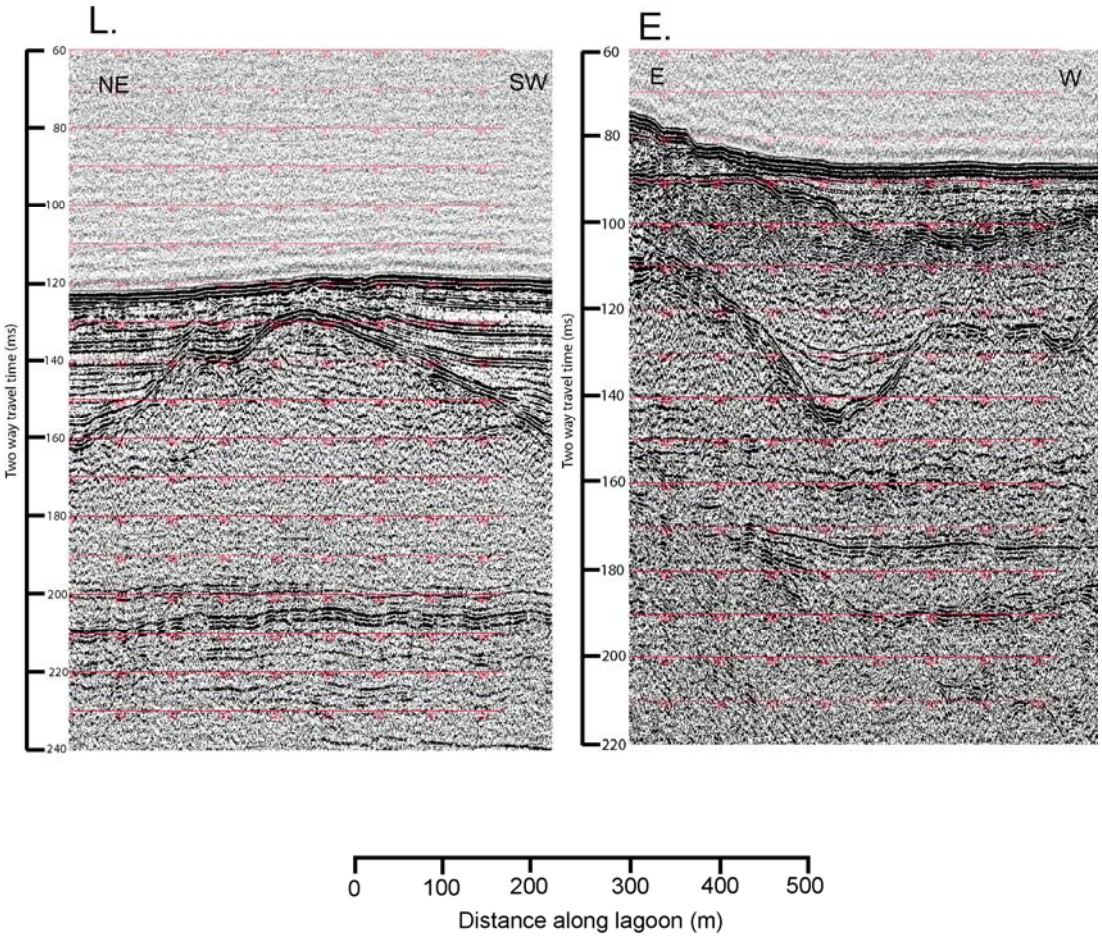

Figure 5.7 Seismic profiles of buried moraines in Laguna San Rafael, reflecting standstills during recession, followed by significant draping of distal fines over submarine topography.

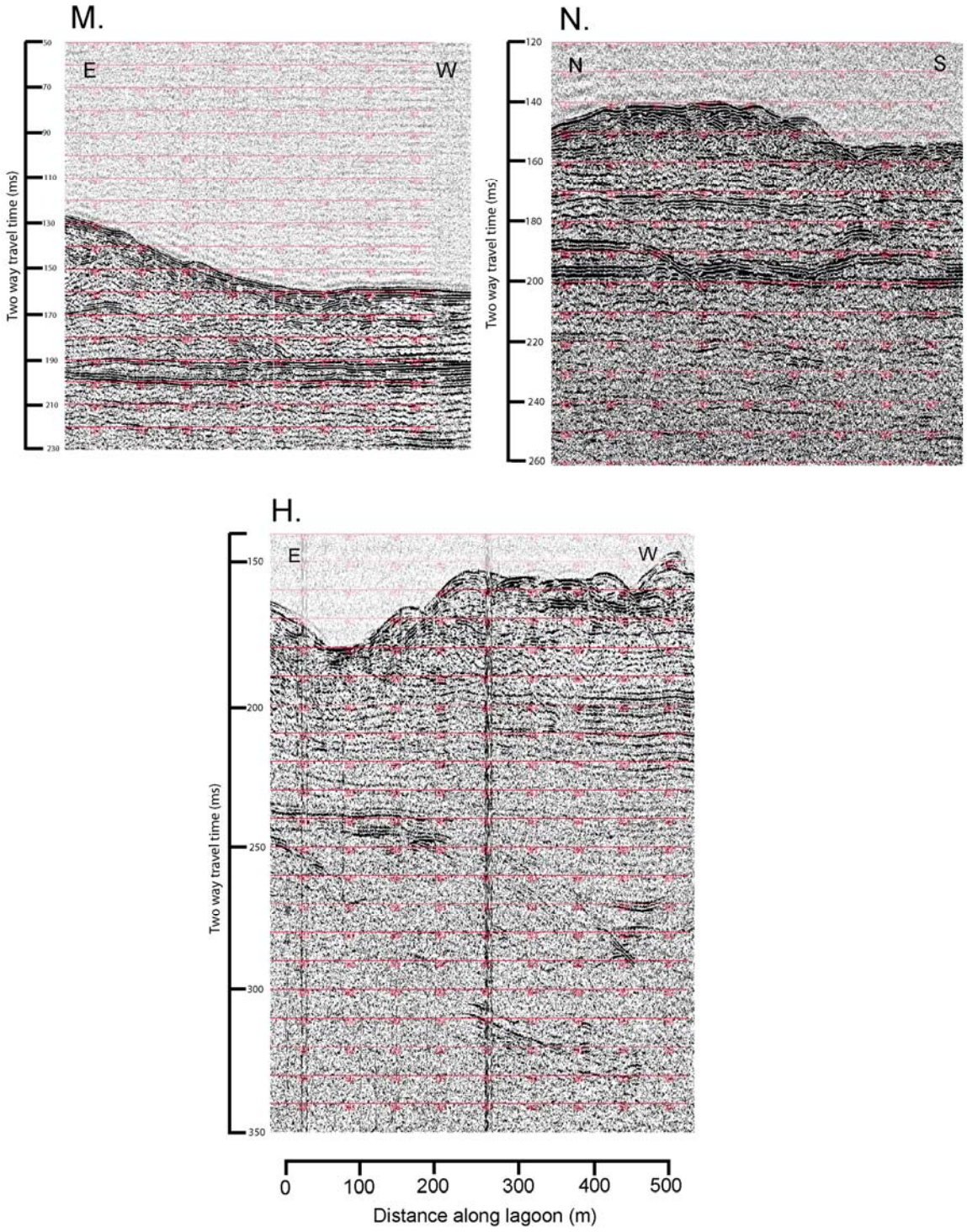

Figure 5.8 Seismic profiles of ice proximal deposits in Laguna San Rafael. The ice proximal facies is characterized by hummocky, chaotic reflectors overlying a distinct planar reflector.

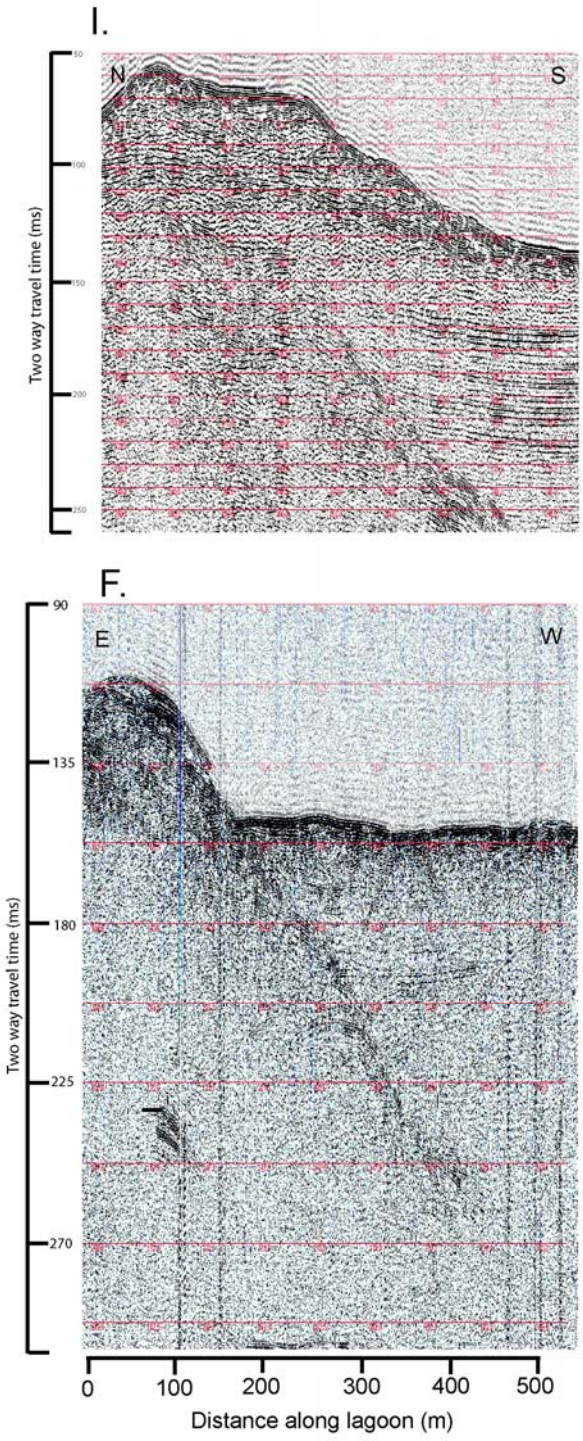

Figure 5.9 Seismic profiles across the Liquine-Ofqui fault scarp (F) and associated slump deposits along the rangefront (I) .

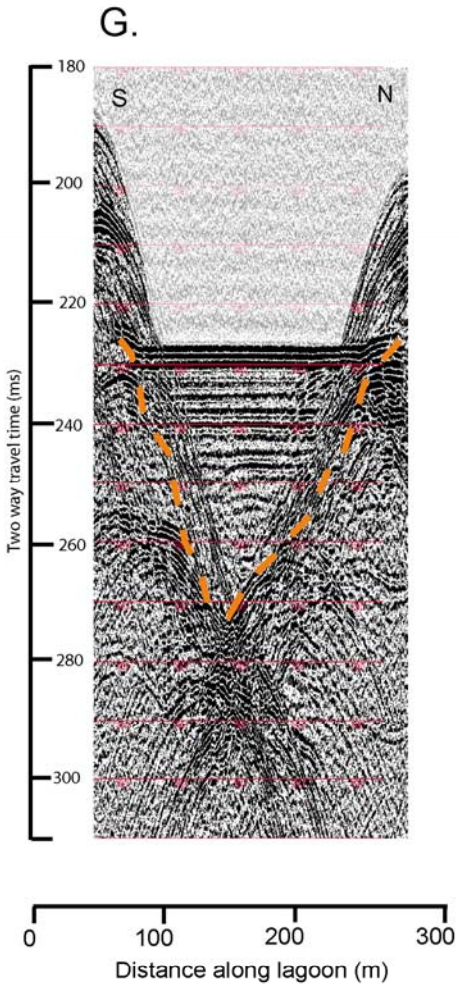

Figure 5.10 Seismic profile across a bedrock channel filled with ice-distal deposits. The channel is located in the inner fjord, close to the terminus position in 1979.

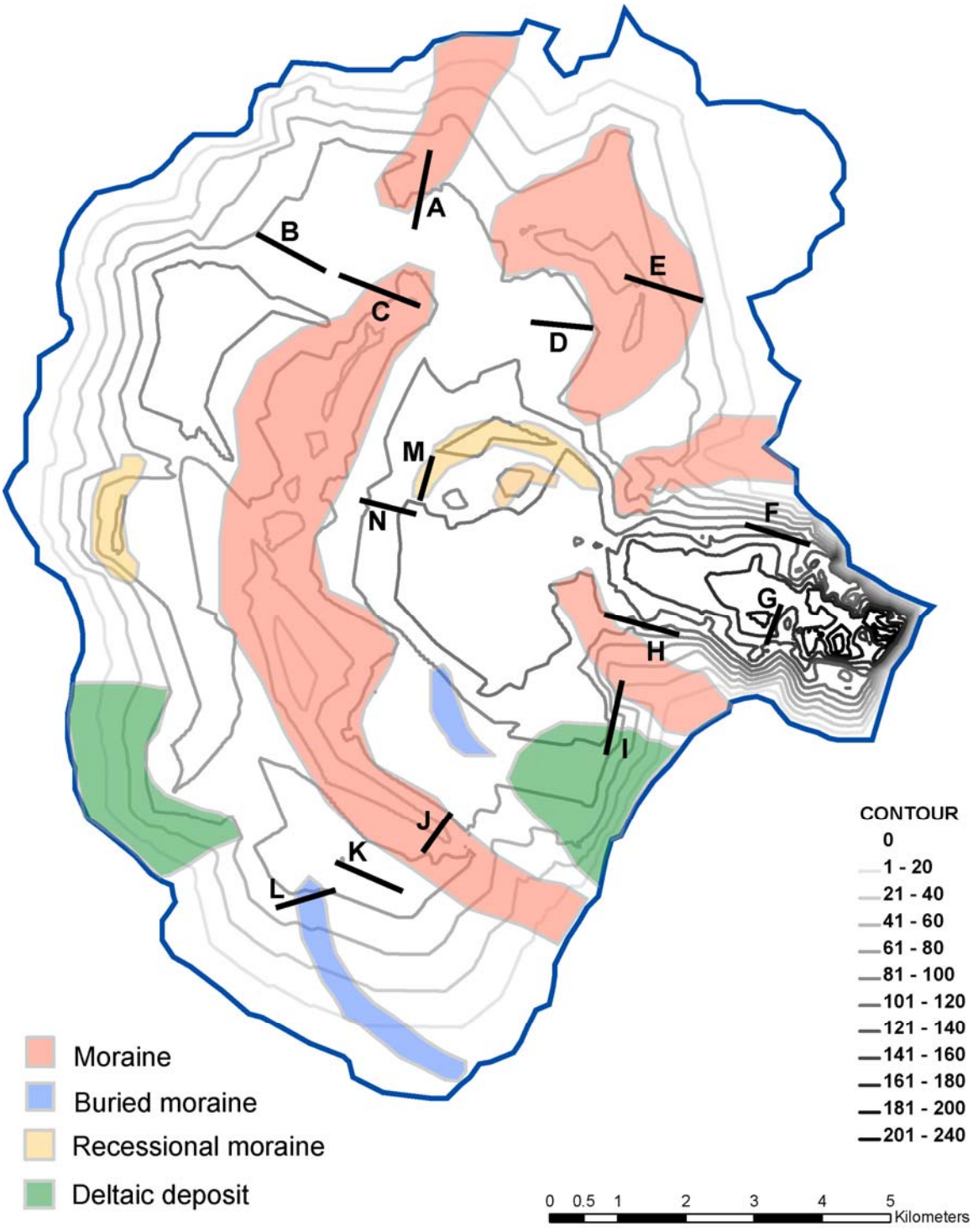

Figure 5.11 Distribution of the major submarine landforms in Laguna San Rafael

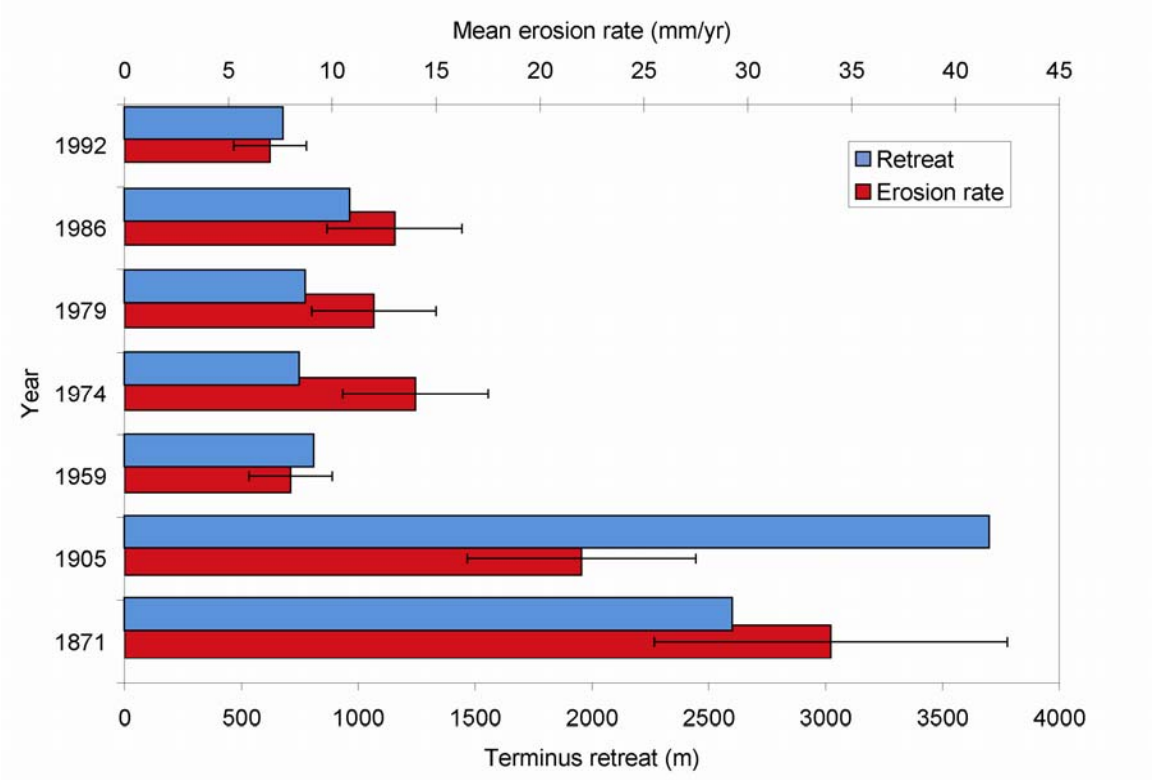

Figure 5.12 Rate of erosion (top axis) and retreat of the terminus (bottom axis) averaged over selected time intervals since the Little Ice Age synthesized from published terminus positions and sediment volume measurements. The year (y-axis) indicates the start of each period of measurement.

CHAPTER 6.

Recent erosion rates at Tyndall Glacier, Southern Patagonian Icefield

The icefields of the Patagonian Andes currently comprise the most extensive concentration of ice outside of the polar ice sheets (Dyurgerov and Meier, 1997). The icefields, and the glaciers that drain them, are situated along a dramatic latitudinal band that stretches from the Northern Patagonian Icefield (HPN) at 46ºS to the Cordillera Darwin at 55ºS. The vast majority of the glaciers that drain the icefields are currently thinning and retreating, reflecting a regional shift in climate (Rignot et al., 2003), with a potential for large changes in contemporary glacial erosion. The dramatic retreat of glacier termini along and across the icefields have been measured from repeat aerial photography and satellite images over the past few decades (Aniya et al., 1997; Rivera et al., 2005), and a few of the glaciers have been the subject of direct measurements of ice thickness and ice motion, but little is known about the sediment yields generated from this dynamic body of ice. In this study, I was able to capitalize on several prior studies of ice front bathymetry, ice motion and terminus change from a glacier in the middle of this latitudinal transect, Tyndall Glacier. Benefiting from the one location in the Patagonian icefields where ice thickness and ice motion near the ELA of a glacier have been measured successfully, I could rely on direct measurements of ice flux, and hence did not have to estimate ice fluxes via modeling. Building on these prior measurements, I calculate recent erosion rates, ice loss and ice fluxes through Tyndall Glacier in the early 21st century, and compare these to measurements of glacial erosion and ice loss from the San Rafael and Marinelli glaciers, at the northern and southern ends of the transect.

Tyndall Glacier drains the southeastern corner of the Southern Patagonian Icefield (Campo de Hielo Patagonico Sur, or HPS) at 51º15’ S, 73º16’ W, within Torres del Paine National Park. Not to be confused with its namesake glacier in Icy Bay, Tyndall Glacier in Chile calves into two freshwater lakes: the main portion of the glacier terminates in a 2 km wide calving front in Lago Geike, while a small lobe along the eastern margin calves into smaller Lago Tyndall. For the purposes of this study, any sediment accumulation and calving into Lago Tyndall was neglected, due to its minute size. Lago Geike is an overdeepened basin that formed as the glacier receded from the

moraines created during late Holocene Neoglacial advances (Naruse et al, 1987; Rivera and Casassa, 2004), the most recent of which occurred ~300 years ago (Aniya, 1995). The lake drains through a spillway at ~30 m.a.s.l. in its southeast margin. Observations of wave-cut beaches and boulder lags in the spillway indicate that lake levels fluctuate around 1-2m, when icebergs periodically block the spillway.

In this study, I took advantage of a bathymetric survey of the lake collected in March 2001 by Bernard Hallet, which we resurveyed in March 2005. The difference between the two bathymetric surveys was used to estimate volumetric differences in sediment near the ice front, and in turn estimate the average annual sediment yield and basin-wide erosion rate from the glacier during the 2001-2005 period. The bathymetry of the lake was also used to estimate volumetric ice loss from the front of the glacier between 2001 and 2005, and compare recent changes to prior observations of thinning and retreat of the glacier between 1945 and 2002 (Rivera and Casassa, 2004).

In focusing efforts on Tyndall Glacier, I was also able to benefit from measurements of ice thickness and motion collected by Japanese researchers in the 1980s (Naruse et al., 1987) and Chilean and U.S. researchers in 1999, 2001 and 2002 (Casassa and Rivera, 1998; Raymond et al., 2005). The overlap in timing between the ice thickness measurements and our repeat bathymetry provides the opportunity to compare the sediment flux out of the glacier estimated from the bathymetric surveys to the ice flux through the ELA of the glacier, at the turn of the century.

Calculating sediment accumulation in Lago Geike

The bathymetric surveys of 2001 and 2005 were conducted with a sonar depth profiler (commonly known as a ‘fish finder’) deployed from a zodiac. An effort was made to repeat tracks as closely as possible between the surveys in the zone close to the ice front (Fig. 6.1). In 2001, the location of the tracks were collected with a handheld Garmin GPS, and the depth profiles measured with a single-channel sonar, which had a detection limit of 350 m. The 2001 survey indicated that maximum water depths in the center of the lake near the ice front exceeded the detection limit of the sounder. In 2005, a Lowrance 18-C acoustic profiler with incorporated GPS and a dual channel 50/200 Hz transducer was used, which had a detection limit of >500 m water depth. The 2005 survey indicated that maximum water depths reached 415 m within 1 km of the ice front

at the center of the fjord (Fig. 6.2), the deepest by far of all the fjords surveyed for this project.

From the two surveys, bathymetric maps were generated by triangulating between known depths along the tracklines using the TIN function in ArcGIS (Figs. 6.3, 6.4). As the general triangulation method may introduce significant error (~20%) between known depths (for analysis of error see Chapter 1) that would be compounded in comparing two TIN surfaces taken at different times with different tracklines, it was decided that only the cross-profiles from the surveys where the tracklines overlapped to within 50m in XY space would be used for comparing depths. Lake depths between these overlapping profiles were then estimated by triangulation in the zone where there were measurable differences in depth between 2001 and 2005. The error in the newly triangulated depths is ~15% (calculated by comparing the estimated depth in the 2005 surface between the overlapping profiles to direct measurements of depth from 2005 profiles that did not fall within the overlap criteria). Outside of the deep central section of the lake there was no difference in depths observed from 2001 to 2005. A difference in the bathymetry, with a noticeable shallowing of lake depths by sediment infilling in 2005 was evident in the first two km from the ice front (Fig. 6.5), with no measurable difference further out in the lake.

Sediment flux and ice loss from Tyndall glacier, 2001-2005

A total sediment volume of 3.2×10^7 m^3 accumulated within 2 km of the ice front between 2001 and 2005, averaging 8×10^6 m^3 per year. The current basin area of Tyndall Glacier, measured from the SRTM DEM, is 408 km^2 (Fig. 6.6). Dividing the annual sediment flux by this basin area, and accounting for the difference in density between lake sediments and bedrock, the basin-wide erosion rate from Tyndall glacier for 2001 to 2005 averaged 14 ± 3 mm/a. This rate is similar to the average erosion rate over the past 40 years from San Rafael glacier, a significantly larger system to the north, and up to 9 times less than erosion rates during the last few years from Marinelli glacier to the south. Assuming that this recent erosion rate is not significantly greater than the average erosion rate from the glacier since it started to retreat, this result suggests that Tyndall glacier currently ranks among the most erosive glaciers worldwide, on par with the largest tidewater glaciers in Alaska (Fig. 8.1 in Summary).

The areal extent of ice lost from the terminus during this period was 1.63 km^2, an average of 0.405 km^2/a. This matches average ice losses from the terminus of 0.5 km^2/a estimated by Rivera and Casassa (2004) during the 1990s, continuing the trend of accelerated retreat since 1945 (Raymond et al., 2005). The volume of ice lost from the glacier snout since 2001 was 0.145 km^3,or 3.6 x 10^7 m^3/a. The volume removed from the terminus is almost an order of magnitude less than the minimum estimate of annual volume of ice lost via thinning at the glacier surface, 3.3 x 10^8 m^3/a, estimated from mean thinning rates of 2.8 m/a in the center of the glacier (Raymond et al., 2005) applied over the entire ablation area, ~120 km^2 (Nishida et al., 1995).

Ice flux out of Tyndall glacier, 2001-2005

Direct measurements of ice motion and ice thickness on Tyndall Glacier were collected in 1985, 1999 and 2002 at two locations on the glacier: at 420 m.a.s.l. (9 km from the 2000 terminus) (Raymond et al., 2005), and at 700 m.a.s.l. (14 km from the 2000 terminus, and 200 m below the equilibrium-line altitude (ELA), estimated at 900 m (Nishida et al., 1995)). Using a 2MHz impulse ice-penetrating radar, the centerline ice thickness at the upper profile, near the ELA, was 740 m in 1999; at the lower profile, the centerline thickness in 2002 was about 530 m. (Raymond et al., 2005). Short-term ice surface velocity measurements near the centerline of the upper profile show a decrease in flow speed from 700 m/a in 1985 (Naruse et al., 1987), to 550 m/a in 1995 and 430 m/a in 2000 (Rignot, unpublished work based on InSAR), to 350 ± 10 m/a in 2002 (Raymond et al., 2005). Although the steady decrease in flow speed is over the past two decades is intriguingly similar to decreases observed at San Rafael glacier during the same period, observations of large seasonal variability in speeds at Tyndall Glacier (Nishida et al., 1995), speculated to be controlled by changes in sliding processes across a hard bed (Raymond et al., 2005), suggest that these short-interval measurements should be interpreted with caution. However, the sole inter-annual surface velocity measurement, based on a rock marker located at the lower profile and surveyed over a two-year period from 2000 to 2002, estimated an average speed in the ablation zone of 323 ± 10 m/a, within the range of summer flow speeds measured in 2002 (Raymond et al., 2005).

Raymond et al. (2005) calculated a theoretical maximum ice speed of 243 m/a and a width-averaged and cross-section averaged speed of the glacier at the upper profile of 130 m/a, assuming Glen's flow law for temperate ice (Paterson, 1994), no basal slip, and a surface slope of 0.03. Using similar parameters and recalculating the cross-section averaged ice speed to reflect the actual surface speeds measured (~330 m/a), then multiplying this speed by the width (7 km) of the glacier and the width-averaged depth of the ice estimated from the radio-echo traverse (Fig. 6.7), the ice flux near the ELA can be estimated to first order. By these estimates, the ice flux through the glacier near the ELA (~14 km from the terminus) in 2002 was ~8.3 x 10^8 m^3/a. The average annual loss of ice from the terminus in 2001-2005 hence was ~4% of total ice flux through the system; the annual loss of ice via thinning is ~40% of this flux.

Implications

That the rate of thinning of Tyndall Glacier approaches half of the total ice flux suggests that the glacier has been experiencing a strong negative mass balance over the past decade (or more). The flux of ice through the ELA at Tyndall glacier in 2001-2005 is approximately 6 times less at San Rafael in 2001, yet the average erosion rate from Tyndall during 2001-2005 is 1-2 times greater thanat San Rafael for the same time period (Fig. 4.15 in Chapter 4). One possible reason for this difference is bed lithology: San Rafael glacier is underlain by the highly resistant granites of the North Patagonian Batholith, whereas Tyndall Glacier overrides more erodable marine sedimentary sequences and conglomerates of Upper Jurassic to Cretaceous ages, with outcrops of rhyolites and andesitic lavas of the Tobifera Formation (SERNAGEOMIN, 2003). Contrary to observations made at Columbia glacier (Van der Veen, 1996) over the past two decades and more recently at the outlet glaciers of Greenland (e.g., Rignot and Kanaparatnam, 2006; Howat et al., 2005; Krabill et al., 2004), and similar to observations at San Rafael, ice velocities at Tyndall glacier appear to have slowed as the glacier continued to thin and retreat over the past few decades. This is perplexing, as one would assume that ice flux to the terminus would be increasing in response to the continued thinning of the glacier surface and the steepening of the upstream surface profile (Raymond et al., 2005). The impact of the increase in water depth at the calving front over the past decade would also lead one to assume that, if calving is a function of

water depth, calving rates and longitudinal stretching rates have increased during this time. Perhaps the drop in ice flux is indicative of an increasingly efficient basal hydrologic system over a hard bed delivering meltwater to the terminus without an commensurate increase in basal ice motion.

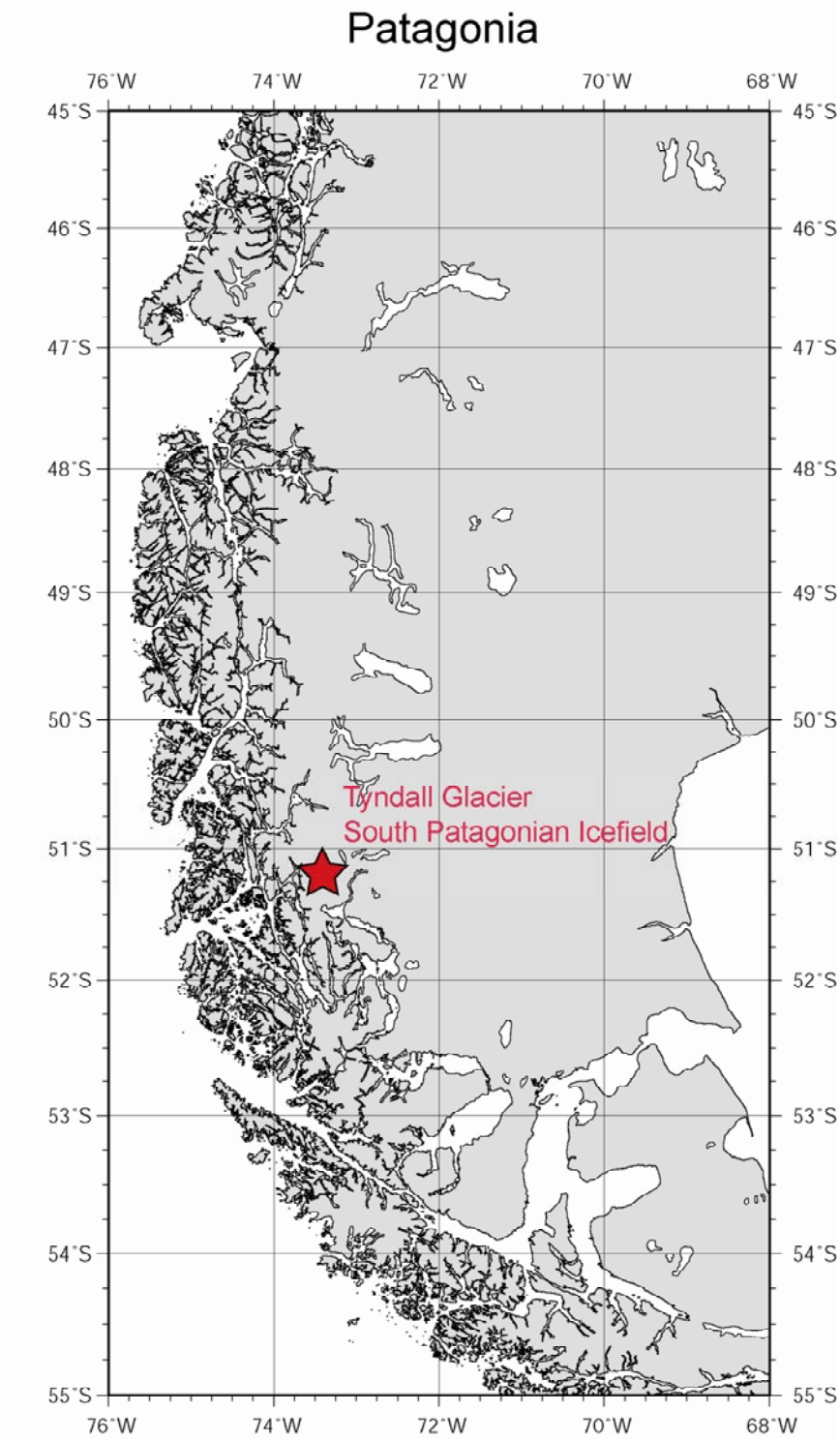

Figure 6.1. Location of Tyndall Glacier, South Patagonia Icefield.

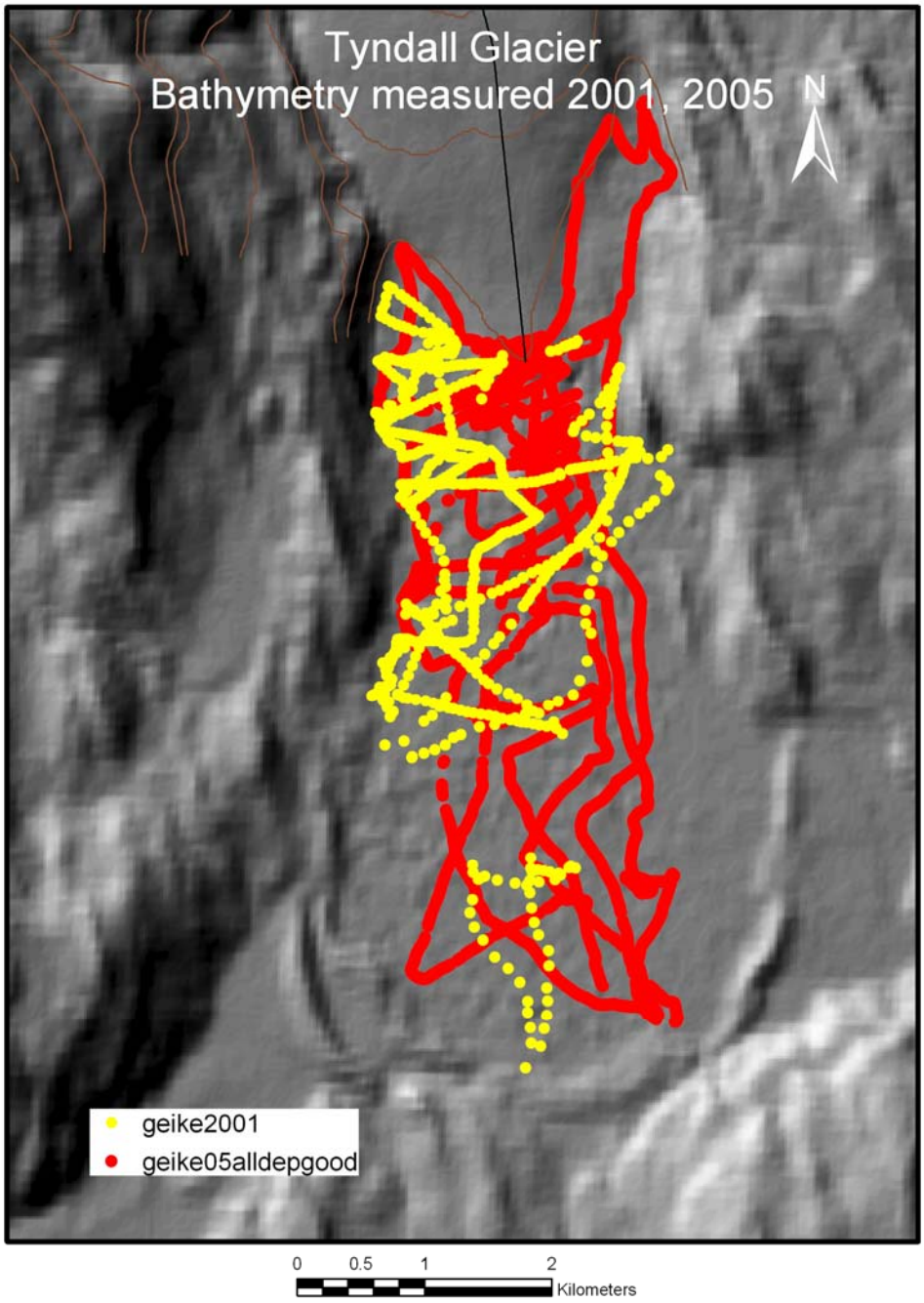

Figure 6.2 Tracklines of the 2001 and 2005 bathymetric surveys superimposed on a shaded-relief DEM of Lago Geike. Spot depth measurements from the 2001 survey are in yellow; depths measuremed in 2005 are in red.

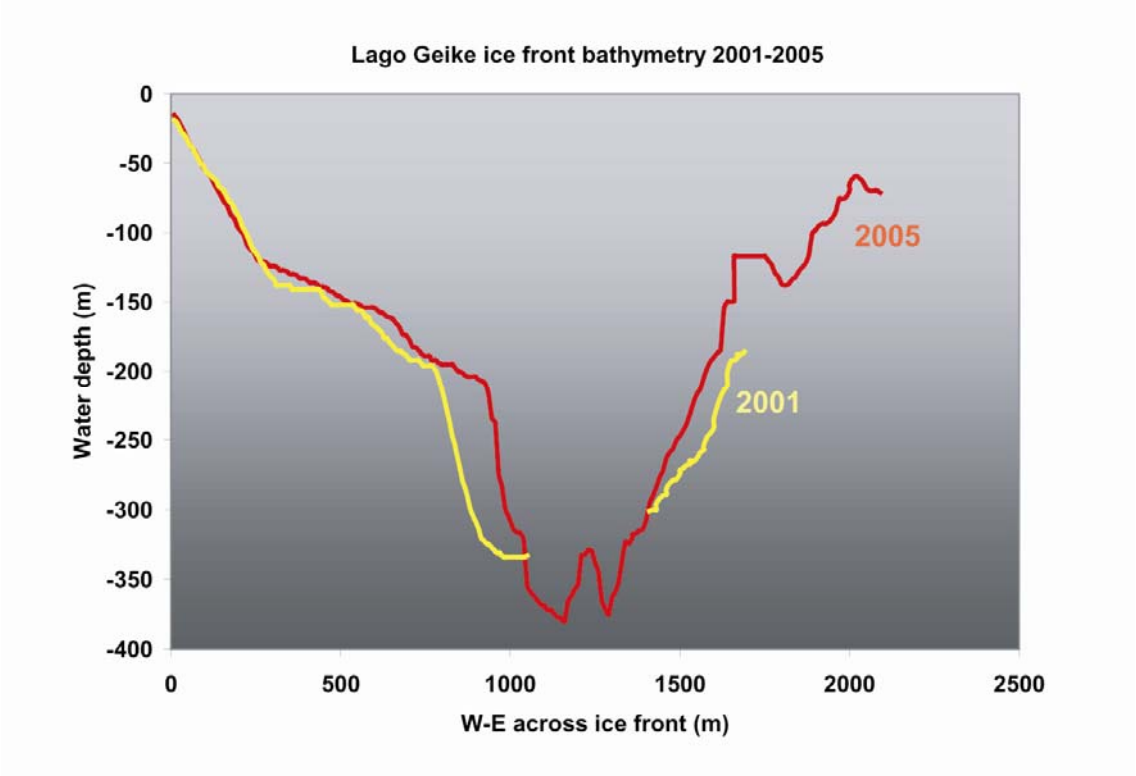

Figure 6.3 Cross section of the bed of Lago Geike across the ice front in 2005, as determined from acoustic soundings in 2001 and 2005. The 2001 profile is in yellow, the 2005 profile in red. Location of the profile in marked in black in Figure 3.

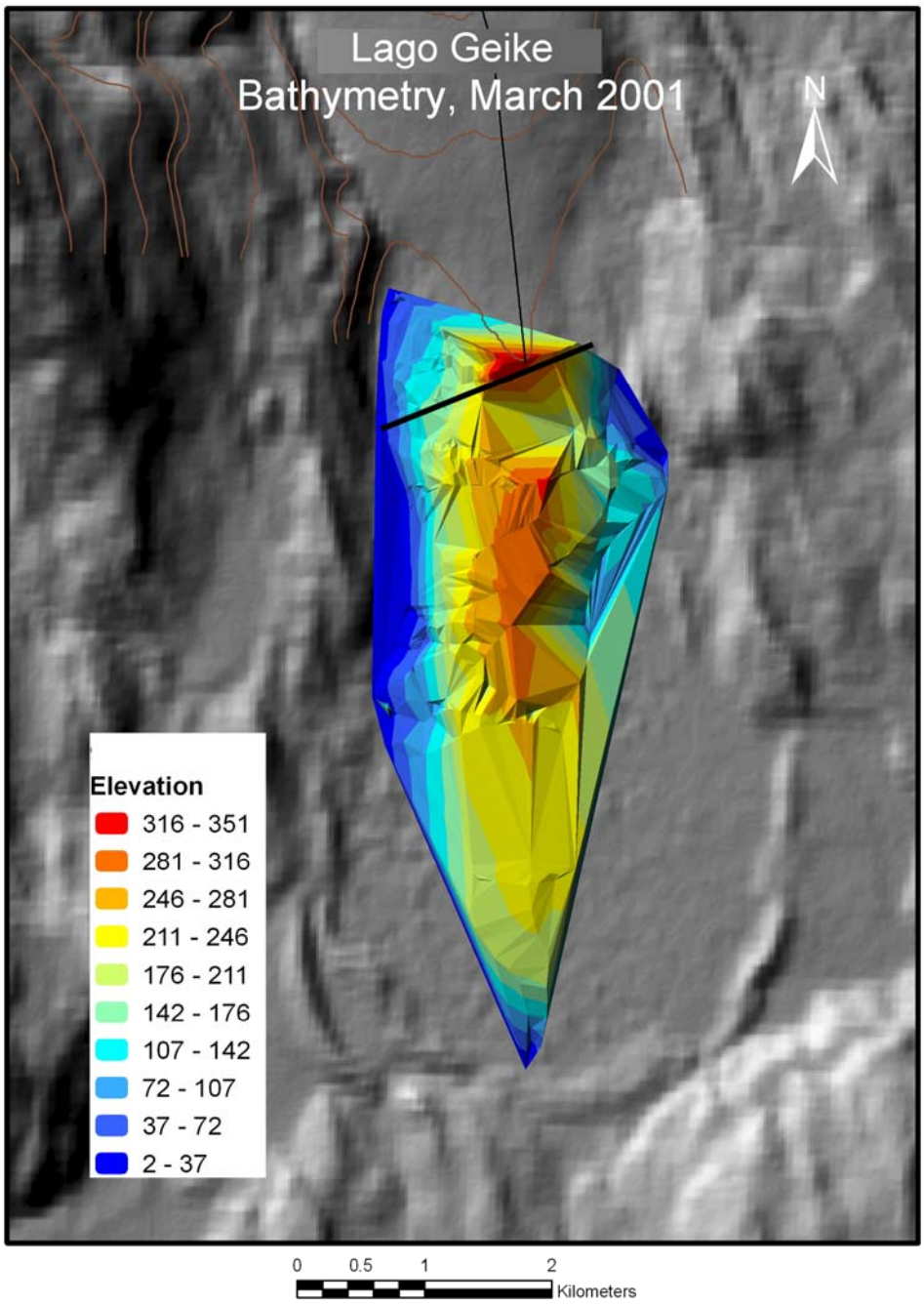

Figure 6.4 The bathymetry of Lago Geike in March, 2001 determined from acoustic soundings along tracklines (yellow dots in Fig. 1) and interpolated between known depths using a triangulated irregular network (TIN). Black line is the profile in Figure 2.

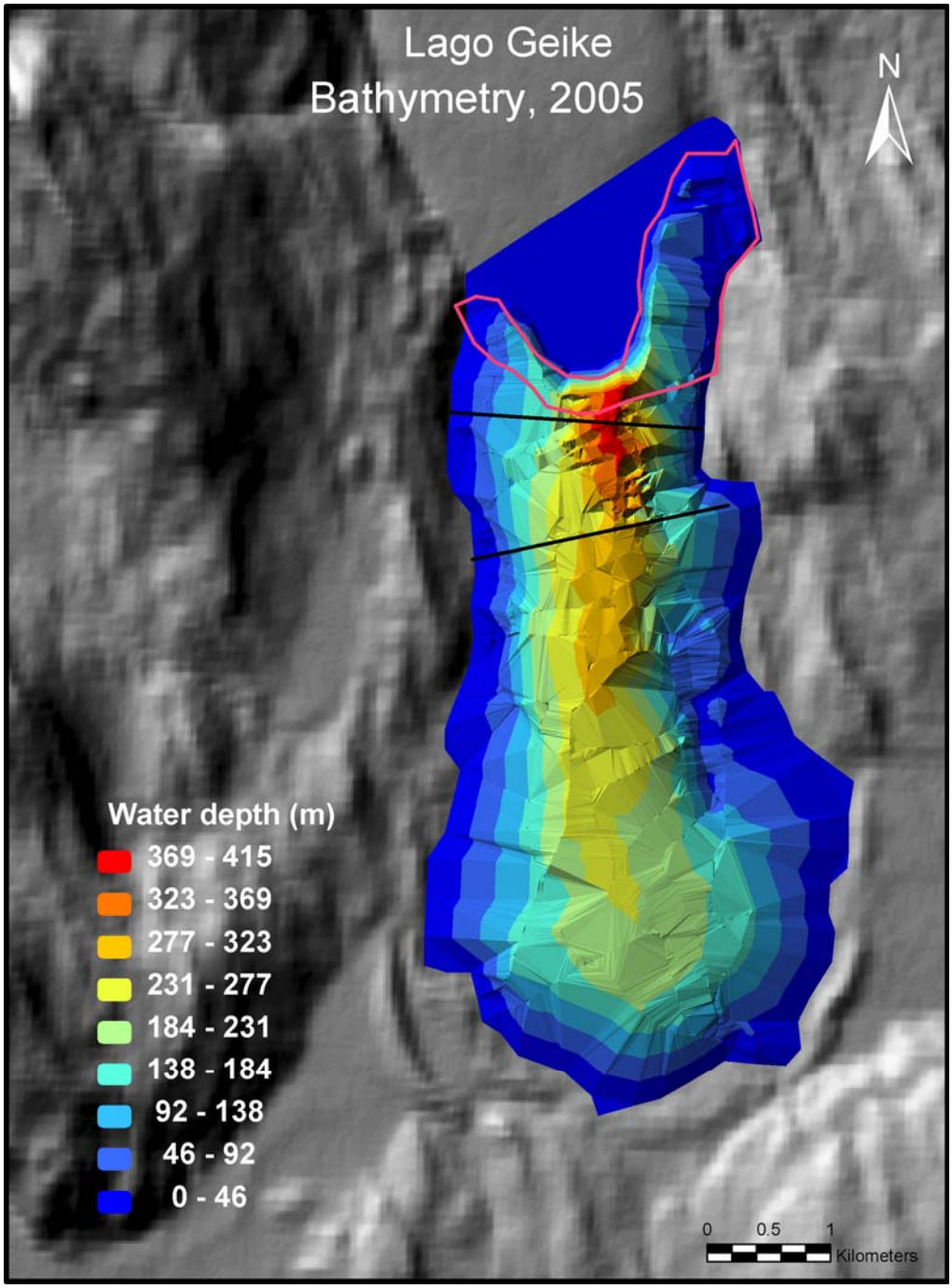

Figure 6.5 The TIN bathymetry of Lago Geike in March, 2005 determined from acoustic soundings along the tracklines (red dots in Figure 1) and interpolated between known depth. Red polygon delineates the ice lost from the terminus between 2001 and 2005. Black lines indicate location of profiles in Figure 5.

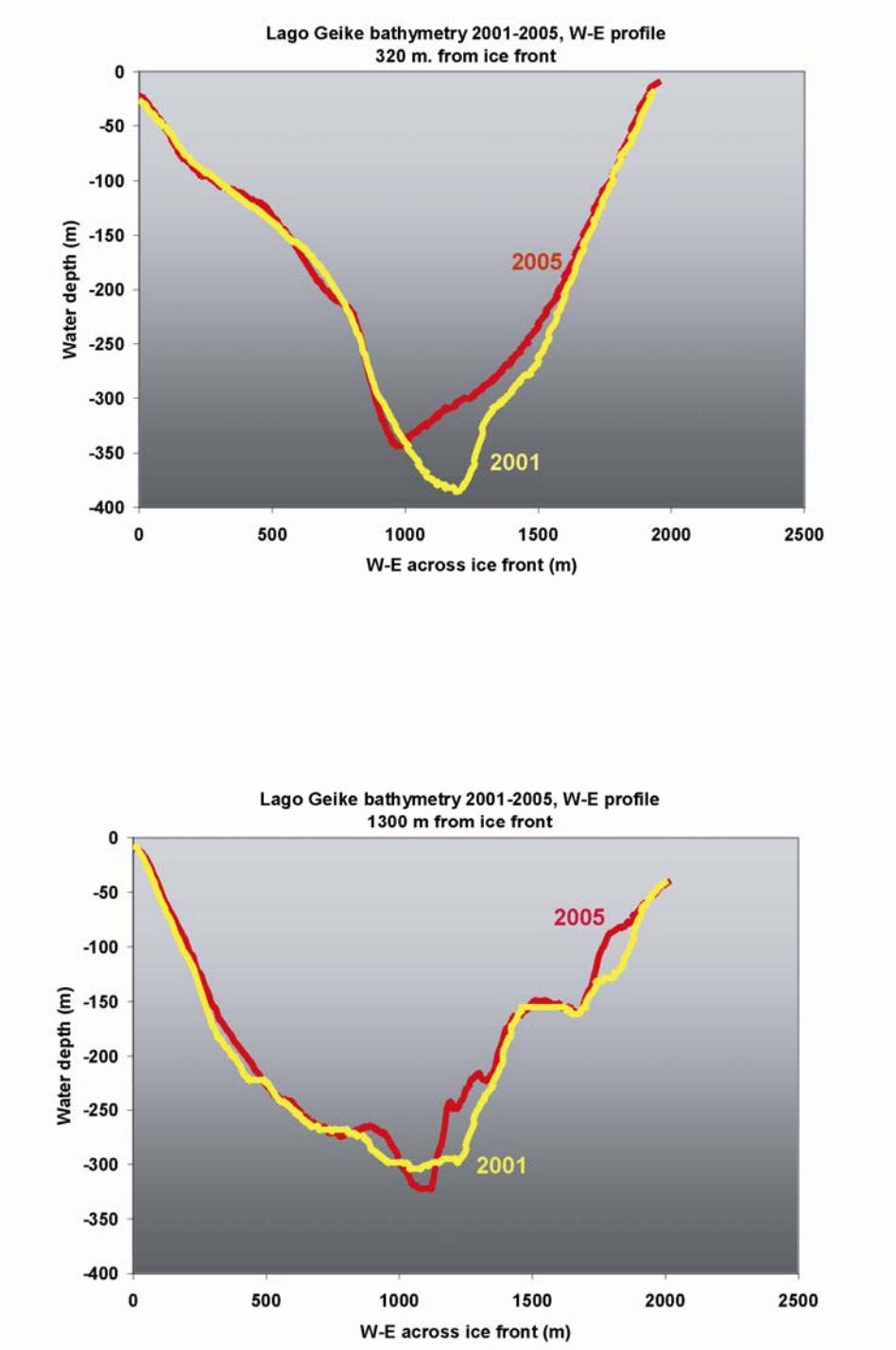

Figure 6.6 Profiles of the bed across Lago Geike, as determined from acoustic soundings in 2001 (yellow) and 2005 (red). a) Cross-section at 320 m from the 2005 ice front. b) Cross section 1300 m from the 2005 ice front.

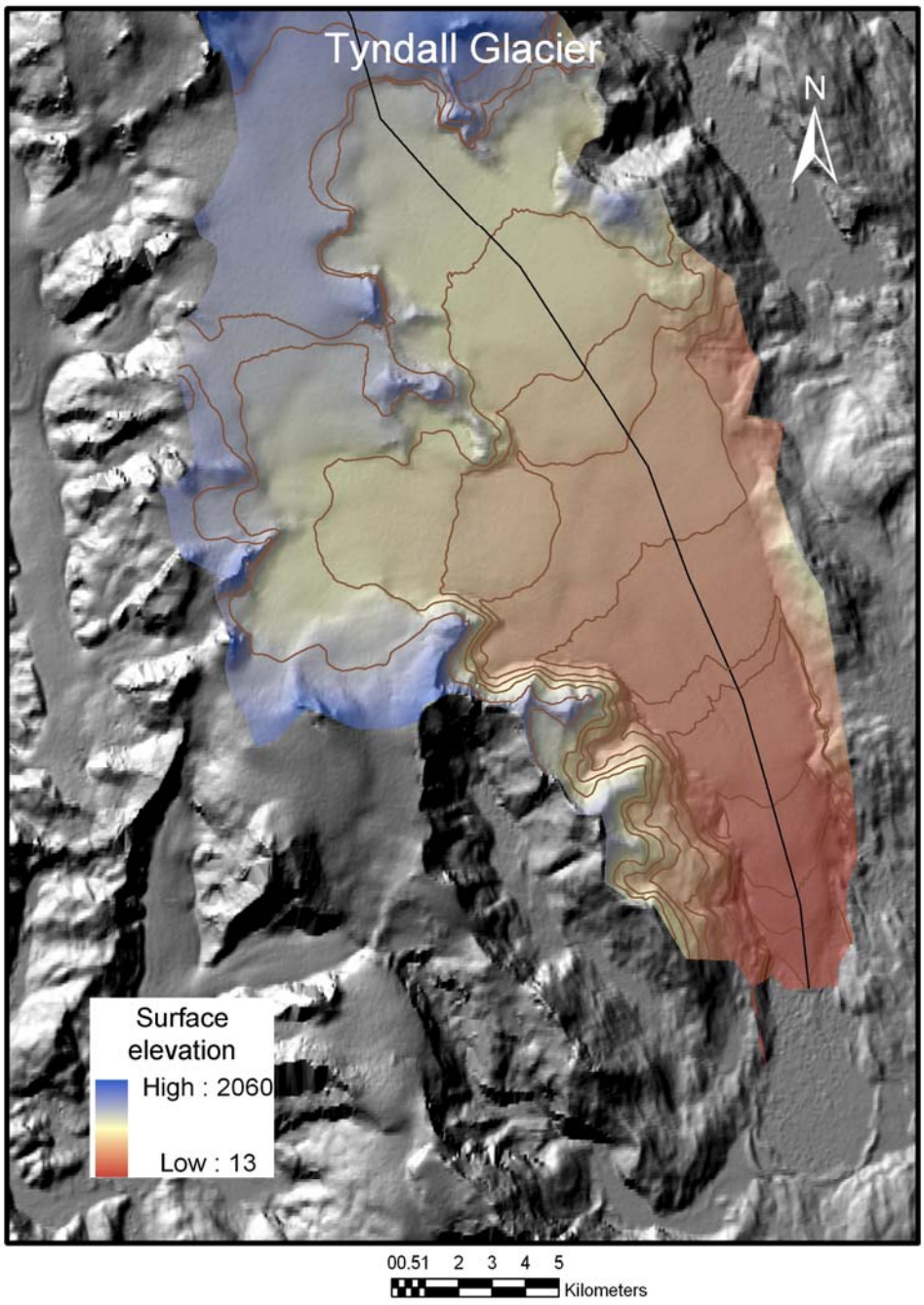

Figure 6.7 DEM of Tyndall Glacier, derived from the 30m global SRTM DEM dataset. Brown contours indicate 50m increments on the glacier surface, with elevation bands indicated in colour. The surface area of the glacier is 418 km^2, the basin area is 403 km^2. Lago Geike is in the bottom right hand corner of the image.

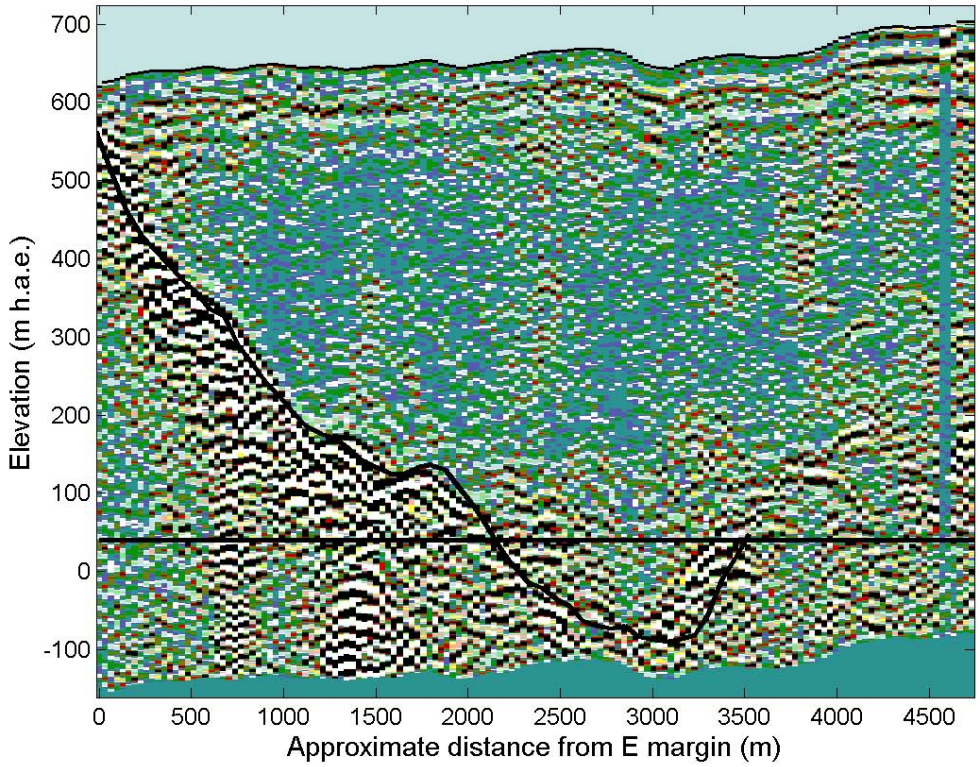

Figure 6.8 Cross-section of Tyndall glacier at 700 m.a.s.l. revealed by radio-echo sounding traverse of the eastern half-width of the glacier (Fig. 2 from Raymond et al. (2005)). The centerline is 740 m deep.

CHAPTER 7.

Exhumation rates from glaciated basins in the Patagonian Andes

The short term (10^1-10^2 yr) erosion rates from temperate, glaciated basins presented in the previous chapters, based on recent sediment yields into Alaskan and Patagonian fjords, appear to exceed 10 mm/a and are some of the fastest rates measured worldwide (Hallet et al., 1996). This suggests that temperate glaciers are exceptionally erosive and capable of easily keeping pace with rock uplift in active orogens, thereby acting as a buzzsaw, at least on centennial time scales. If the rapid pace of the erosion suggested by these short term rates persist over orogenic time scales (10^5 - 10^7 yrs), glaciers are indeed a major climatic driver with the potential to shape mountain belts.

Given the role of erosion in the partitioning of strain and the thermal structure of orogenic belts (e.g., Koons et al., 2002), understanding how fast glaciers erode over full glacial-interglacial time scales, approaching 10^4-10^6 yrs, is needed to elucidate the interaction of tectonics and climate. If glaciers are indeed acting as topographic buzzsaws, they should produce clear patterns of denudation ofnglacial and orogenic time scales, with denudation rates increasing as a function of the period of glacial occupation. Recent advances in low temperature thermochronometry have yielded estimates of the importance of glacial erosion on these orogenic time scales. These studies take advantage of the low temperature crystallization threshold of radiometric thermochronometers such as helium, argon, and apatite and zircon fission tracks to estimate the time since rocks cooled beyond the threshold until they arrive at the surface, i.e., the exhumation age (e.g., Reiners and Brandon, 2006). The exhumation ages can be used to estimate the rate of erosion, integrated over timescales of 10^5 -10^7 yrs (e.g., Ruhl and Hodges, 2005) -- scales of both orogenic and climatic processes. Recent studies of the denudation of heavily glaciated orogens in Alaska and British Columbia have produced integrated long-term (10^6 yr) erosion rates of 0.6 to 1 mm/a (Spotila et al., 2004; Densmore et al., 2006). The same studies, however, indicate increasing topographic relief and higher denudation rates approaching 3-5 mm/a in the valleys of these catchments (Spotila et al., 2004; Schuster et al., 2005), where glaciers

may be eroding most rapidly. None of the thermochronometric studies, however, have found exhumation ages that approach recent erosion rates from the same orogens.

To better understand the role of glaciers in mountain building, and to quantify the temporal variation in glacial erosion though time, we need to compare recent glacial erosion rates to a measure of glacial erosion on the time scale of orogenic processes. This chapter presents preliminary thermochronometric data that reflect long-term exhumation rates from the Patagonian Andes and Cordillera Darwin. The exhumation rates are derived from detrital apatite fission track ages sampled at the mouths of two glaciated basins, San Rafael and Marinelli, where recent erosion rates were also measured (Chapters 3 and 4). The samples were in the process of being analyzed by Dick Stewart prior to his passing in April 2006. The erosion rates inferred from apatite fission track ages are compared to recent erosion rates for the same basins. The difference in erosion rates across time scales from 10^1 to 10^6 yrs provides insight into the transience of contemporary glacial erosion processes and into the temporal variation in erosion, and sediment delivery, from glaciated orogens.

Regional tectonic and glacial influences

Exhumation rates on orogenic time scales are influenced by both changes in tectonic uplift and variations in the types of surface processes that control erosion, most particularly the onset of glaciation. To better understand long-term denudation of a basin, one must first take into account the regional tectonic setting and the period when changes in the style and rates of erosion likely occurred, such as when glaciers were first present in the catchment.

San Rafael

The North Patagonian icefield is found in a unique tectonic environment at the southern end of the Andean magmatic arc, created by the convergence of the Nazca and South American plates and the subduction of an active ocean ridge north of the Chile triple junction, directly west of San Rafael glacier. Since ca. 25 Ma, the Nazca plate has been converging with the South American plate along an ENE trend, oblique to

the Peru-Chile trench, prompting the uplift of the modern Andes (Pardo-Casas and Molnar, 1987; Thomson, 2002). The dextral Liquine-Ofqui fault, a trench-parallel strike-slip fault extending from the Golfo de Penas at 47ºS northwards for 1000 km, is the result of strike-slip partitioning of weak crustal lithosphere near the Andean magmatic arc (Thomson et al., 2001). The fault initiated in the late Miocene; at its southern end near Laguna San Rafael, Quaternary displacement has been recorded on land (Wood, 1989) and imaged in seismic lines in the Golfo de Penas (Forsythe and Prior, 1992) (see Fig. 5.1 for location), indicating continuous activity since initiation.

East of the Liquine-Ofqui fault, underlying the San Rafael glacier, the dominant rock type is the calc-alkalic plutonic North Patagonian Batholith (NPB) (Fig. 7.1). The NPB was emplaced in episodes lasting from the early Cretaceous to the early Miocene (Pankhurst et al., 1999). Al-in-hornblende geobarometry of the youngest zones of the pluton, in the southern portion of the NPB near the Liquine-Ofqui fault, indicates crystallization at depths of 11± 2 km (Herve et al., 1996). This implies a post-Miocene average denudation rate of up to ~1 mm/a close to the fault (Thomson, 2002), beneath the current glacier.

The first recognizable glaciation in the Patagonian Andes occurred between 7 and 4.6 Ma (Mercer and Sutter, 1982). Since that time, the region has experienced as many as 40 glacier advances (Mercer and Sutter, 1982; Rabassa and Clapperton, 1990; Lliboutry, 1999); the most extensive happened 1.2 Ma (Mercer, 1976). The last major glacial advance to occupy the entire continental margin out to the shelf break was the Llanquihue glaciation, 14-34 ka (Mercer, 1976). That glaciations have occurred in the region over millions of years is a function of the moisture–bearing Southern Westerlies, a long-standing feature of southern hemisphere atmospheric circulation that has delivered moisture to the Patagonian Andes since uplift of the orogen began.

Marinelli

Tierra del Fuego lies at the junction of the South American, Scotia and Antarctic plates. An active left-lateral strike-slip margin, the Magallanes-Fagnano transform (MFT) system, cuts ESE across the southern part of the Strait of Magellan and along the Seno Almirantazgo in the center of Tierra del Fuego, and forms the northern boundary of the Cordillera Darwin (Fig. 7.2). The MFT separates the metamorphic core complex of the

Cordillera Darwin from an 8km-thick sedimentary rift basin, the Magellan Basin, to the north (Diraison et al., 1997). Transpressional deformation has occurred along the MFT and parallel faults since the mid-late Cretaceous (Cunningham, 1995). Exhumation of the metamorphic complex that makes up the cordillera, which began in the late Cretaceous-early Tertiary, is presumed to be the result of erosional unloading (Diraison et al., 1997). A series of granitic bodies intrude the complex, the products of Late-Cretaceous subduction-related magmatism in the region (Cunningham, 1995).

Several large ice sheet advances have extended from the Andean Cordillera to the northwest of Tierra del Fuego into the region, dating to as far back as 1.1-1.4 Ma (Clapperton, 1993). At least five major glacial advances crossed the Magellan Strait and extended southward to entirely cover the Cordillera Darwin and Fagnano Strait (Fig. 7.2), the last major glaciation culminating 18 ka (Rabassa and Clapperton, 1990; Sugden et al., 2005). Little is known of the history of local glacier advances from the Cordillera Darwin Icefield, but one can assume that outlet glaciers persisted in the Cordillera Darwin between ice sheet advances as well as since the last advance, with possible northward Holocene advances corresponding to the Ushuaia (10-12 ka), Vinguerra (1.5-5 ka) and Martial (Little Ice Age) drifts in the Beagle Channel, the southern margin of the cordillera (Rabassa et al., 1992).

Fission Track Methods

The detrital fission track (FT) method capitalizes on the damage produced by fission decay of ^{238}U to ^{235}U in nonconductive minerals. Fission causes ^{238}U to split into two atomic fragments which repel one another, and ionization damage is produced along their respective paths (Reiners and Brandon, 2006). If the temperature of the mineral remains low (≤110ºC for zircon, ≤75ºC for apatite), thermal diffusion is not sufficiently activated to anneal the tracks, and the number of tracks can be counted to estimate the age since the mineral cooled past the respective closure temperature.

Apatite grains were extracted from samples of fine/medium sand collected from the shores of each fjord within 10 km of the current ice front (see Figs. 7.1-7.5 for sample locations and lithologies). The grains were mounted, polished and chemically etched, and the tracks counted and measured according to the techniques outlined in

Reiners and Brandon (2006). The mounted crystals were irradiated with a uranium-free mica sheath, which induces fission of ^{235}U into the mica. The induced fission tracks in the mica sheath were then counted and compared to the natural tracks. This method yields the natural age of ^{235}U in the mineral. The FT age of the sample is then based on an average of many grain ages. Probability density function (PDF) plots for the sample age were generated using the BINOMFIT program (Brandon, 2002), with an F-test confidence level set at ≤ 5 % (Fig. 7.6).

The mean erosion rate that would result in the sample age was then calculated using Mark Brandon's AGE2EDOT erosion curve (Fig. 7.7, adapted from Brandon (2005)). The AGE2EDOT curve assumes that a) erosion was occurring into a flat surface, b) material is advected to the surface along vertical pathways, and c) the apatite thermochronometric clock was set at a closure depth of 75ºC, with no complications from partial annealing. The current near-surface geothermal gradient of 34 ± 11ºC/km (Thomson, 2002) was assumed to have persisted throughout the Cenozoic, and used to estimate the depth of the closure isotherm. Because the sediment samples were glacially-derived, and were collected at the mouths of fjords that were deglaciated within the last few decades, any lag time between the denudation of the sediment and its deposition at the sample site is considered negligible (i.e., we are assuming that there has been minimal recycling of detrital sediments).

Exhumation ages

The samples collected along the shores of Laguna San Rafael, close to the position of the terminus in 1959, yielded 34 apatite grains suitable for FT analysis. Fitting a PDF to the grain ages, two peaks emerged, with cooling ages of 2.2 Ma and 7.7 Ma (Fig. 7.6). These correspond to a catchment denudation rate of ~0.9 -1.3 mm/a averaged over the past few million years, which is indistinguishable from late Cenozoic denudation rates derived from geobarometry of the NPB pluton (Herve et al., 1996; Seifert et al., 2004).

32 apatite grains were analyzed from the samples collected on the inner shore of the Little Ice Age moraine in Marinelli fjord. Fitting the grain ages to a PDF produced a peak at 3.4 Ma (N.B., the PDF of apatite FT ages from Marinelli fjord generated by Dick

Stewart and shown in Figure 7.6 was created prior to completion of the grain analyses, and does not represent the final sample size, which he completed in early April 2006. Unfortunately, no plots were created of the final analyses, and the samples and software are unavailable at this time). The mean age FT age corresponds to a 10^6-yr averaged catchment denudation rate of ~1.1 mm/a.

Findings

The long-term exhumation rates of around 1mm/a found at the North Patagonian Icefield are over one order of magnitude less than recent sediment yields from the same catchment. In the Cordillera Darwin, the exhumation rate, also ~1 mm/a, is up to 40-fold slower than recent erosion rates from Marinelli fjord. Exhumation ages at both localities are similar to exhumation ages seen in the Chugach-St. Elias range (Spotila et al., 2004) (Fig. 7.8) and in the Coast Mountains of British Columbia (Densmore et al., 2006), also tectonically active glaciated orogens where estimates of recent erosion exceed 10 mm/a. The thermochronometric ages from Patagonia, as from Alaska, suggest that glacially influenced denudation rates measured over 10^6 yr time scales are significantly lower than those on 10^2 yr time scales, thus supporting the assertion that sediment yields in recently deglaciated fjords reflect erosion rates that are transient and not sustained throughout the orogenic cycle.

The difference in short-term and long-term denudation rates highlights the limitations of assuming that erosion has been in steady state and that the fluvial and glacial evacuation of crustal material is balancing the tectonic influx, an assumption commonly made in landscape evolution models (e.g., Willett, 1999). Glaciers have been advancing and retreating across these orogens for several million years, driving changes in the erosion processes acting on the landscape, as well as changes in sediment evacuation and delivery from the orogen, over time scales closer to 10^2-10^4 yrs. The advance and retreat of glaciers promotes transient responses in the landscape: as glaciers retreat, the sudden drop in base level and the seismic response to ice unloading can help to unravel oversteepened slopes (e.g., Meigs, 1998). During the subsequent advance, the glacier must erode and evacuate the thick sediment package that fills the basins between glaciations before it can start to denude and exhume any new material,

results in a time lag between the growth of the glacier and an increase in bedrock erosion.

The efficiency of glacier erosion itself may vary over a glacier cycle, as changes in regional climate drive changes in the basal ice conditions, by delivering more or less meltwater to the bed and/or promoting changes in ice fluxes and ice speeds. Significant variability at the ice-bed interface would have been particularly prevalent in the glaciers and ice sheets of Tierra del Fuego, which were located at the margin of polar (atmospheric) conditions during the Last Glacier Maximum (da Silva et al., 1997). Heusser (2003) demonstrated that the strong N-S precipitation gradient in the Patagonian Andes, driven by the Southern Westerlies, shifted 5º latitude northwards in glacial times. The global atmospheric changes that resulted in a northward shift in the westerlies would also have affected the Antarctic circumpolar current, pushing it into the southern tip of south America. The northward shift in cooling may have resulted in polar conditions around and under the icefields during the peak of the glacial cycle. Lowered basal temperatures would have slowed or effectively stopped sliding and decreased erosion, counteracting potential increases in regional denudation from the overall increase in ice cover.

The order of magnitude difference between recent erosion rates and exhumation rates suggests that the timing of rapid erosive events is short-lived over the glacial-interglacial cycle. To first order, the 10- to 40-fold difference between recent erosion rates, which represent only the last 0.1% of the period since glaciers first occupied the basins, and glacial-interglacial rates suggests that the decadal and centennial yields documented from glaciers in rapid retreat may represent no more than a fraction of the overall impact of glaciers on the orogenic development.

The difference in denudation rates also highlights the limitations of a 1D interpretation of erosion rates from thermochronometric ages. The linear age-exhumation relationship can be compromised not only by changes in erosion over thermonochronometric time scales, but also by changes in topography and structural unloading that alter the depth of the closure isotherm, and by non-vertical exhumation pathways that can increase the length of time the mineral takes from the isotherm to the surface. In particular, structural features such as the major transpressional faults that bound both orogens - the Liquine-Ofqui mega fault along the western edge of the North Patagonian batholith, and the Magallanes-Fagnano transform fault along the northern

edge of the Cordillera Darwin - can both enhance exhumation via structural weakening, and provide potential cooling at depth. Downward advection of isotherms would steepen the local thermal gradient, and cooling ages would appear older, resulting in lower estimates of exhumation.

Conclusions

Temporal variations in erosion over the long-term has significant implications for the coupling between glacial erosion and orogenic development. Variations in denudation rates over glacial-interglacial timescales, with intermittent periods of rapid erosion, can force landscapes out of isostatic/geodynamic balance. That denudation rates over million-year time scales are an order of magnitude lower than short term rates based on decadal sediment yields suggests that exhumation results from rapid bursts of glacial erosion during the shift from glacial to interglacial conditions.

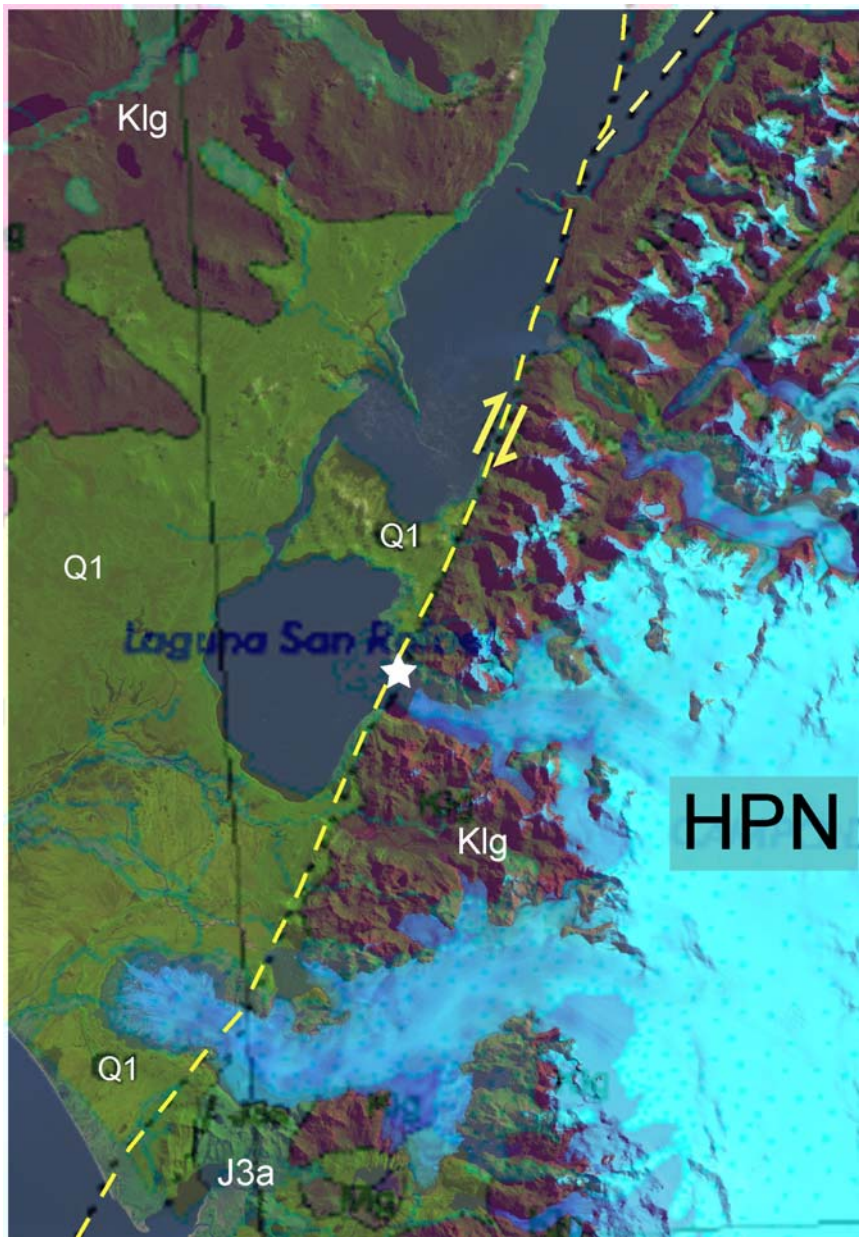

Figure 7.1 Location of apatite FT samples collected in Laguna San Rafael. Samples were collected from a beach on the north shore of the lagoon (white star), approx. 1 km west of the Liquine-Ofqui fault (yellow dash). Major geologic formations, published by SERNAGEOMIN (2003), are overlain on a 2001 Landsat image of the region. Klg (pink) = Cretaceous granites of the North Patagonian Batholith, Q1 (yellow) = Quaternary alluvium, J3g (green) = rhyolites and andesites of the Tobifera Formation.

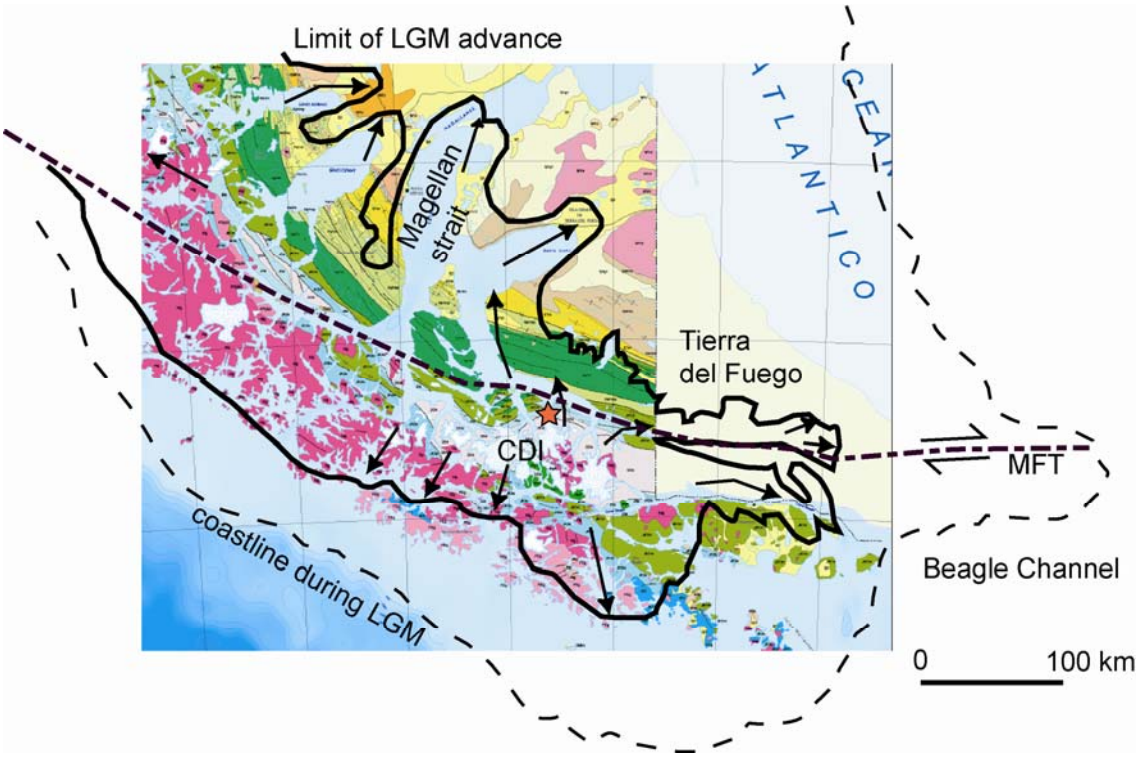

Figure 7.2 Major geologic formations and extent of Last Glacial Maximum ice sheet advance in Tierra del Fuego. Geology from SERNAGEOMIN (2003), extent of the LGM ice limits and LGM coastline from Clapperton (1993). The Magallanes-Fagnano transform (MFT) is marked as a dashed line across the center of the island.

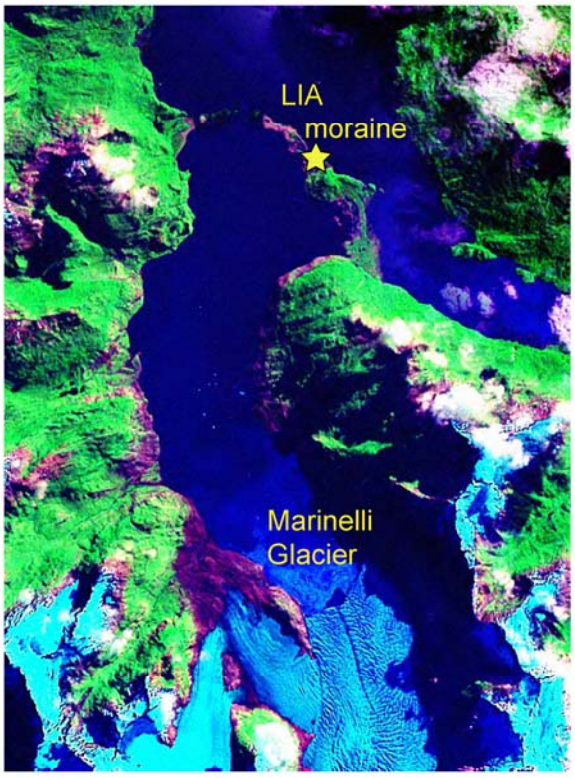

Figure 7.3 Location of apatite FT samples collected in Marinelli fjord. Samples were collected from the Neoglacial terminal moraine that crosses the mouth of the fjord.

Figure 7.4 Photograph of cobbles at Laguna San Rafael sample site, showing granites and granodiorites derived from the North Patagonian Batholith.

Figure 7.5 Photograph of cobbles at Marinelli sample site, size 9 (W) boot for scale. Samples included greenschists, gneisses, granodiorites and metavolcanics, derived from the Cordillera Darwin core complex.

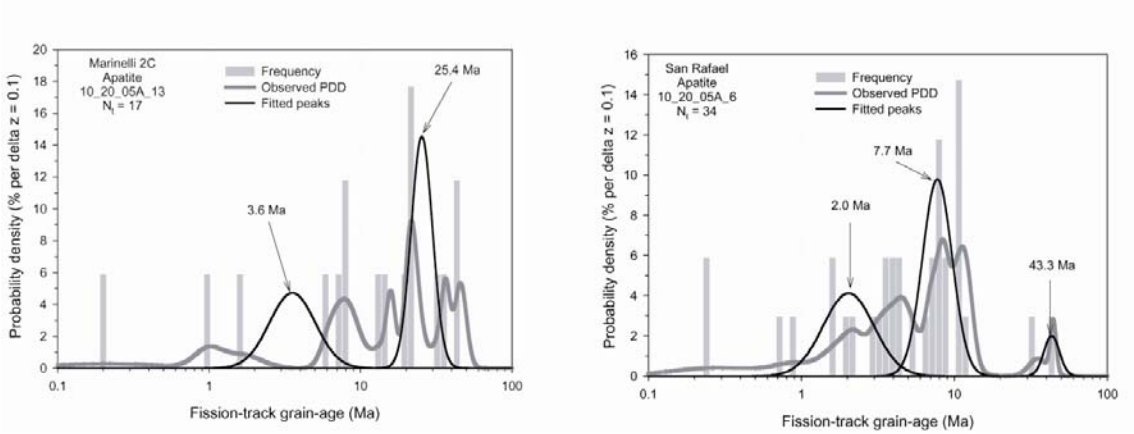

Figure 7.6 Probability density function plots of apatite FT ages from San Rafael glacier (a) and Marinelli glacier (b). Fitted peaks indicate pooled ages.

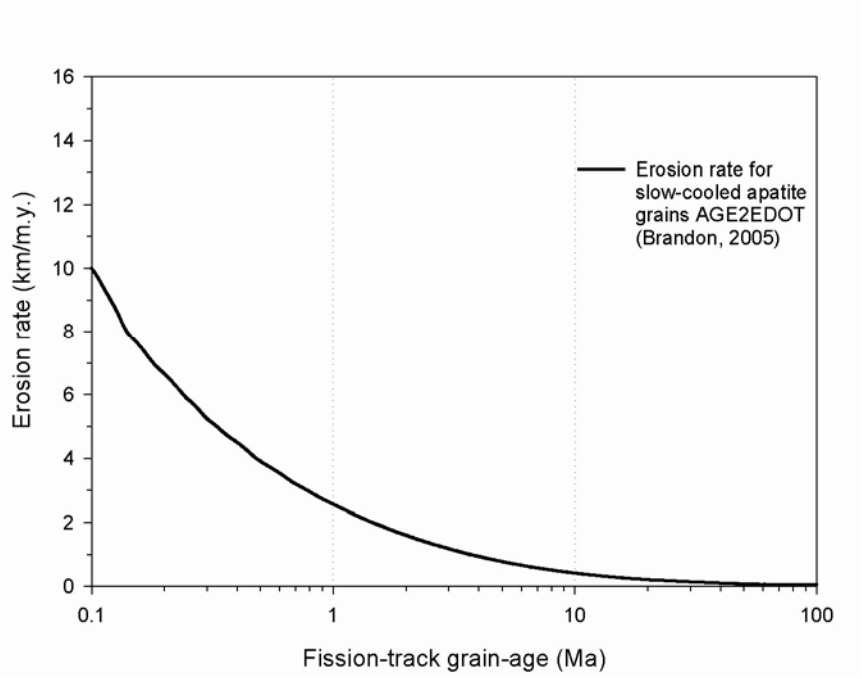

Figure 7.7 Relationship of cooling age to erosion rate, at exhumational steady state, for apatite FT thermochronometers, determined from the AGE2EDOT program, Brandon (2005).

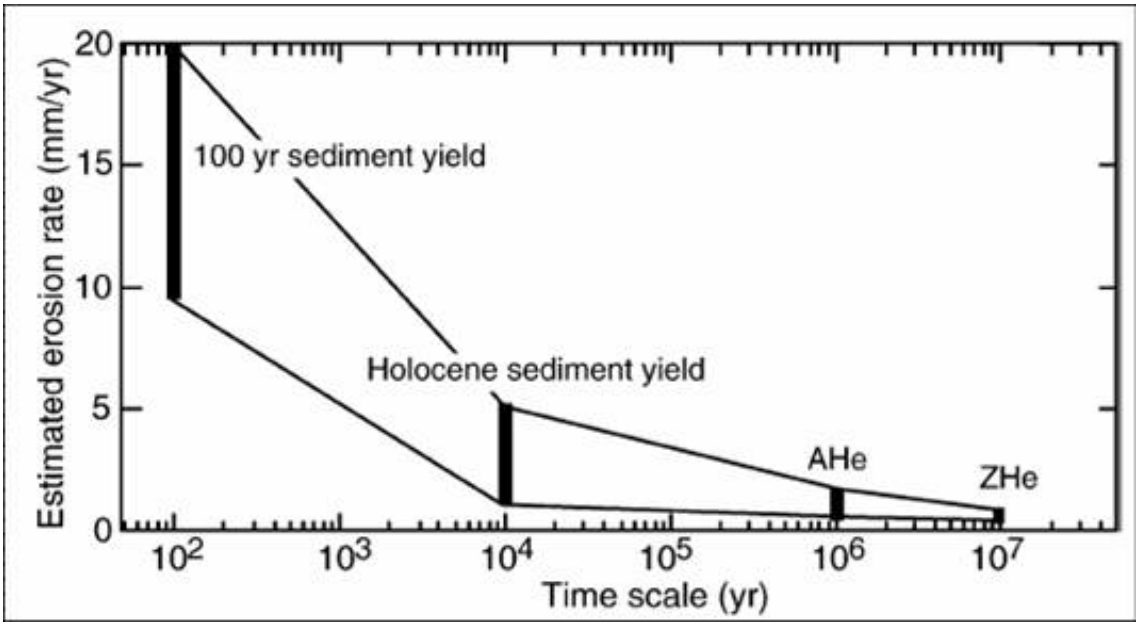

Figure 7.8 Erosion/exhumation rate vs. time scale of observation for glacially-dominated Chugach-St. Elias orogen, coastal Alaska. Rates inferred from 100-yr sediment yield are measured from recently deglaciated fjords (Hallet et al., 1996); Holocene sediment yields are measured seismostratigraphically from the Gulf of Alaska shelf (Jaeger et al., 1998; Sheaf et al., 2003). Average apatite helium (AHe) and zircon helium (ZHe) were measured from bedrock samples along a transect across the range. Figure from Spotila et al (2004).

CHAPTER 8. SUMMARY

The glacial erosion rates measured in this study are a substantial new contribution to the relatively sparse data set on erosion rates from glaciated catchments worldwide. The data from three Chilean glaciers – San Rafael, Tyndall and Marinelli -- also provide the first documented estimates of glacier erosion rates from Patagonia and Tierra del Fuego, two of the last remaining regions of substantial ice cover outside of the polar ice sheets. Recent erosion rates from these glaciers, which range from 14 to 39 mm/a averaged over the past 50 years, are similar to erosion rates estimated from the large Alaskan tidewater glaciers, which were previously known to be among the most erosive worldwide (Fig. 8.1). Moreover, the data collected represent a range of geologic and tectonic settings, suggesting that the rapid erosion is not due to unusually erodible substrates because of inherently weak lithologies or fracturing along fault zones.

At all three tidewater glaciers, spanning two continents, sediment yields have increased as the glaciers began to retreat rapidly in the latter half of the 20th century. The similarities in sediment yield data from a number of glaciers in two different hemispheres imply that, in general, basin-wide erosion rates for fast-moving tidewater temperate glaciers tend to be very high, exceeding 10 mm/a. The data also suggest that erosion rates over the last few decades greatly exceed glacial erosion rates over the entire glacier advance-retreat cycle. The marked retreat and thinning of these glaciers during this period of exceptionally rapid ice motion reflect much more ice being conveyed from the high regions of accumulation to the fjords below than can be sustained by the current influx of snow to the basins and the loss of ice through ablation.

From direct measurements of erosion and ice motion at San Rafael glacier, there appears to be a positive, linear relationship between erosion rate and ice flux through the glacier system. This relationship is modulated by other factors including the erodability of the substrate, such that measurements of erosion or ice motion in one glacier basin are not directly transferable to another glacier basin, as suggested by similar erosion rates but much lower ice fluxes measured at Tyndall glacier (Chile). The co-variation between erosion and ice flux in a single glacier basin over time, however, supports the hypotheses that erosion rates increase with ice flux and that the correlation between erosion and retreat observed at San Rafael and at the other study glaciers is the result of the drawdown of the glacier surface during retreat, which steepens the

glacier profiles and results in an increase in ice flux to the terminus. That a robust relationship between erosion and ice motion exists and would be observed during glacier retreat is also supported by two sets of observations at other tidewater glaciers: a) that ice velocities, thinning rates and retreat rates all increased in concert at Columbia Glacier in Alaska over the past two decades, and at Helheim Glacier and Jakobshaven Isbrae in Greenland over the past decade, and b) that sediment fluxes increased with ice velocity during surges and short periods of acceleration at Variegated Glacier and Bench Glacier (a non-calving glacier) in Alaska.

The marked acceleration of the retreat of these glaciers in the latter half of the 20th century appears to be driven by warmer and drier climatic conditions across the icefields. Variations in the rate of retreat, however, have been modulated by changing topography at the ice front, which changes the surface area of the terminus subject to submarine melting and calving. For example, the retreat of Marinelli Glacier in the early 1960s accelerated rapidly when the terminus pulled away from the end moraine into deep water. Conversely, after 1997, when half the terminus emerged onto land, the rate of retreat of Marinelli slowed considerably. Similarly, at San Rafael glacier, the retreat of the terminus from the open lagoon into a valley constriction led to a temporary standstill in 1986-1987, a period when a model of the mass budget of the glacier indicates strongly negative mass balance due to warmer and drier conditions.

Most tidewater glaciers spend significantly longer periods of their advance-retreat cycle in an advance phase or quasi-stable mode, and tend to retreat quite quickly at the end of the cycle. To obtain an index of the 'long-term' erosion rate for these glaciers on millenial time scales (i.e., over one or several glacial advance-retreat cycles), we can extrapolate the least-squares regression line between erosion rate and retreat rate to periods of no retreat, represented by the intercept of a linear best-fit relationship of the data. The extrapolated erosion rate is the best estimate we have of the rate of erosion during periods of standstills or relative stability. During the first phase of an advance the rate of bedrock erosion may tend to be minimal, at least in the lower reaches of the glacier, since considerable proglacial sediment has to be evacuated before the glacier can erode the bed. Accordingly, since a substantial portion of a normal tidewater glacier cycle is spent in a quasi-stable phase, and the relatively short period of rapid erosion during the retreat phase tends to be offset by the slower bedrock erosion during the longer advance phase, we can assume that the extrapolated erosion rate is most

representative of the ‘long-term’ erosion rate for the glaciers. For all three glaciers, this long-term erosion rate approaches 9-10 ± 3 mm/a, which is 2 to 4 times lower than the average rates over the past 50 years, and up to an order of magnitude lower than peak erosion rates when the glaciers were retreating most rapidly.

The results showing that sediment yields are high when these glaciers were retreating rapidly, together with similar results for Muir Glacier (Koppes and Hallet, 2002), suggest that most of the sediment yield data from retreating tidewater glaciers collected to date correspond to contemporary erosion rates that are significantly higher than those in the long-term. This bias towards unusually high sediment yields in the short-term is also present in other published rates of erosion for tidewater glaciers, since most other studies were measured using similar methods from calving glaciers that have also been steadily thinning and retreating since the end of the Little Ice Age. Accordingly, the estimates of contemporary and long-term (millennial) erosion rates presented in this study suggest that contemporary measurements of glacier erosion from basins drained by retreating temperate tidewater glaciers be reduced by up to a factor of four to conservatively approach their ‘long-term’ rates, such as those derived for Tyndall, San Rafael and Marinelli glaciers.

For all of these heavily glaciated basins, even after taking into account a 4-fold decrease in erosion due to glacier standstills and advances as well as the contribution of sediment from mass movements triggered by changes in base level as the glaciers oscillate in their catchments, the estimated long-term glacier erosion rates remain among the highest known erosion rates worldwide. Exhumation rates measured by thermochronometry in Patagonia, as in Alaska, are closer to 1 mm/a, up to an order of magnitude lower than the long-term glacier erosion rates. That glacially influenced denudation rates measured over 10^6 yr time scales are significantly slower than erosion rates on 10^2 -10^3 yr time scales suggests that the erosion rates we deduce from sediment yields in recently deglaciated fjords are transient, and thus not sustained throughout the orogenic cycle. The stochastic nature of glacial erosion, with rapid, highly erosive events punctuating the shift from glacial to interglacial conditions, has significant implications for the coupling of climate and tectonics in the evolution of orogens, and needs to be incorporated into landscape evolution models.

FUTURE WORK

Though I found that erosion rates tend to increase with ice flux in temperate glaciers, I still know very little about the controls on basin-wide erosion at the ice-bed interface, particularly the role of temperature and melt-water changes on basal processes. If basal temperatures dip below the pressure melting point and there is little melt-water available to lubricate the bed, dramatically reducing basal ice motion, would we see a commensurate drop in erosion rates? To what degree does ablation play a role in providing melt-water to the bed and hence increase basal ice motion and erosion? Addressing the contribution of melt-water to basal ice motion, and in turn to erosion, requires approaching the same problem by measuring sediment yields from tidewater glaciers in more polar conditions. I just returned from a research expedition to the Antarctic Peninsula, where we collected seismic profiles, swath bathymetry and shallow cores to quantify modern sedimentation rates from outlet glaciers in polythermal and polar settings. We also measured ice thickness and ice motion close to the ELA of these outlet glaciers in order to derive the ice fluxes through a number of tidewater glaciers. Once the data are processed, I will be able to assess whether erosion rates drop sharply as basal temperatures drop below freezing and glaciers become frozen to their beds.

If erosion rates vary as a function of retreat, understanding the energy balance at the calving front may provide insight into controls on short-term sediment yields. In particular, quantifying melt rates of the submarine ice front will help to better understand the fluxes across the ice face, and their temporal variation – the largest unknown in the glacier mass budget model. During mid-winter research cruises in Laguna San Rafael and Marinelli, we collected several conductivity, temperature and depth profiles near the calving front (sample CTD profiles collected in June 2005 at Laguna San Rafael are included in Fig. 2). Returning to these fjords and collecting similar measurements at the ice front in the summer will provide constraints on estimates of the seasonal changes in ice front melt rates that may control seasonal variations in calving flux (Motyka et al., 2003).

Finally, the modeling of mass gain and loss from the glaciers, and the estimates of the relationship of these modeled fluxes to the actual ice flux through these systems, suffers from a lack of ground control measurements. This research benefited from

collaborations with Eric Rignot at NASA-JPL, Howard Conway at the UW, and Gino Casassa and Andres Rivera from the Centro de Estudios Cientificos in Valdivia, Chile. These collaborators are building radio-echo sounding systems that can be operated from a small plane, and can greatly facilitate ice thickness measurements over vast regions without the dangers and logistical constraints of glacier travel. Preliminary flights in Alaska last summer demonstrated that the radar systems can penetrate well over 1000 m of warm ice and image the bed of some of the largest temperate icefields on Earth. We intend to fly this system over the Patagonian glaciers highlighted in this study in the near future, from which we will be able to estimate ice thicknesses along a profile from the terminus to the accumulation area. Combined with surface velocities of the same glaciers measured using InSAR, currently being collected and analyzed by Eric Rignot, we hope to soon have measurements of recent ice motion and ice thickness from which to estimate contemporary ice fluxes through the ELA of Marinelli and San Rafael glaciers. These measurements will be used to further constrain the model of mass transfer of ice, based on climate, through these systems.

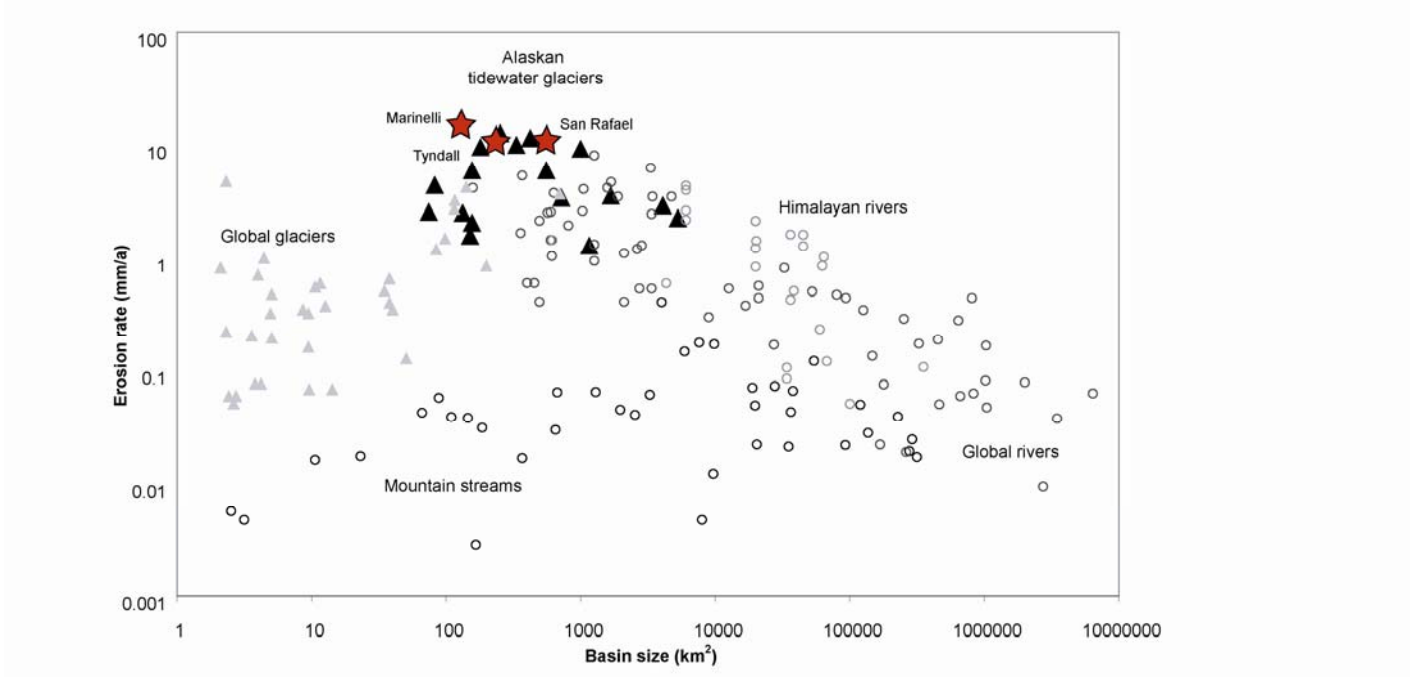

Figure 8.1 Erosion rates for glaciated and non-glaciated basins worldwide, revised from data originally compiled by Hallet et al. (1996), including the newly measured erosion rates from the Chilean glaciers (red stars) in this study.

LIST OF REFERENCES

Aalto, R. and Dunne, T., 2006. Geomorphic controls on Andean denudation rates. *Journal of Geology,* 114: 85-99.

Abdalati, W., Krabill, W., Frederick, E., Manizade, S., Martin, C., Sonntag, J., Swift, R., Thomas, R., Wright, W., and Yungel, J., 2001. Outlet glacier and margin elevation changes: Near-coastal thinning of the Greenland ice sheet. *Journal of Geophysical Research-Atmospheres* 106: 33729-33741.

Ahnert, F., 1987. The fundamental principles of landscape evolution. *Catena Supplement*, 10: 199-210.

Alley. R., 2000. Continuity comes first: recent progress in understanding subglacial deformation. In: *Deformation of glacial materials* (Ed. by Maltman, A.J., Hubbard, B. and Hambrey, M.J.), *Geological Soc. London Special Pubs.*, 176: 171-179.

Alley, R. B., Lawson, D. E., Larson, G. J., Evenson, E. B., and Baker, G. S., 2003. Stabilizing feedbacks in glacier-bed erosion, *Nature*, 424: 758–760.

Anderson, J.B. and Ashley, G.M., 1991. Glacial marine sedimentation; Paleoclimatic significance; A discussion, in *Glacial marine sedimentation; Paleoclimatic significance, Geological Society of America Special Paper 261*, edited by J.B. Anderson and G.M. Ashley, 223-226.

Anderson, J.B.,1999. Antarctic Marine Geology. Cambridge: Cambridge University Press. 289 pp.

Anderson, R.S., Anderson, S.P. , MacGregor, K.R., Waddington, E.D., O'Neel, S., Riihimaki, C.A., and Loso, M.G., 2004. Strong feedbacks between hydrology and sliding of a small alpine glacier. *Journal of Geophysical Research,*109: F03005, doi:10.1029/2004JF000120

Andrews, J.T., Domack, E.W., Cunningham, W.L., Leventer, A., Licht, K.J., Jull, A.J.T., DeMaster, D.J. and Jennings, A.E., 1999. Problems and possible solutions concerning radiocarbon dating of surface marine sediments, Ross Sea, Antarctica. *Quaternary Research*, 52: 206-216.

Andrews, J.T., Milliman, J.D., Jenning, A.E., Rynes, N. and Dwyer, J., 1994. Sediment thicknesses and Holocene glacial marine sedimentation rates in three East Greenland fjords (ca. 68°N). *Journal of Geology*, 102: 669-683.

Aniya, M., 2001, Glacier variations of Hielo Patagonico Norte, Chilean Patagonia, since 1944/45, with special reference to variations between 1995/96 and 1999/2000. *Bulletin of Glacier Research*, 18: 55-63.

Aniya, M., 1999. Recent glacier variations of the Hielos Patagonicos, South America, and their contribution to sea-level change., *Arctic Antarctic and Alpine Research,* 31 (2): 165-173.

Aniya, M., 1995. Holocene glacial chronology in Patagonia: Tyndall and Upsala glaciers. *Arctic and Alpine Research*, 27(4): 311–322.

Aniya, M., 1988. Glacier inventory for the Northern Patagonia Icefield, Chile, and variations 1944/45 to 1985/86. *Arctic and Alpine Research* 20: 179–187.

Aniya, M. and Wakao, Y., 1997. Glacier variations of Hielo Patagónico Norte, Chile, between 1944/45 and 1995. *Bulletin of Glacier Research,* 15:11-18.

Aniya, M., and Skvarca, P., 1992. Characteristics and variations of Upsala and Moreno glaciers, Southern Patagonia, *Bulletin of Glacier Research,* 10:39-53.

Aniya, M., Dhakal, A.S., Park, S. and Naruse, R., 2000, Variations of Patgonian glaciers, South America, using RADARSAT and Landsat images. *Canadian Journal of Remote Sensing,* 26 (6): 501-511.

Aniya, M., Naruse, R., Casassa, G. and Rivera, A., 1999. Variations of Patgonian glaciers, South America, utilizing RADARSAT images. Proceedings of the International Symposium on RADARSAT Application Development and Research Opportunity, Montreal, Canada, Oct. 13-15, 1998: 1-10.

Aniya, M., Sato, H., Naruse, R., Skvarca, P., and Casassa, G., 1997. Recent glacier variations in the Southern Patagonia Icefield, South America, *Arctic and Alpine Research,* 29: 1-12.

Arendt, A., Echelmeyer, K.A., Harrison, W.D., Lingle, C. and Valentine, V.B., 2002. Rapid wastage of Alaska glaciers and their contribution to rising sea level. *Science,* 297(5580): 382-386, DOI: 10.1126/science.1072497

Bangs, N.L. and Cande, S.C.,1997. Episodic development of a convergent margin inferred from structures and processes along the Southern Chile margin. *Tectonics*, 16: 489 - 503.

Bart, P.J. and Anderson, J.B., 1995. Seismic record of glacial events affecting the Pacific margin of the northwestern Antarctic Peninsula. In: *Geology and Seismic Stratigraphy of the Antarctic Margin*, (Ed. By Cooper, A.K., Barker, P.F., Brancolini, G.), *Antarctic Research Series*, 68: 75-95.

Bartek, L.R., Vail, P.R., Anderson , J.B., Emmet, P.A. and Wu, S., 1991. Effect of Cenozoic ice-sheet fluctuations in Antarctica on the stratigraphic signature of the Neogene. *Journal of Geophysical Research*, 96: 6753-6778.

Beaumont, C., Munoz, J.A., Hamilton, J. and Fullsack, P., 2000. Factors controlling the Alpine evolution of the central Pyrenees inferred from a comparison of observations and geodynamical models. *Journal of Geophysical Research,* B105 (4): 8121-8145.

Bendick, R. and Bilham, R., 2001. How perfect is the Himalayan Arc? *Geology*, 29(9):791-794.

Bentley, M.J. and McCulloch, R.D., 2005. Impact of neotectonics on the record of glacier and sea level fluctuations, Strait of Magellan, southern Chile. *Geografiska Annaler,* 87 A (2): 393-402.

Berner, R.A., 1991. A model for atmospheric CO_2 over Phanerozoic time. American *J. Science*, 291(4): 339-376.

Bird, P.,1996. Computer simulations of Alaskan neotectonics, *Tectonics*, 15: 225-236.

Boulton, G.S., 1979. Process of glacial erosion on different substrata. *Journal of Glaciology* 23: 15-37.

Boulton, G.S., 1974. Processes and patterns of glacial erosion. In *Glacial Geomorphology* (Ed. by Coates, D.R.), State University of New York, 41-87.

Braithwaite, R. J. and Olesen, O.B., 1989. Calculation of glacier ablation from air temperature, West Greenland. In *Glacier Fluctuations and Climatic Change*, J. Oerlemans (Ed.), Kluwer Academic, 219-233.

Braun, J., Zwartz, D. and Tomkin, J.H., 1999. A new surface-processes model combining glacial and fluvial erosion. *Annals of Glaciology*, 28: 282-290.

Brown, C.S., M.F. Meier, and A. Post (1982), Calving Speed of Alaska Tidewater Glaciers, with Application to Columbia Glacier, *U.S. Geological Survey Professional Paper 1258-C*, 13p.

Brozovic, N., Burbank, D.W., and Meigs, A.J., 1997. Climatic limits on landscape development in the northwestern Himalaya. *Science*, 276:571-574.

Bruhn, R. L., T.L. Pavlis, G. Plafker, and L. Serpa (2004), Deformation during Terrane Accretion in the Saint Elias Orogen, Alaska, *Geological Society of America Bulletin* 116: 771-787.

Burbank, D. W., Leland, J., Fielding, E., Anderson, R. S., Brozovic, N., Reid, M. R., and Duncan, C., 1996, Bedrock incision, rock uplift, and threshold hillslopes in the northwestern Himalaya: *Nature*, 379: 505-510.

Cai, J.; Powell, R.D.; Cowan, E.A.; Carlson, P. R.1997. Lithofacies and seismic-reflection interpretation of temperate glacimarine sedimentation in Tarr Inlet, Glacier Bay, Alaska. *Marine Geology*, 143(1-4): 5-37.

Carlson, P.R., 1989. Seismic reflection characteristics of glacial and glacimarine sediment in the Gulf of Alaska and adjacent fjords. *Marine Geology*, 85: 391-416.

Carlson, P.R., Wheeler, M.C., Molnia, B.F., Post, A. and Powell, R.D., 1983. Maps showing post-Neoglacial sediment thickness and bathymetry in Tarr Inlet, Glacier Bay, Alaska. Scale, 1:31,680. *U.S. Geol. Surv. Misc. Field Stud.* Map MF-1456, 1 sheet.

Carrasco, J., Casassa, G. and Rivera, A., 2005. Meteorological and climatological aspects of the Southern Patagonia ice cap, Patagonia. In *The Patagonian Icefields: A Unique Natural Laboratory for Environmental and Climate Change Studies*. (Eds. G. Casassa, F. Sepúlveda and R. Sinclair.) Series of the Centro de Estudios Científicos. Kluwer Academic/Plenum Publishers, New York.

Casassa, G. 1987. Ice thickness deduced from gravity anomalies on Soler Glacier, Nef Glacier and the Northern Patagonia Icefield. *Bulletin of Glacier Research* 4: 43-57.

Casassa, G. and Rivera, A.,1998. Digital radio-echo sounding at Tyndall Glacier, Patagonia. *Anales Instituto Patagonia, Serie Cs. Nat. (Chile)*, 26:129–135.

Cassasa, G. and Marangunic, C.,1987. Exploration history of the North Patagonian Icefield. *Bulletin Glacier Research*, 4:163-175.

Casassa, G., Rivera, A., Aniya, M. and Naruse, R., 2002. Current knowledge of the Southern Patagonia Icefield. In *The Patagonian Icefields: A Unique Natural Laboratory for Environmental and Climate Change Studies.* Eds. G. Casassa, F. Sepúlveda and R. Sinclair. Series of the Centro de Estudios Científicos. Kluwer Academic/Plenum Publishers, New York.

Casassa, G., Rivera, A., Aniya, M. and Naruse, R., 2000, Características glaciológicas del Campo de Hielo Patagónico Sur. *Anales Instituto Patagonia,* Serie Cs. Nat. (Chile) 28: 5-22.

Church, M. and Slaymaker, O., 1989. Disequilibrium of Holocene sediment yield in glaciated British Columbia, *Nature,* 337*:* 452-454.

Clapperton, C.M., 1993. Quaternary geology and geomorphology of South America. Amsterdam: Elsevier. 779 pp.

Cook, K.H., Yang, X., Carter, C.M. and Belcher, B.N., 2003. A modeling system for studying climate controls on mountain glaciers with application to the Patagonian Icefields. *Climate change*, 56: 339-367.

Cowan, E.A. and Powell, R.D. 1990. Suspended sediment transport and deposition of cyclically interlaminated sediment in a temperate glacial fjord, Alaska, U.S.A. In: *Glacimarine Environments: Processes and Sediments* (Ed. by J.A. Dowdeswell and J.D. Scourse), *Geol. Soc. Special Pub*., 53:75-89.

Cowan, E.A. and Powell, R.D., 1991. Ice-proximal sediment accumulation rates in a temperate glacial fjord, southeastern Alaska, in *Glacial marine sedimentation; Paleoclimatic significance, Geological Society of America Special Paper 261*, edited by J.B. Anderson and G.M. Ashley, 61-74.

Cuffey, K. M., Conway, H; Gades, A.M., Hallet, B., Lorrain, R., Severinghaus, J.P., Steig, E.J., Vaughn, B., White, J.W.C., 2000. Entrainment at cold glacier beds, *Geology*, 28 (4) : 351-35

Cunningham, W. D., 1995. Orogenesis at the southern tip of the Americas:The structural evolution of the Cordillera Darwin metamorphic complex, southern Chile. *Tectonophysics*, 244: 197–229.

Dalziel, I.W.D. and Cortes, R., 1972. Tectonic style of the southernmost Andes and the Antarctandes. 24th InternationalGeological Congress, Montreal, Section 3, 316-327.

DaSilva, J.L., Anderson, J.B. and Stravers, J., 1997. Seismic facies changes along a nearly continuous 24 degreee latitudinal transect: the fjords of Chile and the northern Antarctic Peninsula. *Marine Geology*, 103:103-123.

Densmore, M.S., Ehlers, T.A., Farley, K.A. and Woodsworth, G.J., 2006. Spatial and temporal variations in topography and glacial erosion from apatite (U-Th)/He thermochronology, southern British Columbia. *EOS Transactions, AGU* 87(52), Fall Meet. Suppl., Abstract C33A-1256.

Denton, G.H., Heusser, C.J., Lowell, T.V., Moreno, P.I., Andersen, B.G., Heusser, L.E., Schluchter, C., Marchant, D.R., 1999. Interhemispheric linkage of paleoclimate during the last glaciation. *Geogr. Ann.* 81A:107–153.

Derry, Louis A. and France-Lanord, C., 1997. Himalayan weathering and erosion fluxes; climate and tectonic controls. In*: Tectonic uplift and climate change* (Ed. by Ruddiman, W. F.). Plenum Press, New York, NY, 289-312.

Diraison, M., Cobbold, P.R., Gapais, D. and Rossello, E.A., 1997. Magellan Strait: part of a Neogene rift system. *Geology*, 25: 703–706.

Domack, E.W. and Ishman, S., 1993. Oceanographic and physiographic controls on modern sedimentation within Antarctic fjords. *Geological Society of America Bulletin*, 105: 1175-1189.

Dowdeswell, J. A., Whittington, R.J., and Marienfeld, P., 1994. The origin of massive diamicton facies by iceberg rafting and scouring, Scoresby Sund, East Greenland: *Sedimentology*, 41: 21-35.

Drewry, D.J., 1986. Glacial geologic processes. London: Edward Arnold, 276 pp.

Dyurgerov, M. B. and Meier, M. F., 1997. Year-to-year fluctuations of global mass balance of small glaciers and their contribution to sea level changes. *Arctic and Alpine Research*, 29(4): 392–402.

Ehlers, T.A., Chaudhri, T., Kumar, S., Fuller, C.W., and Willet, S.D., 2005. Computational tools for low-temperature thermochronometer interpretation. In Reiners PW, Ehlers TA,eds, 2005. *Low-temperature Thermochronology: Techniques, Interpretations, Applications. Reviews in Mineralogy and Geochemistry,* 58. Mineralogical Society of America, 622 pp.

Elverhøi, A., LeB. Hooke, R. and Solheim, A., 1998. Late Cenozoic erosion and sediment yield from the Svalbard-Barents Sea region: Implications for understanding erosion of glacierized basins, *Quaternary Science Reviews*, 17: 209-241.

Elverhøi, A., Svendsen J.I., Solheim, A., Andersen, E.S., Milliman, J., Mangerud, J. and Hooke, R.LeB., 1995. Late Quaternary sediment yield from the high Arctic Svalbard area. *Journal of Geology*, 103 (1): 1-17.

Enomoto, H., and Nakajima, C., 1985. Recent climate-fluctuations in Patagonia. In *Glaciological Studies in Patagonia Northern Icefield 1983-1984*, Nagoya (Japan), Nakajima, C, *Ed.*, 7-14.

Escobar, F., Vidal, F., Garin, R. and Naruse, R., 1992. Water balance in the Patagonain Icefield. In *Glaciological Researches in Patagonia, 1990*, Naruse, R. and Aniya, M. (eds.). Japanese Society of Snow and Ice, 109-119.

Finlayson, D., Montgomery, D.R. and Hallet, B. 2002. Spatial coincidence of rapid inferred erosion with young metamorphic massifs in the Himalayas, *Geology,* 30:219-222.

Forsythe, R., and Prior, D. 1992. Cenozoic continental geology of South America and its relations to the evolution of the Chile triple junction, in Behrmann, J.H., Lewis, S.D., Musgrave, R.J., et al., eds., *Proceedings of the Ocean Drilling Program, Initial Reports*, 141: 23-31.

Fujiyoshi, Y., Kondo, H., Inoue, J. and Yamada, T., 1987. Characteristics of precipitation and vertical structure of air temperature in northern Patagonia. *Bulletin Glacier Research,* 4: 15-24.

Furbish, D.J. and Andrews, J.T., 1984. The use of hypsometry to indicate long-term stability and response of valley glaciers to changes in mass transfer, *Journal of Glaciology* 30(105): 199-211.

Glasser, N. F., Jansson, K., Mitchell, W. A., and Harrison, S., 2006. The geomorphology and sedimentology of the 'Tempanos' moraine at Laguna San Rafael, Chile. *Journal of Quaternary Science*, (in press). ISSN 0267–8179. DOI: 10.1002/jqs.1002

Glasser, N. F., Jansson, K., Harrison, S. and Rivera, A., 2005. Geomorphological evidence for variations of the North Patagonian Icefield during the Holocene. *Geomorphology*,71:263-277.

Glasser, N.F., Jansson, K., 2005. Fast-flowing outlet glaciers of the Last Glacial Maximum Patagonian Icefield. *Quaternary Research* 63: 206–211.

Glasser, N.F., Harrison, S., Winchester, V. and Aniya, M., 2004, Late Pleistocene and Holocene paleoclimate and glacier fluctuations in Patagonia. *Global and Planetary Change,* 43: 79-101.

Griffith, T.W. and Anderson, J.B., 1989. Climatic control of sedimentation in bays and fjords of the northern Antarctic Peninsula*. Marine Geology*, 85:181-204.

Grikurov, G.E., 1978. Geology of the Antarctic Peninsula. New Delhi: Amerind, 140 pp.

Gulick, S., Jaeger, J. Freymueller, J. Koons, P. Pavlis, T. and Powell, R., 2004. Examining tectonic-climatic interactions in Alaska and the northeastern Pacific, *EOS Transactions AGU* 85(43): 433-439.

Gurnell, A., Hannah, D. and Lawler, D., 1996. Suspended sediment yields from glacier basins. In *Erosion and Sediment Yield: Global and Regional Perspectives*, IASH. Pub. No. 236, 97-104.

Hack, J.T., 1975. Dynamic equilibrium and landscape evolution, in *Theories of Landform Evolution*, Melhorn, W.N. and Flemal, R.C. (eds.), Boston: Allen and Unwin, 87-102.

Hallet, B. 1996. Glacial quarrying: a simple theoretical model. *Annals of Glaciology*, 22: 1-8.

Hallet, B. 1979. A theoretical model of glacial abrasion. *Journal of Glaciology,* 23: 29-50.

Hallet, B., Hunter, L. and Bogen, J., 1996. Rates of erosion and sediment evacuation by glaciers: A review of field data and their implications. *Global and Planetary Change*, 12: 213-235.

Harbor, J., and Warburton, J., 1993. Relative rates of glacial and nonglacial erosion in alpine environments. *Arctic and Alpine Res*earch, 25: 1-7.

Harden, S.L., DeMaster, D.J., and Nittrouer, C.A., 1992. Developing sediment chronologies for high-latitude continental shelf deposits: a radiochemical approach. *Marine Geology*, 103: 69-97.

Harrison, S. and Winchester, V., 1998. Historical fluctuations of the Gualas and Reicher Glaciers, Northern Patagonian Icefield, Chile. *Holocene* 8(4): 481-485.

Hay, W.W., 1998. Detrital sediment fluxes from continents to oceans. *Chemical Geology*, 145(3-4): 287-323.

Hay, W.W., Sloan, J.L., and Wold, C.N., 1988. Mass/age distribution and composition of sediments on the ocean floor and the global rate of sediment subduction. *Journal of Geophysical Research,* 93:14933–40.

Hebbeln, D., Lamy, F., Mohtadi, M., Echtler, H., 2007. Tracing the impact of glacial-interglacial climate variability on erosion of the southern Andes. *Geology,* 35(2):131-134.

Hervé, F., Pankhurst, R. J., Demant, A. and Ramirez, E. 1996. Age and Al-in-hornblende geobarometry in the north Patagonian batholith, Aysen, Chile, Third ISAG, St. Malo (France), abstract volume, 17-19.

Heusser, C.J., 1960, Late-Pleistocene environments of the Laguna San Rafael area, Chile. *Geogaphical Reviews,* 50: 555-577.

Heusser, C.J. and Streeter, S.S., 1980, A temperature and precipitation record of the past 16,000 years in southern Chile. *Science*, 219: 1345-1347.

Hicks, D. M., Hill, J. and Shankar, U. 1996. Variation of suspended sediment yields around New Zealand: the relative importance of rainfall and geology. In *Erosion and Sediment Yield: Global and Regional Perspectives*, IASH. Pub. No. 236, 149-156.

Hodson, A. J., Tranter, M., Dowdeswell, J.A., Gurnell, A.M., and Hagen, J.O., 1997. Glacier thermal regime and suspended-sediment yield: a comparision of two high-Arctic glaciers. *Annals Glaciology*, 24:32-37.

Holmlund, P. and Fuenzalida, H., 1995, Anomalous glacier responses to 20th century climatic changes in Darwin Cordillera, souther Chile. *Journal of Glaciology*, 41 (139): 465-473.

Hooke, R. LeB., and Elverhøi, A., 1996. Sediment flux from a fjord during glacial periods, Isfjorden, Spitsbergen. *Global and Planet*ary *Change*, 12: 237-249.

Hooke, R. LeB., Wold, B. and Hagen, J.O., 1985. Subglacial hydrology and sediment transport at Bondusbreen, southeast Norway. *Geological Society of America Bulletin,* 96: 388-397.

Howat, I.M., Joughin, I., Tulaczyk, S. and Gogineni, S., 2005. Rapid retreat and acceleration of Helhiem Glacier, east Greenland. *Geophysical Research Letters,* 32, L22502, doi:10.1029/2005GL024737.

Hubbard, A.L., 1997, Modelling climate, topography and paleoglacier fluctuations in the Chilean Andes. *Earth Surface Processes and Landforms*, 22: 79-92.

Hulton, N., Sugden, D., Payne, A. and Clapperton, C., 1994, Glacier modeling and the climate of Patagonia during the Last Glacial Maximum. *Quaternary Research*, 42: 1-19.

Hulton, N.R.J., Purves, R.S., McCulloch, R.D., Sugden, D.E. and Bentley, M.J., 2002, The Last Glacial Maximum and deglaciation in southern South America. *Quaternary Science Reviews*, 21: 233-241.

Humphrey, N.F. and Raymond, C. F., 1994. Hydrology, erosion and sediment production in a surging glacier: Variegated Glacier, Alaska, 1982-1983. *Journal of Glaciology*, 40:539-552.

Hunter, J.A. and S.E. Pullan, 1990. A vertical array method for shallow seismic refraction surveying of the sea floor, *Geophysics,* 55*:* 92-96.

Hunter, L.E., Powell, R.D. and Lawson, D.E., 1996. Flux of debris transported by ice at three Alaskan glaciers. *Journal of Glaciology*, 42(140):123-135.

Jaeger, J.M. and C.A. Nittrouer, 1999. Sediment deposition in an Alaskan fjord: Controls on the formation and preservation of sedimentary structures in Icy Bay, *Journal of Sedimentary Research,* 69*:* 1011-1026.

Jaeger, J.M. and Nittrouer, C.A., 1998. Sediment accumulation along a glacially impacted mountainous coastline: Northeast Gulf of Alaska. *Basin Research*, 10:155-173.

Kalnay, E., Kanamitsu, M., Kistler, R., Collins, W., Deaven, D., Gandin, L., Iredell, M., Saha, S., White, G., Woollen, J, Zhu, Y., Chelliah, M., Ebisuzaki, W., Higgins, W., Janowiak, J., Mo, K.C., Ropelewski, C., Wang, J., Leetmaa, A., Reynolds, R., Jenne, R., Joseph, D., 1996. The NCEP/NCAR 40-year reanalysis project. *Bulletin American Meterological Society*, 77: 437-471.

Kamb, B., Raymond, C.F., Harrison, W.D. , Engelhardt, H., Echelmeyer, K.A., Humphrey, N., Brugman, M.M., and Pfeffer, T., 1985. Glacier surge mechanism: 1982-1983 surge of Variegated Glacier, Alaska, *Science, 227*(4686): 469-479.

Kerr, A.R., Sugden, D.E., 1994. The sensitivity of the southern Chilean snowline to climatic change. *Climate Change* 28: 255– 272.

Klepeis, K. A., 1994., The Magallanes and Deseado fault zones: Major segments of the South American–Scotia transform plate boundary in southernmost South America, Tierra del Fuego: *Journal of Geophysical Research*, 99: 22001–22014.

Kobayashi, S., and Saito, T., 1985. Meteorological observations on Soler Glacier. In *Glaciological Studies in Northern Patagonia Icefield*, 1983-1984. Data Center for Glacier Research, Japanese Society of Snow and Ice, 32-36.

Kondo, H. and Yamada, T., 1988. Some remarks on the mass balance of the terminal-lateral fluctuations of San Rafael Glacier, the Northern Patagonia Icefield. *Bulletin of Glacier Research,* 6: 55-63.

Koons, P.O., Zeitler, P.K., Chamberlain, C.B., Craw, D., and Meltzer, A.S., 2002. Mechanical links between erosion and metamorphism in Nanga Parbat, Pakistan Himalaya, *American Journal of Science,* 302:749-773.

Koppes, M. and Hallet, B., 2006. Erosion rates during rapid deglaciation in Icy Bay, Alaska. *Journal of Geophysical Research* 111: F02023, doi:10.1029/2005JF000349.

Koppes, M. N. and Hallet, B., 2002. Influence of rapid glacial retreat on the rate of erosion by tidewater glaciers, *Geology* 30(1):47-50.

Koppes, M., 2000. "Influence of rapid glacial retreat on erosion rates for tidewater glaciers." University of Washington, M.S. Thesis, 43 pp.

Krabill, W, Hanna, E., Huybrechts, P., Abdalati, W., Cappelen, J., Csatho, B., Frederick, E., Manizade, S., Martin, C., Sonntag, J., Swift, R., Thomas, R., Yungel, J., 2004.

Greenland Ice Sheet: Increased coastal thinning, *Geophysical Research Letters* 31 (24): Art. No. L24402.

Kuriger, E.M., Bucki, A.K.., Motyka, R.J., and Truffer, M., 2003. Taku Glacier; proglacial deformation and subglacial erosion, in *Extreme events; understanding perturbation to the physical and biological environment,* AAAS Arctic Division, edited by J. Eichelberger, p. 200.

Lagoe, M.B. and Zellers, S.D., 1996. Depositional and microfaunal response to Pliocene climate change and tectonics in the eastern Gulf of Alaska, *Marine Micropaleontology,* 27*:*121-140.

Lagoe, M.B., Eyles, C.H., Eyles, N., and Hale, C., 1993. Timing of late Cenozoic tidewater glaciation in the far North Pacific, *Geological Society of America Bulletin,* 105: 1542-1560.

Lavé, J. and Avouac, J.P., 2001. Fluvial incision and tectonic uplift across the Himalayas of central Nepal. *Journal of Geophysical Research*, 106(B11): 26561-26591.

Lawrence, D.B., Lawrence, E.G., 1959. Recent glacier variations in southern South America. Technical Report, Office of Naval Research, American Geographical Society: New York; 39.

Lliboutry, L., 1999. Glaciers of the Wet Andes, *in* Williams, R.S., and Ferrigno, J.G., eds., *Satellite image atlas of glaciers of the world: South America*: U.S. Geological Survey Professional Paper 1386-I, http://pubs.usgs.gov/prof/p1386i/index.html

Lowell, T.V., Heusser, C.J., Andersen, B.G., Moreno, P.I., Hauser, A., Heusser, L.E., Schluchter, C., Marchant, D.R., Denton, G.H., 1995. Interhemispheric correlation of Late Pleistocene glacial events. *Science* 269:1541– 1549.

Luckman, A., Murray, T., de Lange, R. and Hanna, E., 2006. Rapid and synchronous ice-dynamic changes in East Greenland. *Geophysical Research Letters,* 33: L03503, doi:10.1029/2005GL025428.

Ludwig, W. and Probst, J.-L., 1998. River sediment discharge to the oceans; present-day controls and global budgets. *American Journal of Science*, 298(4): 265-295.

MacGregor, K. R., 2002. Modeling and field constraints on glacier dynamics, erosion, and alpine landscape evolution, Ph.D. dissertation thesis, Univ. of Calif., Santa Cruz.

MacGregor, K. R., Riihimaki, C. A. and Anderson, R. S., 2005, Spatial and temporal evolution of sliding velocity on a small alpine glacier: Bench Glacier, Alaska 1999 and 2000, *Journal of Glaciology.*, 51:49-63.

MacGregor, K. R., Anderson, R. S., Anderson. S.P., and Waddington, E.D., 2000. Numerical simulations of glacial-valley longitudinal profile evolution, *Geology,* 28(11):1031-1034.

Matsuoka, K. and Naruse, R., 1999. Mass balance features derived from a firn core at Hielo Patago´nico Norte, South America. *Arctic, Antarctic and Alpine Research,* 31(4): 333–340.

Meier, M. F., 1984. Contribution of small glaciers to global sea level. *Science*, 226(4681): 1418–21.

Meier, M.F. and Post, A., 1987. Fast tidewater glaciers, *Journal of Geophysical Research,* 92(B9): 9051-9058.

Meigs, A.,1998. Bedrock Landsliding Accompanying Deglaciation: Three Possible Examples From the Chugach/St. Elias Range, Alaska, *EOS Transactions AGU*, 79(45), Fall Meet. Suppl., Abstract F337.

Meigs, A. and Sauber, J., 2000. Southern Alaska as an example of the long-term consequences of mountain building under the influence of glaciers*, Quaternary Science Reviews*, 19:1543-1562.

Meigs, A., Krugh, W.C., Davis, K., and Bank, G., 2006.Ultra-rapid landscape response and sediment yield following glacier retreat, Icy Bay, southern Alaska, *Geomorphology* (in press).

Mercer, J. H., 1976. Glacial history of southernmost South America. *Quaternary Research*, 6: 125–166.

Mercer, J.H., and Sutter, J.F., 1982. Late Miocene–earliest Pliocene glaciation in southern Argentina: Implications for global ice-sheet history: *Palaeogeography, Palaeoclimatology, Palaeoecology*, 38: 185–206.

Merrand, Y. and Hallet, B., 2001. Climate controls on glacial erosion and sediment transfer: modeling a South Alaskan glacial basin from range divide to shelf break. *EOS Transactions*, AGU Fall Meeting Suppl., 82(47): F653.

Merrand, Y., and Hallet, B. 1998. Modeling the Evolution of Glaciated Mountain Ranges Guided by Field Studies in the High Coastal Mountains of Southern Alaska. *EOS Transactions,* AGU 79(45): F337.

Milliman, J.D. and Syvitski, J.P.M., 1992. Geomorphic/tectonic control of sediment discharge to the ocean: The importance of small mountainous rivers. *Journal of Geology*, 100: 525-544.

Milliman, J.D., 1997. Fluvial sediment discharge to the sea and the importance of regional tectonics. In: *Tectonic uplift and climate change* (Ed. by Ruddiman, W. F.). Plenum Press, New York, NY, 239-257.

Molnar, P. 2004. Late Cenozoic increase in accumulation rates of terrestrial sediment: how might climate change have affected erosion rates? *Annual Reviews, Earth and Planetary Science*, 32: 67-89.

Molnar, P., and England, P., 1990. Late Cenozoic uplift of mountain ranges and global climate change: Chicken or egg?, *Nature,* 346: 29-34.

Molnia, B.F., 1979. Sedimentation in coastal embayments in the northern Gulf of Alaska. *Procs. Offshore Tech. Conf*., 11: 665-676.

Molnia, B. F., Post, A., and Carlson, P.R., 1996. 20th-century glacial-marine sedimentation in Vitus Lake, Bering Glacier, Alaska, U.S.A. *Annals Glaciology*, 22: 205-210.

Molnia, B.F., T.J. Atwood, P.R. Carlson, A. Post, and S.C. Vath, 1984. Map of marine geology of upper Muir and Wachusett Inlets, Glacier Bay, Alaska: Sediment distribution and thickness, bathymetry and interpreted seismic profiles, *Open-File Map 84-632*, U.S. Geological Survey.

Montgomery, D.R., 2002. Valley formation by fluvial and glacial erosion. *Geology* 30:1047–50.

Montgomery, D.R., and Dietrich, W.E., 1992. Channel initiation and the problem of landscape scale, *Science*, 255:826-830.

Montgomery, D., Balco, G. and Willett, S.D., 2001. Climate, tectonics and the morphology of the Andes. *Geology*, 29(7):579-582.

Moreno, P.I., 2005. Western Patagonia: a key area for understanding Quaternary paleoclimate at southern mid-latitudes. In *The Patagonian Icefields: A Unique Natural Laboratory for Environmental and Climate Change Studies.* Eds. G. Casassa, F. Sepúlveda and R. Sinclair. Series of the Centro de Estudios Científicos. Kluwer Academic/Plenum Publishers, New York.

Motyka, R., Kuriger, E., and Truffer, M., 2005. Excavation of sediments by tidewater glacier advance and implications for the oceanic sediment record, Taku Glacier, Alaska, USA, *EGU Geophysical Research Abstracts,* 7:02901.

Motyka, R.J., Echelmeyer, KA., 2003. Taku Glacier (Alaska, U.S.A.) on the move again: active deformation of proglacial sediments. *Journal of Glaciology* 49: 50–58.

Motyka, R.J., Hunter, L., Echelmeyer, K.A and Connor, C., 2003. Submarine melting at the terminus of a temperate tidewater glacier, LeConte Glacier, Alaska, U.S.A., *Annals of Glaciology*, 36:57-65.

Muller, E.H., 1960. Glacial chronology of the Laguna San Rafael area, Southern Chile. *Bulletin of the Geological Society of America* 71:2106.

Naruse, R., 1985. Flow of Soler Glacier and San Rafael Glacier, In Glaciological Studies in Northern Patagonia Icefield, 1983-1984. Data Center for Glacier Research, Japanese Society of Snow and Ice, 32-36.

Naruse, R. and Skvarca, P., 2000, Dynamic features of thinning and retreating Glaciar Upsala, a lacustrine calving glacier in southern Patagonia. *Arctic, Antarctic, and Alpine Research,* 32 (4): 485-491.

Naruse, R., Aniya, M., Skvarca, P. and Casassa, G., 1995. Recent variations of calving glaciers in Patagonia, South America, revealed by ground surveys, satellite-data analyses and numerical experiments. *Annals of Glaciology* 21:297-303.

Naruse, R., Pena, H., Aniya, M., and Inoue, J., 1987. Flow and surface structure of Tyndall Glacier, the Southern Patagonian Icefiled. *Bulletin of Glacier Research*, 4: 133–140.

Nishida, K., Sataw, K., Aniya, M., Casassa, G. and Kadota, T.,1995. Thickness change and flow at Tyndall Glacier, Patagonia. *Bulletin of Glacier Research*, 13: 29-34.

Nye, J. F., 1965. The flow of a glacier in a channel of rectangular, elliptic and parabolic cross-section. *Journal of Glaciology*, 5(41): 661–690.

Ohata, T., Enomoto, H. and Kondo, H., 1985. Characteristic of ablation at San Rafael Glacier. In *Glaciological Studies in Patagonia Northern Icefield 1983-1984*, Nagoya (Japan), Nakajima, C, *Ed.*, 37-45.

Ohata, T., Kondo, H. and Enomoto, H., 1985, Meteorological observations at San Rafael Glacier. In *Glaciological Studies in Patagonia Northern Icefield 1983-1984*, Nagoya (Japan), Nakajima, C, *Ed.*, 22-31.

Olivero, E.B. and Martinioni, D.R., 2001. A review of the geology of the Argentinian Fuegian Andes. *Journal of South American Earth Sciences*, 14: 175-188.

Pankhurst, R. J., Weaver, S. D., Hervé, F., and Larrondo, P., 1999. Mesozoic-Cenozoic evolution of the North Patagonian Batholith in Aysén, southern Chile, *Journal of the Geological Society*, London, 156: 673-694.

Pardo-Casas, F., and Molnar, P., 1987, Relative motion of the Nazca (Farallon) and South American plates since Late Cretaceous times, *Tectonics,* 6: 233–248.

Paterson, W.S.B., 1994. The Physics of Glaciers. 4th ed., Oxford: Pergamon Press. 480 pp.

Pelto, M.S. and Warren, C.R., 1991. Relationship between tidewater calving velocity and water depth at the calving front, *Annals of Glaciology*, 15:115-118.

Pena, H. and Escobar, F., 1987. Aspects of glacial hydrology in Patagonia, *Bulletin of glacier research*, 4: 141-150.

Plafker, G., Moore, J.C., and Winkler, G.R.,1994. Geology of the southern Alaska margin, in *The geology of Alaska*, *Geology of North America, G-1*, G. Plafker and H.C. Berg (eds.), Geological Society of America, Boulder, Colorado, 389–449.

Porter, C. and Santana, A., 2003. Rapid 20th century retreat of Ventisquero Marinelli in the Cordillera Darwin Icefield, *Anales Instituto Patagonia (Chile)*, 31: 17-26.

Porter, S.C., 2000. Onset of Neoglaciaion in the Southern Hemisphere. *Journal of Quaternary Science* 15: 395-408.

Porter, S.C., 1989. Late Holocene fluctuations of the fiord glacier system in Icy Bay, Alaska, U.S.A., *Arctic and Alpine Research*, 21: 364-379.

Porter, S.C., 1981. Pleistocene glaciation in the southern Lake District of Chile. *Quaternary Research*, 16: 263-292.

Post, A., 1997. Active and passive calving. In: Van der Veen, C.J. (ed), Calving Glaciers, Reports of a Workshop. Byrd Polar Research Center, The Ohio State University, BPRC Report No. 15.

Post, A., 1983. Preliminary bathymetry of upper Icy Bay, Alaska, *Open File report 83-256*, 1 sheet, U.S. Geological Survey.

Post, A. and Sylwester, D., 1981. Preliminary sub-bottom profiling map of upper Icy Bay, Alaska, *USGS Working File*. Unpublished.

Powell, R.D., 1991. Grounding-line systems as second-order controls on fluctuations of tidewater termini of temperate glaciers, in *Glacial marine sedimentation; Paleoclimatic significance, Geological Society of America Special Paper 261*, edited by J.B. Anderson and G.M. Ashley, 75-94.

Powell, R.D., 1990. Glacimarine processes at groundling line fans and their growth to ice-contact deltas. In: *Glacimarine Environments: Processes and Sediments* (Ed. by J.A. Dowdeswell and J.D. Scourse), *Geol. Soc. Special Pub*., 53: 53-74.

Powell, R.D., and Alley, R.B., 1997. Grounding-line systems: processes, glaciological inferences, and the stratigraphic record. In: *Geology and Seismic Stratigraphy of the Antarctic Margin 2* (Ed. By P.F. Barker and A.K. Cooper), *Antarctic Research Series*, 71: 169-187.

Powell, R.D., and Molnia, B.F., 1989. Glacialmarine sedimentary processes, facies, and morphology of the south-southeast Alaska shelf and fjords. *Marine Geology* 85: 359-390.

Powell, R.D., Dawber, M., McInnes, J.N., and Pyne, A.R., 1996, Observations of the grounding-line area at a floating glacier terminus: *Annals of Glaciology*, 22: 217-223.

Rabassa, J., and Clapperton, C.M., 1990. Quaternary glaciations of the southern Andes. *Quaternary Science Reviews,* 9:153-174.

Rabassa, J., Bujalesky, G.G., Megioli, A., Coronato, A., Gordillo, S., Roig, C. and Salemme, M., 1992. The Quaternary of Tierra del Fuego, Argentina: the status of

our knowledge, *Quaternary stratigraphy, glacial morphology and environmental changes,*81 (1): 249-256.

Rasmussen, L.A., 1991. Piecewise Integral Splines of Low Degree, *Computers & Geosciences*, 17: 1255-1263.

Rasmussen, L.A. and Conway, H., 2004. Climate and glacier variability in western North America, *Journal of Climate*, 17:1804-1815.

Rasmussen, L.A., and Conway, H., 2001. Estimating South Cascade Glacier (Washington, U.S.A.) mass balance from a distance radiosonde and comparison with Blue Glacier. *Journal of Glaciology*, 47 (159): 579-588.

Rasmussen, L.A., Conway, H., and Hayes, P.S., 2000. The accumulation regime of Blue Glacier, U.S.A., 1914-96. *Journal of Glaciology*, 46(153): 326-334.

Raymo, M. E., and Ruddiman, W. F., 1992. Tectonic forcing of late Cenozoic climate. *Nature*, 359 (6391): 117-122.

Raymo, M.E., W.F. Ruddiman, and P.N. Froelich, 1988. Influence of late Cenozoic mountain building on ocean geochemical cycles, *Geology,* 16*:* 649-653.

Raymond, C., Neumann, T.A., Rignot, E., Echelmeyer, K., Rivera, A. and Casassa, G., 2005. Retreat of Glaciar Tyndall, Patagonia, over the last half-century. *Journal of Glaciology*, 51 (173): 239-247.

Reiners, P.W., and Brandon, M.T, 2006. Using thermochronology to understand orogenic erosion. *Annual Review of Earth Planetary Sciences*, 34:419-466.

Reiners, P.W., and Ehlers, T.A., 2005. *Low-temperature Thermochronology: Techniques, Interpretations, Applications. Reviews in Mineralogy and Geochemistry,* 58. Mineralogical Society of America, 622 pp.

Reiners, P.W., Ehlers, T.A., Mitchell, S.G., and Montgomery, D.R., 2003. Coupled spatial variations in precipitation and long-term erosion rates across the Washington Cascades. *Nature,* 426:645–47.

Rignot, E. and Kanagaratnam, P., 2006. Changes in the Velocity Structure of the Greenland Ice Sheet, *Science,* 311(5763): 986-990.

Rignot, E., Rivera, A. and Casassa, G., 2003, Contribution of the Patagonia Icefields of South America to sea level rise. *Science*, 302: 434-437.

Rignot, E., Forster, R. and Isacks, B., 1996. Interferometric radar observations of Glaciar San Rafael, Chile, *Journal of Glaciology,* 42 (141): 279-291

Riihimaki, C. A., MacGregor, K. R., Anderson, R. S., Anderson, S. P., and Loso, M. G., 2005. Sediment evacuation and glacial erosion rates at a small alpine glacier, *Journal of Geophysical Research*, 110, F03003, doi:10.1029/2004JF000189.

Riis, F., and Fjeldskaar, W., 1992. On the magnitude of the late Tertiary and Quaternary erosion and its significance for the uplift of Scandinavia and the Barents Sea. In: *Structural and tectonic modelling and its application to petroleum geology* (Ed. by Larsen, R.M.). Norwegian Petroleum Soc., Special Pub., 1:163-185.

Riis, F., 1992. Dating and measuring of erosion, uplift and subsidence in Norway and the Norwegian shelf in glacial periods. *Norsk Geologisk Tidsskrift*, 72(3): 325-331.

Rivera, A. and Casassa, G., 2004. Ice elevation., areal, and frontal changes of glaciers from National Park Torres del Paine, Southern Patagonia Icefield. *Arctic, Antarctic, and Alpine Research,* 36 (4): 379-389.

Rivera, A. and Casassa, G., 2002. Detection of ice thickness using radio-echo sounding on the Southern Patagonia Icefield. In *The Patagonian Icefields: A Unique Natural Laboratory for Environmental and Climate Change Studies.* (Eds. G. Casassa, F. Sepúlveda and R. Sinclair.) Series of the Centro de Estudios Científicos. Kluwer Academic/Plenum Publishers, New York.

Rivera, A. and Casassa, G., 1999. Volume changes on Pio XI glacier, Patagonia: 1975-1995. *Global and Planetary Change*, 22: 233-244.

Rivera, A., Benham, T., Casassa, G., Bamber, J., Dowdeswell, J., 2006. Ice elevation and areal changes of glaciers from the North Patagonia Icefield, Chile. *Global and Planetary Change* (in press) doi:10.1016/j.gloplacha.2006.11.037

Rivera, A., Casassa, G., Bamber, J. and Kääb, A., Thomas, R., Rignot, E., 2003. Ice elevation changes in the Southern Patagonia Icefield, using ASTER DEMs, aerial photographs and GPS data. EGS - AGU - EUG Joint Assembly, Meeting Abstracts, #7355.

Roche, J. W., 1996. Lithologic controls on rapid frost-induced breakdown of rock, Icy Bay, Alaska: Implications for enhanced sediment production during glacial-interglacial cycles, (MS Thesis), University of Washington.

Roe, G.H., 2005. Orographic precipitation. *Annual Reviews Earth Planetary Sciences*, 33:645-671.

Roe, G.H., Stolar, D.R., and Willett, S.D., 2006. Response of a steady-state critical orogen to changes in climatic and tectonic forcing, in *Tectonics, Climate, and Landscape Evolution, GSA Special Paper 398, Penrose Conference Series*, Willett, S.D., Hovius, N., Brandon, M.T., and Fisher, D.M.(eds), 227-239.

Rosenblüth, B., Casassa, G. and Fuenzalida, H., 1995. Recent climatic changes in western Patagonia. *Bulletin of Glacier Research*, 13: 127-132.

Rothlisberger, H., 1972. Water pressure in intra- and subglacial channels, *Journal of Glaciology*, 11:177–203.

Rothlisberger, H., 1968. Erosive processes which are likely to accentuate or reduce the bottom relief of valley glaciers, Int. Union Geodesy Geophysics, General Assembly of Bern, 1967, *Int. Assoc. Scientific Hydrology Pub. No. 79*, p. 87-97.

Rubio, E., Torné, M., Vera, E. and Diaz, A., 2000. Crustal structure of the southernmost Chilean margin from seismic and gravity data. *Tectonophysics*, 323: 39-60.

Ruddiman, W. F., Raymo, M.E., Prell, W.L., and Kutzbach, J.E., 1997. The uplift-climate connection; a synthesis. In*: Tectonic uplift and climate change* (Ed. by Ruddiman, W. F.). Plenum Press, New York, NY, 471-515.

Ruhl, K.W. and Hodges, K.V., 2005. The use of detrital mineral cooling ages to evaluate steady-state assumptions in active orogens: an example from the central Nepalese Himalaya. *Tectonics*, 24:TC4015, doi:10.1029/2004TC001712

Rundle, A.S., 1970. Snow accumulation and ice movement on the Anvers Island ice cap, Antarctica; a study of mass balance. In: *International symposium on Antarctic glaciological exploration*, Intl. Assoc. Scientific Hydrology, 86: 377-390.

Schmidt, K.M., and Montgomery, D.R., 1995. Limits to relief, *Science* 270:617-620.

Schneider, C. and Gies, D, 2004. Effects of El Nino-Southern Oscillation on southernmost South America precipitation at 53ºS revealed from NCEP-NCAR reanalyses and weather station data. *International Journal of Climatology* 24: 1057-1076.

Schneider, C., Glaser, M., Kilian, R., Santana, A., Butorovic, N. and Casassa, G., 2003. Weather observations across the southern Andes at 53ºS, *Physical Geography,* 24 (2): 97-119.

Seifert, W., Rosenau, M., and Echtler, H., 2004. Crystallization depths of granitoids of South Central Chile estimated by Al-in-hornblende geobarometry: implications for mass transfer processes along the active continental margin. *N. Jb. Geol. Paläont.* (in press).

SERNAGEOMIN, 2003. Mapa Geológico de Chile: versión digital. *Servicio Nacional de Geología y Minería, Publicación Geológica Digital,* No. 4 (CD-ROM, versión1.0, 2003). Santiago.

Sheaf, M.A., Serpa, L., and Pavlis, T.L., 2003. Exhumation rates in the St. Elias mountains, Alaska, *Tectonophysics,* 367(1): 1-11.

Shevenell, A. E., Domack, E. W., and Kerman, G. M., 1996. Record of Holocene paleoclimate change along the Antarctic Peninsula: evidence from glacial marine sediments, Lallemand Fjord. *Papers and Proceedings of the Royal Society of Tasmania*, 130: 55-64.

Shuster, D.L., Ehlers, T.A., Rusmore, M.E., and Farley, K.A., 2005. Rapid glacial erosion at 1.8 Ma revealed by 4He/3He thermochronometry. *Science* 310:1668-1670.

Simpson, E.M., 1875. Esploraciones hechas por la corbeta Chacbuco..*Anuario Hidrografico de la Marina de Chile* 1: 3– 166.

Skinner, B.J. and Porter, S.C., 2000. *The Dynamic Earth: An Introduction to Physical Geology*. 4nd edition. New York: John Wiley and Sons, 575 pp.

Sklar, L. and Dietrich, W.E, 1998. River longitudinal profiles and bedrock incision models: Stream power and the influence of sediment supply. In *Rivers over Rock, Fluvial Processes in Bedrock Channels,* Tinker, T.J., and Wohl, E.L. (eds)., AGU Geophysical Monograph, 107:237-260.

Small, E.E. and Anderson, R.S, 1998. Pleistocene relief production in Laramide mountain ranges, western United States. *Geology,* 32:501-504.

Smith, A.M., Murray, T., Nicholls, K.W., Makinson, K., Aðalgeirsdóttir, G., Behar, A.E., and Vaughan, D.G., 2007. Rapid erosion, drumlin formation, and changing hydrology beneath an Antarctic ice stream . *Geology,* 35(2):127-130.

Smith, R.B. and Barstad, I., 2004. A linear theory of orographic precipitation. *Journal of the Atmospheric Sciences*, 61:1377-1391.

Spotila, J., Buscher, J., Meigs, A., and Reiners, P., 2004. Long-term glacial erosion of active mountain belts: Example of Chugach-St. Elias range, Alaska, *Geology,* 32: 501-504.

Spotila, J.A. and Buscher, J., 2002. Measuring crustal convergence using rock exhumation along the complex glaciated Chugach mountains, Southeast Alaska. *EOS Transactions*, AGU Fall Meeting Suppl., 83(47): T71B-1173.

Steffen, H., 1910. Viajes de esploracion y estudio en la Patagonia Occidental, 1892-1902, vol. 2.

Steig, E.J., et al., 1998. Synchronous climate changes in Antarctica and the North Atlantic. *Science* 282: 92– 95.

Stock, J.D. and Montgomery, D.R., 1999. Geologic constraints on bedrock river incision using the stream power law. *Journal of Geophysical Research*, 104: 4983-4993.

Stoker, M.S., J.B. Pheasant, and H. Josenhans, 1997. Seismic methods and interpretation, in *Glaciated continental margins: an atlas of acoustic images*, edited by T.A. Davies et al., London, Chapman & Hall, 9-26.

Stravers, J.A. and Syvitski, J.P.M., 1991. Land-sea correlations and evolution of the Cambridge Fiord marine basin during the last glaciation of northern Baffin Island, *Quaternary Research*, 35: 72-90.

Stravers, J.A., Miller, G.H. and Kaufman, D.S., 1992. Late glacial ice margins and deglacial chronology for southeastern Baffin Island and Hudson Strait, *Canadian Journ. Earth Sciences* 29(5): 1000-1017.

Sugden, D.E., Bentley, M.J., Fogwill, C.J., Hulton, N.R.J., McCulloch, R.D., and Purves, R.S., 2005. Late-glacial glacier events in southernmost South America: a blend of 'northern' and 'southern' hemispheric climatic signals? *Geografiska Annaler,* 87 A (2): 273-288.

Sugden, D.E., Hulton, N.R.J. and Purves, R.S. 2002. Modelling the inception of the Patagonian icesheet. *Quaternary International*, 95-96: 55-64

Summerfield, M. A. and Hulton, N. J., 1994. Natural controls of fluvial denudation rates in major world drainage basins. *Journal of Geophysical Research*, B99 (7): 13871-13883.

Syvitski, J.P.M., 1994. Glacial sedimentation processes, *Terra Antarctica*, 1: 251-253.

Syvitski, J.P.M., 1989. On the deposition of sediment within glacier-influenced fjords: oceanographic controls, *Marine Geology,* 85: 301-329.

Thomas, R.H., 2004. Force-perturbation analysis of recent thinning and acceleration of Jakobshavn Isbrae, Greenland, *Journal of Glaciology* 50(168): 57-66.

Thomas, R. H., Abdalati, W., Frederick, E., Krabill, W.B., Manizade, S., and Steffen, K., 2003. Investigation of surface melting and dynamic thinning on Jakobshavn Isbrae, Greenland. *Journal of Glaciology* 49: 231-239.

Thomson, S.N., Hervé, F. and Stöckhert, B., 2001. Mesozoic-Cenozoic denudation history of the Patagonian Andes (southern Chile) and its correlation to different subduction processes. *Tectonics*, 20 (5): 693-711.

Thomson, S.N., 2002. Late Cenozoic geomorphic and tectonic evolution of the Patagonian Andes between latitudes 42ºS and 46ºS: An appraisal based on fission-track results from the transpressional intra-arc Liquine-Ofqui fault zone. *Geological Society of America Bulletin*, 114 (9): 1159-1173.

Tomkin, J.H., 2003. Erosional feedbacks and the oscillation of ice masses, *Journal of Geophysical Research,* 108(B10): 2488, doi:10.1029/2002JB002087.

Tomkin, J.H., and Braun, J. 2002. The influence of alpine glaciation on the relief of tectonically active mountain belts. *American Journal of Science*, 302: 169-190.

Truffer, M., Motyka, M. J., Harrison, W. D., Echelmeyer, K. A., Fiske, B., and Tulaczyk, S., 1999. Subglacial drilling at Black Rapids Glacier, Alaska, U.S.A.: drilling method and sample descriptions. *Journal of Glaciology*, 45(151): 495–505.

Tucker, G.E. and Slingerland, R.L., 1997. Drainage basin response to climate change. *Water Resources Research*, 33: 2031-2047.

Van der Veen, C. 1996. Tidewater calving. *Journal of Glaciology*, 42: 375-385.

Venteris, E.R., 1999. Rapid tidewater glacier retreat: a comparison between Columbia Glacier, Alaska and Patagonian calving glaciers. *Global and Planetary Change*, 22:131-138.

Venteris, E.R., Whillans, I.M., and Van der Veen, C.J., 1997. Effect of extension rate on terminus positions, Columbia Glacier, Alaska, USA. *Annals of Glaciology* 24:49-53.

Vieira, R., 2006. Interpretação integrada de sísmica de alta-resolução e da morfologia submarina da Costa de Fiordes da Patagônia Central-Chile. PhD thesis, UFRGS, Porto Alegre, Brazil. 181 pp..

Vorren, T.O., Richardsen, G., Knutsen, S.M. and Henriksen, E., 1991. Cenozoic erosion and sedimentation in the western Barents Sea. *Marine and Petroleum Geology*, 8(3): 317-340.

Warren, C.R., 1993, Rapid recent fluctuations of the calving San Rafael Glacier, Chilean Patagonia: climatic or non-climatic? *Geografiska Annaler,* 75 A (3): 111-125.

Warren, C.R. and Aniya, M., 1999. The calving glaciers of southern South America. *Global and Planetary Change*, 22:59-77.

Warren, C.R. and Sugden, D.E., 1993. The Patagonian Icefields: a glaciological review, *Arctic and Alpine Research,* 25(4):316-331.

Warren, C.R., Glasser, N.F., Harrison, S., Winchester, V., Kerr, A., and Rivera, A., 1995. Characteristics of tide-water calving at Glaciar San Rafael, Chile. *Journal of Glaciology*, 41(138): 273-289.

Weber, M.E., Niessen, F., Kuhn, G., and Wiedicke, M., 1997. Calibration and application of marine sedimentary physical properties using a multi-sensor core logger. *Marine Geology*, 136:151-172.

Whipple, K.X. and Tucker, G.E., 1999. Dynamics of the stream-power river incision model: Implications for height limits of mountain ranges, landscape response timescales, and research needs. *Journal of Geophysical Research*, 104(B8): 17661-17674.

Whipple, K., Kirby, E. and Brocklehurst, S., 1999. Geomorphic limits to climatically induced increases in topographic relief. *Nature*, 401:39-43.

Willett, S., Beaumont, C., and Fullsack, P., 1993. Mechanical model for the tectonics of doubly vergent compressional orogens. *Geology*, 21: 371-374.

Willett, S.D., Slingerland, R. and Hovius, N., 2001. Uplift, shortening, and steady state topography in active mountain belts. *American Journal of Science*, 301: 455-485.

Wilson, J.G. and Overland, J.E., 1987. Meteorology, in *The Gulf of Alaska: Physical environment and biological resources*, edited by D.W. Hood and S.T. Zimmerman, Nat. Ocean Atmos. Adm., U.S. Dept. Commerce, 31-56.

Winchester, V., and Harrison, S., 1996. Recent oscillations of the San Quintin and San Rafael Glaciers, Patagonian Chile. *Geografisk. Annaler,* 78 A (1): 35-49.

Winslow, M.A., 1982.The structural evolution of the Magallanes basin and neotectonics in the southernmost Andes, in *Antarctic geosciences*, C. Craddock (ed.) Madison: University of Wisconsin Press, 143-154.

Wood, R.M., 1989. Recent normal faulting at Laguna de San Rafael, Aisen Province, southern Chile, Departamento de Geologı´a, Universidad de Chile, *Comunicaciones*, no. 40, 57–68.

Yamada, T. 1987. Glaciological characteristics revealed by 37.6m deep core drilled at the accumulation area of San Rafael Glacier, the Northern Patagonia Icefield. *Bulletin of Glacier Research,* 4: 59–67.

Zhang, P., Molnar P., and Downs, W. R., 2001. Increased sedimentation rates and grain sizes 2–4 Myr ago due to the influence of climate change on erosion rates. *Nature,* 410:891–97

Zeitler, P.K., Meltzer, A.S. , Koons, P., Craw, D., Hallet, B., Chamberlain, C.P., Kidd, W., Park, S., Seeber, L., Bishop, M., and Shroder, J., 2001. Erosion, Himalayan geodynamics and the geology of metamorphism, *GSA Today,* 11: 4-8.

Zeitler, P.K., Koons, P.O., Bishop, M.P., Chamberlain, C.P., Crew, D., Edwards, M., Hamidullah, S., Jan, M.Q., Khan, M.A., Khattak, M.U.K., Kidd, W.S.F., Mackie, R.L., Meltzer, A.S., Park, S.K., Pecher, A. Poage, M.A., Sarker, G., Schneider, D.A., Seeber, L. and Schroeder, J.F., 2001. Crustal reworking at Nanga Barbat, Pakistan: Metamorphic consequences of thermal mechanical coupling facilitated by erosion. *Tectonics*, 20 (5): 712-728.